Measurement of Spin Correlation in top quark pair production at ATLAS

Thomas McLaughlan

Thesis submitted for the degree of

Doctor of Philosophy

Particle Physics Group,

School of Physics and Astronomy,

University of Birmingham.

January 9, 2014

Abstract

This thesis presents a study of spin correlation in $t\bar{t}$ production in the ATLAS detector, in proton-proton collisions, corresponding to an integrated luminosity of 4.7fb^{-1}, with a centre of mass energy of $\sqrt{s} = 7$ TeV. Both the dilepton and single lepton channels are considered, the latter providing a greater challenge due to the neccessity to reconstruct the down-type quark resulting from the W boson decay.

A simple technique is employed to reconstruct single lepton $t\bar{t}$ events, with the transverse angle between the charged lepton and down-type quark used as a probe of the spin correlation. In the dilepton channel, the transverse angle between both charged leptons is used.

The extracted value of spin correlation in each channel is consistent with Standard Model predictions, with the result in the eμ channel alone sufficient to exclude a model without spin correlation at 7.8σ.
Also described is the author's contribution to the maintenance and development of the Atlantis Event Display.

Author's Contribution

The successful running of ATLAS and the LHC is the result of many thousands of scientists' and engineers' work, spanning many years. Over the course of the last three and a half years, I have made contributions to both technical and scientific areas within ATLAS, the results of which are detailed in this thesis.

The opening chapters of this thesis detail the design and operation of the LHC and ATLAS; work with which I have not been directly involved, which it is necessary to describe for the context of the latter chapters.

My main contribution to the technical operation of the ATLAS experiment has been in developing and maintaining the event displays. This involves conceptualising and implementing the features described in section 4.4, as well as providing on-call support for the event display hardware and software to the shifters in the ATLAS control room. Related to my work with event displays, I have contributed significantly to the organisation and running of several outreach 'Masterclasses', both building on the work of others before me, and developing new exercises for students wishing to learn more about particle physics.

The analysis section of this thesis is my own work, and was carried out in parallel to other similar analyses in progress by Simon Head at Birmingham, as well as groups in Manchester and Göttingen.

For Emily

Acknowledgements

I owe a debt of gratitude to a great many people, without whom I would not have been able to complete this thesis.

Firstly I would like to thank John Wilson for his help and guidance throughout the last three and a half years, both with physics and in outreach. Thanks also to Pete Watkins for introducing me to many concepts of event displays and outreach, always spurring me on to do bigger and better things with the time available. Despite the time investment required, physics outreach has become a thoroughly enjoyable experience.

Everyone in West 316 past and present; Chris C, Mark S, Joseph, Neil, Dave, Tim, Jody, Hardeep, Andy, Benedict, Javier, Richard, Andrew and Mark L, (Honourable mention to Tony and Patrick, part time office mates) for excellent conversation, excellent pub time, and most of all, excellent procrastination.

To the inhabitants of all the other, lesser, offices, both at Birmingham and CERN for film nights, cocktails, music and more.

Thanks to Simon Head, for sticking with me for a whole analysis and teaching me the finer points of 'particle politics'. And pointing out the flaws, and blatant errors, in my grammar, and my excessive use, sometimes unnecessarily, of commas.

Thanks to Paul Newman for his advice, guidance and trusting me to organise the office Christmas party.

Thanks to Juergen for event display advice mixed with every conversation topic imaginable.

Finally, thanks to my parents for moral (and logistical) support throughout, and to Emily for keeping me sane.

Cyberspace. A consensual hallucination experienced daily by billions of legitimate operators, in every nation, by children being taught mathematical concepts...
A graphic representation of data abstracted from banks of every computer in the human system.
Unthinkable complexity.

William Gibson - *Neuromancer*

Contents

List of Figures

List of Tables

List of Acronyms

AD Antiproton Decelerator

ALICE A Large Ion Collider Experiment

AOD Analysis Object Data

ATLAS A Toroidal LHC ApparatuS]

CDF Collider Detector at Fermilab

CERN Organisation Européenne pour la Recherche Nucléaire

CKM Cabbibo-Kobayashi-Maskawa

CMS Compact Muon Solenoid

CNGS CERN Neutrinos to Gran Sasso

CSC Cathode Strip Chambers

DPD Derived Physics Data

EF Event Filter

EM Electromagnetic

ESD Event Summary Data

FSR Final State Radiation

GRL Good Runs List

GUI Graphical User Interface

ID Inner Detector

ISR Initial State Radiation

JES Jet Energy Scale

JVF Jet Vertex Fraction

LEIR Low Energy Ion Ring

LEP Large Electron Positron collider

LHC Large Hadron Collider

LHCb LHC-beauty

LO Leading Order

MC Monte Carlo

MDT Monitored Drift Tubes

MINERVA Masterclass INvolving Event Recognition Visualised with Atlantis

MPI Multiple Parton Interaction

NLO Next to Leading Order

NNLL Next to Next to Leading Log

NNLO Next to Next to Leading Order

PDF Parton Distribution Function

PS Proton Synchrotron

PSB Proton Synchrotron Booster

QCD Quantum Chromodynamics

RF Radio Frequency

ROI Region of Interest

RPC Resistive Plate Chambers

SCT Semi Conductor Tracker

SPS Super Proton Synchrotron

SVN Subversion

TGC Thin Gap Chambers

TRT Transistion Radiation Tracker

Chapter 1

Non-Technical Overview

1.1 Introduction

Particle physics is often called *High Energy Physics*, or *Elementary Particle Physics*. The former term is descriptive of the means of study, while the latter is descriptive of the motive; high energy beams of particles are used in order to study the elementary constituents of matter.

The idea that matter is composed of elementary 'building blocks' can be traced back at least as far as Ancient Greece, where the philosophers proposed that all matter can be split into indivisible components, or *atoms*. It is only in the last century or so that experiment has been able to study the constituents of matter. The discovery of the electron in the late 1800's spurred many advances in the field of particle physics, and since then, particle after particle has been discovered and added to a still growing list.

Early particle physics experiments used cosmic rays as the source of high energy particles, while developments in accelerating charged particles in an electric field [1] allowed for collisions between beams of particles and stationary targets and later,

collisions of beams of particles from both linear and circular accelerators. As the energy of the beams used in collider experiments increases, the effective resolving power of the experiment improves. Assuming the particles in the beam are point-like (e.g. electrons), the resolving power can be approximated by the de Broglie wavelength of the particle,

$$\lambda = \frac{h}{p}, \tag{1.1}$$

where h is Planck's constant and p the momentum of the particle. Thus, higher energy experiments can probe smaller distances. This is useful, for example, in probing the structure of the proton, revealing its nature as a composite particle (composed of triplets of quarks).

Using the energy mass equivalence,

$$E = mc^2, \tag{1.2}$$

entirely new particles can be created. For example, if an electron annihilates with a positron with at least 91 GeV centre of mass energy, a Z boson may be created.

1.1.1 Units in Particle Physics

In particle physics, typical energies expressed in SI units tend to be of the order 10^{-10} Joules, and masses around 10^{-27} kg. This makes using SI units to describe physics on such small scales quite cumbersome. Instead, units based on the amount of energy gained by an electron moving across a potential of 1 V (1 electronVolt $\approx 1.6 \times 10^{-19}$ J) are used. An additional convenience is to absorb some frequently used constants c and $\hbar$, into the units themselves, effectively setting $c = 1$ and $\hbar = 1$.

For example, the mass-energy of a proton would be expressed as

$$E = mc^2 = (1.67 \times 10^{-27})(3 \times 10^8)^2/(1.6 \times 10^{-19})\text{eV} = 0.939 \text{ GeV} \tag{1.3}$$

and the proton mass can thus be written

$$m = E/c^2 = 0.939 \text{ GeV}/c^2 \tag{1.4}$$

Similarly, momentum can be expressed the units of GeV/c.

1.2 The Standard Model

1.2.1 Fermions

The myriad of particles discovered and studied since the discovery of the electron [2] have mostly been determined to be composite particles. Just as a helium atom can be split into two protons, two neutrons and two electrons, in the simplest view, a proton comprises two up quarks and a down quark, bound together by the gluons of the strong force. A composite particle formed of three quarks like this is called a *baryon*. Similarly, there can exist particles consisting of a quark and an anti-quark, such as a pion. These particles are known as *mesons*. Both baryons and mesons are made up of quarks and can be further grouped into *hadrons*. All hadrons are formed of quarks, but not all quarks share the same properties. Up quarks have electric charge $+\frac{2}{3}$ while down quarks have electric charge $-\frac{1}{3}$, in units of the electron charge. A proton, made of two up quarks and a down quark, then has total charge +1, and a neutron, made of two down quarks and an up quark, has charge 0.

While many baryons have been discovered, they are not all made of the same two quark types, or *flavours*. In order to describe the intrinsic properties of the so called *particle zoo*, additional flavours were introduced to the quark model [3]. In fact, there have been discovered three 'generations' of quarks [4], each generation having a positively and negatively charged member. The first generation contains the familiar *up* (u) and *down* (d) quarks. The second generation contains *charm*

Family	Particle	Charge
lepton	$e\ \mu\ \tau$	-1
	$\nu_e\ \nu_\mu\ \nu_\tau$	0
quark	$u\ c\ t$	$+\frac{2}{3}$
	$d\ s\ b$	$-\frac{1}{3}$

Table 1.1: The fermion sector of the Standard Model.

(c) and *strange* (s) quarks, carrying the same respective charges but with different quantum numbers, as well as higher masses. Finally there is a third generation of quarks, the *top* (t) and *bottom* (b) quarks, which again have the same respective charges but still higher masses. In fact, the top quark is the most massive elementary particle yet to be discovered.

Returning to the Helium atom, in addition to quarks making up the protons and neutrons in the nucleus, the Helium atom also contains two electrons. Similar to the generations of quarks, there have been discovered 'heavier electrons'. The *muon* is similar to the electron but with a larger mass, and the *tau* is more massive than the muon. Each of these particles has a charge of -1 and a corresponding electrically chargeless partner, called a *neutrino*. These six particles form a group called *leptons*, and along with the quarks, are members of a larger group called *fermions* (see table 1.1).

All particles possess another quantum property called *spin*. Spin is a form of angular momentum, though unlike angular momentum in classical physics, spin is quantised, i.e. it takes on only discrete values. Fermions can be classified as elementary particles which carry spin $\frac{1}{2}$ (in units of $\hbar$). The spin can take on two possible orientations, $+\frac{1}{2}$ or $-\frac{1}{2}$, commonly called spin-up and spin-down. Composite particles with half-integer spin other than $\frac{1}{2}$ (such as $\frac{3}{2}$), would also be described as fermions, though all known elementary fermions carry spin $\frac{1}{2}$.

The fermions are responsible for making up 'everyday matter'; particles such as

protons, neutrons and electrons are fermions which form the atoms that make up elements and the Periodic Table. There are also particles which possess integer spin, known as bosons. Integer spin particles may be composite; made up of two quarks whose spin is arranged such that the sum is an integer (Mesons).

1.2.2 Bosons

Particle physics is concerned also with the interactions between particles. These interactions are mediated by 'force carrying' particles. These particles are all fundamental bosons. There are four fundamental interactions (see table 1.2), or forces, which may occur between particles:

- Electromagnetic - The electromagnetic force is responsible for most phenomena occurring on scales larger than the size of the atomic nucleus such as: the binding of an electron in orbit around a nucleus and atoms in molecules; the energy released when these bonds are broken (i.e. chemistry); magnetism and electricity; cohesion in liquids leading to the surface tension of water; and even light is a phenomena explained by the electromagnetic interaction. The electromagnetic force is carried by the *photon* and acts only on electrically charged particles.

- Weak - The weak force is responsible for the process of β decay, the conversion of a neutron to a proton via emission of an electron and a neutrino (see figure 1.1), as well as other more exotic processes, such as the decay of the top quark. The weak force is experienced by all particles, and is mediated by three massive bosons, the $W^{\pm}$ and the Z^0. Mathematically, the Weak and Electromagnetic force are described by the same underlying theory, called *Electroweak* [5]. This implies that at high energy scales, the two separate forces become unified. This unification has led to many theories attempting to unify all of the Standard Model forces. Such a theory is called a *Grand Unified Theory* [6].

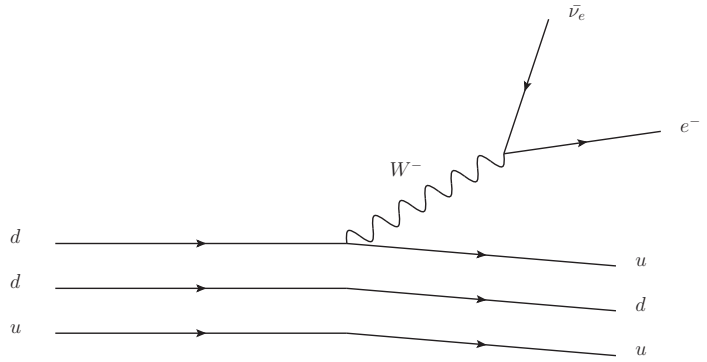

Figure 1.1: A Feynman Diagram showing the process of β decay. One of the down quarks in the incoming neutron emits a W^- boson, turning it into an up quark. The W^- boson then decays to an electron and anti-neutrino pair.

- Strong - The strong force is, as the name suggests, the strongest of the four forces. The strong force interacts with particles carrying the 'charge' of the strong force, *colour* (ie. quarks and gluons). The interactions of the strong force are governed by Quantum Chromodynamics (QCD). Theoretically, due to the mediator of the strong force, the *gluon*, being massless, the strong force should have an infinite range. Gluons themselves carry colour charge and as such are self interacting, so can only have a short range before interacting. This makes the strong force one of the shortest range forces. The strong force is responsible for binding the quarks together inside protons and neutrons (and other hadrons).

- Gravity - Gravity is probably the most familiar force, yet it is the only force not described in the Standard Model. There are theories which propose a mediator particle, the *graviton*, though none of these theories are supported with experimental evidence. However, experiments to search for gravitational waves are in progress [7, 8], which may yet shed light on possible properties of the graviton.

All of the bosons associated with the fundamental forces (with the exception of gravity) carry a spin of 1. The Standard Model Higgs boson is the only known

Force	Boson	Electric Charge
Electromagnetic	γ (photon)	0
Strong	g (gluon)	0
Weak	$W^{\pm}$, Z^0	± 1, 0
Gravity	G (graviton)	0

Table 1.2: The boson sector of the Standard Model.

particle expected to differ from this, carrying a spin of 0. If a graviton were to be discovered, it is predicted to carry a spin of 2.

The Higgs Boson

In the Standard Model the $W^{\pm}$ and Z bosons do not have mass, yet when these particles, and others, are produced and observed experimentally, they do. Simply adding as mass term into the mathematics does not work, so some form of mechanism acting on the particles must be introduced.

In 1964, three independent groups proposed such a mechanism [9–11], now commonly called the *Higgs mechanism*, which preserves all of the mathematical elegance and consistency of the Standard Model, yet acts in such a way to allow certain particles to have mass (such as the $W^{\pm}$ and Z bosons), while leaving other particles massless (like the photon). This mechanism is predicted to have an associated boson, the Higgs boson, which could be produced and indirectly observed experimentally. While the Higgs boson mass is not theoretically predicted, its coupling to mass means that it would preferentially decay to the heaviest possible particles, for example, a 180 GeV Higgs boson could decay to two real Z bosons, with 90 GeV mass each.

In July 2012, at a meeting at CERN, the observation of a new particle, with a mass around 125 GeV was announced, and the results from the two experiments responsible, ATLAS and CMS, were published shortly after [12, 13]. In March 2013, a

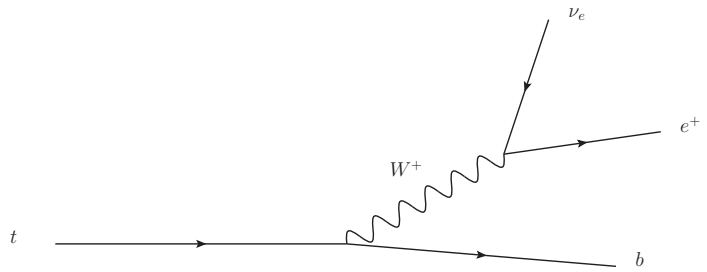

Figure 1.2: A Feynman Diagram showing the process of top quark decay, via the weak interaction. This is the same interaction as is responsible for beta decay (see figure 1.1), but the top quark decays before it has chance to form a bound state.

study of the spin of the new particle was presented by ATLAS at a conference [14–16], suggesting that the new particle has spin 0, consistent with a Standard Model Higgs boson.

1.3 The top quark

The top quark is the most massive particle yet discovered and has the interesting property that it decays very quickly, before the strong force can interact with it, as shown in figure 1.2. Quarks in the Standard Model carry a colour charge (introduced in section 1.2.2), *red*, *green* or *blue*. A phenomenon called confinement requires that no coloured particle can exist on its own; it must form a colourless bound state, by either combining red, green and blue, or by combining any colour with its corresponding anti-colour. If a quark is produced on its own, the strong force will create other quark anti-quark pairs until no colour charge exists on its own. This is called hadronisation. The top quark is the only quark which is massive enought to decay directly to a W boson before it has chance to hadronise, allowing some of its properties to be passed on to the decay products. The top quark, like all fermions, has spin $\frac{1}{2}$, which can have two possible orientations, $+\frac{1}{2}$ or $-\frac{1}{2}$. These orientations are often called spin up or spin down. In the LHC, top quarks are mostly produced in quark-antiquark pairs.

1.3.1 Spin Correlation

For spin $\frac{1}{2}$ fermions, produced in quark-antiquark pairs, the number of times the spin directions are alike ($\uparrow\uparrow$ or $\downarrow\downarrow$) compared to the number of times they are different ($\downarrow\uparrow$ or $\uparrow\downarrow$) is predicted to be non-zero in the Standard Model [17]. This property may be verified by studying top quarks produced in pairs, providing a strong test of the Standard Model. The top quark system is particularly suited to the study of spin correlation, due to the fact that top quarks do not hadronise. This means the spin of the top quarks at production is unaffected by the strong force, so the spin information is propagated to the decay products.

The spin of a particle directly influences the angular distribution of its decay products, which can then be used to determine the amount of correlation in the spins of the parent particles. The next chapters present a study of the spin correlation in the $t\bar{t}$ system, starting with a description of the experimental apparatus used.

Chapter 2

CERN and the LHC

2.1 The CERN Accelerator Complex

The Organisation Européenne pour la Recherche Nucléaire (CERN) complex (figure 2.1) is the largest particle physics lab in operation, with a diverse range of experiments working with many different accelerators, the most well known being the LHC. CERN was founded in 1954, on the Franco-Swiss border near Geneva, by a council of 12 European governments. Since its foundation, CERN has expanded to include 20 European member states and several 'observer' states, which are not directly involved in Council decisions. CERN itself employs around 2400 people, but over 10,000 visiting scientists from 608 institutes and 113 nationalities contribute to research, maintenance and building of the many experiments. Since its inception, CERN has been responsible for many important discoveries in the field of particle physics, including the discovery of neutral currents [19] and subsequently the W and Z bosons [20], and more recently, the discovery of a 'Higgs-like' boson [12, 13], which may fill in the final gap in the current Standard Model*.

The current chain of accelerators at CERN (see figure 2.2) is described next.

*with the exception of neutrino oscillations

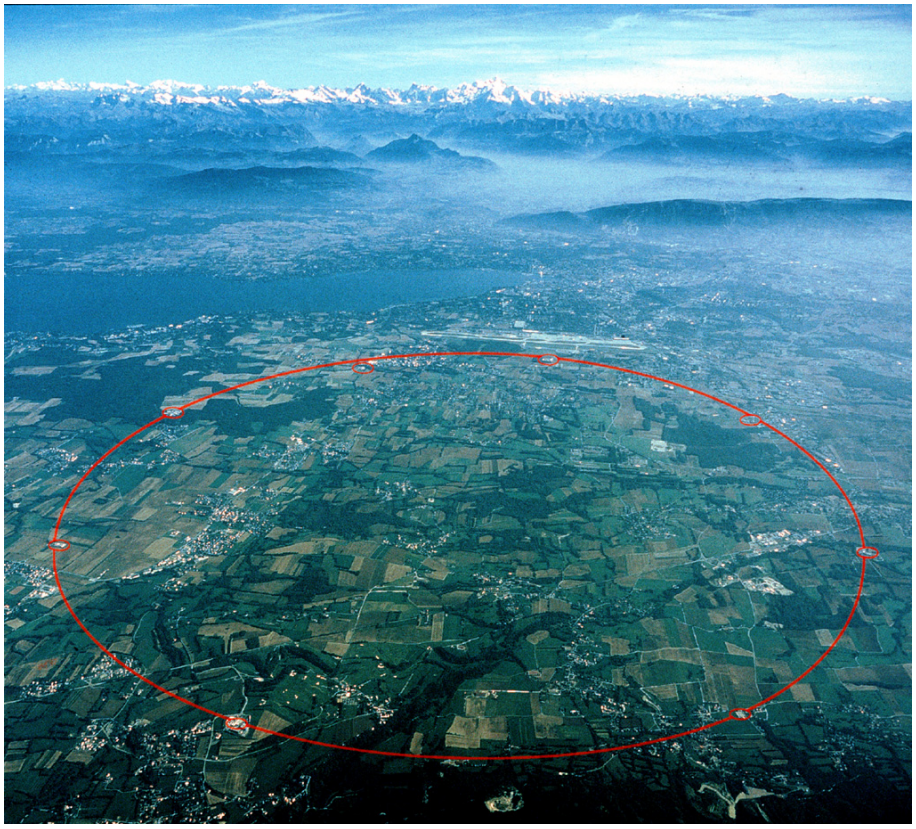

Figure 2.1: An aerial view of the CERN complex and surroundings. The red ring shows the location of the LHC, with the main CERN site touching the upper right of the ring. Moving upwards through the photograph from the ring are Geneva Airport, Lake Geneva, and Mont Blanc and the Alps in the far distance [18].

2.1.1 Luminosity

In a high energy physics experiment, the instantaneous luminosity is a measure of the number of particles per unit area per unit time ($\mathrm{cm}^{-2}\ \mathrm{s}^{-1}$),

$$\mathcal{L} = fn\frac{N_1 N_2}{4\pi\sigma_x\sigma_y}, \tag{2.1}$$

where f is the revolution rate of the beam, n is the number of bunches of particles in the beam, $N_{1,2}$ are the number of particles in bunches $1, 2$, and $\sigma_{x,y}$ are the transverse profiles of the beam.

For a process with a given *cross section*, σ (measured in units of area), the interaction

rate of that process is given by

$$R = \mathcal{L}\sigma, \tag{2.2}$$

where R is the interaction per second for the process, given luminosity, $\mathcal{L}$.

This interaction rate can then be integrated over time to give an estimate of the expected number of interactions in a given data taking period. Since the cross section does not change with time, this simplifies to an integral, over time, of the instantaneous luminosity. The resulting integrated luminosity carries units of cm^{-2}. For convenience, the units are often quoted in inverse barns, b^{-1}, where $1\ b = 10^{-24}$ cm^2. For the 2011 LHC data taking period, the total data recorded by ATLAS corresponds to an integrated luminosity of 4.7 fb^{-1}. Given that the production cross section of top quark pairs at $\sqrt{s} = 7$ TeV[†] is around 170 pb [21], the total number of top quark pairs produced in ATLAS in 2011 is close to 800,000.

[†] $\sqrt{s}$ denotes the centre of mass energy of a collider experiment

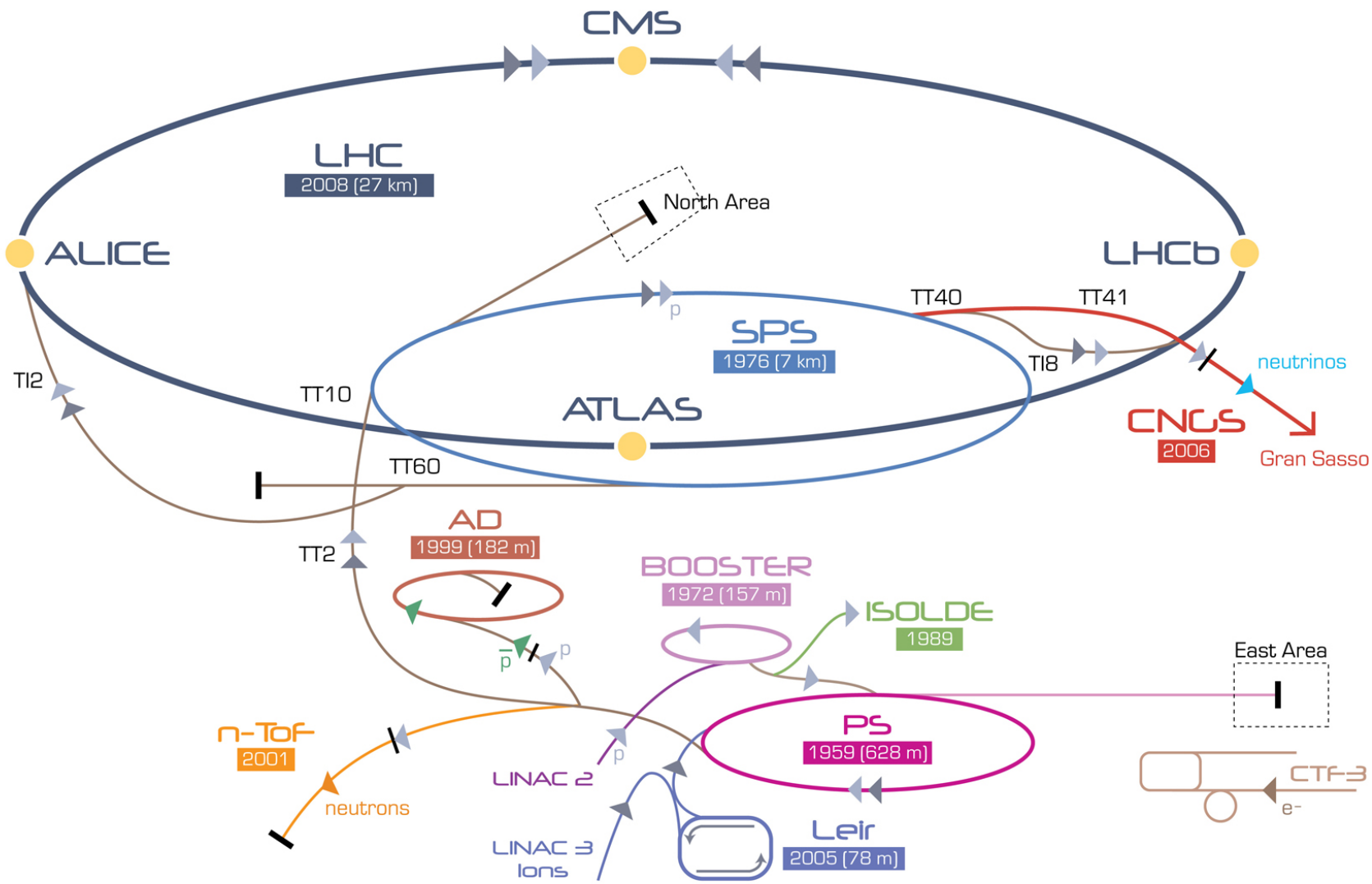

Figure 2.2: A schematic view of the CERN accelerator complex. The largest ring, the LHC is the final step in a chain of increasingly large accelerators, though not the only ring with active experiments. © CERN.

2.1.2 LINAC-2 and Proton Synchrotron Booster

The very beginning of the path of a proton through the LHC (see figure 2.2 for an overview of the accelerator complex) is a bottle of hydrogen at the start of the LINAC-2 accelerator. The hydrogen is ionised and the subsequent protons are injected into LINAC-2. LINAC-2 accelerated its first beam of protons to 50 MeV in 1978, and has been used since to provide pulsed beams of protons to other accelerators before being used for experiments on the Proton Synchrotron (PS), Super Proton Synchrotron (SPS) and now the LHC.

The proton beam from LINAC-2 is injected into the four superimposed rings of the Proton Synchrotron Booster (PSB), which accelerates the beams up to 1.4 GeV ready for injection into the PS.

LINAC-3 is used to provide beams of heavy ions at 4.2 MeV/u (where MeV/u represents energy per nucleon) to Low Energy Ion Ring (LEIR), for further acceleration and injection into the PS, SPS and finally the LHC during heavy ion running.

2.1.3 Proton Synchrotron

The PS accelerated its first protons in 1959, at the time the world's highest energy accelerator with an energy of 28 GeV. Later, in 1971, protons from the PS were injected into the Intersecting Storage Ring, circulating two counter rotating beams of protons, simultaneously. This led to the world's first proton-proton collider.

In 1972, protons from the PS were used to create a muon neutrino beam, directed at the Gargamelle bubble chamber, in order to look for neutral (equation 2.3) and charged current (equation 2.4) events, signatures of the Weak interaction.

$$\nu_\mu/\bar{\nu_\mu} + N \rightarrow \nu_\mu/\bar{\nu_\mu} + hadrons \tag{2.3}$$

$$\nu_\mu/\bar{\nu_\mu} + N \rightarrow \mu^+/\mu^- + hadrons \tag{2.4}$$

The discovery of neutral currents observed in Gargamelle was published in 1973 [19].

The PS consists of 277 electromagnets arranged with a circumference of 628 m. Proton beams of 1.4 GeV are injected into the PS and accelerated up to 25 GeV, ready for injection into the SPS.

2.1.4 Super Proton Synchrotron

The SPS began running in 1976, and since then has been used in a wide range of physics experiments. The SPS has been used to accelerate electrons, positrons, heavy ions, protons and anti-protons, as well as being used to provide muon and neutrino beams to experiments in the North and West Areas of CERN.

In 1983, the W and Z bosons were discovered in proton anti-proton collisions by the UA1 [20] experiment and later confirmed by UA2 [22], which led to a Nobel Prize for Carlo Rubbia and Simon van der Meer.

More recently, the SPS was used to provide beams for NA48, which studied CP violation in kaon decays and will also provide the beams for NA62, the successor to NA48. The SPS also provides beams of neutrinos for CERN Neutrinos to Gran Sasso (CNGS), a tau neutrino detection experiment under the Gran Sasso mountain in Italy. In order to create neutrinos, beams of protons are fired at a fixed target, producing a directed spray of particles, including pions and kaons. The pions and kaons decay to muons and muon neutrinos, and the beam passes an absorber, which stops the remaining undecayed pions and kaons, as well as the muons, leaving a beam of neutrinos.

The SPS uses 1317 electromagnets to guide beams of particles around its 7 km

circumference, attaining energies up to 450 GeV. During LHC running, proton beams at 450 GeV are then removed from the SPS and injected into the LHC at two points to create two counter rotating beams.

2.2 Large Hadron Collider

The LHC is the world's largest particle accelerator; with a total circumference of 26.7 km, and crossing the Franco-Swiss border twice. The same tunnel housing the LHC was used previously for the Large Electron Positron collider (LEP) experiment, which ran from 1989 until 2000. In addition to being the largest particle accelerator, the LHC also holds the world records for highest energy and highest luminosity, running in 2012 with an energy of 8 TeV and an instantaneous luminosity of 7.73×10^{33} cm^{-2} s^{-1}.

To achieve this, the LHC incorporates over 9000 magnets, operating at temperatures under 2 K. The magnets in the LHC can be subdivided into three categories; dipole magnets, quadrupoles and correcting magnets.

The 1232 dipole magnets operate with a nominal current (at 7 TeV per beam) of 11.85 kA, providing a magnetic field of 8.33 T, in order to bend the proton beams around the circumference of the LHC tunnel. In addition to bending the proton beam, it needs to be periodically focussed, since the charged protons will tend to repel and cause the beam to diverge. To do this, 392 quadrupole focussing magnets regulate the horizontal and vertical beam widths. There are several other correcting magnets used to correct orbital perturbations, focussing the beam at the interaction points of the four main experiments and guiding the beam in the occasion of a beam dump.

A cross section of a dipole magnet is shown in figure 2.3. Figure 2.4 shows a typical magnetic field map for an LHC dipole magnet. Figure 2.5 shows the superconducting

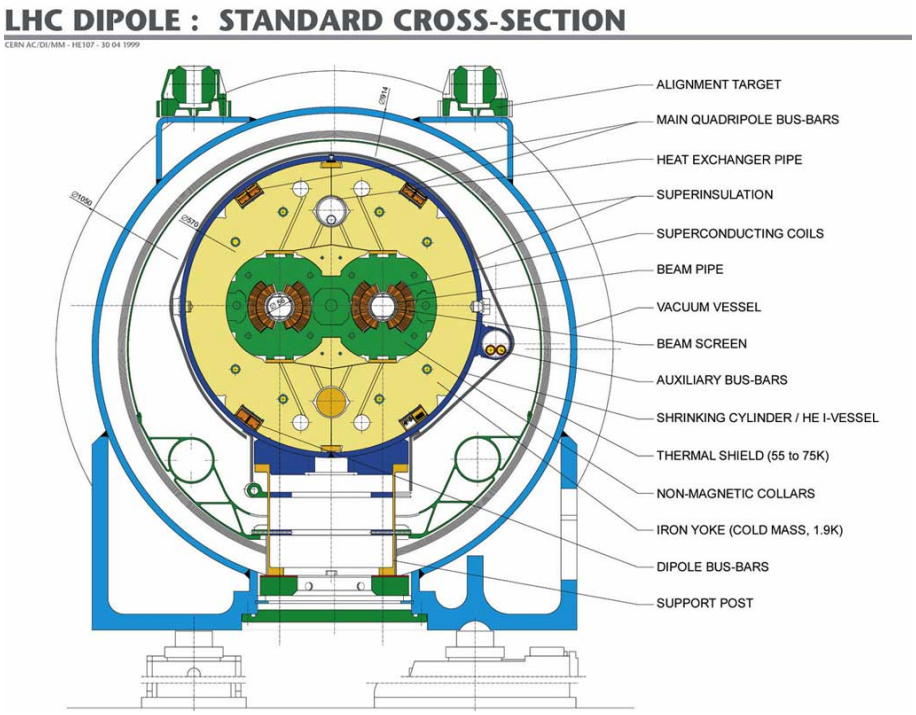

Figure 2.3: A crosssectional slice of an LHC dipole magnet. The two beam pipes circulate counter rotating beams of protons [23].

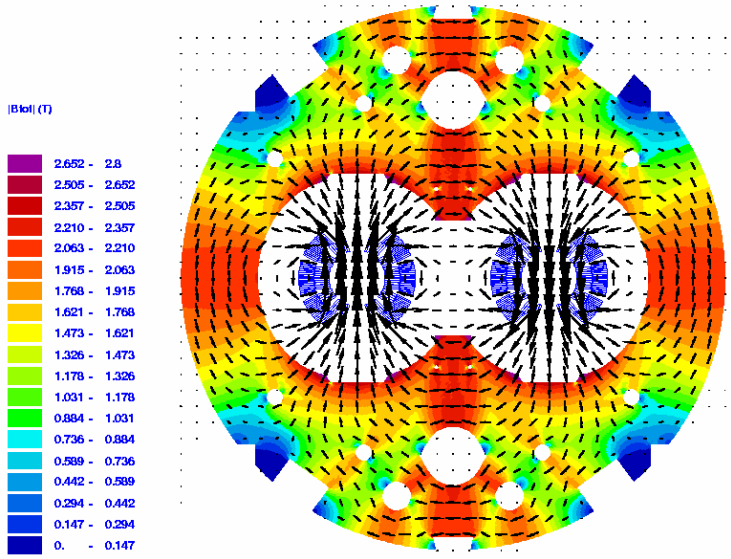

Figure 2.4: A typical magnetic field map for an LHC dipole magnet. The maxima of the field coincide with the two beam pipes, providing the bending field for the proton beams [24].

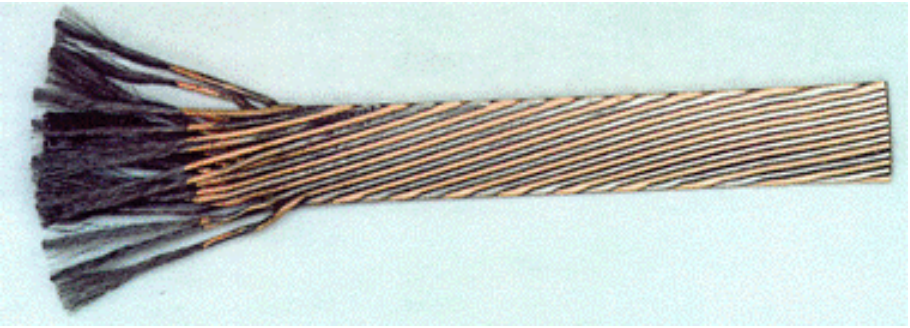

Figure 2.5: An example of the superconducting Ti-Nb cable used to provide the magnetic field in the LHC dipole magnets. From the left of the picture, the cable is deconstructed into its constituent filaments, which are collected in strands. The strands are then wrapped in bunches of 36 to create the complete cable. © CERN. [25]

Nb-Ti cable used throughout the LHC magnets.

2.2.1 Acceleration and bunching

Once the LHC captures the beam injected from the SPS, the beam energy is 450 GeV. In order to reach higher energies, the beam must undergo acceleration. Magnetic fields are able to alter the trajectory of the particles but cannot accelerate them. To do this, an electric field is required. In the LHC, this is provided by the Radio Frequency (RF) cavities. The RF system provides a longitudinal, oscillating electric field in order to provide an accelerating voltage to particles passing through the RF gap. In order for a particle to experience an acceleration each turn rather than a deceleration, the RF frequency must be exactly an integer multiple of the revolution frequency of the particle.

Consider a particle with momentum such that its revolution frequency coincides with the RF frequency. If this particle were to arrive at the RF cavity such that it experiences zero voltage, it would experience zero acceleration and continue with the same momentum and path length around the accelerator, arriving at the same time to the RF cavity each revolution (assuming negligible energy losses). This is called the *synchronous* particle.

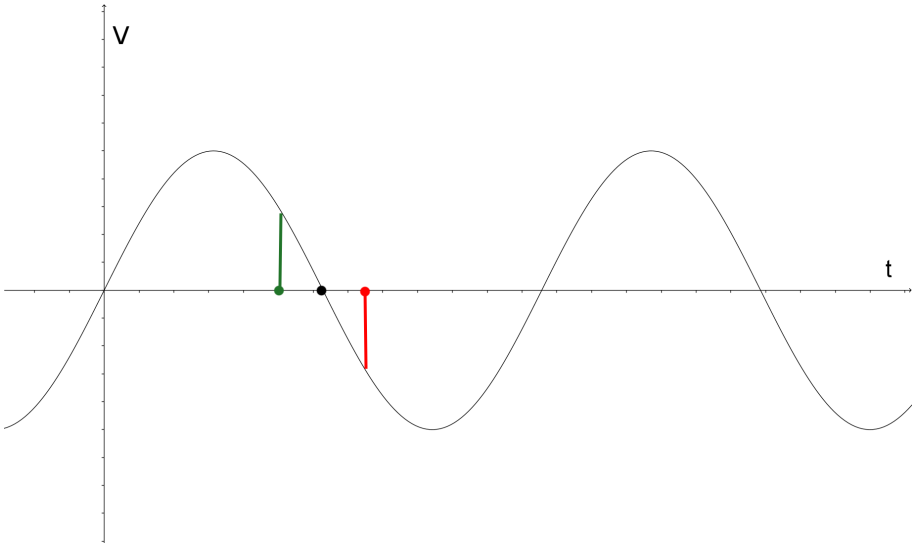

Figure 2.6: Illustration showing acceleration in an RF cavity, V is the voltage at a given time, t. The green particle arrives early to the cavity and experiences a boost to increase its path length, the red particle arrives late on a longer path and so experiences a deceleration. The black particle is the synchronous particle.

Consider another particle arriving simultaneously at the RF cavity, but with lower momentum. This particle would travel a shorter path around the accelerator, arriving earlier than the synchronous particle after the first revolution. This particle then experiences an acceleration, boosting it to a longer path length, making its time of arrival at the RF cavity slightly later. If it arrives later than the synchronous particle, it will experience a deceleration, reducing its path length, and so on. The resulting behaviour is that the particle oscillates around the synchronous particle [26]. This concept is illustrated in figure 2.6.

During the acceleration, or ramping, phase of the LHC, the magnetic field is smoothly ramped up, causing the path lengths of each particle to shorten, making them appear as though they had arrived early and thus receiving a boost at the RF gap.

With many particles in the beam, there tend to be *bunches* forming around the synchronous points in the RF system, known as RF buckets. In the LHC the nominal RF frequency is 400.789 MHz, which corresponds to RF buckets spaced by around 2.5 ns. The design filling scheme for the LHC uses bunches spaced by 25 ns, meaning

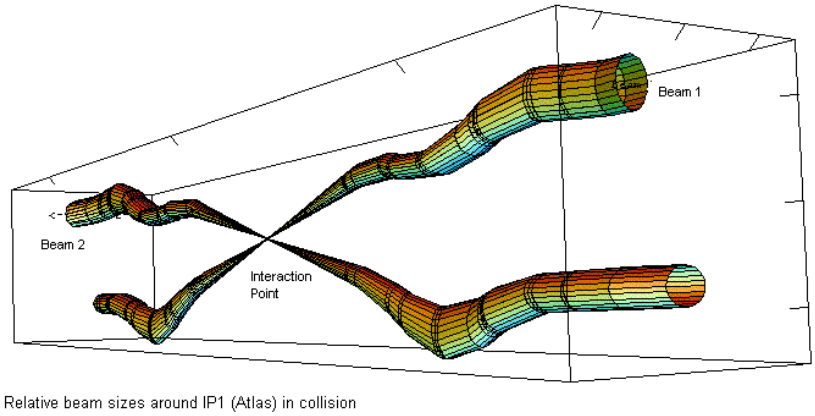

Figure 2.7: Diagram showing beam sizes around the interaction point in ATLAS, Interaction Point 1 (IP1). The beams are focussed and directed towards each other at which point the protons in crossing bunches have a chance of colliding. © CERN. [27]

only every tenth bucket is filled. This is in part to reduce the amount of pileup, but also to allow for different bunch crossing configurations for the different experiments.

2.2.2 Interaction points

Around the LHC ring there are four points at which the two counter rotating beams cross, called *interaction points*. At these points the beams are squeezed to as small a size as possible[‡] at the crossing point to maximise the chance of a collision taking place. Throughout the majority of the LHC ring, the beams are of the order of a millimetre in diameter, being squeezed to around 20 microns at the interaction points. Figure 2.7 shows the relative sizes of the two beams around an interaction point.

At the interaction point, bunches of protons from each beam cross and some of the protons within the bunches collide. In the LHC the number of interactions per bunch crossing is generally between 5 and 30 (see Figure 2.8), depending on the beam parameters.

[‡]With the exception of LHC-beauty (LHCb), where the beam is defocussed to reduce the amount of pileup produced in the collisions.

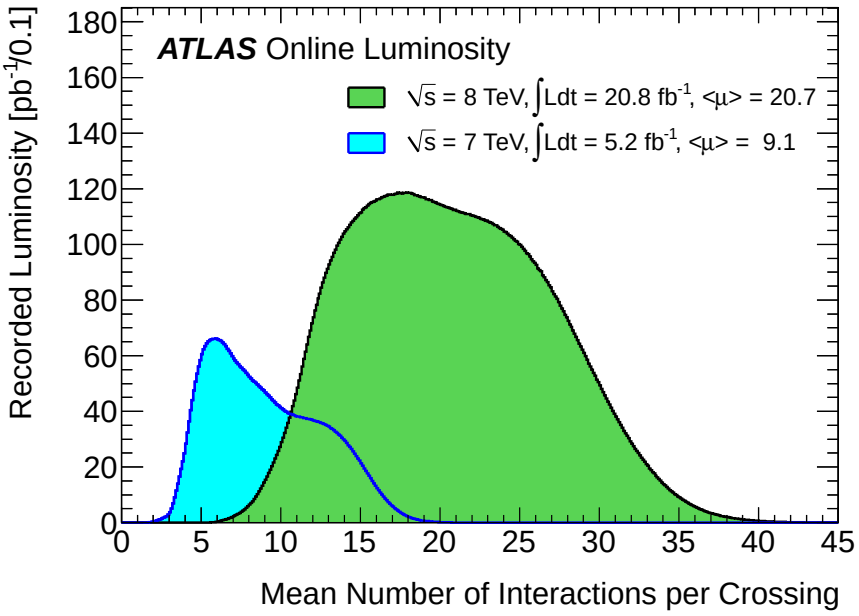

Figure 2.8: The average number of interactions per crossing, measured in 2011 and 2012 data. The average number of interactions is calculated for each lumi block subdivision of data [28].

In 2011, the LHC ran with beams at half the nominal energy, at 3.5 TeV per beam. The maximum number of bunches per beam was 1380, with up to an average 18 interactions per bunch crossing (see figure 2.9), and maximum instantaneous luminosity of 3.65×10^{33} cm^{-2} s^{-1} (see section 2.1.1).

Since the bunches in the LHC contain of around 10^{11} protons, there may be multiple interactions per bunch crossing. The detectors recording these interactions experience *pileup*, when multiple interactions coincide. See section 3.7 for a description of pileup and attempts to manage it with ATLAS.

In order to observe the interactions, at each of the four interaction points stands a purpose built experiment designed to study the collisions and the resulting particles produced. LHCb aims to investigate many areas of flavour and electroweak physics, primarily looking at the decays of B-hadrons. In particular, CP-violation and very rare B-hadron decays are two topics heavily scrutinised by the experiment, leading to such results as the first evidence for the decay $B_s \to \mu^+\mu^-$ [30] and evidence for

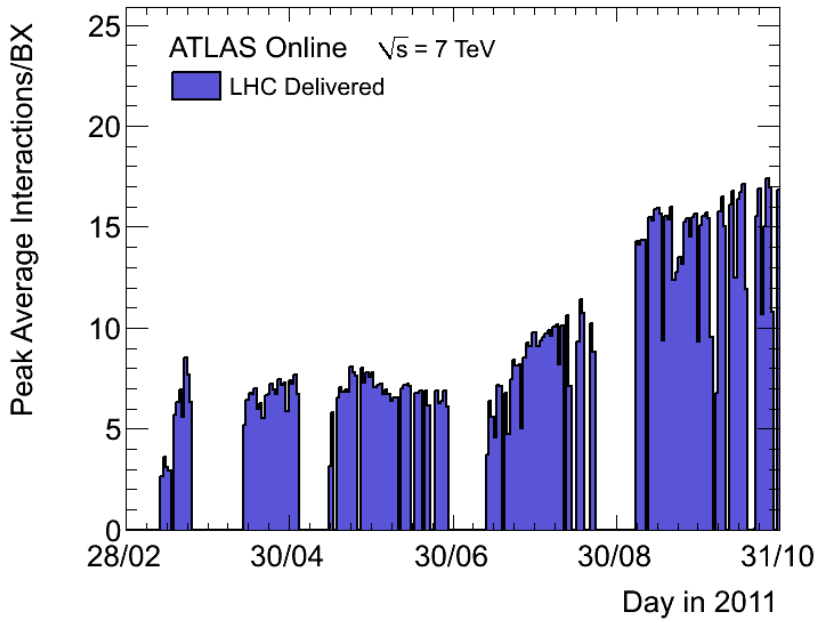

Figure 2.9: Average number of interactions per bunch crossing for the 2011 7 TeV proton-proton running period. The data taking period each day is split into lumi-blocks and the maximum value of the average over all lumi blocks per day is shown in this plot [29].

CP-violation in $B^{\pm}$ decays [31].

A Large Ion Collider Experiment (ALICE) is designed to study collisions of lead nuclei in order to give an insight into the very high temperatures and densities produced, and to study the quark-gluon plasma - a state of matter where quarks and gluons no longer experience confinement. In 2010, the ALICE collaboration published the first study of the quark-gluon plasma at the LHC [32], confirming the theoretical prediction that its properties are consistent with that of an 'ideal liquid'.

Compact Muon Solenoid (CMS) and ATLAS are both 'general purpose' detectors; rather than being designed for specific physics studies like LHCb and ALICE, CMS and ATLAS are intended to record as much data as possible in order to search for new or unobserved physics signatures, such as the Higgs boson or Supersymmetry, and for the further study of known physics such as the top quark.

One of the first discoveries to come from the LHC was of the $\chi_b(3P)$ at ATLAS [33] -

a bound state consisting a b-quark and a b-antiquark, which was predicted to exist but had remained previously unobserved.

In addition, several measurements of previously measured quantities were published, including W and Z boson cross section measurements [34] and a $t\bar{t}$ cross section measurement [35]. This has continued at ATLAS and over 200 physics papers have been published in various journals.

Later, but arguably the most important discovery at the LHC so far was that of a 'Higgs boson-like' particle, announced by both CMS and ATLAS in June 2012 and published in July 2012 [12, 13].

2.2.3 Timeline of LHC running

The first beam of protons circulated in the LHC on the 10th September 2008, successfully steering the beam alternately clockwise, then anti-clockwise.

As mentioned in section 2.2 the very large current needed to maintain the large magnetic fields used in the LHC requires superconducting cable, made of a Niobium-Titanium alloy. The cable itself is composed of 36 strands of wire, with each strand containing around 6500 Nb-Ti filaments. In order to maintain the superconductivity at such high magnetic field strengths, the Nb-Ti cables are cooled with liquid helium to 1.9 K.

In the event that the cable leaves its superconductive state, becoming again a normal conductor, the large current will cause a significant temperature increase in both the cables and surroundings, and the stored energy in the magnet is dissipated. This is called a quench. In order to minimise the potential damage caused by a magnet quench, the LHC has a quench protection system in place. The basic principle of this system is to detect quickly a quench and take measures to ensure the quench happens in a controlled and safe manner. This can be done by allowing the current

to pass through a diode, bypassing a single magnet once it becomes resistive; by introducing a dump resistor to reduce the current; or, by heating the entire magnet in order to force the resistive region to grow more rapidly, effectively spreading the temperature increase over a larger area and reducing the increase at the quench start point.

Not detecting a quench in time to safely reduce the current can cause all of the stored magnetic energy to dump into a small region, which was the cause of the accident on 19th September 2008, in which an interconnecting superconductor, which was not encompassed by the existing quench protection system at the time, developed a resistive region. The energy released by the accident (moving some of the magnets), caused a burst in the liquid helium system, flooding the LHC tunnel with tonnes of helium. The accident damaged several of the dipoles and set back the start of the LHC running by over a year.

Following the accident and subsequent repair effort, the LHC was ready to begin circulating beams once again in November 2009 and the first proton-proton collisions occurred on the 23rd. Then, on the 29th, the LHC broke the world energy record, previously held by the Tevatron accelerator at Fermilab, by accelerating protons to an energy of 1.05 TeV, before continuing to ramp up in energy in order to start taking data from collisions at a centre of mass energy of 7 TeV. In 2010, the instantaneous luminosity reached a maximum of 2.07×10^{32} cm^{-2} s^{-1}, yielding a total delivered luminosity to ATLAS of 48.1 pb^{-1}. 2011 saw an increase in the number of bunches per beam bringing the peak luminosity up to 3.65×10^{33} cm^{-2} s^{-1} and delivering 5.61 fb^{-1} to ATLAS, as well as breaking another of the Tevatron's records; the LHC became the highest luminosity hadron collider.

In 2012, the energy of the LHC was increased to 4 TeV per beam. Coupled with improvements to the beam optics allowing for more tightly squeezed beams, the instantaneous luminosity increased by a factor of 2, the peak luminosity reaching 7.73×10^{33} cm^{-2} s^{-1} and delivering 23.3 fb^{-1} to ATLAS. Although the experiments

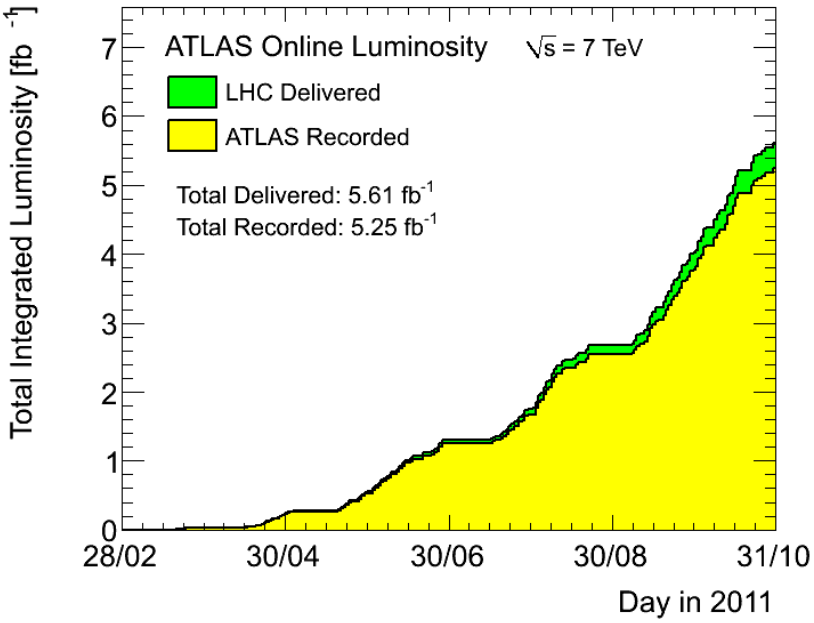

Figure 2.10: Delivered and recorded integrated luminosity for the 2011 7 TeV running period. The yellow plot shows the recorded luminosity from the total delievered luminosity (shown in green) [29].

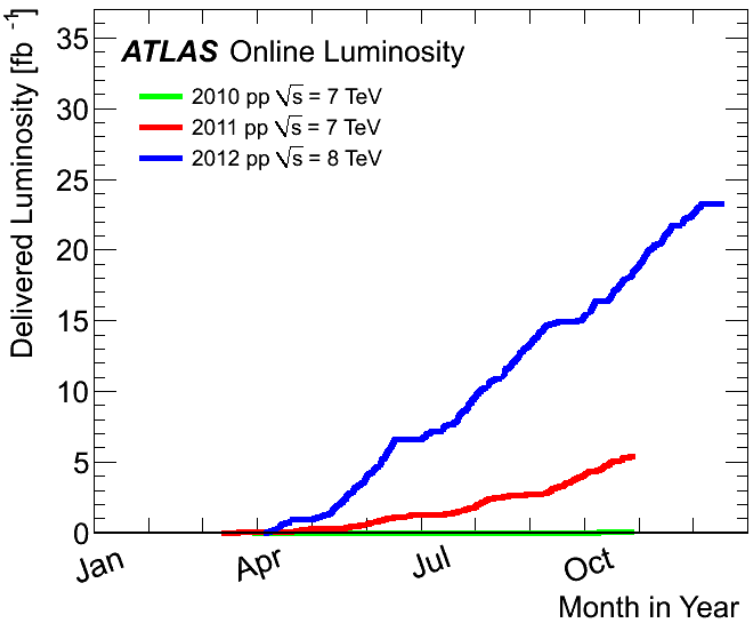

Figure 2.11: Cumulative delivered luminosity to ATLAS for 2010 and 2011 7 TeV running and 2012 8 TeV running [29].

have the potential to record all of the delivered luminosity, downtime and detector inefficiencies mean that a small fraction of the luminosity is lost. Figure 2.10 shows the recorded luminosity for the 2011 proton-proton run overlaid on the total LHC delivered luminosity. Figure 2.11 shows a comparison between the delivered luminosity to ATLAS for each year of the LHC running.

Chapter 3

The ATLAS Detector

ATLAS, shown in figure 3.1 is the largest detector at the LHC, standing 22 m in diameter and 42 m in length. The primary reason for the size of ATLAS is the sophisticated toroidal magnet system which takes up much of the space between the calorimeter and the outer muon chambers.

ATLAS is designed as a 'general purpose' detector, meaning it must be capable of observing both known and as yet unseen processes. The search for the Standard Model Higgs boson was one of the driving factors in evaluating the design and performance of ATLAS during conception. The Higgs boson has a range of production and decay channels, providing ATLAS with a challenge to be able to detect and measure each channel with sufficient experimental resolution in order to be senstive to a discovery. This requires excellent performance in charged particle detection, electron and photon identification, muon identification and jet measurements, as well as accurate missing energy determination. The performance goals for each subdetector are shown in table 3.1.

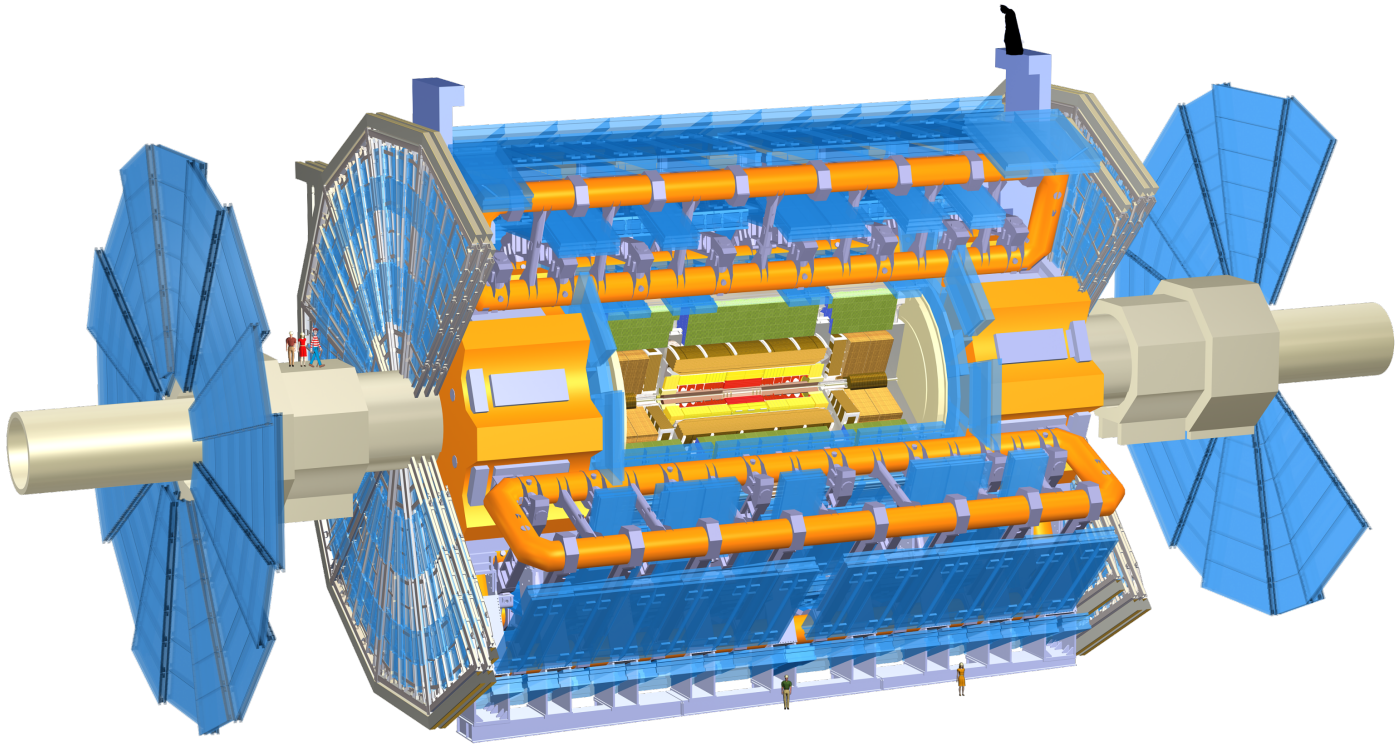

Figure 3.1: The ATLAS detector drawn with a cutaway to illustrate all of the components of the experiment. The largest feature of ATLAS, the toriodal magnet system, is shown in orange. ATLAS Experiment © 2013 CERN.

To achieve this, ATLAS employs a layered structure (seen in figure 3.2, showing how various particles interact with each layer), with a charged particle tracking system enclosed in a 2 T solenoid at the centre, surrounded by electromagnetic and hadronic calorimeters, and finally a large muon tracking system utilising the peak 4 T toroidal magnetic field on the outermost layer.

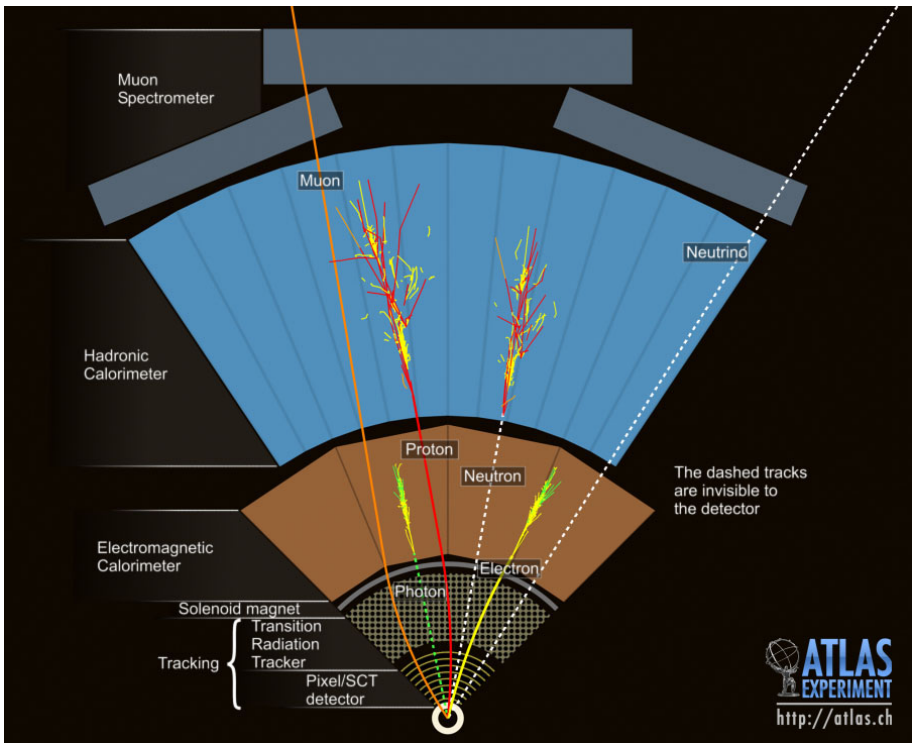

Figure 3.2: Various particles travelling through the layers of ATLAS. Each particle interacts differently with the different parts of the detector. This produces distinct signatures for particles which aid in particle identification. ATLAS Experiment © 2013 CERN.

3.1 ATLAS Coordinate Systems

In high energy physics, collider experiments are often cylindrical in design and, as such, Cartesian coordinates are not always the optimal system in which to perform measurements. In ATLAS, a spherical coordinate system is also employed, where ϕ is the azimuthal angle in the transverse plane, perpendicular to the beam line.

Sub Detector	Required Resolution
Tracker	$\sigma_{p_{\mathrm{T}}}/p_{\mathrm{T}} = 0.05\%\ p_{\mathrm{T}} \oplus 1\%$
EM Calorimeter	$\sigma_E/E = 10\%/\sqrt{E} \oplus 0.7\%$
Hadronic Calorimeter	
barrel and end-cap	$\sigma_E/E = 50\%/\sqrt{E} \oplus 3\%$
forward	$\sigma_E/E = 100\%/\sqrt{E} \oplus 10\%$
Muon Spectrometer	$\sigma_{p_{\mathrm{T}}}/p_{\mathrm{T}} = 10\%$ at $p_{\mathrm{T}} = 1$ TeV

Table 3.1: Performance goals of the ATLAS detector as laid out in Ref. [36]. The notation $\oplus$ indicates the amount to be added in quadrature.

Defining the positive Cartesian x-axis as horizontal towards the centre of the LHC, ϕ is conventially measured in the range $[-\pi, +\pi]$ with $\phi = 0$ corresponding to the direction along the positive x-axis, and increasing towards the positive y-axis, which extends vertically upwards. The z-axis is then defined with a right handed Cartesian system, that is to say ϕ increases clockwise when looking along the positive z-direction.

Due to the slight tilt of the LHC tunnel with respect to the ATLAS cavern, the system is rotated from the LHC coordinate system with the y and z axes offset by 0.7°.

R, or ρ, describes the distance from the centre of the detector, and θ is the angle measured from the positive z-axis. The pseudorapidity, η of a particle is often used in place of the polar angle θ, where η is defined as

$$\eta = -\ln\left[\tan\left(\frac{\theta}{2}\right)\right]. \tag{3.1}$$

The ATLAS coordinate system is illustrated in figures 3.3 and 3.4.

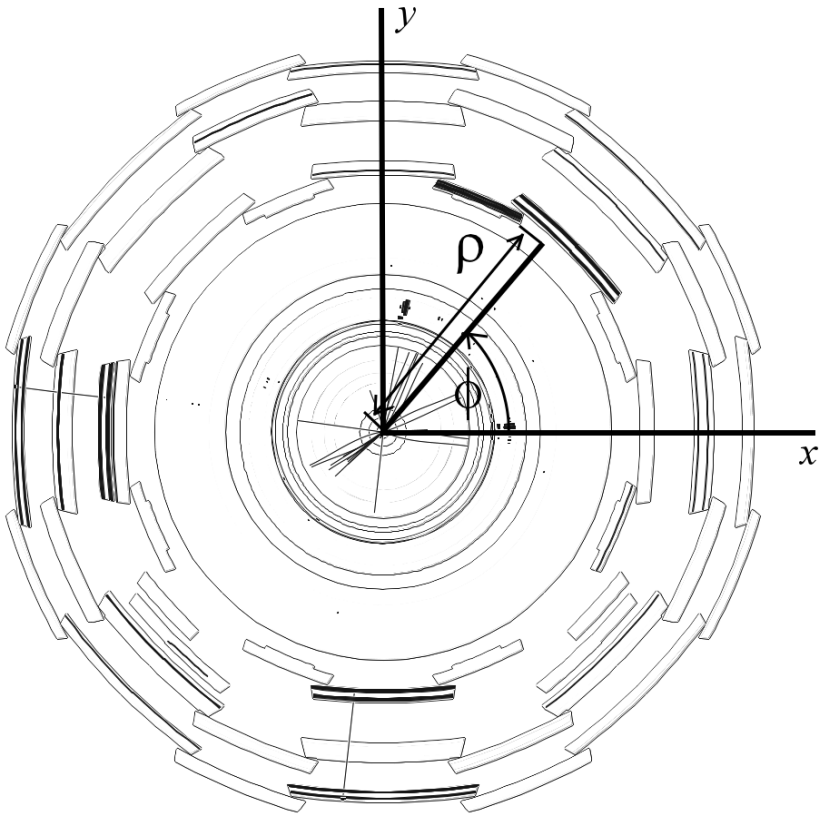

Figure 3.3: The ATLAS detector in the transverse (x, y) plane, showing the definition of the azimuthal angle, ϕ, and radial distance, ρ.

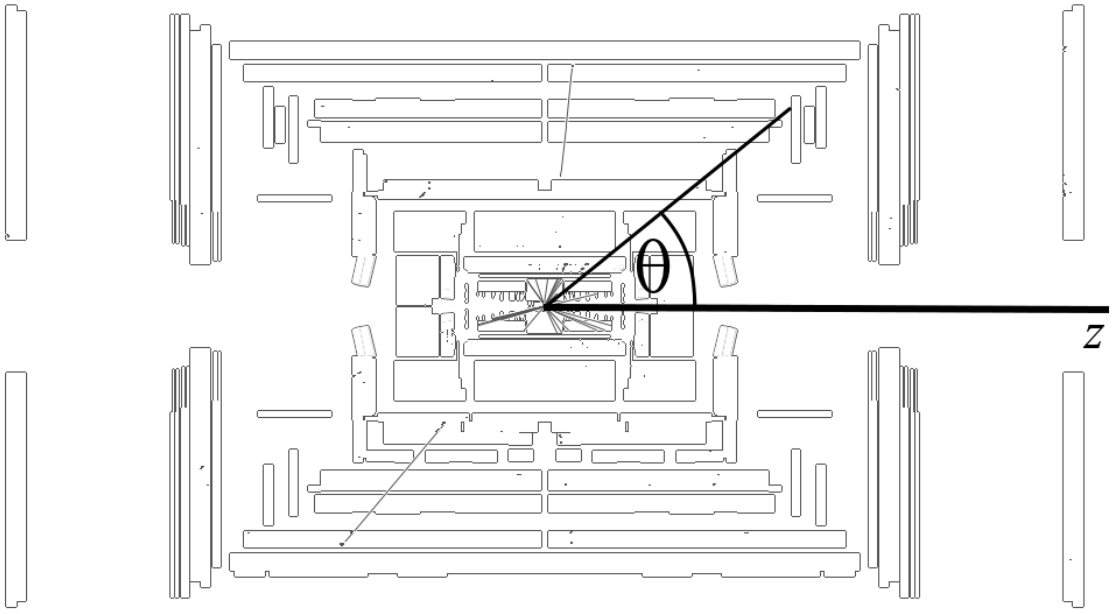

Figure 3.4: The ATLAS detector shown in the longitunal (ρ, z) plane, showing the definition of the polar angle, θ.

3.2 Inner Detector

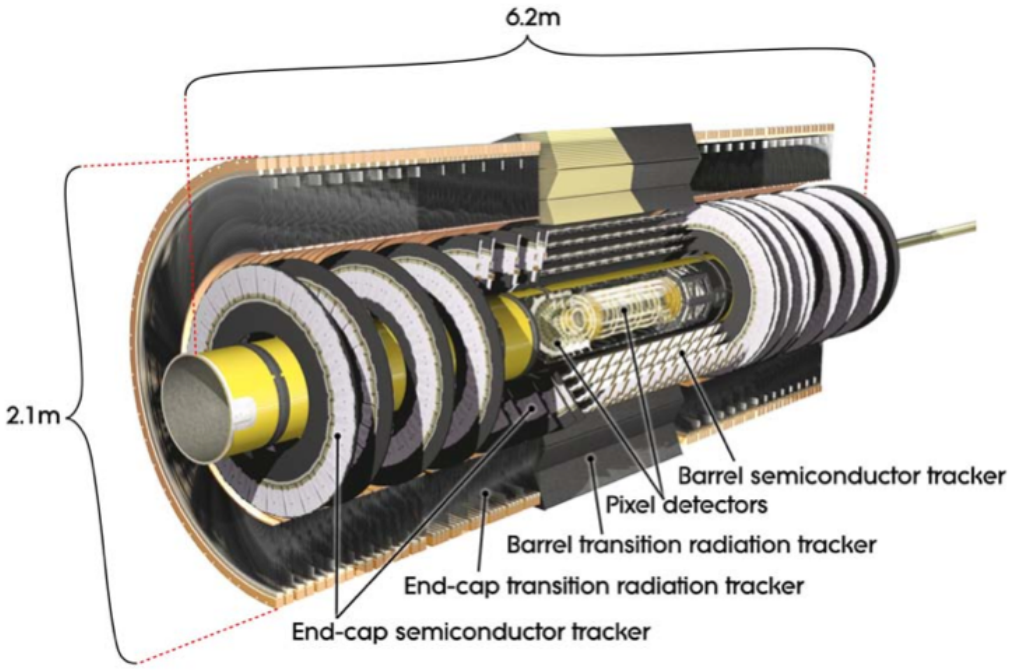

Figure 3.5: The ATLAS Inner Detector [37].

With tens of interactions per bunch crossing, ATLAS could see of the order 10^3 charged particles emerging from the interaction point every bunch crossing. Such high track multiplicities warrant excellent tracking and vertexing in order to disentangle the events. The Inner Detector (ID) in ATLAS extends to $|\eta| < 2.5$, and approaches as close as 50 mm to the beam line, with the goal of detecting, with a high granularity, charged particles to allow reconstruction of tracks and vertices to a high precision. Figure 3.5 shows a schematic diagram of the ATLAS ID. The momentum resolution as a function of momentum is shown in figure 3.8.

The material budget in the ID must be kept low to minimise photon conversions and nuclear interactions. The material usage in the ID, measured in radiation lengths, is shown in figure 3.6. In the range $|\eta| < 0.6$ the material budget is very low, but beyond this range the geometry of the detector and the need for services, including

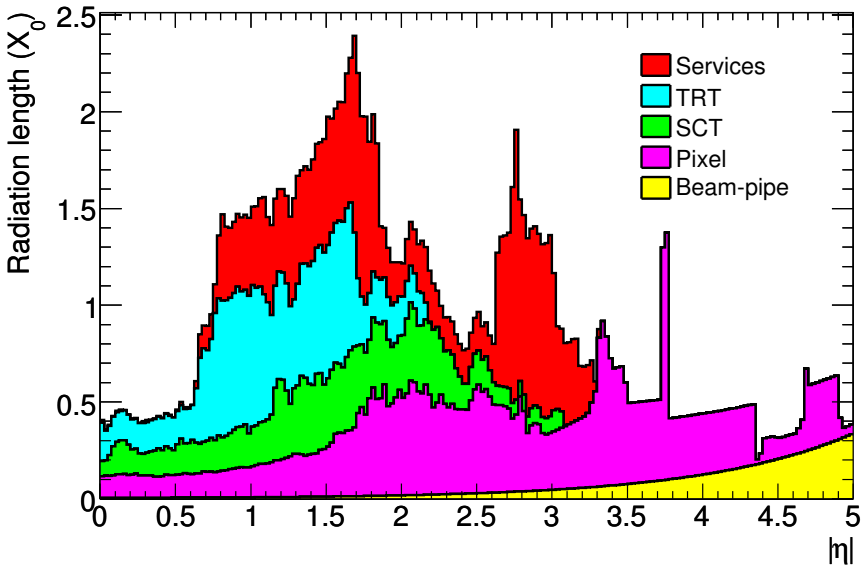

Figure 3.6: The material usage of the ATLAS Inner Detector, measured in radiation lengths $(X_0)^*$ [37].

read out channels, means the material in the ID unavoidably increases.

3.2.1 Pixel Detector

The closest instrumentation to the beam pipe is the pixel detector, which constitutes three concentric cylinders in the barrel region and three disks on each end cap. Overall, the pixel tracking volume extends to a total length of 1.3 m with a barrel outer radius of around 12 cm [39].

The pixels on each module have a minimum size of 50 μm $\times$ 400 μm, and the first layer has an inner radius of around 50 mm. Each track will generally pass through three pixel layers, with a high granularity in the ϕ and z coordinates, allowing for accurate vertex determination of the interaction point, which is of particular interest when identifying displaced vertices.

*Radiation length is a measure of the energy loss of a high energy particle equal to the average distance an electron can traverse a material before losing all but $1/e$ of its energy by

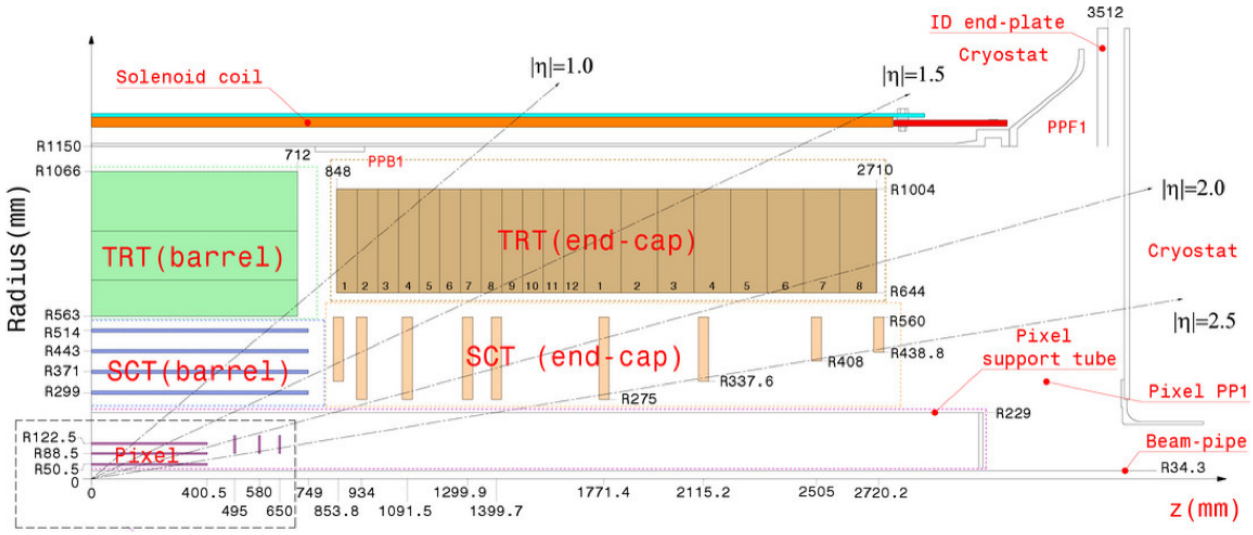

Figure 3.7: Schematic showing the $|\eta|$ acceptance of the components of the ID [37].

3.2.2 Semi Conductor Tracker

The Semi Conductor Tracker (SCT) lies concentric to the pixel detector, with a sensitive barrel region 1.5 m in length and 30–51 cm in radius. The SCT barrel consists of 4 layers of tracker, with 9 disks on each endcap, extending the forward η acceptance, as shown in figure 3.7.

Each SCT barrel module is made up of two silicon micro-strip sensors with a stereo angle of 40 mrad, with each 12 cm long strip separated by 80 μm and with 768 strips per sensor. The strips run parallel to the beamline, giving a fine granularity in ϕ, with a resolution of around 17 μm in $R\phi$ [36]. The stereo angle allows a measurement in the z direction (Figure 3.9) with resolution of around 580 μm, while remaining a small enough angle to reduce 'ghost' hits.

The SCT endcap modules are wedge shaped and arranged into disks. The strip pitch of the modules varies with radius between around 55 μm and 95 μm, and the pairs of strip sensors are arranged with a stereo angle of 40 mrad. The endcap modules

Bremsstrahlung.

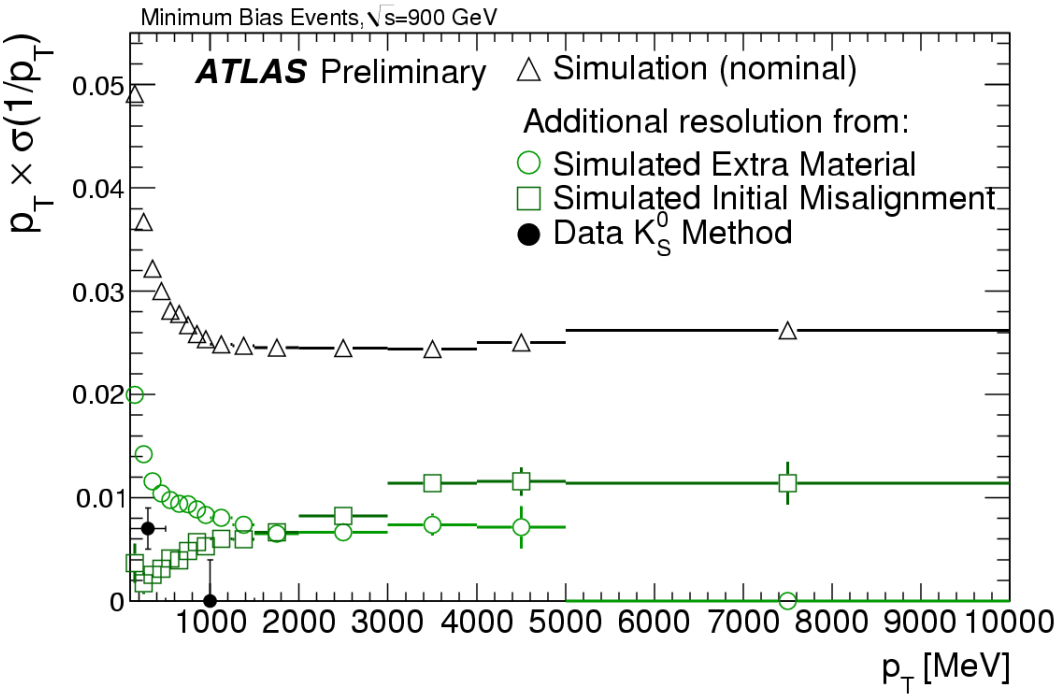

Figure 3.8: Momentum resolution of the ATLAS Inner Detector, as a function of transverse momentum [38].

give a stereo measurement resolution of around 500 μm, and perpendicular to the strips, a resolution of around 20 μm [36].

3.2.3 Transition Radiation Tracker

The Transistion Radiation Tracker (TRT) uses an array of 144 cm long drift tubes to make measurements of charged particles. Each gas filled tube is around 4 mm in diameter and gives a spatial resolution in $R\phi$ of about 130 μm per tube [36], from the drift time information. The TRT is designed such that particles with $p_{\mathrm{T}} > 0.5$ GeV cross around 36 drift tubes, allowing for high accuracy momentum measurements in the $r\phi$ plane, and improving on the momentum resolution of tracks reconstructed only with silicon hits. In addition to the tracking, the TRT provides separation of electrons from hadrons in the momentum range 1–150 GeV, due to transition

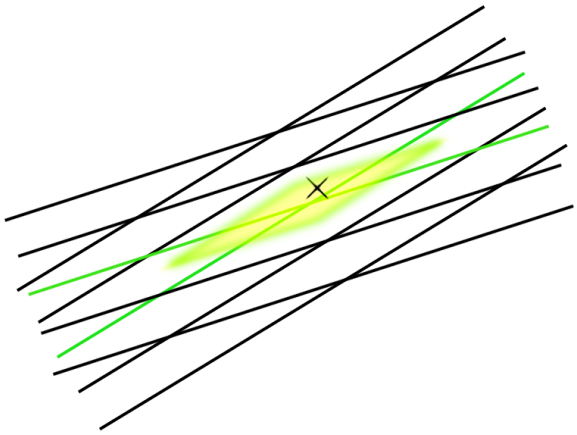

Figure 3.9: The SCT uses two layers of strips oriented at an angle relative to each other to obtain a rough measurement in z. If a particle is incident at the X, then a hit will be reconstructed in the highlighted area.

radiation[†].

3.3 Calorimetry

The goal of the ATLAS calorimeters is to provide accurate measurement of the position and energy of electrons, photons and jets, as well as accurate determination of the missing transverse energy[‡], $E_{\mathrm{T}}^{\mathrm{miss}}$, in an event. The calorimeter can also provide particle identification, and is used to select events at the triggering level.

The ATLAS calorimetry is split into two sections. An EM calorimeter [41] covers the range $|\eta| < 3.2$, with a hadronic calorimeter [42] outside the EM calorimeter, covering the range $|\eta| < 1.7$ in the barrel and $1.5 < |\eta| < 3.2$ in the endcaps. There are also forward calorimeters each side of the barrel, covering the pseudorapidity

[†]Transition radiation occurs when a high γ particle (such as an electron) crosses a transition region between two materials with differing electric constants. For electrons this radiation can be detected to aid in particle identification [40].

[‡]The initial momentum in the xy plane is zero, as the incident beam is oriented along the z axis. To conserve momentum, the final state momentum must also sum to zero. Any discrepancy is called 'missing'

range $3.1 < |\eta| < 4.9$.

Figure 3.10 shows the extent in η for each of the calorimeter components, where each component of the hadronic calorimeter is divided into its constituent layers. The bottom unmarked layer corresponds to material before the calorimeter, which includes the ID material and the solenoid magnet. The hadronic tile calorimeter is shown extending over the range $|\eta| < 1.7$. Also shown are the hadronic endcap calorimeters (HEC) and the forward calorimeters (FCAL). The large material budget is required in order to contain electromagnetic or hadronic showers, absorbing all of the energy before the shower is able to exit the extent of the calorimeter. The ATLAS calorimetry uses a sampling technique, where two different materials are used in order to cause first a particle to interact, and second, detect the showered particles. This is as opposed to a homogenous calorimeter in which the showering material and the sampling material are one and the same.

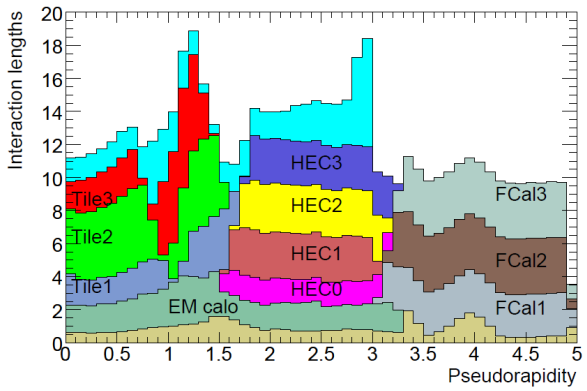

Figure 3.10: Material content of the ATLAS calorimeters over $|\eta|$, expressed in interaction lengths[§]. This plot also includes contributions from material before the calorimeter (the bottom most layer), and from the muon system after the calorimeter (the top most layer) [37].

The technologies used for the Electromagnetic calorimeter and the Hadronic calorimeters in ATLAS are described in the next sections.

[§]The interaction length of a material denotes how much material is needed to reduce a number of high energy neutrons to $1/e$ their original number.

3.3.1 Electromagnetic Calorimeter

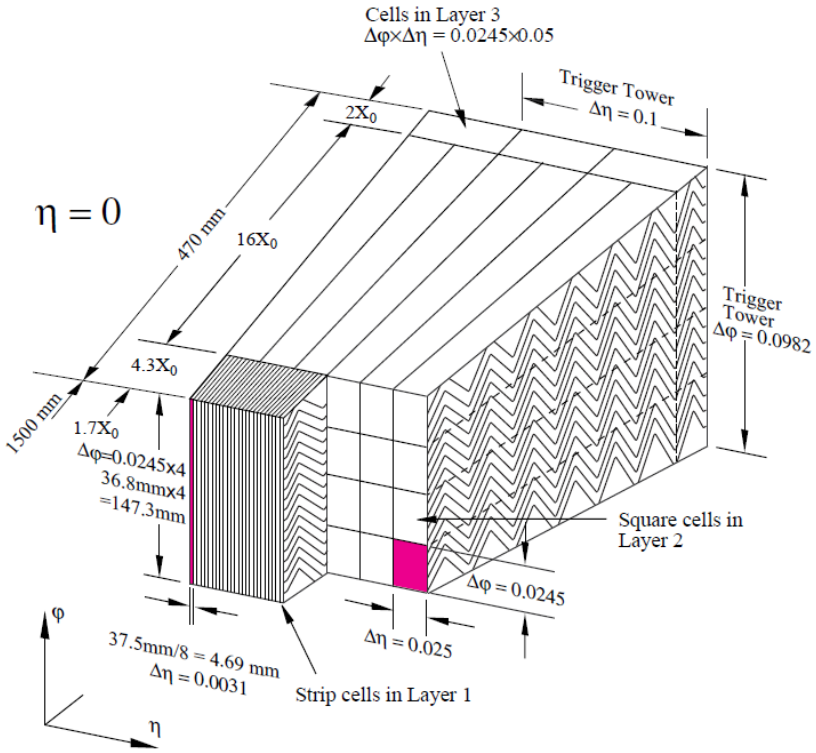

Figure 3.11: The Liquid Argon calorimeter is constructed with an accordion pattern to reduce potential cracks in acceptance [37].

The EM calorimeter uses a lead and liquid argon system, with electrodes arranged in an accordion pattern to minimise cracks in the ϕ coverage, and constructed in two separate halves, with a small gap at $\eta = 0$ to allow for services. Figure 3.11 shows the accordion structure of the LAr calorimeter. In the region $|\eta| < 2.5$, the EM calorimeter is segmented into three samplings, the first having a depth of $4.3X_0$, constant in η and finely segmented to provide an accurate η measurement. The second sampling is split into towers of $\Delta\eta \times \Delta\phi = 0.025 \times 0.025$, with depth $16X_0$ and the third sampling has towers twice the size, at $\Delta\eta \times \Delta\phi = 0.05 \times 0.025$, with depth varying with η from $2X_0$–$12X_0$ [41].

The remaining EM calorimetry, in the end-cap for $|\eta| > 2.5$, uses the same lead-liquid argon technology, but with a coarser granularity while still being sufficient to

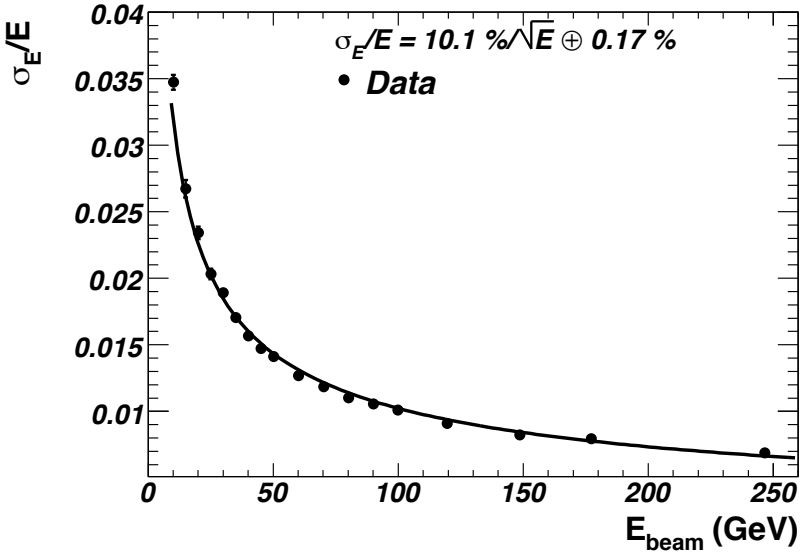

Figure 3.12: Energy resolution as a function of electron beam energy for LAr barrel modules of the EM calorimeter.

fulfill the $E_{\mathrm{T}}^{\mathrm{miss}}$ and jet measurement requirements. Figure 3.12 shows the fractional energy resolution in the EM calorimeter as a function of electron beam energy [36].

3.3.2 Hadronic Calorimeter

The hadronic calorimeter in ATLAS uses a similar LAr technology as the EM calorimeter in the endcaps and forward calorimeter, though with a copper absorber in the endcaps and the first forward calorimeter layer, and a tungsten absorber in the latter layers of the forward calorimeter. The hadronic endcap (HEC) covers a pseudorapidity range of around $1.5 < |\eta| < 3.2$ and the forward calorimeter (FCAL) continues the coverage from $3.1 < |\eta| < 4.9$.

In the barrel region ($|\eta| < 1.7$) ATLAS employs tile calorimetry. The tile calorimeter uses an iron absorber with scintillating tiles, attached to photomultiplier tubes to read out the energy deposition. Each of the iron tiles is 3 cm thick, perpendicular to the beam and staggered with radius. In total, the calorimeter system provides

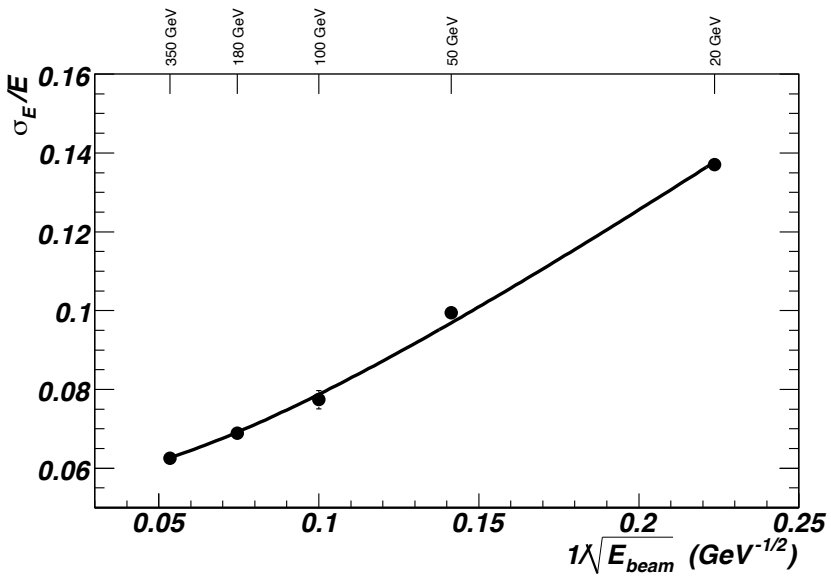

Figure 3.13: Fractional energy resolution as a function of the inverse square of energy for pions up to 350 GeV in the ATLAS hadronic calorimeter.

around 11 interaction lengths at $\eta = 0$, which is sufficient to reduce the amount of hadronic punch through to the muon system to a negligible amount. Around 10 interactions lengths are sufficient for the required resolution performance of high energy jets [43]. Figure 3.13 shows the fractional energy resolution of pions in the hadronic calorimeter as a function of pion energy [36]. The tile cells are segmented into towers of $\Delta\eta \times \Delta\phi = 0.1 \times 0.1$, giving around 10,000 readout channels.

3.4 Muon Spectrometer

The ATLAS muon system sits on the outside of the detector, operating conceptually similarly to the ID. Particles leaving the calorimeters are measured in the muon spectrometer. If the track, reconstructed in the muon system, matches a track reconstructed in the ID, both tracks are combined as a 'muon'. Due to the bending direction in the toroidal magnetic field being perpendicular to that in the ID, the

muon spectrometer allows an independent measurement of the muon momentum.

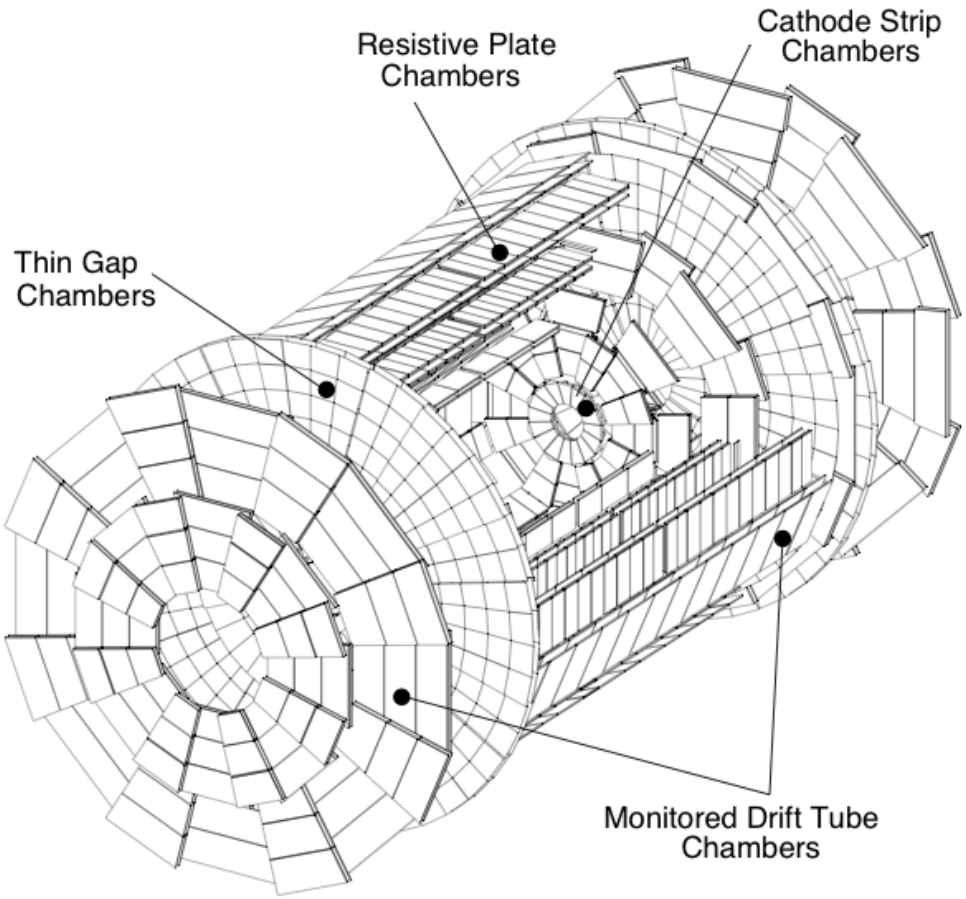

Figure 3.14: Overview of the ATLAS muon system [44].

3.4.1 Monitored Drift Tubes

The Monitored Drift Tubes (MDT) detector provides the primary momentum measurement in the muon system, with an area of almost 5500 m^2 covering ATLAS over the full ϕ range and $|\eta| < 2$. An aluminium drift tube of 30 mm diameter filled with a gas mixture composed of $Ar/N_2/CH_4$ (91%/4%/5%) with a central wire measures the ionisation of muons as they traverse the chamber, with a spatial resolution of 80 μm. The MDT are aligned perpendicular to the beam, such that an accurate mea-

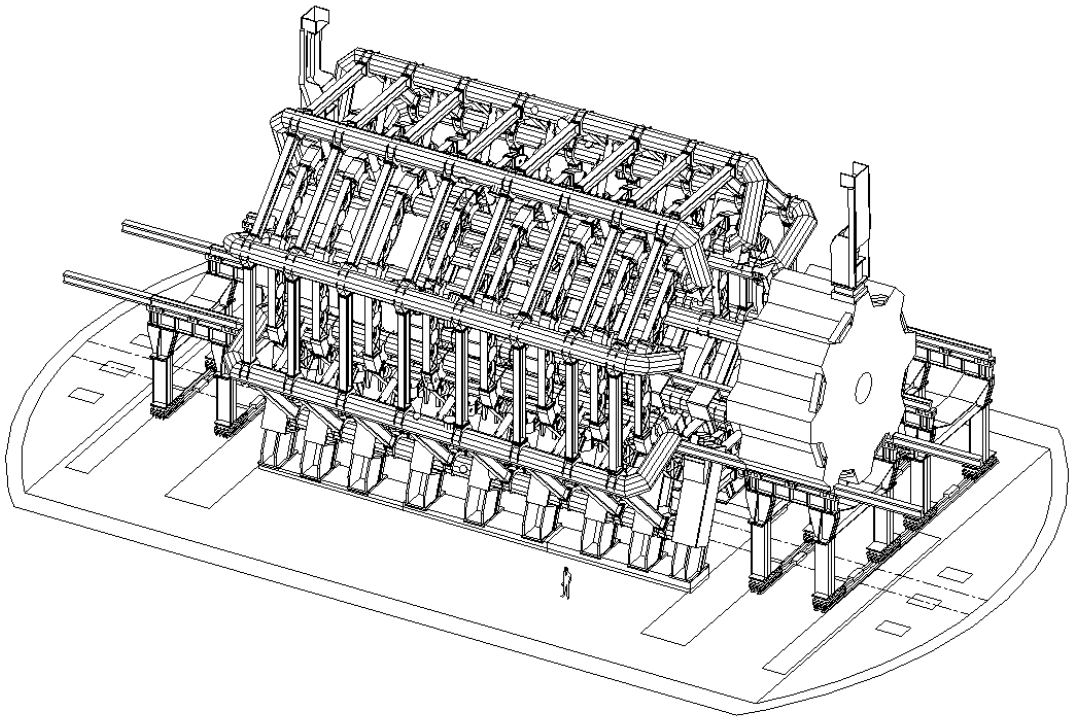

Figure 3.15: Overview of the ATLAS toroid magnet system. © CERN.

surement can be made in the R–z projection, while the positioning of the tube gives very rough positioning information in ϕ. As the MDT are fairly long (between 1 and 6 m) and cover such a large area, it is difficult to maintain constant environmental conditions, such as gas temperature and composition, as well as sagging in the tubes themseleves, so these conditions are monitored closely to allow for corrections and calibrations to be made. The MDT detectors are present in the barrel and endcaps of ATLAS, and make up the largest part of the muon system.

3.4.2 Cathode Strip Chambers

While the MDT detector performs well in the barrel and $|\eta| < 2$ endcap ranges, the large particle fluxes at high pseudorapidity make them unsuitable for use in the

$2.0 < |\eta| < 2.7$ range. At these forward regions, Cathode Strip Chambers (CSC) are used. The CSC are multiwire proportional chambers, providing a spatial resolution of 80 μm with a short drift time. In comparison with the MDT, which have a maximal drift time of 500 ns, the CSC are more than 10 times faster, with drift times less than 30 ns.

3.4.3 Resistive Plate Chambers

Resistive Plate Chambers (RPC) and Thin Gap Chambers (TGC) have a fast readout and are used mainly for triggering rather than precision measurement. The RPC provide triggering in the barrel region and are made of two resistive plates with a gas gap. A muon ionises the gas and the electric field in the chamber produces an avalanche of electrons. The signal is then read out to provide a coarse position measurement, along with $\sim$ 1ns precision timing information, which is used for the trigger.

3.4.4 Thin Gap Chambers

The TGC provide triggering in the endcap regions, as well as providing an azimuthal measurement to complement the MDT measurement. The TGC are similar to multiwire proportional chambers, which allow a $2 - 3$ mrad azimuthal resolution by measuring which wires in the chamber register, while staggering their placement. As with the RPC, the TGC have a fast readout time, which is required for the fast response of the ATLAS trigger system.

3.5 Magnetic Field

The magnetic fields in ATLAS are used for momentum measurement of charged particles in the ID and muon system. Two separate systems are used to provide the fields for the ID and muon system; the solenoid and toroids, respectively. The ATLAS solenoid is an Al and NbTi/Cu superconductor, located within the LAr cryostat, cooled to 4.5 K. The solenoid provides a magnetic field of 2.0 T to the tracking volume for momentum measurement.

The toroid system is the largest magnetic system in ATLAS, as well as the system giving ATLAS its name. The toroidal field is provided in the barrel region by 8 large superconducting coils, situated outside of the hadronic calorimeter. The coils are cooled to 4.6 K for a current of up to 20.5 kA to provide a peak field of 3.9 T. The barrel toroids are completed on each end by two end cap toroids. Because the toroidal field is created by three separate magnets, the transition regions between each magnet can be complicated, and in order to achieve accurate momentum measurements, this transition region must be modelled very well. Magnetic field maps in the transverse and longitudinal planes are shown in figures 3.16 and 3.17.

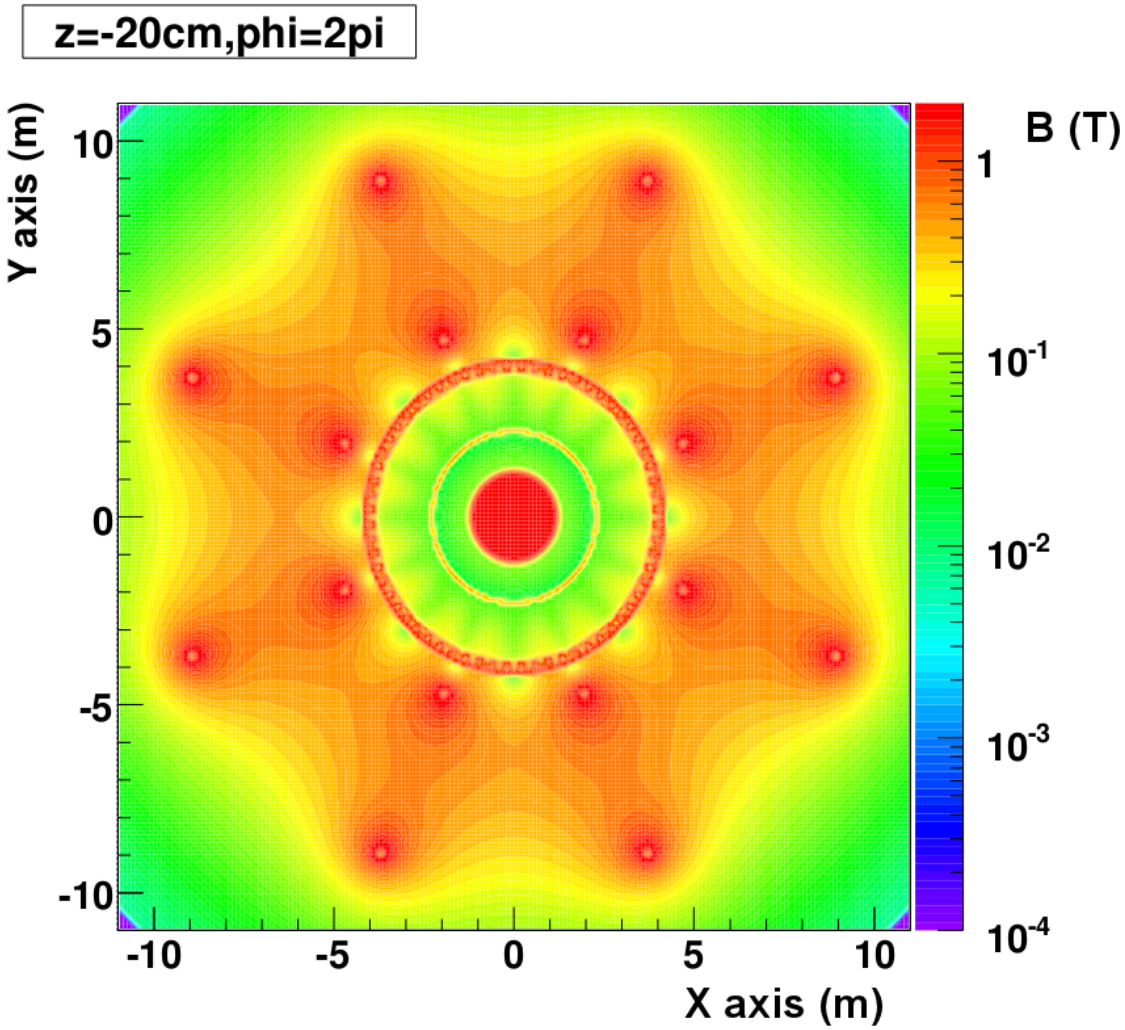

Figure 3.16: Magnetic field map in the transverse plane at fixed $z = -20$ cm [45].

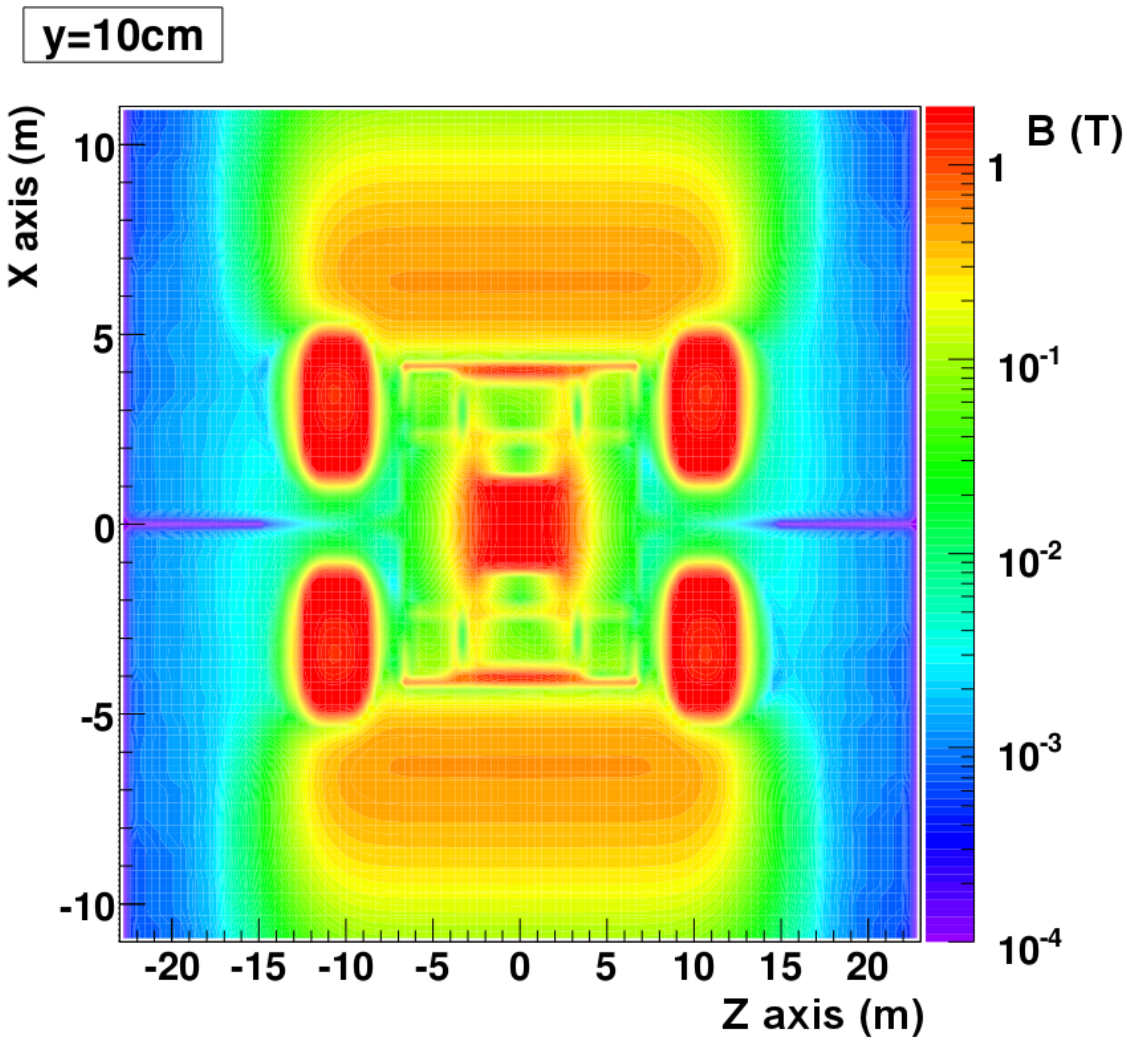

Figure 3.17: Magnetic field map in the longitudinal plane at fixed $y = 10$ cm [45].

3.6 Trigger

The LHC can provide a bunch crossing, or event, in ATLAS as frequent as every 25 ns, a rate of 40 MHz. This rate is far too high to write to disk, both due to the speed needed to write the events to disk, as well as the storage space needed, given that each event can be up to 1.6 MB in size (see section 3.8). Fortunately, not every bunch crossing will contain an event interesting enough to record, so some events can be thrown away. In order to do this, ATLAS employs an online trigger system, which decides whether or not to record an event based on activity within the event.

The ATLAS trigger is split into three layers, each looking in more detail at the event. The Level 1 Trigger must decide every 25 ns if an event should pass to the next level or not, which poses a problem, as the signals from the detector cannot reach the trigger hardware in such a short timescale. In order to compensate for this, the trigger uses an event pipeline, which stores data in a buffer to allow more time to make a decision. The pipeline allows 2.5 μs for a decision, before the on-detector memory fills up, of which 1 μs is allocated to the transfer of data from the detector to the trigger, which is located outside of the main detector cavern. A further 0.5 μs is left as contingency, leaving 1 μs to make the decision.

The Level 1 Trigger looks at a limited selection of data from the detector, including a coarse summary of calorimeter activity, without depth information, as well as hits from the muon RPC and TGC. A set of fast algorithms looks at this information and decides if the event is interesting or not based on a menu of items, as well as creating an Region of Interest (ROI) for each interesting object. Even after the events are filtered in this way, the rate of interesting events may still be too high, at high luminosities. To address this, a prescale is implemented which takes a random sample from events satisfying a certain item in the menu. The output rate of the Level 1 Trigger is defined by the input rate to the Level 2 Trigger, which is 75–100 kHz. The prescale is set through keys, where a key of X means only a fraction

$1/X$ events are saved.

The Level 2 Trigger looks at the ROIs from Level 1 with higher granularity calorimeter information, as well as using the tracking information, to make a further decision on whether the Level 1 passed events are interesting or not. The Level 2 trigger has a more relaxed time limit, of around 10 ms, in which to make its decision, given the lower input rate, which affords it the ability to look in much more detail than Level 1. The Level 2 Trigger aims to reduce the event rate to around 1 kHz, at which point the Event Filter (EF) can run more sophisticated algorithms to make a final decision if the event should be stored, with a goal rate of around 200–400 Hz, a much more manageable rate for data storage.

3.7 Pileup

The total interaction cross section for proton-proton collisions at 7 TeV is around 69 mb [46], and with a luminosity close to 10^{34} cm^{-2} s^{-1} gives around 25 interactions per bunch crossing. If an interesting interaction takes place, the trigger will fire and decide whether or not to record the event. The cross section for an 'interesting interaction' which fires the trigger may be several orders of magnitude lower than the total proton-proton cross section (see Figure 3.18). The other interactions in the bunch crossing will likely be from soft QCD interactions. The extra hits in the detector can create problems when reconstructing, by introducing extra tracks or jets, as well as producing additional displaced vertices. Pileup resulting from extra interactions within the same bunch is called 'in time' pileup. In addition, interactions in neighbouring bunch crossings can be seen by some subdetectors, due to the long readout times with respect to the bunch spacing. This is called 'out of time' pileup.

As pileup presents a significant challenge in untangling recorded events, accurate

tracking and good vertexing are needed to identify the extra vertices, and a good pileup simulation helps to understand the effects of pileup on a given analysis.

3.8 ATLAS Event Data Model

ATLAS can record several events per second, with billions of events stored on disk each year. A typical event in its 'RAW' format is around 1.6 MB, so storage space for datasets must be of the order of petabytes. This poses a problem to an end user intending to analyse this data, due to limited computing power available. In order to combat this issue, the data are processed into smaller formats, removing much of the information a typical analyser does not need.

Event Summary Data (ESD) contains output from the detector reconstruction, such as tracks and tracking hits, calorimeter cells and muon hits, as well as further reconstructed objects like jets and electrons. The ESD contains information sufficient for calibration studies, tracking algorithm tuning and particle identification. The target size for ESD is less than half that of the RAW data, at 500 kB, though this is still too large for frequent and fast analysis algorithms.

Analysis Object Data (AOD) provides a general summary of the event, containing only information relevant to common physics analyses. AOD contains reconstructed physics objects, trigger information and tracks, but removes much of the unnecessary detail with respect to the ESD, such as tracking hits and calorimeter cells. The target size of 100 kB per event is over tenfold reduced from RAW, though for analyses of large datasets may still be too large.

Since specific analyses may require only a subset of the physics objects available, so the ESD and AOD formats may be customised and reduced even further. Derived Physics Data (DPD) is a customised subset of AOD containing only the information required for a given analysis. This customisation means that different analyses will

require different DPD datasets, though the benefit being a much reduced size, with even the possibility of storing a full dataset on a local system. DPD can be reduced even further via a few different methods:

- Skimming removes entire events that are not considered interesting for a given analysis. For example, a $Z \to e^+e^-$ analysis may remove events which do not contain two good electron candidates.
- Trimming removes containers of data from the whole dataset, which may not be needed in the analysis. A $t\bar{t}$ analysis may have no need to look at photons, and so the photon containers would be trimmed from the file.
- Thinning removes objects from a container, where certain conditions are required of the object. This may be removal of electrons with $p_{\mathrm{T}} < 15$ GeV, or jets with $|\eta| > 2.5$, for example.
- Slimming is the removal of specific parts of an object which are not needed, such as electron track parameters, where other properties of the electron are kept.

In order to reduce the size of the dataset used for this thesis, skimming is used to remove events not containing at least one electron or muon candidate, trimming is used to remove data such as photon containers, and slimming removes unnecessary parts of the object containers, such as alternative $E_{\mathrm{T}}^{\mathrm{miss}}$ calculation parameters.

3.8.1 Grid Computing

Even after the data have been reduced to more managable sizes, there may not be sufficient resources for a user to run a full analysis on a local system. The LHC computing grid [48] is a distributed computing system to allow a user to split an analysis into subjobs to submit to computers around the world. This distributed

system makes a large amount of computing power available to every user, as well as alleviating the burdon of storing vast amounts of data locally.

The grid is split into 'tiers', with Tier-0 being the onsite CERN computing facility, which provides the initial event reconstruction from the raw detector data. The data are then sent to several Tier-1 sites which provide further reprocessing of the data as well as a large amount of storage for the raw and reconstructed data. The data are largely duplicated across Tier-1 sites to provide a backup system. Further data storage is provided by Tier-2 sites, as well as a large amount of computing power used for large scale MC simulations (described in section 6.3.1). Finally, Tier-3 refers to the local resources, amounting to desktop computers and laptops, which users can utilise to access the grid. Tier-3 is responsible for submission of analysis jobs to grid resources.

Figure 3.19 shows a topological diagram of the distributed computing model in ATLAS and the LHC.

For this thesis, the grid was mainly used in order to perform the previously mentioned data reduction techniques, allowing the required datasets to be downloaded and analysed locally and offline.

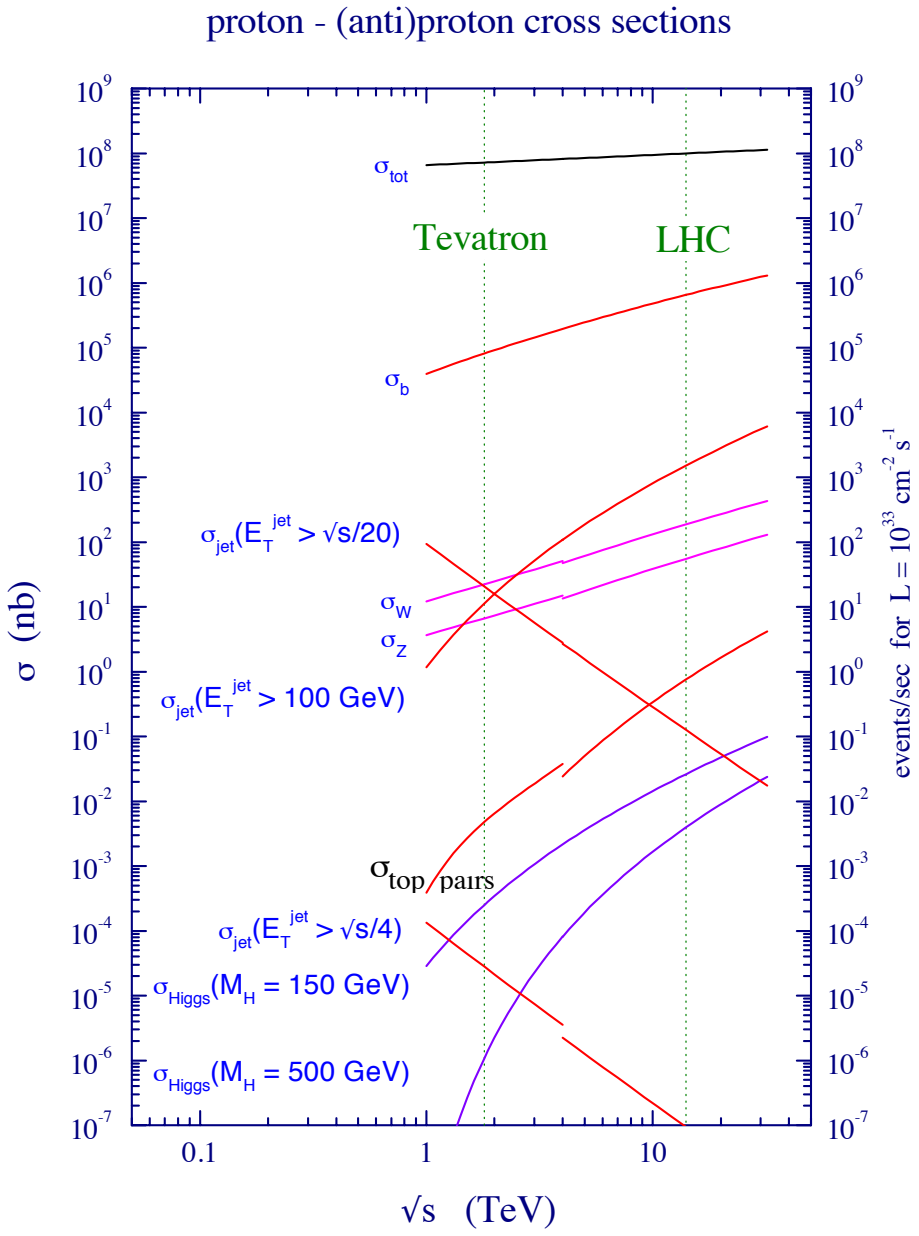

Figure 3.18: Cross section for various interesting processes versus collision energy, for proton-(anti)proton collisions. The total interaction cross section is the top line. The discontinuity in the lines corresponds to the transition from $p\bar{p}$ to pp in the calculation of the cross sections [47].

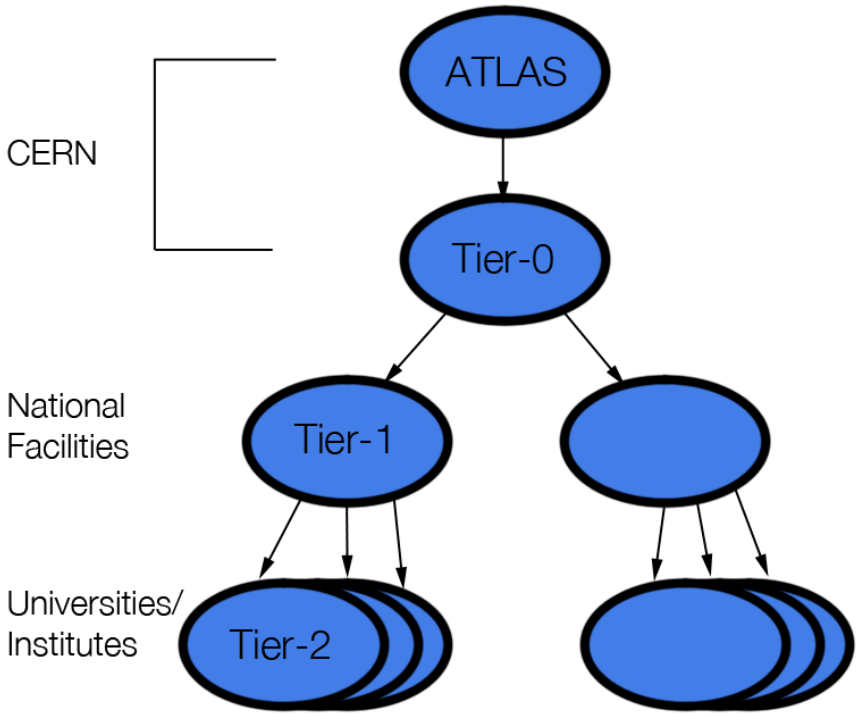

Figure 3.19: Overview of the distribution of resources in the grid computing model.

Chapter 4

Atlantis - The ATLAS Event Display

An event display is software used to present a visual representation of collision data recorded in a particle physics experiment. This allows for online monitoring of the detector whilst it is running, as well as production of images for scientific papers and press release. Atlantis is one of the event displays used at ATLAS, providing an interactive visualisation of events within the detector, using several data oriented projections. Figure 4.1 shows the interactive canvas which displays the events, as well as the Graphical User Interface (GUI).

Atlantis is written in the Java language, separate from the integrated ATLAS software framework (Athena), making the event display portable and cross platform compatible. The event files used in Atlantis must first be produced from an ATLAS data format using JiveXML, an Athena package which encodes the event as an XML file, which can then be downloaded to a computer running Atlantis. The following chapter will give a brief overview of Atlantis, as well as a description of development of the software and outreach activities using Atlantis.

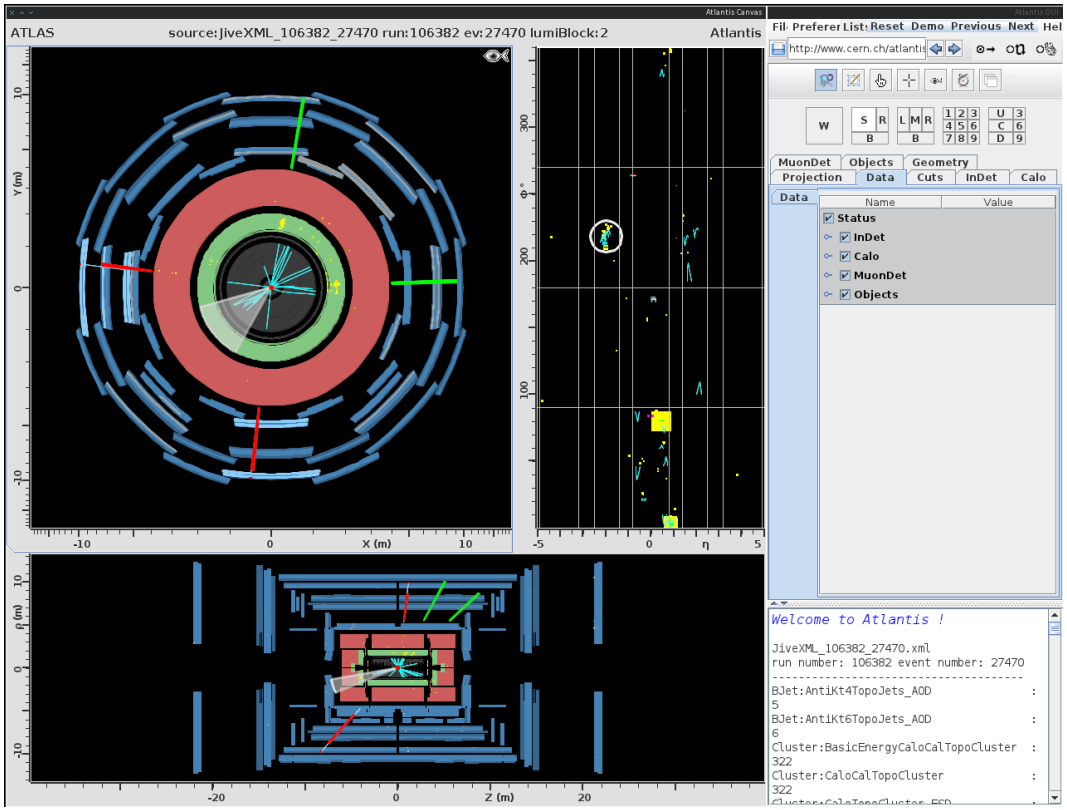

Figure 4.1: Atlantis, the ATLAS Event Display. Atlantis is formed of two parts, the Canvas on the left and the GUI on the right.

4.1 Structure of Atlantis

4.1.1 JiveXML

JiveXML is a C++ software package within the Athena framework, to allow for the production of events as XML files readable by Atlantis. JiveXML supports production of events from both simulated events as well as recorded data, from a variety of ATLAS data formats, including ESD and AOD. Since the ESD format contains more information than AOD, users wishing to display as much information as possible, including tracking hits and calorimeter cells, tend to run JiveXML production on ESD. JiveXML can in addition be run during event reconstruction, producing event XML files readable by Atlantis from events shortly after they are read out from the detector.

A user may specify options within the Athena reconstruction job to process only certain data types, which allow customisation of the JiveXML output for specific needs. In this way, for example, secondary vertices from long lifetime particles may be processed and displayed in Atlantis. Users wishing to display an event containing only physics objects such as electrons, muons, jets, missing energy or reconstructed tracks, can produce smaller XML files from the AOD format.

JiveXML is split into several components, each handling a specific part of the detector, for example *CaloJiveXML* deals with the output of calorimeter related information, and *TrkJiveXML* deals with the tracking information. Each component is managed and maintained through a Subversion (SVN) repository, centrally located at CERN.

4.1.2 AtlantisJava

AtlantisJava, commonly referred to simply as Atlantis, is the primary graphical component of the Event Display. Atlantis is able to run on any computer with any operating system supporting a Java 1.6+ environment. Atlantis is able to load XML files output by JiveXML and render the information over a variety of projections. Projection here refers simply to the coordinate system, based on the ATLAS coordinate system defined in section 3.1, used to display the data, including, but not limited to:

- XY
- ρZ
- $\eta\phi$
- $\phi\rho$
- ϕZ
- $\eta\phi$ LegoPlot

An overview of these projections is shown in figure 4.2.

As well as the ability to present data in a range of projections, Atlantis allows the user a degree of interaction with the event, allowing for manipulation of the projections such as rotation or zooming, as well as extracting further information from parts of the display through the pick tool. In addition to this, the display can be customised in other ways, hiding unwanted data, highlighting important data, or linking different data types together, for example, colouring inner detector tracks based on their associated object. Much of this customisation can be saved and reloaded at a later date through the use of configuration files, streamlining the creation of customised 'versions' of Atlantis. This flexibility makes Atlantis ideal for

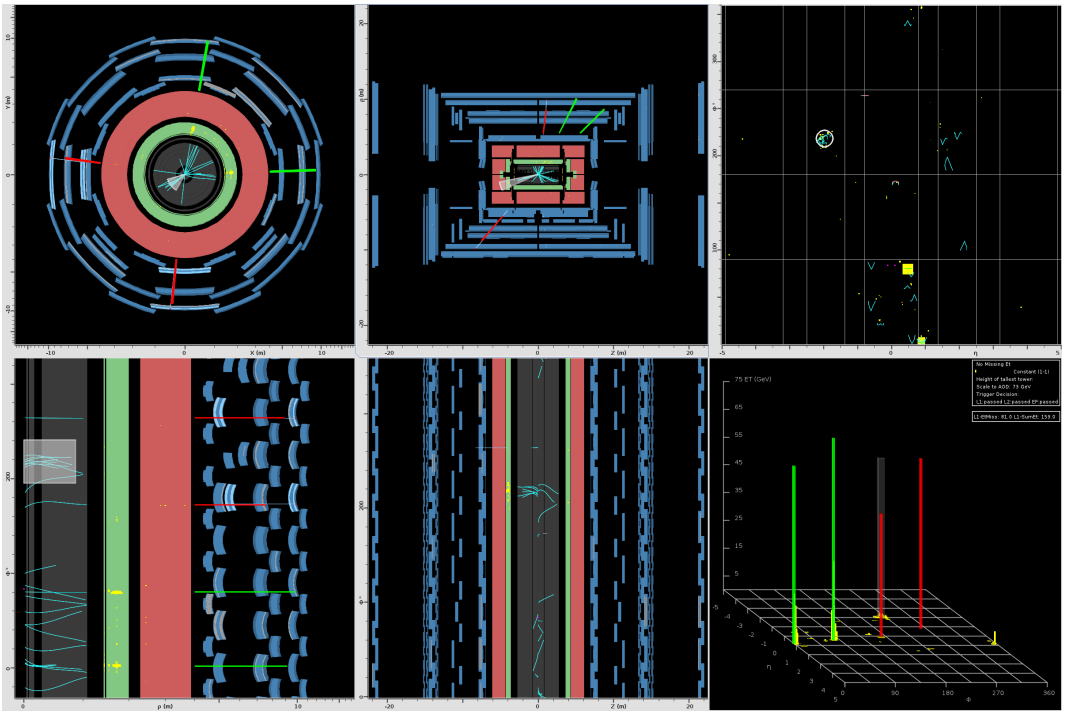

Figure 4.2: A screen capture of Atlantis, showing a simulated $H \rightarrow ZZ \rightarrow 4l$ event in six different projections. Clockwise from top left: XY, ρZ, $\eta\phi$, $\phi\rho$, ϕZ and the $\eta\phi$ LegoPlot.

creating event displays for presentations, papers, press releases and media events, as well as lending itself to the creation of interactive outreach activities.

4.2 Projections

This section describes some of the most commonly used projections in Atlantis.

4.2.1 XY

One of the primary projections in Atlantis, the XY projection shows data overlaid on a transverse slice of ATLAS. This projection lends itself well to showing data in the barrel region, as illustrated in figure 4.3. Only calorimeter cells and tracking hits in the barrel region of each subdetector can be shown on this projection, as

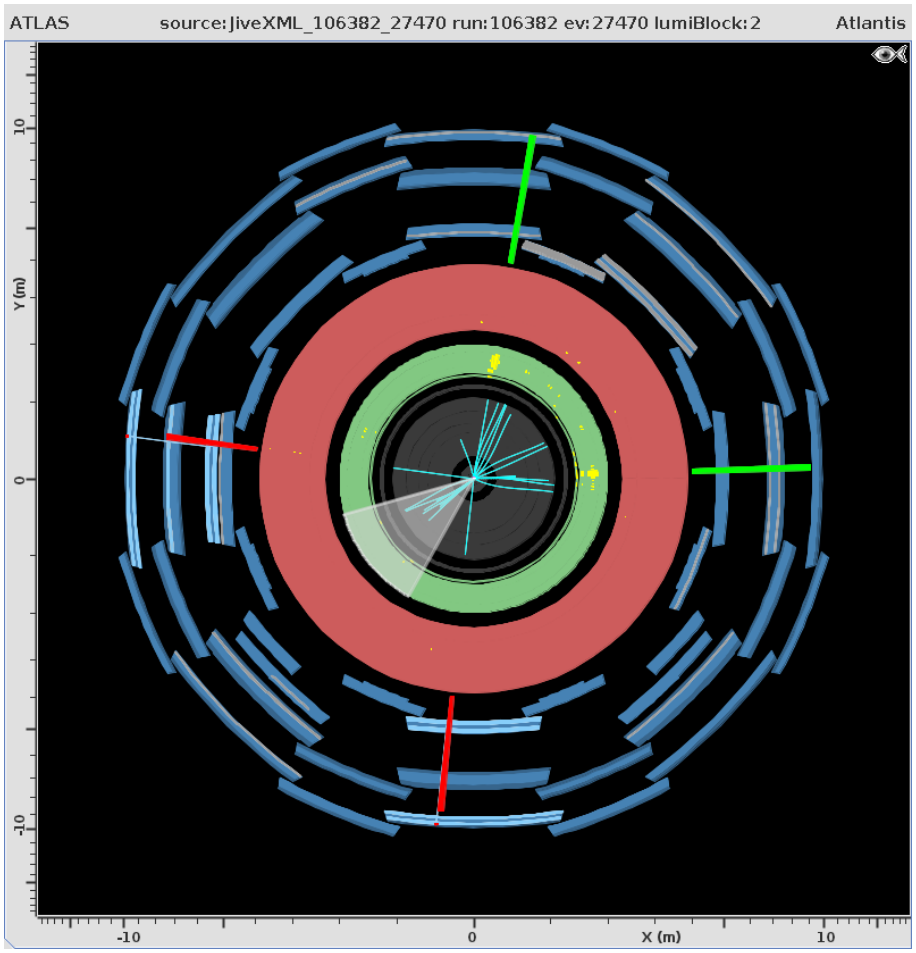

Figure 4.3: The XY projection only shows the geometry of the detector in the barrel region. Both raw data and reconstructed objects are shown here, including calorimeter cells (yellow), tracks (blue), electrons (green) and muons (red). Reconstructed objects may be shown for the full η range, or only up to a threshold in η.

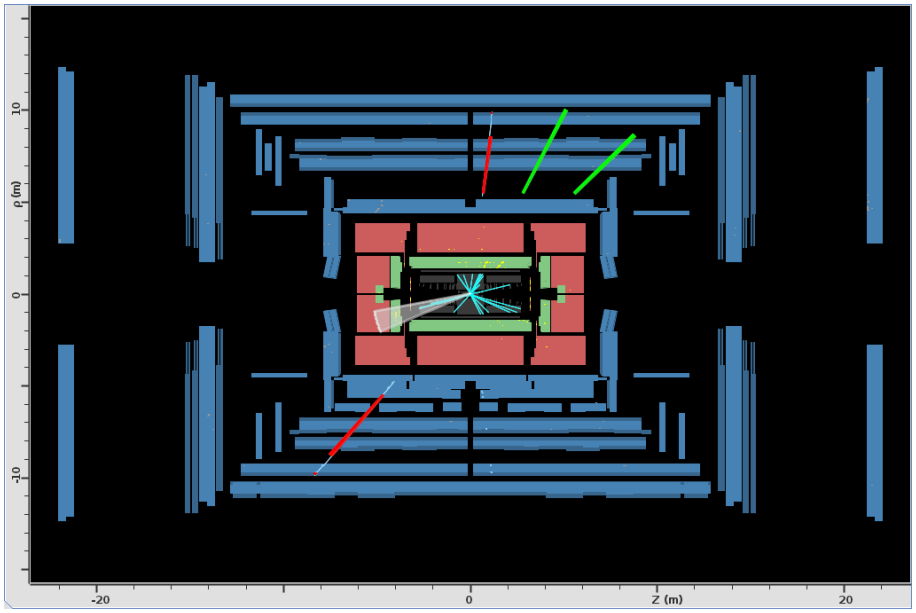

Figure 4.4: The ρZ (or RZ) projection represents a longitudinal slice through ATLAS, with the transverse coordinate being replaced by ρ.

the geometry of the endcap is hidden. Reconstructed objects, such as tracks, jets, electrons, or muons may be shown over the full η range. Displaying tracks over the full η range can lead to 'half tracks', owing to the fact that forward tracks will leave the tracking volume before reaching the maximum transverse extent of the tracker. Missing transverse energy is also shown as a dashed line or arrow, with the thickness of the line or length of the arrow dependent on the amount of missing energy.

4.2.2 ρZ

The second most commonly used projection is ρZ, or RZ (shown in figure 4.4). This shows a pseudo-longitudinal slice along the z–axis, allowing both barrel and endcaps to be shown.

To allow a clearer display, rather than using simply yz or xz, ρ is defined as:

$$\rho = \sqrt{x^2 + y^2}. \tag{4.1}$$

Take a track as an example. If the track is pointing exactly along the y–axis, then in a xz projection, this track would show up as a point. Using the coordinate ρ instead allows the track to show its full extent in the projection. In effect, this projection combines both a side view and a top view in a single projection.

4.2.3 $\eta\phi$ (V plot)

The $\eta\phi$ projection displays data in ATLAS using the azimuthal coordinate, ϕ, and pseudorapidity, η, in a regular two dimensional grid. Tracking hits, calorimeter cells, reconstructed tracks, reconstructed physics objects and reconstructed vertices can all be represented in this plot, as illustrated in figure 4.5.

This projection is often called the 'V plot' due to the way it displays tracks. At the production point of the track, the point will have a ϕ value and an η value. The value of ϕ will change as it traverses the tracking volume, owing to the magnetic field. Without modification, this plot would display the track as a straight line at constant η originating at the start of the track, and ending at the point the track leaves the tracking volume. This has the benefit of distinguishing low and high p_{T} tracks, given that a low p_{T} particle would bend more in the tracking volume, giving a larger range of ϕ values at each point. The disadvantage of displaying tracks in this way is that it is impossible to determine the direction of bending, and thus charge. The V plot addresses this by applying a transformation to the η coordinate

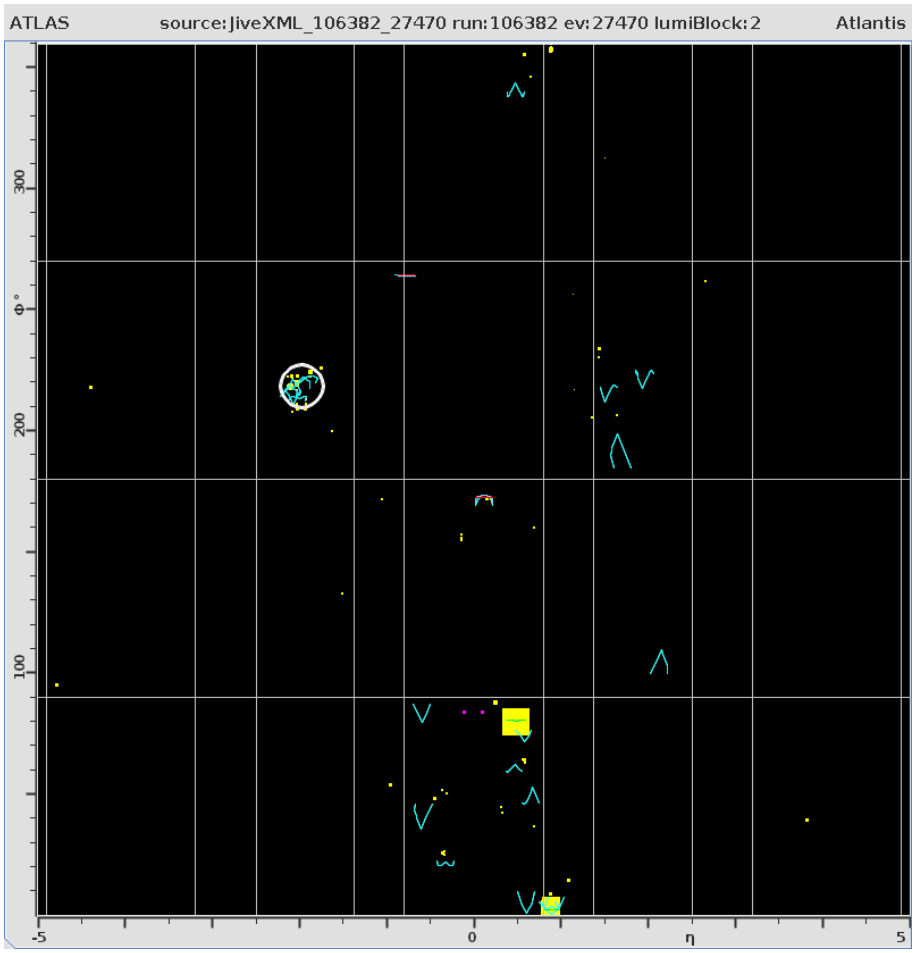

Figure 4.5: The $\eta\phi$ projection shows data in ATLAS on a grid with the azimuthal coordinate, ϕ, and pseudorapidity, η. Tracks are represented by the 'V' shaped lines, giving this projection its nickname of the 'V plot'. Calorimeter deposits are shown as yellow boxes, with area proportional to the energy content, and reconstructed objects such as jets are shown as circles.

of the track:

$$\eta \rightarrow \eta \pm k(\rho_{\max} - \rho), \tag{4.2}$$

where ρ is the radial distance of the point from the vertex, $\rho_{\max}$ is the maximum radial extent of the inner detector, and k is an arbitrary constant. This transformation will draw two points for each η point, giving the track a V shape, with the apex of the V corresponding to the point at which the track exits the tracking volume, with the V opening towards the origin of the track. The variable k controls the width of the widest point of the V. High momentum tracks bend less in the tracking volume, leading to a short V in this projection, where a low momentum track would make a more elongated V. In addition, the charge of the particle determines which direction the V is displayed.

This transformation is applied with η measured with respect to the primary vertex, such that a track originating from the primary vertex would have a constant η, while a track from a secondary vertex would have varying η, making it look like a distorted V in this projection. This gives the ability to distinguish tracks from primary and secondary vertices. The same transformation is also applied to hits in the tracker.

4.2.4 Lego Plot

The LegoPlot (shown in figures 4.6 and 4.7) uses the same coordinates at the V plot, though it is designed for displaying calorimeter data, while the V plot works better for displaying tracks. Calorimeter activity is represented in the LegoPlot as yellow towers, with the height of the tower depending on the transverse energy deposited in a given $\Delta\eta \times \Delta\phi = 0.05 \times 0.05$ region of the calorimeter.

In addition to calorimeter cells, reconstructed objects may be represented in the LegoPlot as towers centred on their η and ϕ position, with height again determined

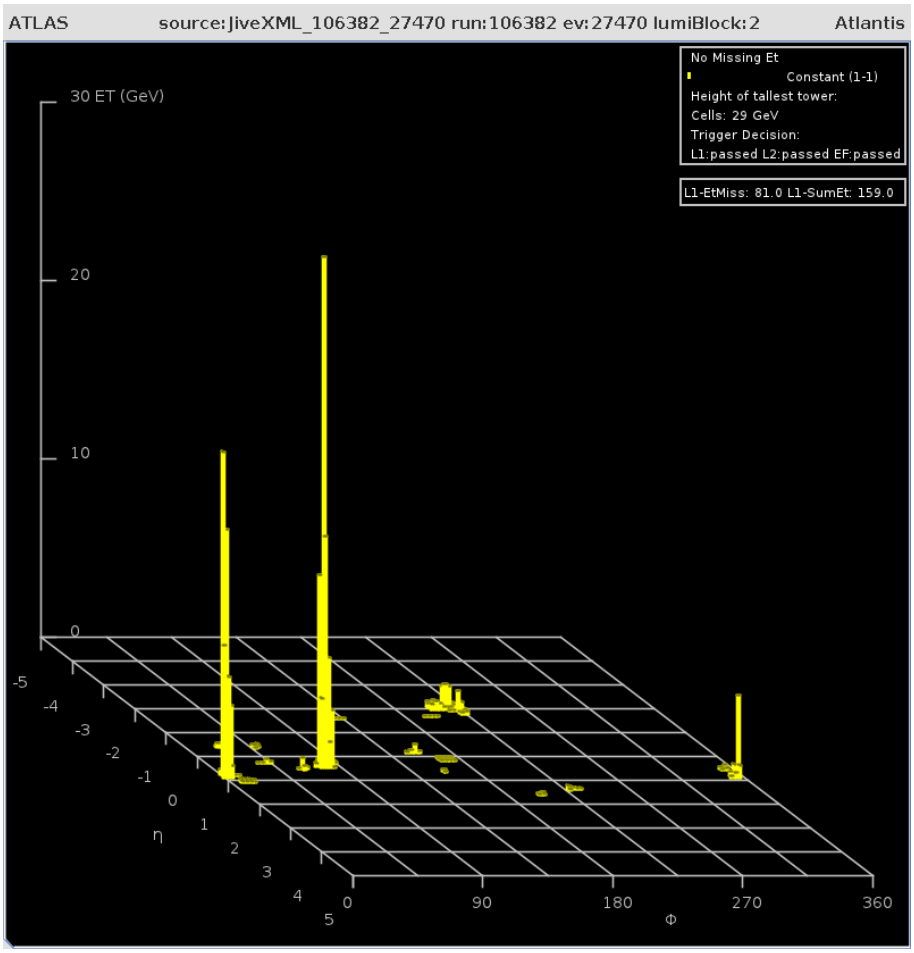

Figure 4.6: The LegoPlot uses the same $\eta\phi$ coordinates as the V-plot, though it does not show tracking information, instead focussing on a clearer display of calorimeter activity. The LegoPlot is segmented in η and ϕ, and any energy in calorimeter cells falling within a single segment contributes to the height of the calorimeter tower.

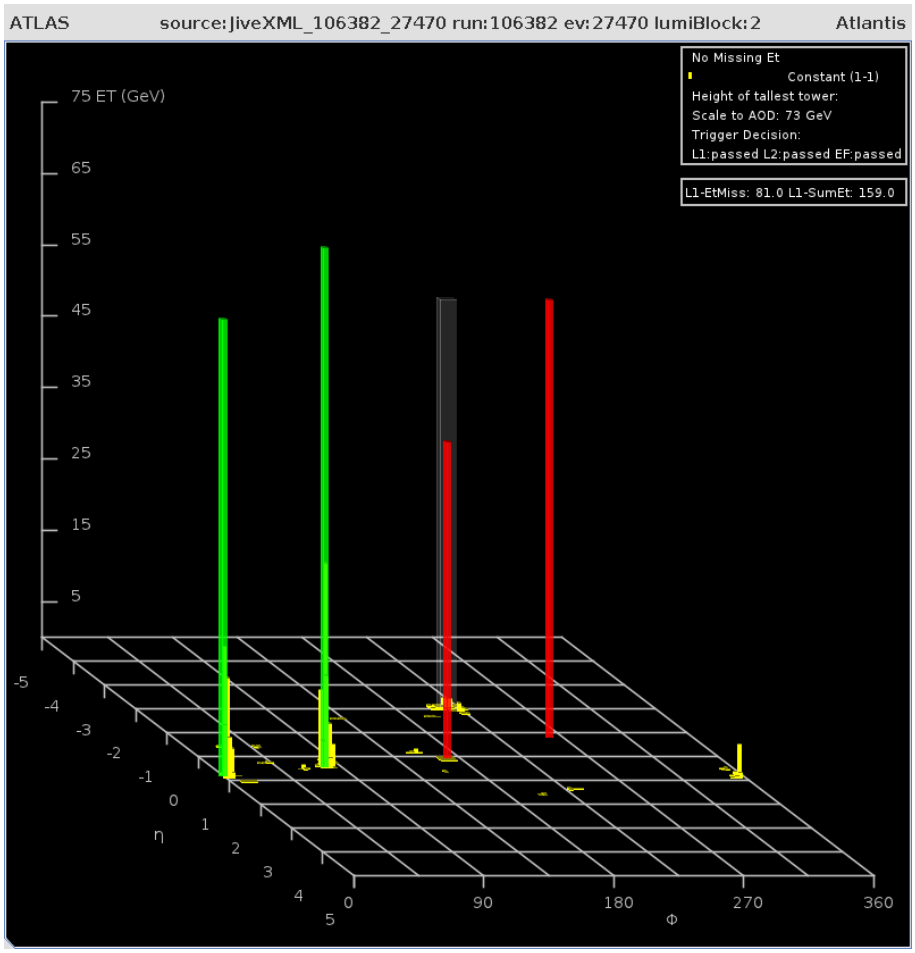

Figure 4.7: The LegoPlot, in addition to showing calorimeter activity, is able to give an overview of event activity by showing AOD objects. The transverse energy of the object determines the size of the tower. Here, green towers represent electrons, red towers represent muons, and transparent grey towers represent jets.

by the transverse energy of the object.

Missing transverse energy, by definition, only has a ϕ direction, and as such is displayed on the lego plot as a dashed line at constant ϕ, over the full η range. The magnitude of the $E_{\mathrm{T}}^{\mathrm{miss}}$ is shown in a summary box to the top right of the LegoPlot.

4.3 Interaction with Atlantis

Atlantis has the capability to not only display events, but to allow a degree of interaction with the events. The following section describes some of the ways that Atlantis allows a user to further scrutinise an event using the available interactions. Each of the interactions has a corresponding icon, allowing it to be selected from the GUI.

4.3.1 Zoom/Move/Rotate (ZMR)

The ZMR, or Zoom Move and Rotate interaction, allows a user to move the display within a given projection, zoom in to a specific region, or rotate the display logically given the projection. For example, the XY projection rotates intuitively around the z–axis, but the ρZ projection is slightly more complicated.

The ρZ coordinate system projects the magnitude of the tracks onto a pseudo-longitudinal plane slice of the detector (with $\rho^2 = x^2 + y^2$), with a split at fixed ϕ_{split} along the centre. Objects in the upper half of the detector (defined by ϕ_{split}) are projected upwards, and objects in the lower half downwards. The rotate tool allows the user to alter the ϕ_{split} value.

4.3.2 Rubberband

The Rubberband tool allows for batch selection of objects in order to create a 'List' of objects, which is useful for categorisation and colouring, or to zoom into the selected region. In addition to these functions, the Rubberband tool can print a 'summary' of the selected objects, which includes an invariant mass calculation for all of the selected objects.

4.3.3 Pick

The Pick tool allows a user to select individual objects, accompanied by information pertaining to that object printed in the output window. For example, picking a track will show the η, ϕ, p_{T}, number of hits from each tracking layer, etc. Picking a jet shows the measured energy and transverse energy, as well as the η and ϕ directions.

Additional utilities of the Pick tool are facilitated through keyboard shortcuts. An example is the invariant mass calculation, accessed with the keyboard shortcut 'M'. Clicking a track followed by another, and potentially more tracks, while holding down the 'M' key calculates the invariant mass of the selected system, with the assumption of a pion mass for each track. This calculation was extended for use with an outreach exercise to allow for calculation of invariant mass with respect to a secondary vertex (requiring a recalculation of track parameters), and assuming different masses for different possible decay modes.

4.3.4 Fisheye

The Fisheye tool works in a similar manner to Zoom, but instead of a simple zoom, Fisheye transforms the radial coordinate of the display by

$$\rho \rightarrow \frac{1 + c_f \rho_{\max}}{1 + c_f \rho} \rho, \tag{4.3}$$

where c_f is a constant determining the extent of the Fisheye transformation and $\rho_{\max}$ is defined as the maximum radial size of the detector.

Fisheye allows a user to keep a full picture of the event, while focussing more on the inner regions of the detector.

4.4 Atlantis Development

Atlantis is a constantly developing software package, with several UK and CERN based developers working on both bug fixing and maintenance as well as adding new features, or removing obsolete code. Atlantis is managed through an SVN repository, with frequently frozen (tagged) snapshots of the codebase. This allows development to continue on experimental features, whilst maintaining a stable version for use in the ATLAS control room as the online event display, for subdetector commissioning and debugging, or as an outreach tool. Described in this section are some of the recent features added to Atlantis by the author.

4.4.1 Event Properties Dialogue

A dialogue box showing an overview of every item available to display, populated by the contents of the XML event file, has been extended to show the items remaining after the selected cuts in the currently active display window have been applied.

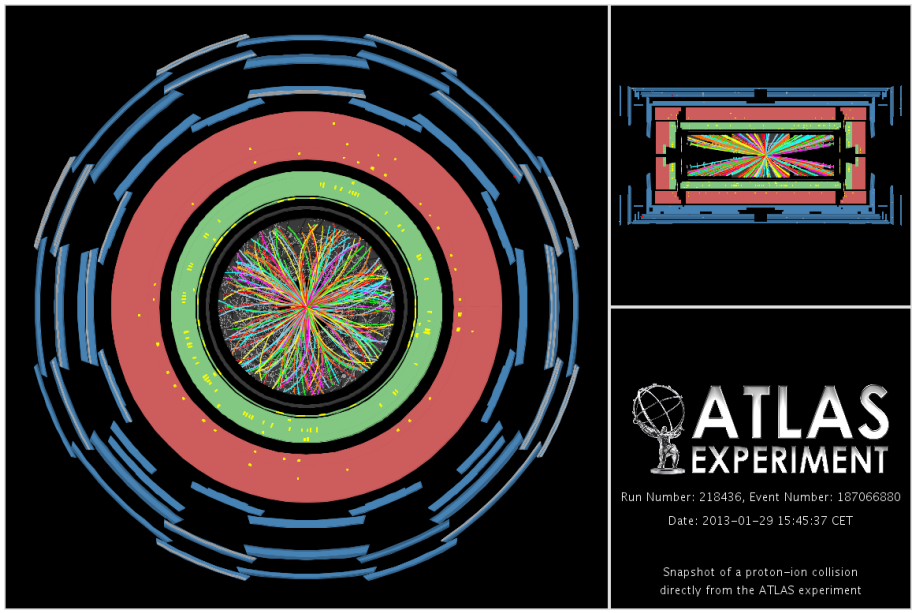

Figure 4.8: ATLAS live is a publicly available webpage, showing events soon after they are recorded in the detector. This event was recorded during the early 2013 proton-lead run.

This gives a quantitative idea of the effect of applying certain cuts on an event; applying a cut to a group of objects will remove any objects which do not pass the cut from this list.

4.4.2 Event Information Projection and Overlay

The EventInfo 'projection' is a pseudo-projection added to aid in the production of public event displays, simply displaying the run and event number, the time and date, and the ATLAS logo. This projection is also used in the public live event display webpage, *ATLAS live*[*], which displays events soon after they are recorded (see figure 4.8). The EventInfo projection was also extended to be more flexible in terms of the positioning of the logo, as well as relaxing the restriction that a space potentially available to show another physics oriented projection be taken up by the logo.

The 'Overlay' is a utility added in Atlantis to allow flexible position of the ATLAS

[*]http://atlas-live.cern.ch/

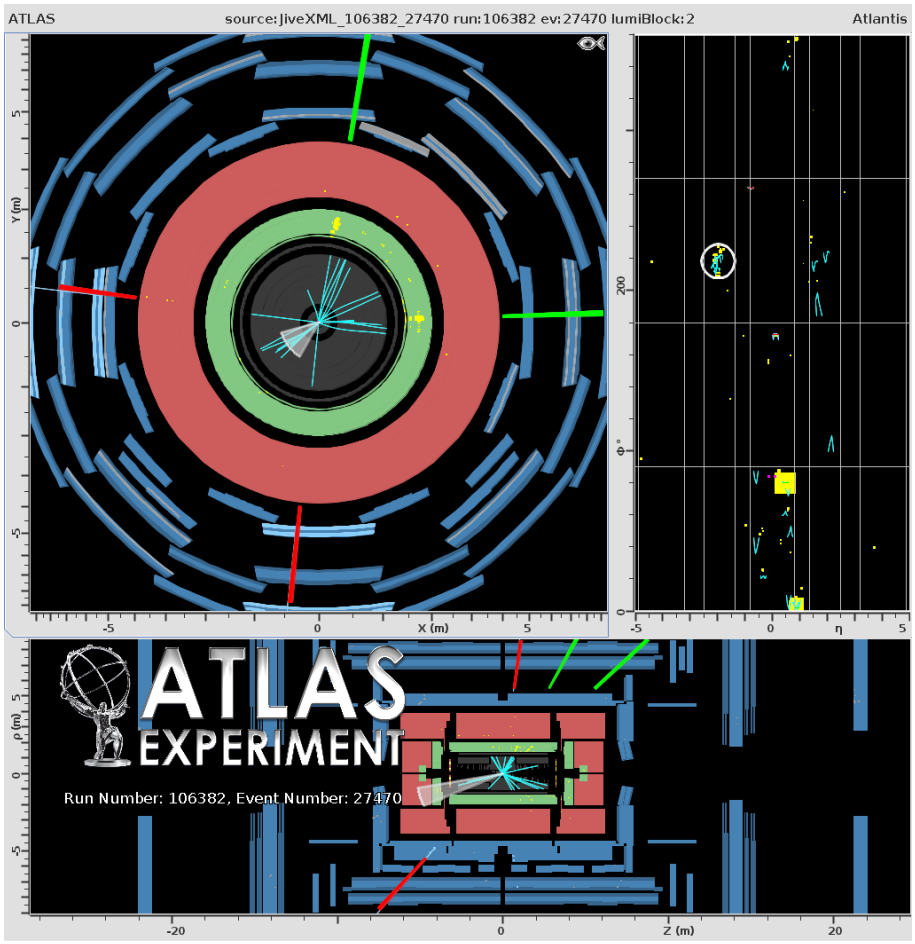

Figure 4.9: A simulated $H \rightarrow ZZ \rightarrow 4l$ event shown in Atlantis with the ATLAS logo display in the Overlay. The ATLAS logo is configurable in both position and size.

logo and run/event information, without having to take up a projection space. A 'GlassPane', from Java's Swing library, was added over the event display with the ability to float an image containing the ATLAS logo, and other information available in the EventInfo projection. The horizontal and vertical position is chosen freely as a fraction of the event display proportions, as well as the size being user configurable. Figure 4.9 shows an event display with a logo displayed in the Overlay. The Overlay was designed such that other information or images may be added and drawn over the event display in the future.

4.4.3 Missing ET Display

Missing transverse energy is a derived quantity based on activity in the detector. The initial state of a parton-parton collision in ATLAS has zero transverse momentum, though its momentum is not well defined in the longitudinal direction. If a neutrino is produced in an event, it will escape ATLAS without detection. Because of this, the sum of transverse momentum of the event will be non-zero. Missing transverse energy is the negative of the vector sum of transverse momentum:

$$E_{\mathrm{T}}^{\mathrm{miss}} = -\sum_{i} \vec{p_{\mathrm{T}}}^{\,i} \tag{4.4}$$

In Atlantis this is represented by a dashed line, with thickness dependent on the amount of missing transverse energy, or as an arrow (as shown in figure 4.10), with length depending on the amount of missing energy. Missing transverse energy is also displayable in several other projections which represent the ϕ direction, including $\eta\phi$, the LegoPlot, and ϕR.

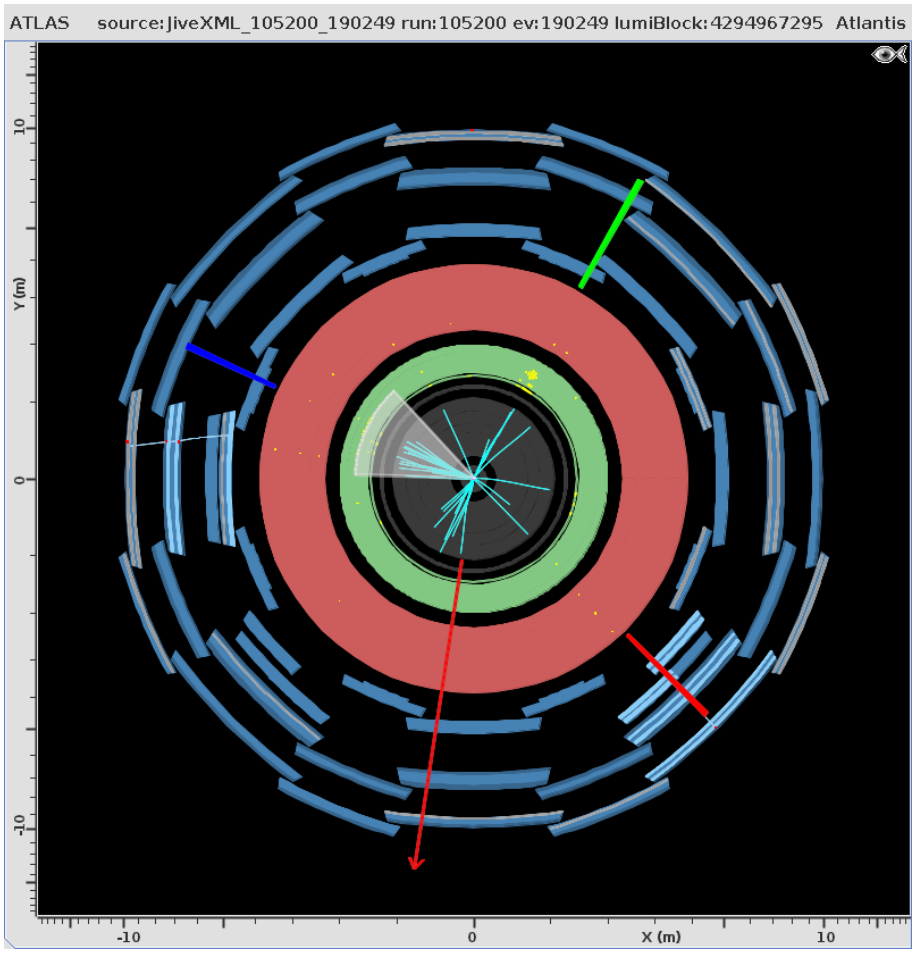

Figure 4.10: Missing transverse energy represented in Atlantis. The arrow pointing to the bottom of the display represents $E_{\mathrm{T}}^{\mathrm{miss}} = 43.8$ GeV. Other features of Atlantis are also shown in this display, including a b-tagged jet, shown as a grey cone leading to a blue box on the outside of the calorimeter. An electron (green) and muon (red) are also shown.

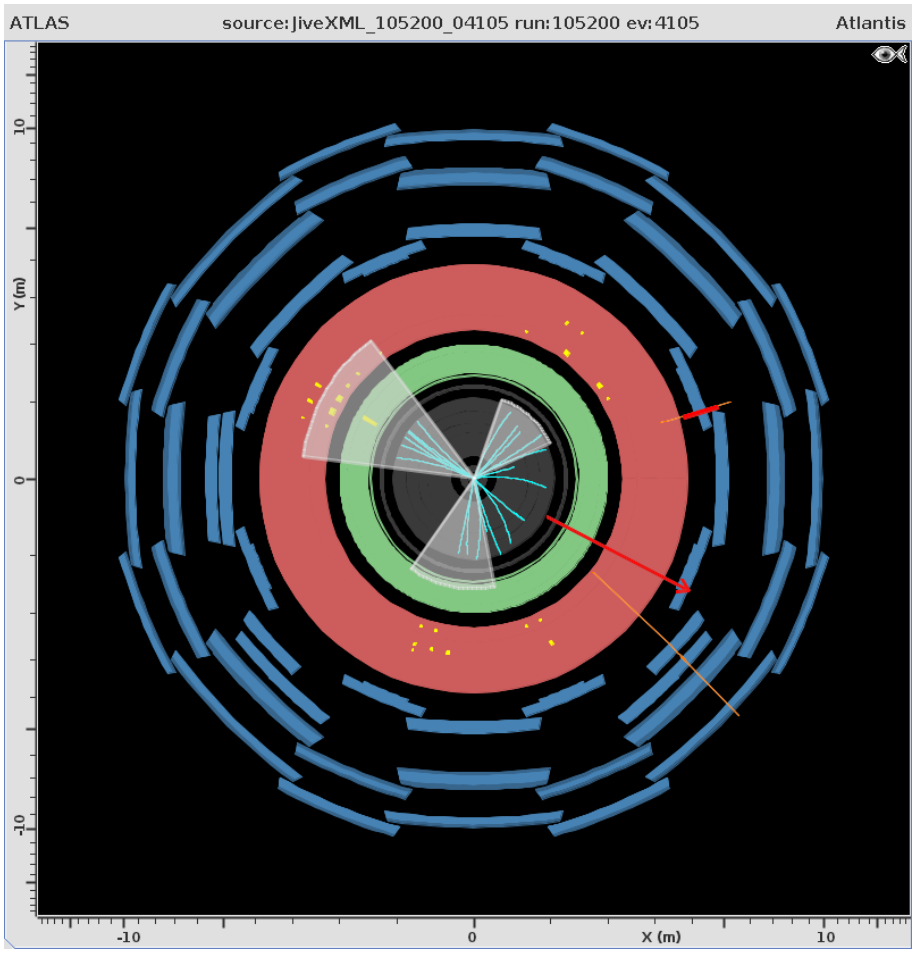

Figure 4.11: A simulated $t\bar{t}$ (dimuon) event in Atlantis with three jets shown as shaded cones. Also shown are two muon tracks (orange lines), with one muon being reconstructed within the barrel region (red box). None of the jets are b-tagged.

4.4.4 Jet Display

Jets displayed in Atlantis have undergone several incarnations, ranging from a small box in the $\eta\phi$ direction of the jet and located on the outside of the detector, to a rough outline of the conical shape of the jet. More recently, the jet drawing method has been modified to allow transparent shaded cones, scaling in length with the jet energy, and in angular extent based on the jet cone size, for example, Anti–k_{T} jets (defined later in section 6.1.3) with a cone size of $\Delta R = 0.4$ are drawn with a smaller arc than those with cone size of $\Delta R = 0.6$. Figure 4.11 shows jets represented as transparent cones in Atlantis.

4.5 MINERVA

Masterclass INvolving Event Recognition Visualised with Atlantis (MINERVA) is an outreach tool, used worldwide by schools and universities to inform students and teachers about the science of the LHC, using Atlantis as a tool to facilitate learning[†]. MINERVA uses a customised configuration of Atlantis, removing much of the unnecessary detail. Figure 4.12 shows two examples of how MINERVA displays ATLAS events.

One basic exercise MINERVA is used for involves simple event categorisation, given a sample of mixed W and Z boson decays, with a small amount of dijet background events included. A further extension to this exercise may be introduced by requesting the student measure the momentum of tracks resulting from the identified Z boson decays, and calculating the invariant mass of the Z using

$$M^2 = (\sum E)^2 - (\sum \boldsymbol{p})^2. \tag{4.5}$$

[†]http://atlas-minerva.web.cern.ch/atlas-minerva/

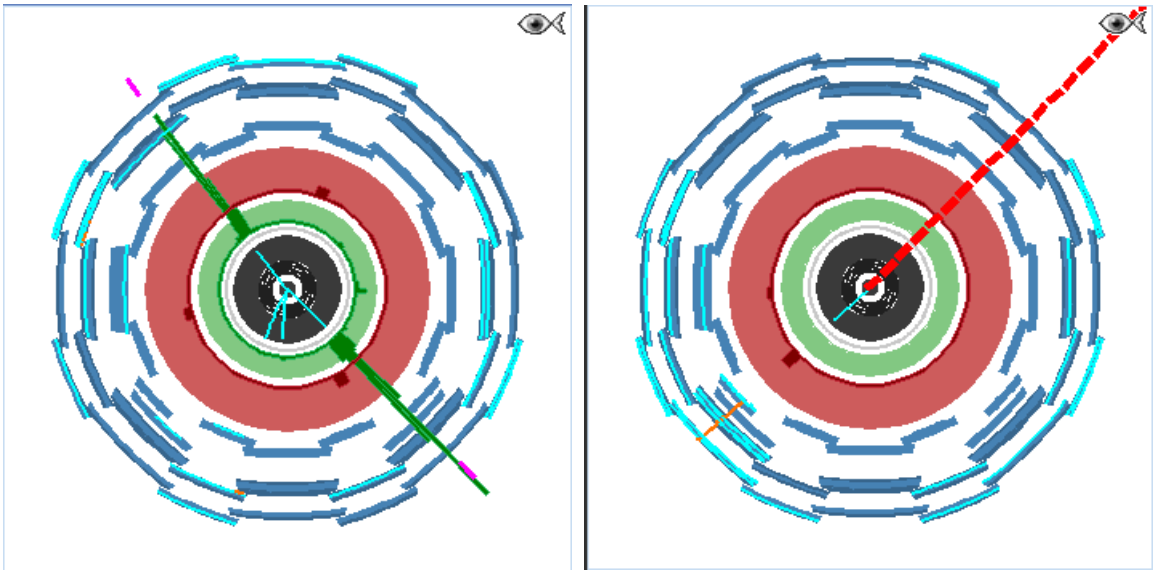

(a) (b)

Figure 4.12: An example of how MINERVA displays events from ATLAS. a) A Z boson decaying to two electrons. b) A W boson decaying to a muon and muon neutrino.

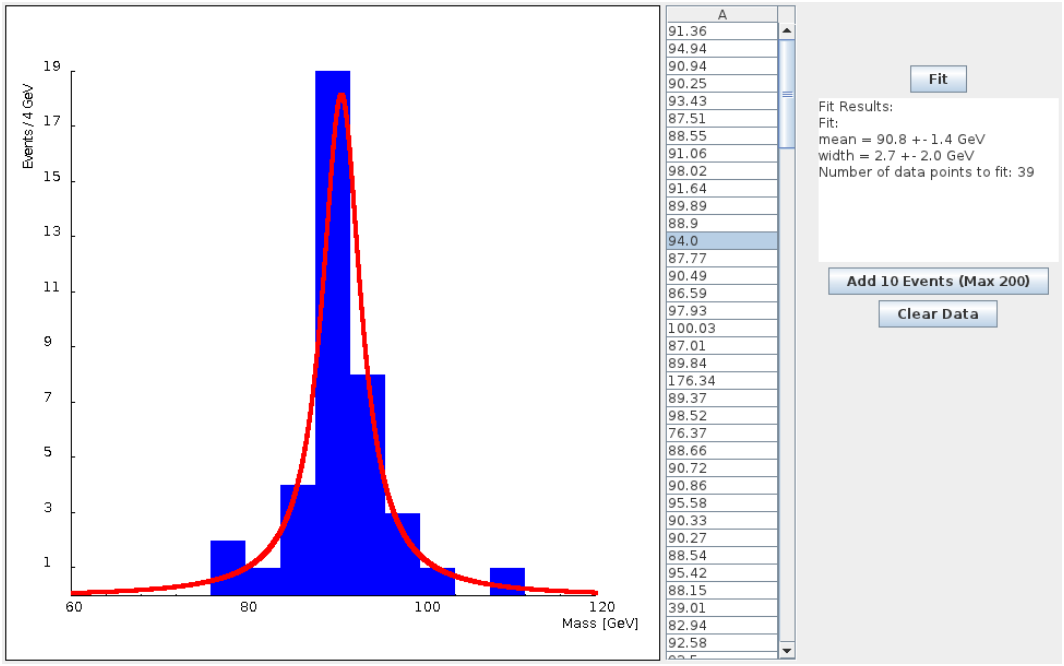

Figure 4.13: An example Z boson mass distribution representative of what may be obtained using the MINERVA outreach tool. The application used to plot the distribution and perform the fit is a custom Java applet written specifically by the author for MINERVA.

With a large enough sample, which may be distributed over several groups of students, enough Z mass measurements may be made to allow a fit to be performed, in order to estimate the average Z mass and width. Figure 4.13 shows a screenshot of an custom Java application, written specifically for the MINERVA tool, used to plot and fit a Z mass distribution. The fit is performed with a Breit-Wigner function to best model the resonance shape of the Z mass distribution.

Also in development for use with MINERVA is an exercise in which students are instructed to identify neutral particle decays, such as K^0 and $\Lambda/\bar{\Lambda}$, as well as γ conversions. Atlantis was modified to calculate an invariant mass for each of the possible neutral decays by recalculating the track parameters with respect to a selected secondary vertex, and making assumptions for the mass of each decay product. The result is three mass calculations, allowing for the neutral decay to be classified, and for the lifetime of the decaying particle to be estimated, based on its distance from the primary vertex.

4.6 Summary

Atlantis is a constantly developing software package used by many people both inside the ATLAS collaboration and outside. It is used to create event displays for public release, as well as to demonstrate typical events within an analysis for a paper or conference talk. The ATLAS control room uses Atlantis to monitor events happening in the detector in almost real time. Schools and universities also use Atlantis, packaged in a customised form as MINERVA, for outreach and teaching activities.

Chapter 5

The Top quark

5.1 Introduction

In 1964, Cronin, Fitch et al. observed CP violation in decays of the neutral K meson [49], ultimately spawning a 30 year quest for the top quark. At the time of the first observation of CP violation, only three quarks had been discovered. The fourth quark, charm, was discovered independently by two groups at Stanford and Brookhaven ten years later, in 1974 [50, 51]. Prior to this discovery, Kobayashi and Maskawa argued the case for the six quark model a year earlier in 1973 [52], which would fit CP violating weak interactions naturally into the quark model.

Given two weak isospin doublets,

$$\begin{pmatrix} u \\ d' \end{pmatrix} \begin{pmatrix} c \\ s' \end{pmatrix}, \tag{5.1}$$

a given up-type quark (u or c) weakly couples to the corresponding down type state

(d' or s'), which corresponds to a superposition of down-type quarks as follows,

$$\begin{pmatrix} d' \\ s' \end{pmatrix} = \begin{pmatrix} V_{ud} & V_{us} \\ V_{cd} & V_{cs} \end{pmatrix} \begin{pmatrix} d \\ s \end{pmatrix}. \tag{5.2}$$

The left hand side of equation 5.2 contains the weak eigenstates, i.e., the states partaking in weak interactions. The right hand side doublet contains the mass eigenstates, which correspond to the particles we observe. The $N \times N$ complex mixing matrix, V_{ij}, must be unitary for N families of quarks. An $N \times N$ matrix then introduces N^2 parameters, of which $2N - 1$ can be absorbed into the $2N$ quark fields via phase transformations. Since the matrix remains invariant under a common transformation on all quarks, one phase remains. This leaves behind, $N^2 - 2N + 1 = (N-1)^2$ parameters, of which $\frac{N(N-1)}{2}$ parameters are rotation angles and $\frac{(N-1)(N-2)}{2}$ parameters are complex phases. For our two generation model, this leaves one parameter, a simple mixing angle and no complex phase. If we introduce a third weak isospin doublet, corresponding to the third generation of quarks,

$$\begin{pmatrix} t \\ b' \end{pmatrix}, \tag{5.3}$$

then the mixing matrix becomes 3×3 and we are forced to introduce an irreducible complex phase. Following the same counting of parameters as above, we are left with three angles and one complex phase. Having a complex phase in the matrix parameters can allow CP violation [53]. The three generation model thus provides an explanation for the CP violation observation, though increasing the number of parameters (and quarks) in the model.

The weak isospin states are then defined as,

$$\begin{pmatrix} d' \\ s' \\ b' \end{pmatrix} = \begin{pmatrix} V_{ud} & V_{us} & V_{ub} \\ V_{cd} & V_{cs} & V_{cb} \\ V_{td} & V_{ts} & V_{tb} \end{pmatrix} \begin{pmatrix} d \\ s \\ b \end{pmatrix}. \tag{5.4}$$

One parameterisation of the matrix, V_{ij}, known as the Cabbibo-Kobayashi-Maskawa (CKM) matrix, is as such,

$$\begin{pmatrix} c_{12}c_{13} & s_{12}c_{13} & s_{13}e^{-i\delta} \\ -s_{12}c_{23} - c_{12}s_{23}s_{13}e^{i\delta} & c_{12}c_{23} - s_{12}s_{23}s_{13}e^{i\delta} & s_{23}c_{13} \\ s_{12}s_{23} - c_{12}c_{23}s_{13}e^{i\delta} & -c_{12}s_{23} - s_{12}c_{23}s_{13}e^{i\delta} & c_{23}c_{13} \end{pmatrix}, \tag{5.5}$$

where, for example, c_{12} and s_{12} represent $\cos\theta_{12}$ and $\sin\theta_{12}$, θ_{12} is a mixing angle and δ is a complex phase. If δ is non zero, the complex phase remains and CP violation is allowed.

In 1975, the τ lepton was discovered [54] which lent credence to the three generation theory of matter, on aesthetic principles; if there are three generations of leptons, then three generations of quarks completes the symmetry. This argument became a successful prediction of the three generation model of quarks when, in 1977 at Fermilab, the Upsilon was discovered; a bound state of $b\bar{b}$ [55]. The three generation theory was then confirmed in 1995 with the discovery of the top quark in experiments at the Tevatron [56, 57]. The current best fit results for the magnitudes of the CKM matrix elements, from Ref. [58], are,

$$\begin{pmatrix} 0.974 & 0.225 & 0.003 \\ 0.225 & 0.973 & 0.041 \\ 0.009 & 0.040 & 0.999 \end{pmatrix}. \tag{5.6}$$

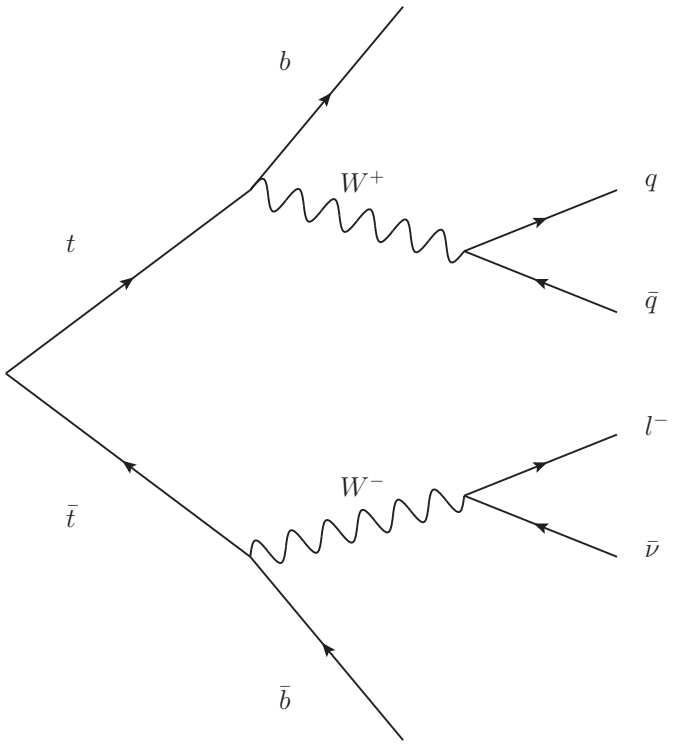

Figure 5.1: A $t\bar{t}$ pair can decay to several final states, which are categorised. For example, a *semileptonic* decay involves one top quark decaying to produce a charged lepton while the other decays to produce hadrons. A dileptonic decay involves both top quarks decaying to produce a charged lepton.

5.2 Phenomenology

The CKM matrix elements are directly related to the probability of a given up-type quark weakly interacting with the corresponding down-type quark. If the Standard Model contains only three generations of quarks, then the 3×3 CKM matrix contains all of the probabilities of weak quark mixing, and assuming there are no exotic decay mechanisms, then the CKM matrix must be unitary. In other words, $|V_{ud}|^2 + |V_{us}|^2 + |V_{ub}|^2 = 1$, for each up type quark, and $V^{-1} = V^\dagger$.

The element $|V_{tb}|^2 \approx 1$ implies that the top quark almost exclusively decays to a bottom quark via emission of a W boson.

Top quarks are predominantly produced in pairs in proton-proton collisions at the

LHC through gluon–gluon fusion, but at lower energies, quark–antiquark annihilation is a large contributor. Each top quark produced then almost always decays to a bottom quark through the weak interaction. The W bosons can then decay leptonically to $e\nu_e, \mu\nu_\mu, \tau\nu_\tau$ or hadronically to $u\bar{d}, c\bar{s}$, allowing $t\bar{t}$ decays to be categorised into dileptonic (two charged leptons in the final state), semileptonic (one charged lepton in the final state) or fully hadronic (zero charged leptons in the final state), depending on the decay products of the W boson. Figure 5.1 shows a Feynman diagram of a semileptonic $t\bar{t}$ decay.

At LO in hadron colliders, pairs of top quarks are produced by quark-antiquark or gluon-gluon fusion. The production mechanisms are dependent on the centre of mass energy of the system. For example, at the LHC with $\sqrt{s} = 7$ TeV, the dominant production mechanism of $t\bar{t}$ pairs is through gluon-gluon fusion. The cross section of $t\bar{t}$ production is given by [59],

$$\sigma_{pp\to t\bar{t}X}(s, m_t^2) = \sum_{i,j=q,\bar{q},g} f_i(\mu_f^2) \otimes f_j(\mu_f^2) \otimes \hat{\sigma}(m_t^2, \mu_f^2, \mu_r^2), \tag{5.7}$$

where s is the centre of mass energy squared, m_t is the top quark mass, $f_{i,j}(\mu_f^2)$ are the proton PDFs*, $\hat{\sigma}(s, m_t^2)$ is the partonic cross section. μ_f^2 is the factorisation scale, which is used as a cutoff between the perturbative and non-perturbative parts of the calculation, and μ_r^2 is the renormalisation scale, which allows for divergences in NLO calculations to be absorbed.

5.2.1 Importance of the Top Quark

The LHC is a top factory. The cross-section for $t\bar{t}$ production at $\sqrt{s} = 7$ TeV is around 170 pb. At $\sqrt{s} = 7$ TeV — with a peak luminosity in 2011 of 7.73×10^{33} cm^{-2} s^{-1}

*The proton PDF describes the fraction of the incoming protons momentum carried by each of the constituent quarks and gluons.

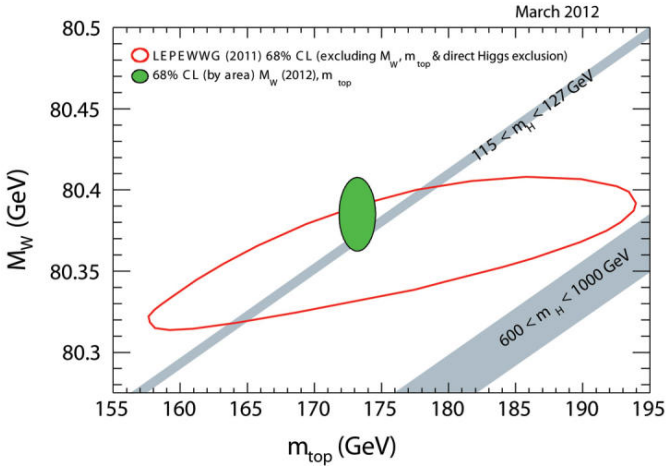

Figure 5.2: The mass of the top quark vs the mass of the W boson. The diagonal bands show the allowed range of Higgs masses for a given set of top and W boson masses. The green oval shows the current world best measurements of the top mass (horizontally) and W boson mass (vertically), constraining the Higgs mass to be less than 152 GeV, to 68% confidence [61].

and a total integrated luminosity of around 4.7fb^{-1} — the number of $t\bar{t}$ pairs produced in ATLAS in 2011 is close to 800,000. As the top quark decays to a W boson and a b quark, the branching ratio of the W defines the possible final states of the decay. For $t\bar{t}$ pairs, roughly $1/9^{th}$ of the time, the final state will contain two charged leptons and two neutrinos, around $4/9^{th}$ of the time, the final state will contain a charged lepton, a neutrino and two extra quarks, while the rest of the time the final state is made up of four extra quarks.

The top quark, though already discovered and studied thoroughly at the Tevatron, is of great importance to LHC physics. Its place in the Standard Model as the most massive fermion means it has a strong coupling to the Higgs boson [60]. NLO calculations of the W boson mass contain corrections proportional to the Higgs and top masses, meaning that accurate measurements at the LHC of the W boson and top mass can impose constraints on the Higgs mass (see Figure 5.2). As of February 2013, the measured Higgs mass from ATLAS and CMS is around 125 GeV [12, 13], which is consistent with theoretical predictions, given the current world best W and top mass measurements [61].

5.3 $t\bar{t}$ Spin Correlation

The study of $t\bar{t}$ pairs allows a further test of the Standard Model by studying the spins of the quarks. The large width of the top quark leads to it having a very short lifetime; at least an order of magnitude smaller than the timescale of the strong interaction [62], meaning the top quark decays before its spin can be depolarised. The spin and polarisation of the top quark then directly affects the angular distributions of the decay products.

For spin $\frac{1}{2}$ fermions produced in pairs at a hadron collider, the production mechanisms at LO[†] can be categorised into:

- $q\bar{q}$
- Unlike helicity gg
- Like helicity gg

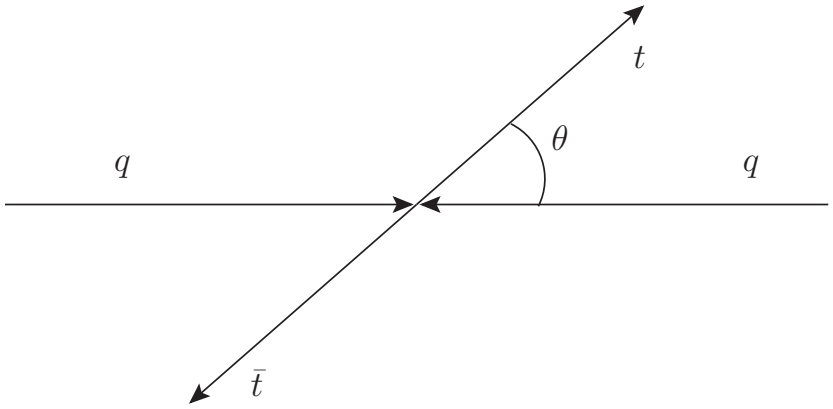

Figure 5.3: $q\bar{q} \rightarrow t\bar{t}$ in the rest frame of the $t\bar{t}$ system. The angle θ is defined as the opening angle between one of the outgoing top quarks and the incoming quark.

Ref. [63] presents an overview of the spin structure of these production mechanisms in terms of the scattering angle, θ, of the top quarks from the incoming beam, and

[†]At Next to Leading Order, a small amount of the production occurs through qg

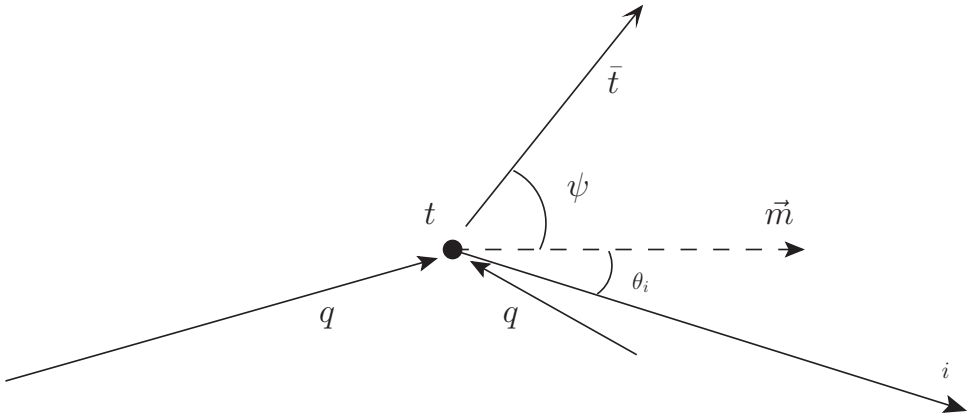

Figure 5.4: The top quark spin vector, $\vec{m}$ in the top quark's rest frame, with angle ψ from the anti-top.

	b-quark	W^+	l^+	$\bar{d}$-quark or $\bar{s}$-quark	u-quark or c-quark
α_i (LO)	-0.41	0.41	1	1	-0.31
α_i (NLO)	-0.39	0.39	0.998	0.93	-0.31

Table 5.1: Spin analysing power for the top quark decay products calculated at LO and NLO. In the case of the anti-top, a negative coefficient is introduced for each value. For example, the charged lepton and the b-quark from the anti-top decay would have $\alpha = -1$ and $\alpha = 0.41$ at LO respectively.

ψ, the direction of the top quark spin vector, measured from the anti-top direction in the top quark rest frame. These angles are illustrated in figures 5.4 and 5.3. Careful selection of the angle ψ can allow enhancements of the correlation between the spins of the $t\bar{t}$ pair, described in more detail in section 5.3.1.

The angular distribution of the top quarks decay products is described in terms of the direction of the spin vector [64] by

$$\frac{1}{N}\frac{dN}{d\cos\theta_i} = \frac{1}{2}[1 + \alpha_i \cos\theta_i], \tag{5.8}$$

where θ_i is the angle between decay product i, and the spin vector in the top quark rest frame. α_i is a coefficient determining the influence of the parent quarks spin on the angular distribution of the decay product, and is given in table 5.1.

Given that the angular distributions of the top decay products are influenced by the spin of the top, the spin correlation of the $t\bar{t}$ system can be probed by angular correlations between the decay products of both tops [63],

$$\frac{1}{N}\frac{d^2N}{d\cos\theta_i d\cos\theta_j} = \frac{1}{4}[1 + \kappa\alpha_i\alpha_j\cos\theta_i\cos\theta_j] \tag{5.9}$$

with

$$\frac{\kappa}{4} = A = \frac{N_{\uparrow\uparrow} + N_{\downarrow\downarrow} - N_{\uparrow\downarrow} - N_{\downarrow\uparrow}}{N_{\uparrow\uparrow} + N_{\downarrow\downarrow} + N_{\uparrow\downarrow} + N_{\downarrow\uparrow}} \tag{5.10}$$

The polarisation of the top can also influence this distribution, but since the electroweak contribution to the $t\bar{t}$ production is very small relative to the QCD production mechanisms, the polarisation is considered negligible [65].

In order to extract A, the spin vector, $\vec{m}(\vec{n})$, from which to measure the angle $\theta_{i(j)}$ must be defined.

5.3.1 Spin Quantisation Bases

The spin information of the top quark can be accessed directly by measuring the angular distributions of its decay products with respect to a spin vector, or quantisation basis. While all of the decay products are influenced by the spin of the parent top quark, the charged leptons and down type quarks are influenced more strongly than, for example, the up type quarks. To define a basis, two vectors are constructed; vector $\vec{m}$ is used to measure the angle of the top quark decay products, and vector $\vec{n}$ to measure the angle of the anti-top quark decay products. The choice of basis affects the amount of observed spin correlation and, for some processes, it is possible to define a basis such that the spins are fully correlated (or anti-correlated). However, for a hadron collider experiment, no single process dominates the $t\bar{t}$ production, due to the quark and gluon content of the interacting hadrons. This makes

it impossible to define a basis where the spin correlation can be observed to 100% level, though knowledge of the dominant production mechanisms allows for the basis choice to be optimised.

Beamline Basis

The simplest basis to define is the beamline basis, with the vector defined along the direction of flight of one of the incoming hadrons

$$\vec{m} = \vec{n} = \vec{p} \tag{5.11}$$

where $\vec{p}$ is the direction of one of the incoming partons in the lab frame. To simplify the construction of the beamline basis, $\vec{p}$ is chosen as the incoming beam direction, which is a close approximation to the direction of flight of the incoming parton. $t\bar{t}$ pairs at the LHC are produced predominantly by the process $gg \to t\bar{t}$ far above the $t\bar{t}$ production threshold and as such, the beamline basis, which tends to be preferable for low $\beta(= v/c)$ top quark pairs, is unsuitable. Conversely, at the Tevatron, where $t\bar{t}$ pairs are mostly produced by $q\bar{q} \to t\bar{t}$ and close to threshold, the beamline basis is one of the best possible choices of spin quantisation basis.

Helicity Basis

The helicity basis is defined as

$$\vec{m} = -\vec{k_{\bar{t}}} = -\vec{n} \tag{5.12}$$

where $\vec{k_{\bar{t}}}$ is the recoil direction of the anti-top quark in the top quark rest frame (see figure 5.5. This basis performs well for high β top quark pairs, making it a good choice at the LHC.

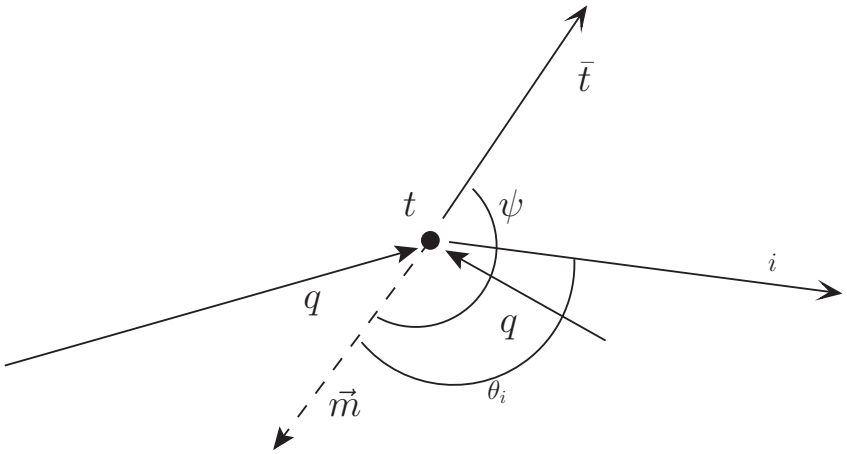

Figure 5.5: The top quark spin vector, $\vec{m}$ in the top quark's rest frame, with angle ψ from the anti-top.

As $\beta \to 1$ the helicity basis allows a 100% description of Standard Model spin correlation for top quark pairs produced by quark-antiquark annihilation and unlike helicity gluon fusion. In the case of like helicity gluon fusion, the helicity basis describes the spin correlation for all β [63]. At the LHC with $\sqrt{s} = 7$ TeV, where $t\bar{t}$ pairs are produced by a mixture of these processes, the helicity basis allows observation of spin correlation around the 31% level [17].

Off Diagonal Basis

The off diagonal basis is chosen to optimise the strength of the spin correlation in the $q\bar{q} \to t\bar{t}$ process. Ref. [64] showed that, in $e^+e^- \to t\bar{t}$ production, a spin basis can be chosen such that the amplitude for like spin $t\bar{t}$ production vanishes, leaving 100% unlike spin correlation ($A = -1$). This can be extended for use in $q\bar{q} \to t\bar{t}$ processes [66].

To construct the off diagonal basis, consider a vector in the top rest frame, with angle ψ from the anti-top (Figure 5.4).

The off diagonal basis is defined by

$$\tan\psi = \frac{\beta^2 \sin\theta\cos\theta}{1-\beta^2\sin^2\theta} \tag{5.13}$$

where θ is the opening angle between the top quark and the incoming quarks (Figure 5.3).

The vector defined by ψ (as illustrated in figure 5.4), can alternatively be written,

$$\vec{m} = \frac{-\vec{p} + (1-\gamma)(\vec{p}\cdot\vec{k})\vec{k}}{\sqrt{1-(\vec{p}\cdot\vec{k})^2(1-\gamma^2)}} \tag{5.14}$$

where $\vec{k}$ is the direction of flight of the top quark in the rest frame of the $t\bar{t}$ system and $\vec{p}$ is the direction of flight of one of the incoming hadrons.

For $q\bar{q}$ production, at low β, $\gamma \to 1$, $\vec{m} = -\vec{p}$ and the off diagonal basis becomes the beamline basis. As $\beta \to 1$, the off diagonal basis becomes the helicity basis, and describes $q\bar{q} \to t\bar{t}$ events high above threshold [63]. At the Tevatron, $t\bar{t}$ production is dominated by the $q\bar{q}$ process, meaning the off diagonal basis is the optimal choice for studying the spin correlation. A high proportion of $t\bar{t}$ pairs are produced by gluon-gluon fusion at the LHC, so these simplifications at high and low β do not hold and the off diagonal basis becomes a suboptimal choice [67].

LHC Optimal (Maximal) Basis

In choosing a basis to maximise the observed spin correlation in gluon-gluon fusion, the basis choice can reduce either the $\uparrow\uparrow + \downarrow\downarrow$ contribution or the $\uparrow\downarrow + \downarrow\uparrow$ contribution to zero, for either unlike helicity, or like helicity gluon fusion, respectively [63]. Due to the mixture of like and unlike helicity gluon fusion in $t\bar{t}$ production at the LHC, there exists no basis to describe exactly the spin correlation. The choice of basis can, however, be optimised. In Ref. [63], it is shown that there exist maxima

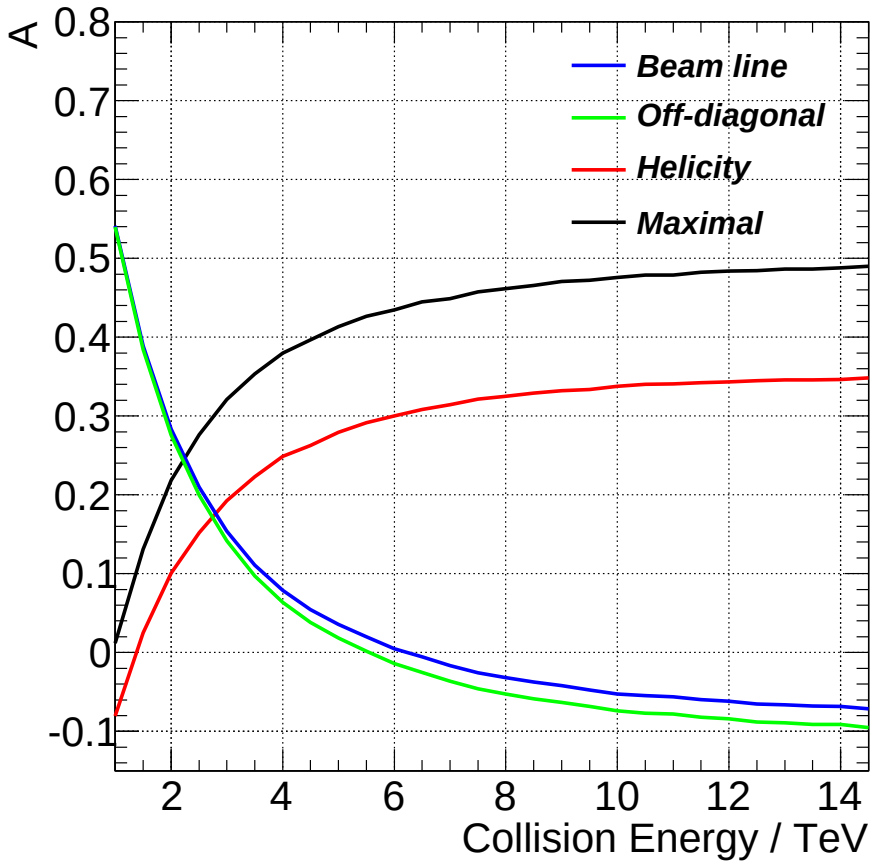

Figure 5.6: The strength of $t\bar{t}$ spin correlation for four bases as a function of collision energy, calculated with MC@NLO.

for both the like and unlike helicity gluon contributions, when

$$\tan 2\psi = \frac{2\gamma^{-1}\sin^3\theta\cos\theta}{\sin^2\theta\cos^2\theta - \gamma^{-2}\sin^4\theta - \gamma^{-2}}. \tag{5.15}$$

This then yields a result for ψ_{like} and ψ_{unlike} which optimise the basis choice for either like or unlike helicity gluon–gluon fusion. Ref. [63] again shows that when $\beta\gamma\sin\theta < 1$, ψ_{like} should be chosen, and when $\beta\gamma\sin\theta > 1$, ψ_{unlike} should be chosen.

Current status

Figure 5.6 illustrates the energy dependence of these four bases. Clearly the basis choice is dependent on the energy of the collider experiment, suggesting the beam line or off-diagonal bases as optimal for the Tevatron, and helicity or optimal bases for the LHC.

The Collider Detector at Fermilab (CDF) experiment performed a study of spin correlation in $t\bar{t}$ pairs decaying to a single lepton at $\sqrt{s} = 1.96$ TeV using both the beamline basis and the helicity basis [68] and measured a helicity basis spin correlation parameter $A = 0.48 \pm 0.48(\text{stat}) \pm 0.22(\text{syst})$, consistent with the Standard Model prediction of $A = 0.35$ at the Tevatron. The DØ collaboration also performed a study of spin correlation, this time with dileptonically decaying $t\bar{t}$ pairs, using the beamline basis [69], finding no significant deviation from the Standard Model hypothesis.

At $\sqrt{s} = 7$ TeV, the ATLAS experiment published a study of spin correlation with 2.1fb^{-1} of data, where the zero spin correlation model was excluded to 5.1σ [70]; the first observation of non zero spin correlation. In addition the CMS experiment performed a study of spin correlation with 5.0fb^{-1} of data, finding results consistent with the Standard Model prediction [71].

The Standard Model expectation for the spin correlation parameter in the helicity basis, at $\sqrt{s} = 7$ TeV is $A = 0.31$ [17].

5.3.2 Observables

Clearly, in the dilepton channel, the choice of analysers with which to access the spin correlation is simple; both charged leptons carry close to 100% of the information from the parent top quarks (as shown in table 5.1). For the semi-leptonic channel,

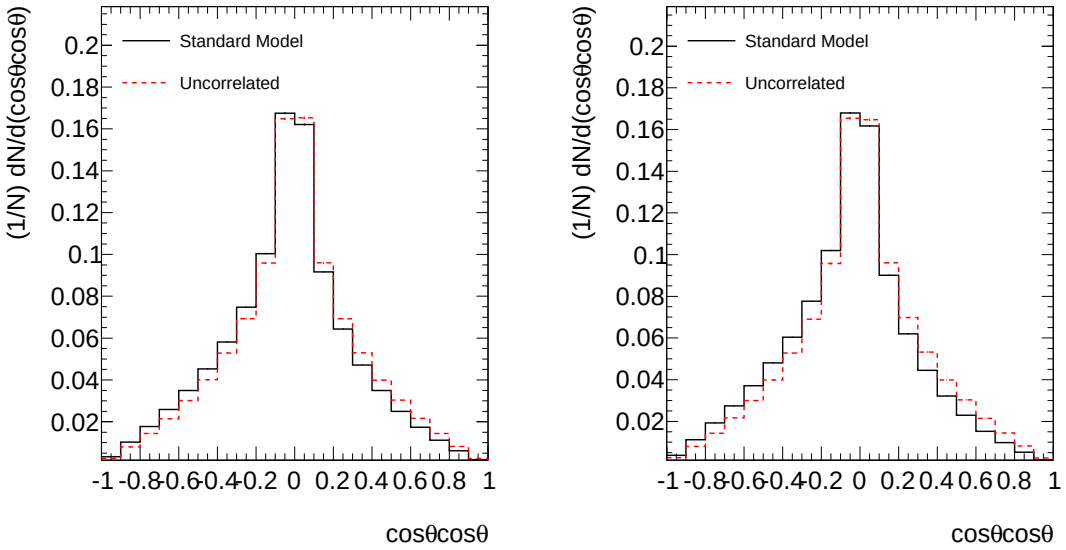

Figure 5.7: The $\cos\theta_i \cos\theta_j$ distribution for (left) the helicity basis and (right) the LHC optimised basis for $t\bar{t}$ events decaying dileptonically. The distributions shown are at parton level, generated with MC@NLO at $\sqrt{s} = 7$ TeV, without cuts and constructed using the two charged leptons as spin analysers.

the charged lepton and the down-type quark are the most effective analysers. Experimentally it is impossible to distinguish a jet originating from an up-type quark from that of a down-type quark, though an interesting property of the weak decay can provide a handle to enhance the selection of down-type quarks. This procedure is discussed further in section 6.6.

From equation 5.9, it is clear that the distribution $\cos\theta_i \cos\theta_j$ contains information on the spin correlation of the $t\bar{t}$ system, where decay products i and j are the chosen spin analysers. In order to extract $A\alpha_i\alpha_j$ from equation 5.9, the unbiased estimator $A\alpha_i\alpha_j = 9\langle\cos\theta_i \cos\theta_j\rangle$, as described in Ref. [72], can be used to extract directly a value for A. In the dilepton channel, using both charged leptons as the spin analysers, this simplifies to $A = -9\langle\cos\theta_i \cos\theta_j\rangle$, where $\alpha_{l^+} = 1$ and $\alpha_{l^-} = -1$. This corresponds to simply taking the mean of the distribution in figure 5.7 and multiplying by -9. In figure 5.7, the Standard Model plot has a mean of -0.0334, which corresponds to $A_{helicity} = 0.301$.

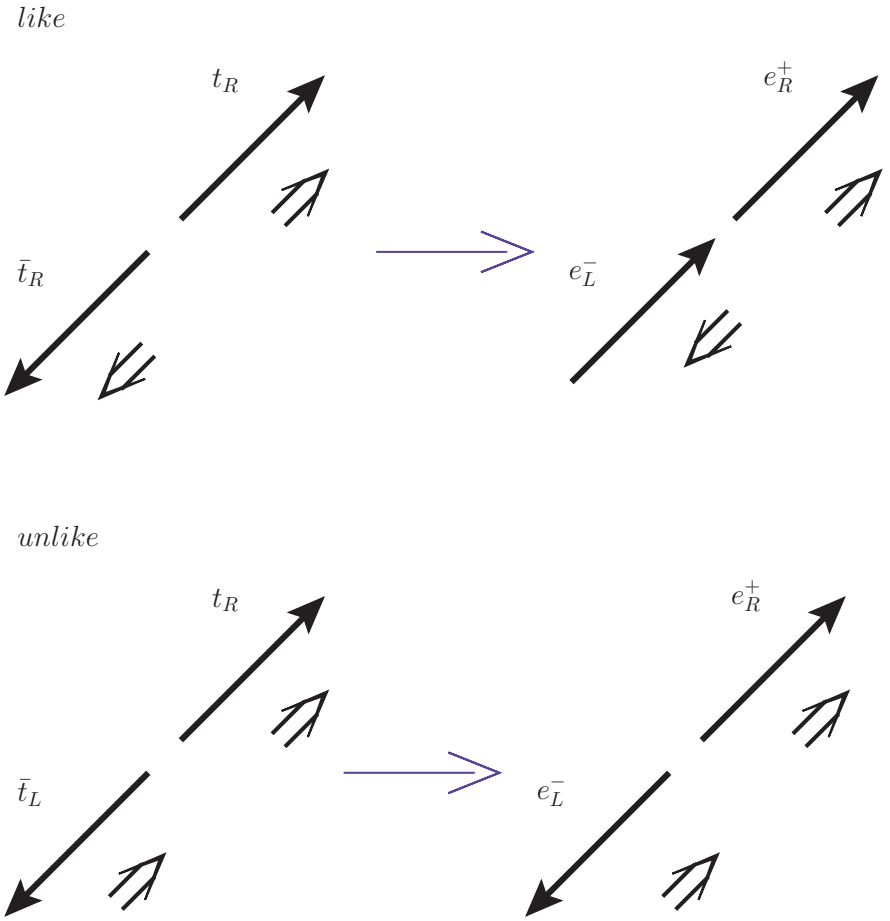

Figure 5.8: Like spin tops will tend to produce leptons with their momentum parallel, whereas unlike spin tops tend to produce back to back leptons. The down-type quark in a weak decay can be viewed as analogous to the charged leptons.

However, in order to perform a spin correlation study directly, utilising the aforementioned bases, it is necessary to fully reconstruct the event. At the LHC, the high pileup in events can complicate this procedure. Instead arguments can be made in favour of observables requiring minimal reconstruction in order to indirectly observe the spin correlation.

To illustrate this, figure 5.8 shows the two possibilities for $t\bar{t}$ spin configuration; like and unlike. In the limit where $\beta \to 1$ for the daughter particles with respect to the $t\bar{t}$ frame, helicity describes the spin direction. For like spin tops, the preferred analysers will tend to decay with their momenta in the same direction. In figure

5.8 electrons are considered to illustrate this. For unlike spin $t\bar{t}$ pairs, the electrons tend to be produced back to back. Since the $t\bar{t}$ system only experiences a significant boost in the z direction, the ϕ of the decay products is largely unchanged. This suggests that the difference between the ϕ of the decay products,$\Delta\phi$, is sensitive to the presence of spin correlation in the $t\bar{t}$ system. This argument is also presented more rigorously in Ref. [63].

For $A = 0$, the electron momenta are produced equally parallel and anti-parallel. If $A > 0$, figure 5.8 suggests an enhancement as $\Delta\phi \to 0$, due to more production of like spin $t\bar{t}$ pairs, than unlike spin. For $A < 0$, the converse is true; more unlike spin $t\bar{t}$ pairs are produced, suggesting an enhancement as $\Delta\phi \to \pi$.

Figure 5.9 shows the parton level distribution for $\Delta\phi$ in the lab frame for dilepton events, showing the enhancement of the Standard Model case where $A > 0$.
The quantity $\Delta\phi$ presents an opportunity to measure the extent of the spin correlation in the $t\bar{t}$ system without requiring a boosted frame. This immediately removes the requirement that the $t\bar{t}$ system be fully reconstructed, which is of significant benefit in the dilepton decay mode, where the presence of two neutrinos in the final state makes reconstruction a difficult process. The single lepton decay mode still presents the problem that one of the desired analysing particles is the down-type quark originating from the W boson decay.
In the following chapters, an analysis of 4.7 fb^{-1} of data taken by the ATLAS experiment, with a centre of mass energy of 7 TeV, recorded in 2011 is presented, using the lab frame variable $\Delta\phi$. Since $\Delta\phi$ is constructed in the lab frame, none of the above bases is used. Therefore, instead of using A as the spin correlation parameter in the extraction of the spin correlation, the value f_{SM} is used, where in the Standard Model case, $f_{\mathrm{SM}} = 1$ and for the zero spin correlation case, $f_{\mathrm{SM}} = 0$. This can be converted back to the spin correlation parameter A by multiplying by the relevant Standard Model value. For example, a measurement of $f_{\mathrm{SM}} = 1$ would correspond to a value of $A_{\mathrm{helicity}} = 0.31$.

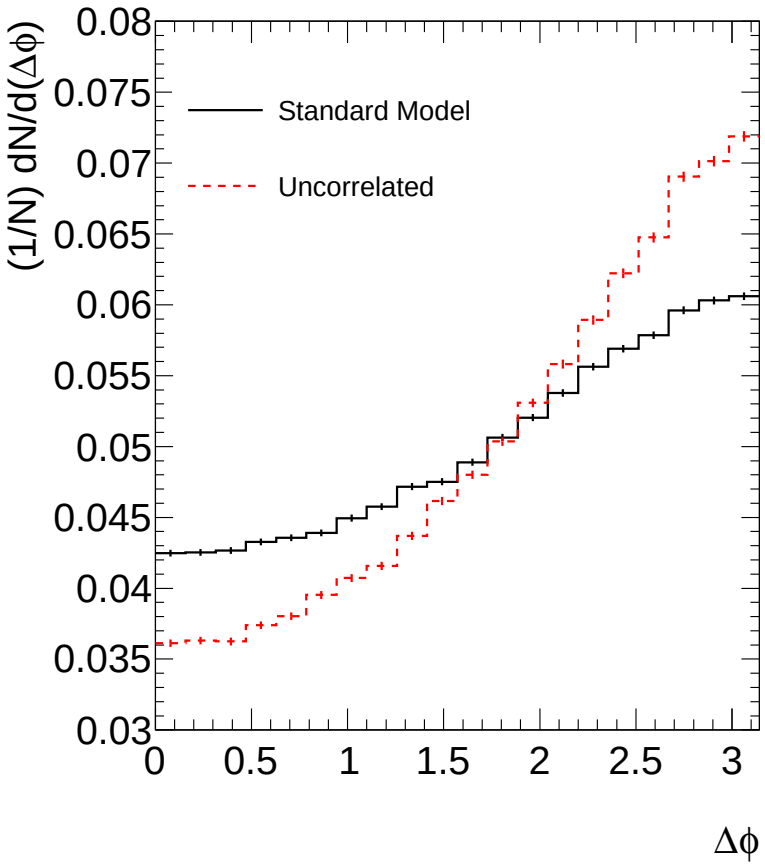

Figure 5.9: The $\Delta\phi$ distribution in the lab frame for $t\bar{t}$ events decaying dileptonically. The distributions shown are at parton level, generated with MC@NLO at $\sqrt{s} = 7$ TeV, without cuts and constructed using the two charged leptons as spin analysers.

In the Standard Model, it would be expected that the measured value of f_{SM} would be 1, though there may be cases beyond the Standard Model which can alter this value. If a charged Higgs boson were to replace the W boson in the decay of the top, the weak coupling to left (right) handed (anti-)fermions only is lost, meaning the momenta of the preferred decay products no longer tends to parallel for like spin $t\bar{t}$ pairs (as shown in figure 5.8). This may tend to reduce the observed amount of spin correlation below the Standard Model expectation, and would be visible in the analysis presented in the following chapters.

Chapter 6

Selecting and reconstructing $t\bar{t}$ events

6.1 Object Definition

This section defines the reconstructed objects used for event selection and analysis. Raw hits data from ATLAS are read out from the detector and processed to form clusters of calorimeter energy deposits and to reconstruct tracks from tracking hits. These are then further reconstructed to create electron, jet or muon objects.

6.1.1 Electrons

An electron, being a charged particle, will ionise the material in the tracking volume, before depositing its energy in the electromagnetic calorimeter. This gives a distinct signature for the electron of a charged track with activity in the EM calorimeter.

For this analysis, an electron is defined as a reconstructed object with a single track, where the track has at least one pixel hit, seven silicon hits and a difference in pseudorapidity, $\Delta\eta$, from the calorimeter cluster of less than 0.015 in the case of 'Loose' electrons, and 0.005 for 'Medium' and 'Tight' electrons. In addition, cuts

on the shower shape in the calorimeter are imposed, with increasingly strict cuts moving from Loose to Medium to Tight electrons. Medium and Tight electrons also have stricter requirements on inner detector activity. Loose, Medium and Tight electrons are required to have at least one pixel hit, and at least seven SCT hits. The Medium classification additionally requires at least one b-layer hit within $|\eta| < 2.01$, while Tight requires a b-layer hit over all η, and adds cuts to reduce electrons from photon conversions. Medium cuts offer an efficiency of 85% for electrons from Z-boson decays, where Tight cuts give a lower efficiency of 78%, but with less 'fake' electron contamination.

The reconstructed electron is required to be isolated; calorimeter activity in a cone of $\Delta R < 0.2$* must not exceed a specified amount (dependent on the energy of the incident electron), where the electron shower itself is excluded by subtracting the calorimeter activity in a cone of $\Delta R < 0.05$. The allowed calorimeter activity is calibrated to achieve a 90% working efficiency for accepting electrons, against 'fake' electrons from misreconstructed jets. In addition, the sum of p_{T} of tracks within a cone of $\Delta R < 0.3$ must not exceed a threshold, again dependent on the p_{T} of the incident electron.

Since an electron deposits energy in the calorimeter, jet finding algorithms (described in section 6.1.3) will reconstruct this calorimeter activity as a jet. Clearly this 'jet' is a duplicate object, and should not be treated as a jet in the analysis. In order to remove it from the object pool, an overlap removal algorithm is applied, in which any reconstructed jet within $\Delta R < 0.2$ of an electron is removed. The jets considered in the overlap removal must satisfy the requirements outlined in section 6.1.3. In addition, any electrons within $\Delta R < 0.4$ of any remaining, selected jet are removed.

Finally, electrons are required to have transverse energy† (E_{T}) greater than 25 GeV and $|\eta| < 2.47$ with electrons falling into the calorimeter crack region ($1.37 < |\eta| <$

*$\Delta R = \sqrt{\Delta\phi^2 + \Delta\eta^2}$

†Transverse energy is defined as $E_{\mathrm{cluster}}/\cosh\eta_{\mathrm{track}}$

1.52) removed.

6.1.2 Muons

Muons are defined as reconstructed objects with a track both in the inner detector and muon spectrometer. A looser definition of a muon requires only a track in the muon spectrometer, extrapolated back to the vertex. Each muon is required to fall within $|\eta| < 2.5$, in order to ensure a single muon will have both an inner detector track and a muon spectrometer track, with transverse momentum greater than 20 GeV, and the additional requirement of having at least two pixel hits and six SCT hits, with quality requirements on the TRT hits.

Similarly to the isolation requirements for the electron, muons are required to have calorimeter activity within a cone of $\Delta R < 0.2$ less than 4 GeV and the summed momentum in the tracker within a cone of $\Delta R < 0.3$ to be less than 2.5 GeV.

Since a jet may contain heavy flavour quarks, which can decay to produce muons, an isolation requirement on muons from jets is also imposed. Any muon within $\Delta R < 0.4$ of a jet (as described in section 6.1.3) is removed.

Finally, pairs of muons considered consistent with a cosmic ray event - muon pairs back to back ($\Delta\phi > 3.1$) with a large displacement from the primary vertex - are removed.

6.1.3 Jets

A single quark or gluon produced in an interaction, such as in figure 6.1, is required to be *confined*; that is, a particle possessing colour charge is required to form a bound state which is colour neutral. In order for this to be satisfied, pairs of quarks and gluons are produced, which may then form a bound state with the initial quark,

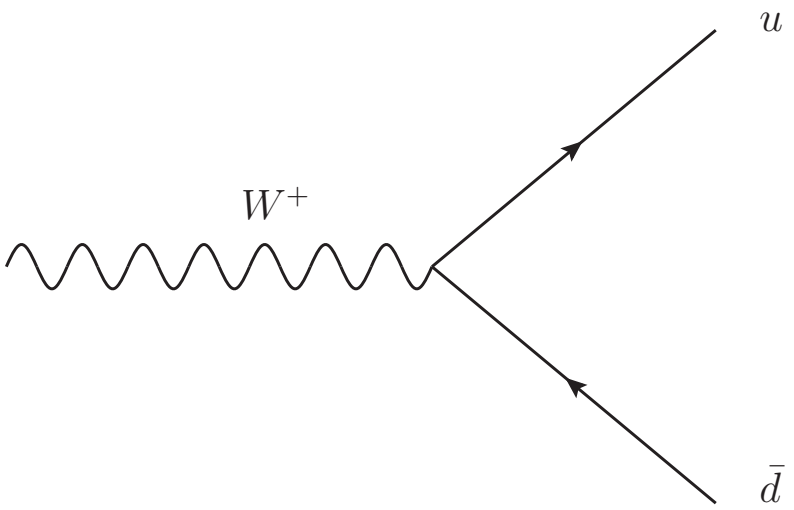

Figure 6.1: A W boson decays to an up quark and down anti-quark. The u and $\bar{d}$ quarks are observed only as jets, streams of particles created by the strong force, produced in the momentum direction of the initial quark.

while others may remain unconfined. More pairs of particles are then produced and the process repeats until the net colour charge is neutral. The result of this process is a *jet* of hadrons produced in the direction of the initial quark.

A jet is an object which attempts to reconstruct the original direction and momentum of the initial parton, which is the object of interest for studying the hard scatter process. To do this, a jet reconstruction algorithm is needed; in this analysis the Anti–k$_t$ algorithm [73] is used.

In the Anti–k$_t$ algorithm, particles are clustered based on two distance measures,

$$d_{ij} = \min(k_{ti}^{2p}, k_{tj}^{2p}) \frac{\Delta R_{ij}^2}{R_{cone}^2}, \tag{6.1}$$

$$d_{iB} = k_{ti}^{2p}, \tag{6.2}$$

where k_{ti} is the transverse momentum of particle i, and R_{cone} is the desired cone radius of the jet. The parameter p is defined as -1 in the Anti–k$_t$ algorithm. If d_{ij} is the smallest distance, then i and j are clustered together, and if d_{iB} is the smallest

distance, i is said to be a jet, and removed from further iterations. This procedure is repeated over all pairs of particles until no particles or clusters remain. The Anti–k_t algorithm is both infrared and collinear safe; for a given system, additional soft radiation from gluons or the splitting of one particle into two collinear particles, does not affect the resulting jets created.

Each jet must satisfy further quality conditions to be considered in the analysis. Only jets with $p_{\mathrm{T}} > 25$ GeV are considered for the final analysis. For each electron in the event, the closest jet, within $\Delta R < 0.2$ is removed. If a jet with $p_{\mathrm{T}} > 20$ GeV, associated with background calorimeter noise, is found the event is removed.

Jet Vertex Fraction

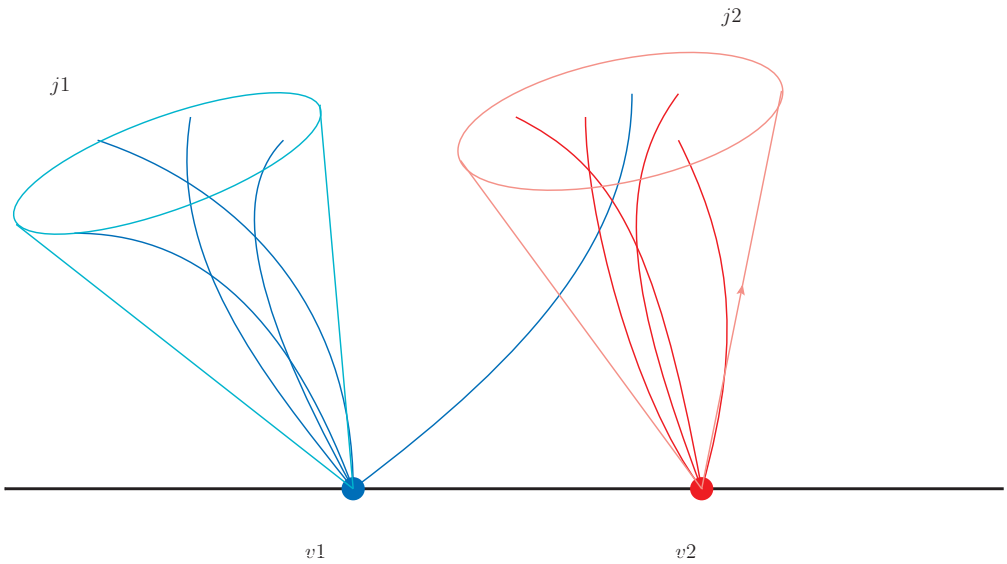

Figure 6.2: A visual representation of the JVF method. Jet $j1$ is composed entirely of tracks originating from the vertex $v1$, while $j2$ is contaminated by a track from vertex $v1$, making its JVF with respect to $v2$ less than 1.

Due to the large amount of extra interactions present in an event from pileup, an extra cut is applied to discriminate jets from the hard scatter and from pileup. This discrimination is achieved using the JVF, a quantity representing the probability that a jet originated from a given vertex [74].

The value of JVF for a given vertex, k, is given by,

$$JVF(jet_i, vtx_k) = \frac{\sum_{l}^{trk} p_{\mathrm{T}}(trk_l, vtx_k)}{\sum_{m}^{vtx} \sum_{n}^{trk} p_{\mathrm{T}}(trk_n, vtx_m)} \tag{6.3}$$

where the numerator is the sum of p_{T} of all of the tracks in the jet which are associated with vertex k, and the denominator is the sum of p_{T} of all of the tracks in the jet associated with any vertex.

Figure 6.2 provides a visual description of the method. Jets in this analysis are only considered if the JVF with respect to the primary vertex is greater than 0.75.

B-Tagged Jets

Each jet is run through b-tagging algorithms to determine if the jet originates from a b-quark. A jet containing a b-hadron would typically have a displaced vertex due to the relatively long lifetime of b-hadrons ($\sim 10^{-13}$ s). Therefore, looking at parameters, such as the track impact parameters (d_0, z_0), within the jet can help discriminate light flavour jets from heavy flavour jets. In addition, algorithms based on MC simulation predictions using variables which provide some discrimination between signal (b-jet MC) and background (light jet MC) are used. These variables are combined using a neural net [75], resulting in a single variable ($MV1$) providing a large discrimination between b-jets and light flavour jets. This analysis uses a 70% efficiency cut for selecting jets originating from b-quarks, which provides a rejection of 99.3% of jets originating from light quarks.

6.1.4 Missing Energy

Protons colliding in ATLAS have their momenta directed entirely in the z–direction. In a proton-proton interaction, it is the constituent partons making up the protons which interact, each of which carries a fraction of the momentum of the proton. This momentum fraction is impossible to determine on an event by event basis, with the result that the z boost of the event is unknown. However, the momentum of the partons in the transverse plane is negligible, allowing conservation of momentum to be imposed in the x and y directions. If a weakly interacting particle such as a neutrino is produced in ATLAS, its momentum will be unmeasured by the detector, leading to an apparent imbalance.

Missing transverse energy is derived by calculating the vector sum of energies in the calorimeter and from muons in the muon spectrometer. Imposing the requirement that the vector sum of energy should be zero, any deficit in energy is defined as missing energy, or $E_{\mathrm{T}}^{\mathrm{miss}}$. This amount is derived using the reconstructed objects in the event, leading to a so called *Object based* $E_{\mathrm{T}}^{\mathrm{miss}}$. Energy deposits outside the objects are attributed to soft particles and calibrated separately [76].

6.2 Event Selection

To select preferentially events originating from $t\bar{t}$ production while suppressing background processes, cuts on the previously mentioned objects, depending on the desired top decay modes, as well as overall event level cuts are applied. Electrons are required to have $E_{\mathrm{T}} > 25$ GeV, muons are required to have $p_{\mathrm{T}} > 20$ GeV and jets are required to have $p_{\mathrm{T}} > 25$ GeV. In addition, the event is required to have a reconstructed primary vertex with at least four associated tracks.

6.2.1 Good Runs List

With ATLAS recording a large amount of physics data, it is impractical to assume the detector is fully operational for the entire data taking period. Downtime for subdetectors, due to hardware or software problems, can impact on the overall quality of recorded data. For example, if a large portion of the tracker is turned off, or the tracking software is disabled, then no track reconstruction is done and reconstructed objects later in the analysis chain will be affected.

To help manage the data and to identify good quality data from potentially unusable data, each data taking period in ATLAS is split into *runs*, with each run being made of smaller luminosity blocks. Each luminosity blocks represents about two minutes of data taking in ATLAS.

Luminosity blocks are marked as good or bad based on the detector conditions during that particular block. For example, if the electromagnetic calorimeter suddenly shuts down, then the luminosity blocks affected are marked bad. The luminosity blocks marked good are then counted and placed into a Good Runs List (GRL).

Each run considered in the GRL is also checked to ensure the subdetectors are behaving as expected. If it is found that something is wrong with a run, such as part of the tracker being offline, or a calorimeter readout failure, first efforts are made to recover as much data as possible, as the data may still be usable for physics.

In April 2011, a hardware failure in the electromagnetic calorimeter caused a problem with the readout capability in a rectangular region of $\Delta\phi \times \Delta\eta = 0.2 \times 1.4$ in size. This was a major problem, affecting electron, jet and $E_{\mathrm{T}}^{\mathrm{miss}}$ reconstruction, present throughout the remainder of the runs until the component was fixed, though the data from the rest of the detector were perfectly suitable for physics. In order to be able to use these data, the hole in the calorimeter had to be modelled, and so a fraction of the MC simulation used for signal and background estimation has the

calorimeter problem simulated to compensate.

Once a GRL is compiled and checked, it can be used to identify the data runs suitable for physics analysis. The GRL has a record of all the lumi blocks and runs present in the dataset, and can be used to calculate the luminosity for that dataset.

6.2.2 Trigger Requirements

Each analysis decay channel discussed here requires every event to have been selected by a single lepton trigger (either electron or muon) which is fully efficient for leptons satisfying the p_{T} cut. The triggers are selected based on the run conditions for a given data taking period. Given that the trigger has a maximum output rate, at very high luminosities it becomes impractical to save every event from every trigger, so some of the trigger items are prescaled. This analysis uses the lowest unprescaled trigger for each data taking period.

Furthermore, the trigger is required to have been fired by one of the selected leptons. To check this, the position of the trigger object is compared to the position of each selected lepton, and the closest lepton (with $\Delta R < 0.15$ from the trigger object) is taken to have fired the trigger.

Table 6.1 shows the trigger configurations for electrons and muons by data taking period. The *EF* in the trigger word refers to 'Event Filter', *e20* states that the trigger threshold corresponds to 20 GeV, for electrons, and *medium* refers to the object quality cuts. In the case of periods L–M, the *v* means the trigger threshold varies with η and *h* states that a veto on hadronic activity is enforced. The electron trigger condition in periods L–M requires either one of two triggers to pass. This is due to the non stable efficiency of the *EF_e22vh_medium1* trigger at high p_{T}, where the *EF_e45_medium1* trigger performs as desired in this high p_{T} range. The overall efficiency shape after the OR requirement then behaves as needed.

Period	Luminosity (pb^{-1})	Electron Trigger	Muon Trigger
B-D	167.249	EF_e20_medium	EF_mu18
E-H	937.71	EF_e20_medium	EF_mu18
I	333.242	EF_e20_medium	EF_mu18
J	223.49	EF_e20_medium	EF_mu18_medium
K	583.266	EF_e22_medium	EF_mu18_medium
L-M	2401.77	EF_e22vh_medium1 OR EF_e45_medium1	EF_mu18_medium

Table 6.1: Trigger requirements for each data period.

6.2.3 Dilepton Selection

For dilepton decay modes, exactly two leptons[‡] of opposite sign and either flavour are required, with at least two jets. Missing transverse energy is required to be greater than 60 GeV for the ee and $\mu\mu$ channels, which allows strong discrimination against $Z \to ll$ events, which typically do not have much $E_{\mathrm{T}}^{\mathrm{miss}}$. To further the $Z \to ll$ rejection, a cut around the Z resonance, requiring that the invariant mass of opposite sign, same flavour lepton pairs differs by more than 10 GeV from the known Z–boson mass is applied. In addition, to ensure compatibility with the MC simulation, and to suppress J/ψ and Υ decays, the dilepton invariant mass is required to be greater than 15 GeV. For the $e\mu$ channel, the scalar sum of the momentum in the event from leptons and jets (H_{T}) is used instead of $E_{\mathrm{T}}^{\mathrm{miss}}$, and is required to be greater than 130 GeV.

6.2.4 Single Lepton Selection

For the single lepton decay modes exactly one lepton is required, with at least four jets. Missing transverse energy is required to be greater than 30 GeV in the electron channel, with the additional constraint that the transverse mass of the leptonically decaying W boson[§], $m_{\mathrm{T}}(W)$, is greater than 30 GeV. In the single muon channel,

[‡]Leptons considered for this analysis are electrons and muons only. Tau leptons which decay to a lighter lepton are considered as the lighter lepton.

[§]Transverse mass, m_{T} is defined as $\sqrt{2 \times p_{\mathrm{T}}^{l} \times E_{\mathrm{T}}^{\mathrm{miss}}(1 - \cos(\phi^{l} - \phi^{\mathrm{miss}}))}$

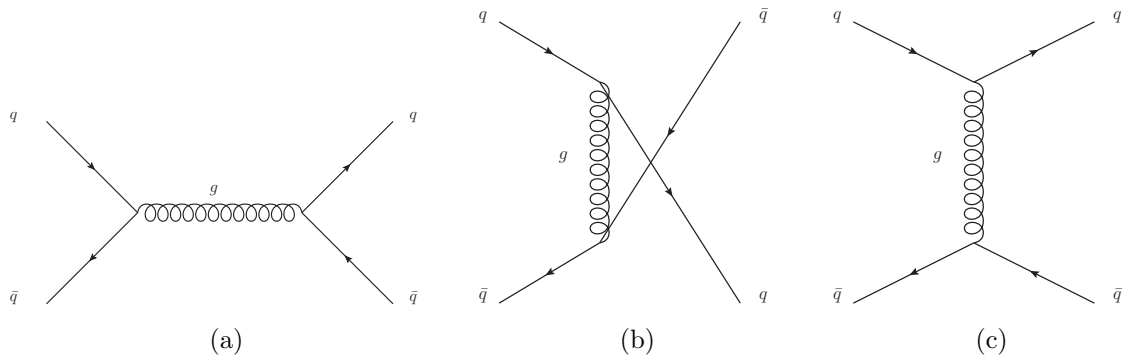

Figure 6.3: A set of tree level (Leading Order) Feynman diagrams describing interactions between two quarks via the strong force.

$E_{\mathrm{T}}^{\mathrm{miss}}$ is required to be greater than 20 GeV, while the sum of $E_{\mathrm{T}}^{\mathrm{miss}}$ and $m_{\mathrm{T}}(W)$ is required to be greater than 60 GeV. Finally, for the single lepton decay modes, at least one b-tagged jet is required in the event, to suppress background contamination from $W \to l$+jets events.

6.3 Monte Carlo Generators

In order to compare data recorded in ATLAS with theoretical models, simulated data are used. To generate the simulated data, a MC generator is needed. The generator may be tuned to simulate the expected outcomes assuming the Standard Model is correct, or can be modified to generate various other interesting models.

The nature of a proton proton collision is very complex. In the simplest view, quarks and gluons inside the proton interact according to the mathematical rules of the Standard Model. The simplest way to represent this is with a Leading Order (LO) Feynman diagram as depicted in Figure 6.3.

It is possible to introduce a particle *loop* into this diagram, while still following the rules of the Standard Model. In fact, perturbation theory allows for an infinite number of loop corrections, which must all be calculated and summed over to give

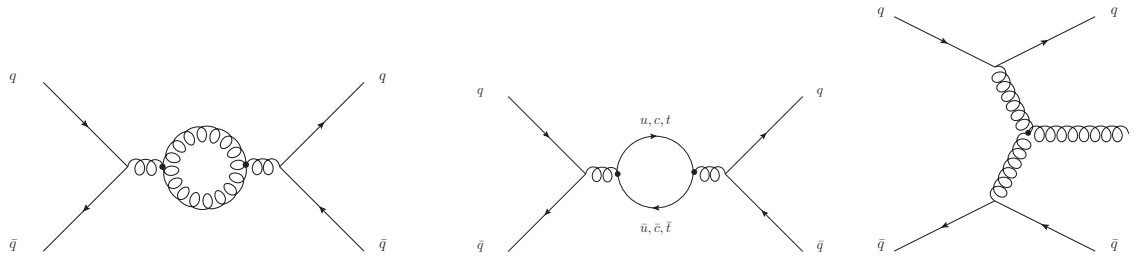

Figure 6.4: A set of NLO Feynman diagrams describing interactions between two quarks via the strong force.

an exact solution. Computationally, this is clearly impossible, so a trade off between computation time and accuracy is needed. Feynman diagrams with one extra loop are called Next to Leading Order (NLO), and there are many more diagrams than at tree level, and of a higher complexity. Each extra order gives a slightly better description of nature, but become increasingly difficult and time consuming to calculate. Figure 6.4 shows a small selection of NLO diagrams for the same process as in figure 6.3.

6.3.1 Monte Carlo Simulation

Generally, MC generators will stop at either LO or NLO, owing to the huge increase in computation time with each added loop, for only a small gain in accuracy. For a given process, the extra loops in NLO calculations can give virtual corrections, such as in figures 6.4(a) and 6.4(b). These corrections add extra vertices without changing the initial or final state. These corrections may alter the calculated cross section or other properties of the process. NLO diagrams can also give extra real emissions (see figure 6.5), which alter the initial or final states of the process, leading to NLO simulations producing different distributions, particularly with respect to the number of jets in the event. NLO generators used for MC simulation in the scope of this thesis are MC@NLO [77] and POWHEG [78].

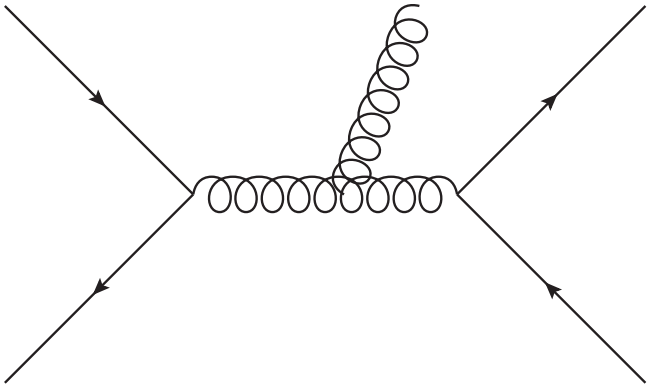

Figure 6.5: A NLO Feynman diagram for a two to two process, with one extra gluon radiated. The extra gluon is naturally a part of the NLO calculation, and this can provide up to one extra hard jet. This diagram may also be used in a 'multi-leg' calculation, as part of a $q\bar{q} \to q\bar{q}g$ process.

LO generators can approximate these extra emissions by using a 'multi-leg' approach. For a given process (for example $q\bar{q} \to q\bar{q}$) all possible Fenyman diagrams at LO are considered. At NLO, the extra diagrams may introduce additional emissions, or virtual corrections. The multi-leg approach only includes the diagrams with real emissions. These could be considered the LO diagrams for $q\bar{q} \to q\bar{q} + 1$ (Figure 6.5 also illustrates this). For N extra emissions, then, the LO diagrams for $q\bar{q} \to q\bar{q} + N$ are considered in the multi-leg approach.

The benefit of this approach is good modelling of extra partons (leading to additional jets) in a process, without having to calculate all possible virtual corrections, but with the sacrifice of precision. Often, LO multi-leg generators can give a much better description of the data, for analyses sensitive to the number of extra jets in the event. One such multi-leg generator used in the scope of this thesis is ALPGEN [79, 80].

A MC simulation consists of several steps, further illustrated in figures 6.6 and 6.7:

- Matrix Element - The initial hard interaction, between quarks and/or gluons within the proton is described by a Matrix Element calculation. This represents the main interaction in an event and generally contains the interesting physics.

- ISR/FSR - Quarks and gluons can undergo QCD Bremsstrahlung, emitting gluons before or after the hard scatter and adding extra partons to the event.

- Resonance Decay - Unstable particles produced in the hard scatter decay into daughter particles. For example, a W boson decaying into a quark anti-quark pair.

- Multiple Parton Interaction (MPI) - The incoming protons in the collision may interact more than once, through different partons, in a single event. The cross section for interesting processes (such as $t\bar{t}$ production) is usually very small, so these extra interactions are often soft QCD interactions. One software package often used to simulate MPI is JIMMY [81].

- Hadronisation - The outgoing partons and beam remnants left after all of the above have been simulated are quarks, gluons and leptons. The quarks and gluons carry colour, and QCD confinement does not allow for coloured partons to exist in isolation. The hadronisation stage of the simulation can be approximated with several different methods. One method, as used with the PYTHIA generator [82], connects all of the coloured partons by colour confinement *strings*, which then fragment to produce colourless hadrons. Another method, used by HERWIG [83], groups neighbouring $q\bar{q}$ pairs into colour neutral *clusters* which then decay isotropically.

Care must be taken to avoid overlap between these steps. For example, the Matrix Element calculation for a process, calculated at NLO or multi-leg, could produce an extra real emission of a quark. This final state then contains $X \rightarrow Y + q$, which may overlap with final states produced by the parton shower. This would then lead to a double counting of a given final state. A matching procedure is used to identify these kinds of overlap in the MC simulation chain, one example of which is the MLM matching performed in ALPGEN [79].

The Monte Carlo event generator sequence gives a software analogy to the LHC; the

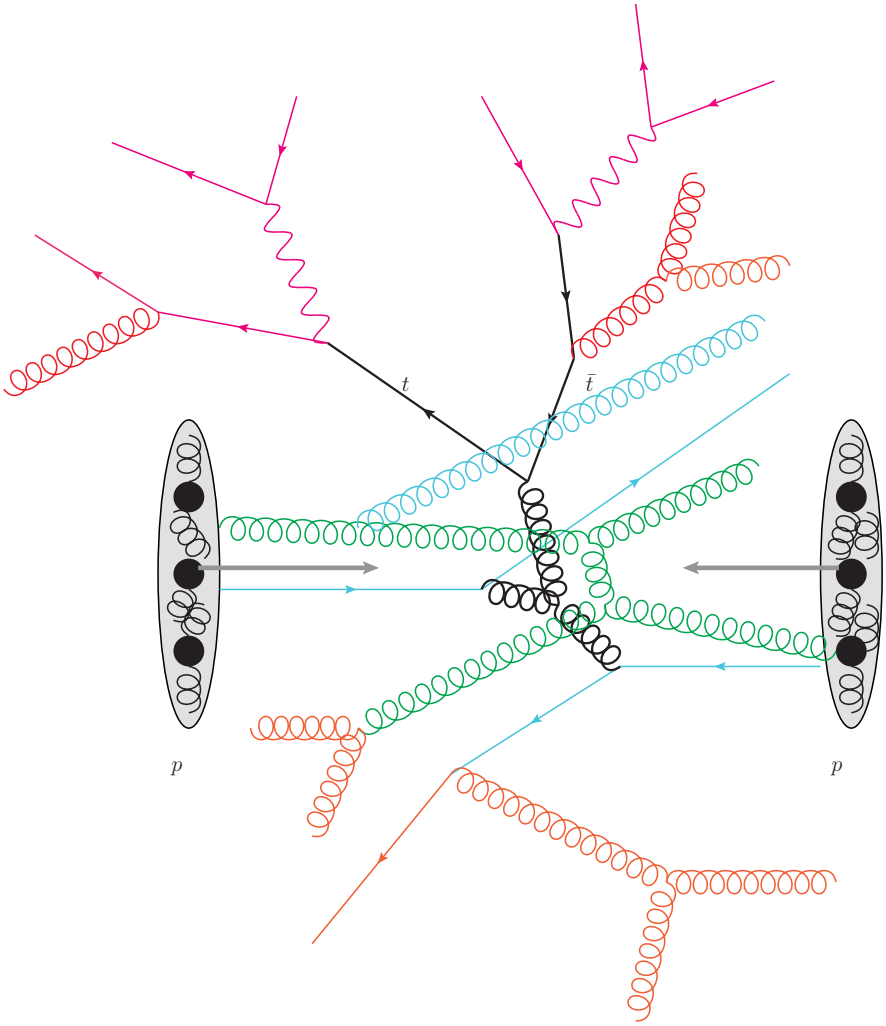

Figure 6.6: Overview of the stages involved in a MC generator simulation of a $t\bar{t}$ event. The black part represents the hard scatter, blue represents ISR and red FSR, the purple part shows the resonance decay, and the green represents MPI. Hadronisation is shown in figure 6.7.

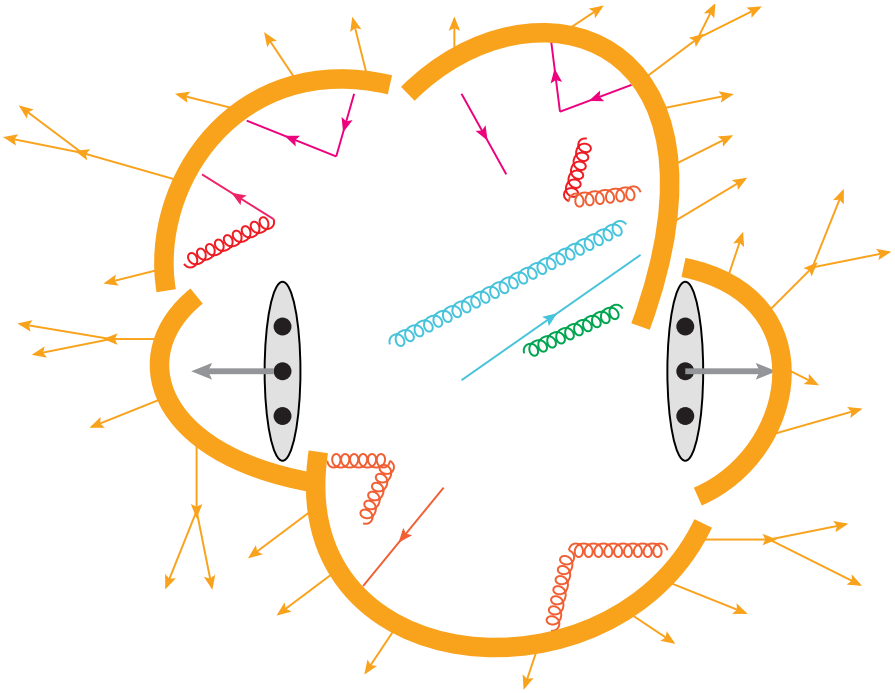

Figure 6.7: The same event as in figure 6.6 at the hadronisation stage. The orange bands represent confinement strings, which undergo fragmentation to produce primary hadrons, which in turn may further decay to stable hadrons.

machinery which collides protons and produces events. The event generator outputs stable hadrons and leptons over the full 4π fiducial range. The ATLAS detector is instrumented up to $|\eta| < 4.9$ and within this acceptance, there are gaps for services and other dead material (such as the magnet system). To provide an accurate comparison with the recorded data, MC events must be put through a detector simulation. In ATLAS, the detector is simulated in GEANT4 [84], which provides an accurate description of the ATLAS detector. Due to the complexity of ATLAS, simulating all of the components of the detector can be time consuming. For this reason it may be preferable in some cases to use instead ATLFAST II [85], which uses a fast calorimeter simulation, giving a ten-fold reduction in required computing time.

6.4 Signal and Backgrounds

The event selection described in the previous chapter is designed to reject background processes while maintaining a strong signal strength. In the dilepton event selection, events from $Z/\gamma^* \rightarrow l^+l^-$ processes with extra jets are one of the main sources of background, due to the two prompt leptons from the Z boson decay. The cut on the Z mass window reduces a large amount of this background, but there still remains an irreducible portion. In addition to the background due to Z/γ^*+jets, events originating from single top, diboson and 'fake' lepton production also contaminate the signal region. The single lepton decay channel also has contamination from W+jets events, owing to the production of a single prompt lepton and $E_{\mathrm{T}}^{\mathrm{miss}}$ from a neutrino. Combined with extra jets, this gives an almost identical signal to that of semileptonic $t\bar{t}$ decays.

6.4.1 Backgrounds

To model the background processes, a combination of Monte Carlo simulation and a data driven technique is employed.

The Z/γ^*+jets background is simulated using the ALPGEN 2.13 [79, 80] Monte Carlo package, within an invariant mass range of 10 GeV $< m_{ll} <$ 2000 GeV. Up to five extra partons are included in the simulation and the cross section normalised to a data driven estimate described in section 6.5.1. Dilepton decays with all lepton flavours are considered in the simulation. The simulated events are then showered with HERWIG [86]. The Z/γ^*+jets background is one of the dominant backgrounds in the dilepton channel.

W+jets background events are simulated with ALPGEN, with up to five extra partons, and showered with HERWIG. W+jets events with extra heavy flavour partons are also simulated ($W + b\bar{b} +$ jets and $W + c(\bar{c}) +$ jets). Again, all lepton

flavours are considered in the W decay. The W+jets simulation is normalised to a data driven estimate obtained by the 'charge asymmetry method', described in more detail in section 7.4.14. The W+jets background is one of the dominant backgrounds in the semileptonic channel.
Diboson events are simulated with ALPGEN for the hard scatter, with HERWIG used for the parton shower, for dilepton final states. The states considered for the dilepton diboson decays are:

- WW, with both $W \to l\nu$
- WZ, with $W \to X$ and $Z \to ll$
- ZZ, with $Z \to X$ and $Z \to ll$

where X represents any possible final state.

In the ATLAS production of 2011 MC samples, no ALPGEN diboson events with single lepton final states were simulated, so the HERWIG LO generator is used to generate the hard scatter and parton shower for these final states. The final states for the HERWIG diboson generation are filtered for one lepton with $p_{\mathrm{T}} > 10$ GeV inside $|\eta| < 2.8$.
Single top events are simulated with the MC@NLO v4.01 [77] generator, with parton shower from HERWIG, for the s and Wt channels. A bug was found in the t channel simulation with MC@NLO+HERWIG, such that unphysical jets were generated in the parton shower. Therefore, the t channel simulation is done by AcerMC+PYTHIA, instead.

For dilepton analyses, single top events with only one real lepton in the final state (s and t channels) can only pass the event selection if a charged lepton is 'faked', so are considered as 'fake lepton' events included in the data driven estimation described in the next section. Events in the Wt channel can include two real leptons, one from

the top decay and one from the W boson decay, so these are not considered in the dilepton fake lepton estimation.

6.4.2 Fake Leptons

Fake lepton events are so called due to leptons being reconstructed where no prompt lepton is present. For example, if a jet from a leptonically decaying W boson in a W+jets event were reconstructed as an electron, there would be two leptons present in the event making it a candidate for passing the dilepton event selection. Similarly, for the s and t single top channels, where only one real lepton is produced in the single top decay, with another lepton being faked. The Wt channel single top decay can produce two real leptons in the final state, from the top decay and from the W boson decay, so events from this channel are not considered as fake lepton events. Fake leptons may also originate from QCD events with hard jets, or as real soft leptons from heavy flavour decays.

The contribution to the background from fake leptons is difficult to model with MC simulations, so a data driven approach is taken to provide an estimate. For this analysis, the *Matrix Method* [87] is used to estimate the fake lepton background.

Matrix Method

To estimate fake lepton events, the quality cuts applied to the leptons are reduced, making a 'Looser' lepton. The efficiency of loose to tight leptons is measured for both prompt and fake lepton sources. To measure the prompt lepton efficiency, ϵ^{real}, a 'tag and probe' method is used with a sample of known prompt leptons, for example $Z \to l^+l^-$. Events from the $Z \to l^+l^-$ sample are selected if they contain two loose leptons, with no requirement on the jet activity. One of these leptons which also passes the tight selection requirements is defined as the 'tag'. The tag is

also required to have fired the trigger for the event. The second lepton, the 'probe', is then used to measure the loose to tight efficiency, ϵ^{real}.

To measure the fake lepton loose to tight efficiency, ϵ^{fake}, a sample with at least one jet with $p_{\text{T}} > 25$ GeV and only one loose lepton is used. To ensure the sample is dominated by fake leptons, $E_{\text{T}}^{\text{miss}}$ is required to be less than 20 GeV. This region is not fully free of signal events, however, so an estimate of the number of signal events is subtracted. The fake efficiency, ϵ^{fake}, is then defined as the fraction of loose leptons that also pass the tight requirement.

A matrix can then be constructed:

$$\begin{pmatrix} N_{\text{loose}} \\ N_{\text{tight}} \end{pmatrix} = \begin{pmatrix} 1 & 1 \\ \epsilon^{real} & \epsilon^{fake} \end{pmatrix} \begin{pmatrix} N_{\text{loose}}^{\text{real}} \\ N_{\text{loose}}^{\text{fake}} \end{pmatrix} \tag{6.4}$$

Inverting this matrix gives,

$$N_{\text{tight}}^{\text{fake}} = \epsilon^{fake} N_{\text{loose}}^{\text{fake}} = \frac{\epsilon^{\text{fake}}}{\epsilon^{\text{real}} - \epsilon^{\text{fake}}} (N_{\text{loose}} \epsilon^{\text{real}} - N_{\text{tight}}) \tag{6.5}$$

where $N_{\text{tight}}^{\text{fake}}$ is the number of fake leptons expected to contaminate the signal region.

In order to use this estimate to produce fake lepton distributions, rather than just a yield, the efficiencies are parameterised in terms of η and p_{T}. This parameterisation can then be used to estimate the fake lepton contribution in data events.

To estimate the fake lepton contribution in dilepton events, the same method can be used, but a larger matrix is constructed for N_{ll}, N_{lt}, N_{tl} and N_{tt}. Figures 6.8 and 6.10 show the description of data in a fake lepton dominated control region for the dilepton and semilepton channels. The dilepton channel has the opposite sign requirement on the leptons reversed for this control region. These figures include an uncertainty band, which is taken from the uncertainty in the data driven fake

estimation, as well as the uncertainty inherent in the remaining background estimates and uncertainty from other sources (discussed in section 7.4). The largest uncertainties in figure 6.8 are due to the fake lepton estimate (see section 7.4.14). The low $E_{\mathrm{T}}^{\mathrm{miss}}$ region in the ee channel shows a particularly large uncertainty due to contamination of the Z/γ^* background, and the large uncertainty associated with that background. Figure 6.9 shows this contamination. A larger veto around the Z boson mass shows a reduction of Z/γ^* events in the control region. Within these uncertainties, the fake lepton dominated regions describe the data reasonably well.

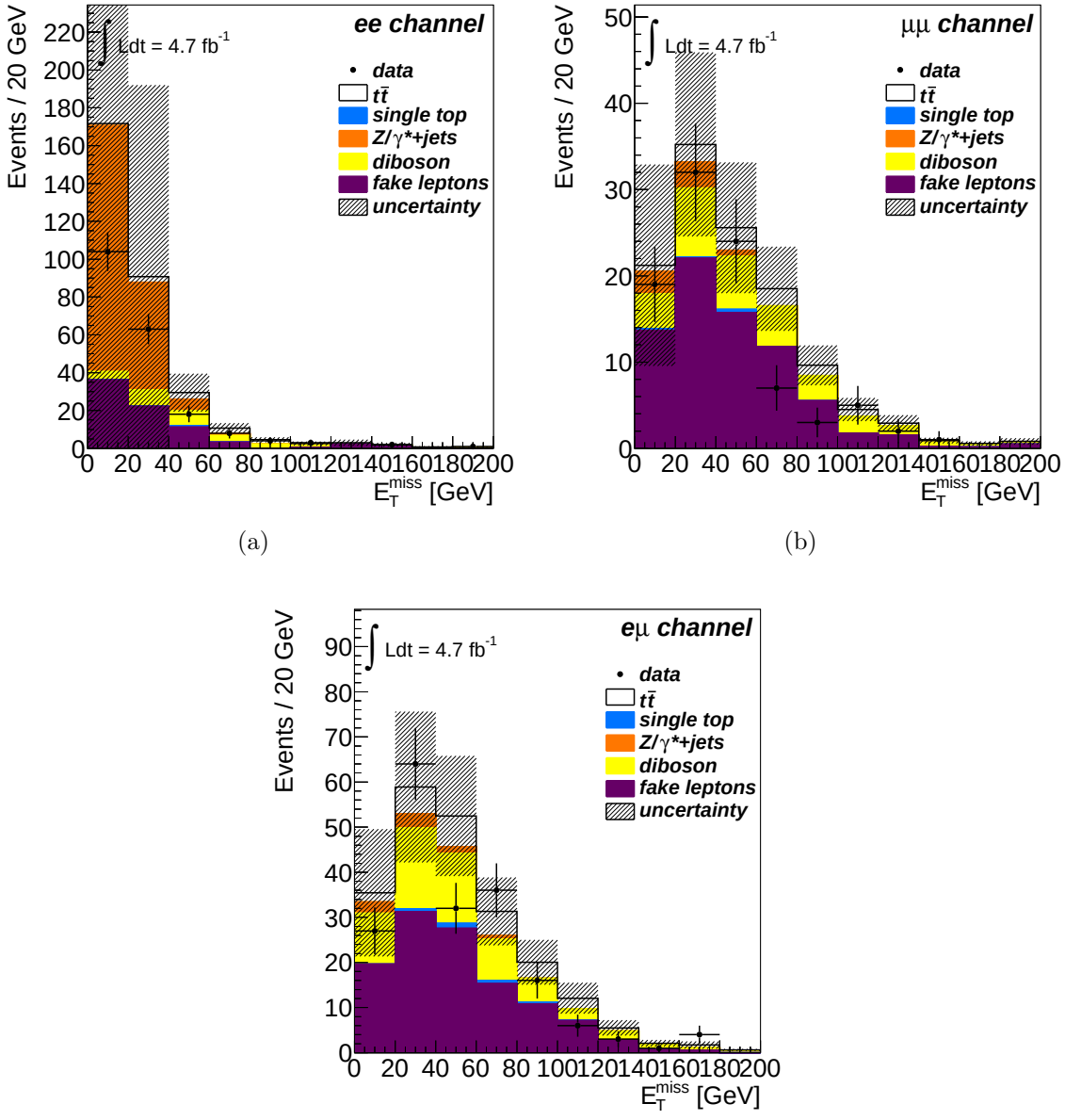

(a) (b)

(c)

Figure 6.8: Missing Transverse Energy in a fake lepton control region for the dilepton channels, where both leptons in the event are required to be the same sign. At least one jet is required for each event, as well as a 10 GeV veto around the Z boson mass.

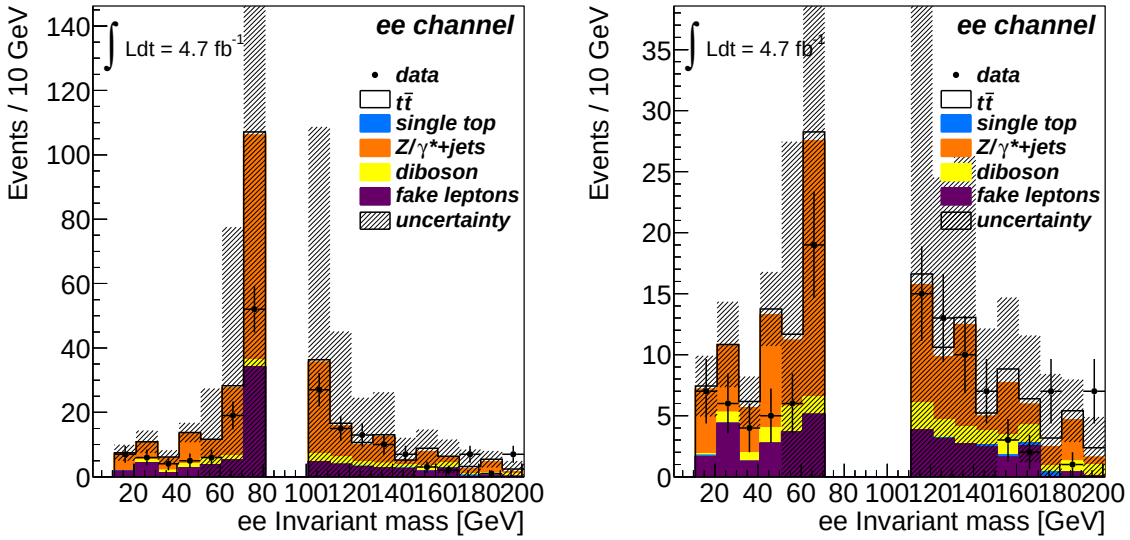

(a) (b)

Figure 6.9: Invariant mass in the *ee* channel in a fake lepton control region. Both leptons are required to be the same sign and at least one jet is required to be present. a) shows the standard 10 GeV veto around the Z boson mass. b) shows a larger veto, reducing the contamination of Z/γ^* events.

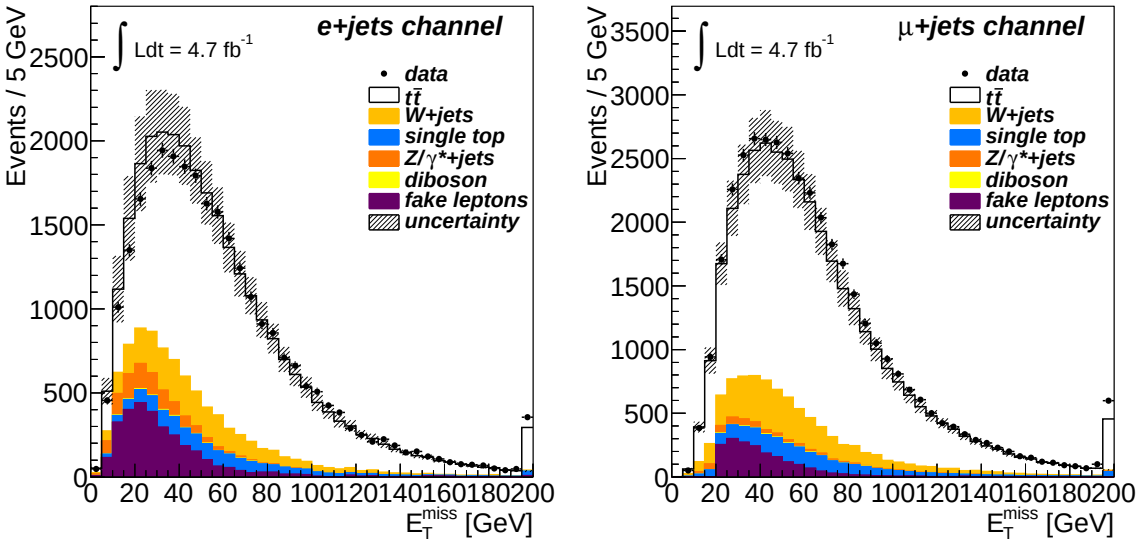

(a) (b)

Figure 6.10: Missing Transverse Energy including a fake lepton control region for the single lepton channels.

6.4.3 Signal

The $t\bar{t}$ signal is generated with MC@NLO+HERWIG, assuming a top quark mass of $m_t = 172.5$ GeV, and is filtered to require that at least one of the top quarks decays leptonically. The cross section of the $t\bar{t}$ sample is normalised to the approximate Next to Next to Leading Order (NNLO) HATHOR [88] calculation of $166.8^{+16.5}_{-17.8}$ pb^{-1}, using the MSTW2008 90% NNLO PDF [89] with PDF+α_S uncertainties according to the MSTW prescription [90]. The calculation is cross checked with the NLO+Next to Next to Leading Log (NNLL) calculation [91] as implemented in TOP++ 1.0 [92].

6.4.4 $t\bar{t}$ Decays without Spin Correlation

MC@NLO handles the propagation of spin information to the decay products of the top quarks correctly, such that the final states are influenced by the spin correlation. In order to create an alternative model where $A = 0$ such that the spins of the top quarks are produced equally alike and unlike in all bases, a modification to the MC generation chain is made.

Once the $t\bar{t}$ pairs are produced in MC@NLO, the spin information is propagated to the decay products. Then, the final state is read in by HERWIG to shower. If, instead, HERWIG reads in the undecayed $t\bar{t}$ pairs, the spin information is lost and the decays are produced independently of the spin of the top. This effectively removes the influence of the spin of the top on its decay products such that no correlation between the spins can affect the final state. The $\Delta\phi$ distribution shown in figure 5.9 utilises both of these signal MC samples with and without spin correlation.

6.4.5 Pileup Simulation

The MC simulation includes an estimation of the different pileup conditions expected in data. However, this does not provide an exact simulation of the observed pileup, and must be reweighted. The average number of interactions per bunch crossing, $< \mu >$, is calculated for each lumi block. The events in the MC simulation — which are produced with a given run configuration in mind — are then reweighted such that the $< \mu >$ distribution matches that observed in data in an analysis independent control region (ie. with no event level cuts applied). Each value for $< \mu >$ in a given run period carries an event weight, which is used to reweight the distribution.

Figures 6.11, 6.12, 6.13, 6.14 and 6.15 show the distribution of the average number of interactions per bunch crossing as simulated in MC and after reweighting, plotted after full event selection. There is only a small difference between the unweighted and reweighted distributions in these figures, due to the MC simulation being targeted for the known run conditions for the collected dataset. In the case where the MC simulation is produced before the full dataset is collected, then the reweighting may have a much larger effect in the case of changing run conditions.

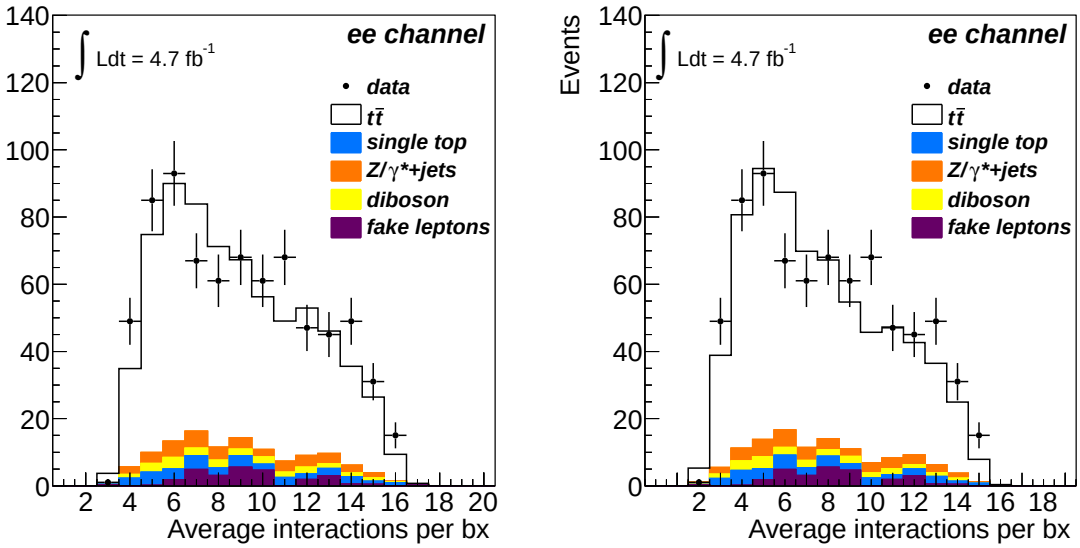

(a) (b)

Figure 6.11: a) Average number of interactions per bunch crossing, a) before, and b) after pileup reweighting, in the *ee* channel.

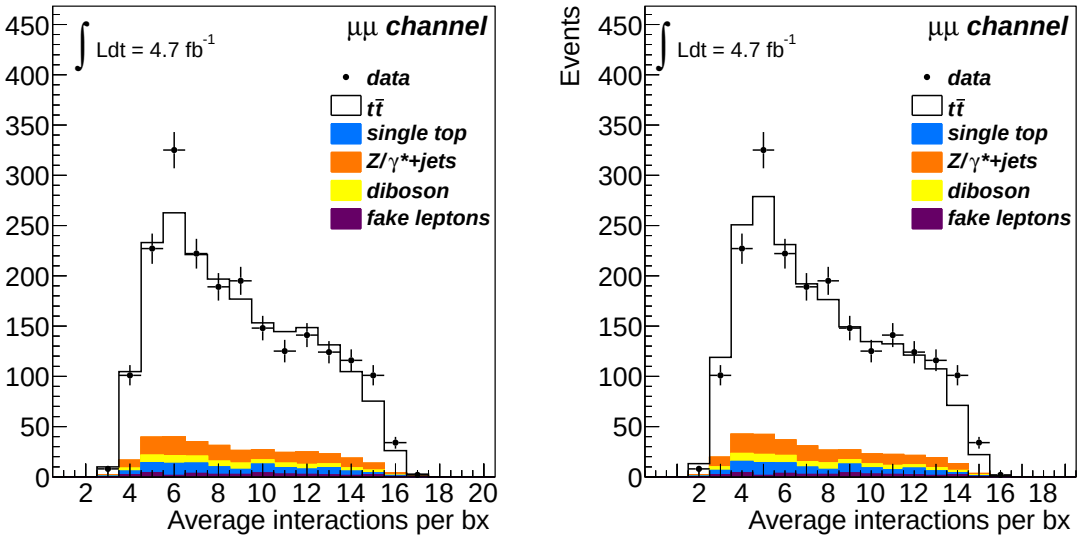

(a) (b)

Figure 6.12: a) Average number of interactions per bunch crossing, a) before, and b) after reweighting, in the $\mu\mu$ channel.

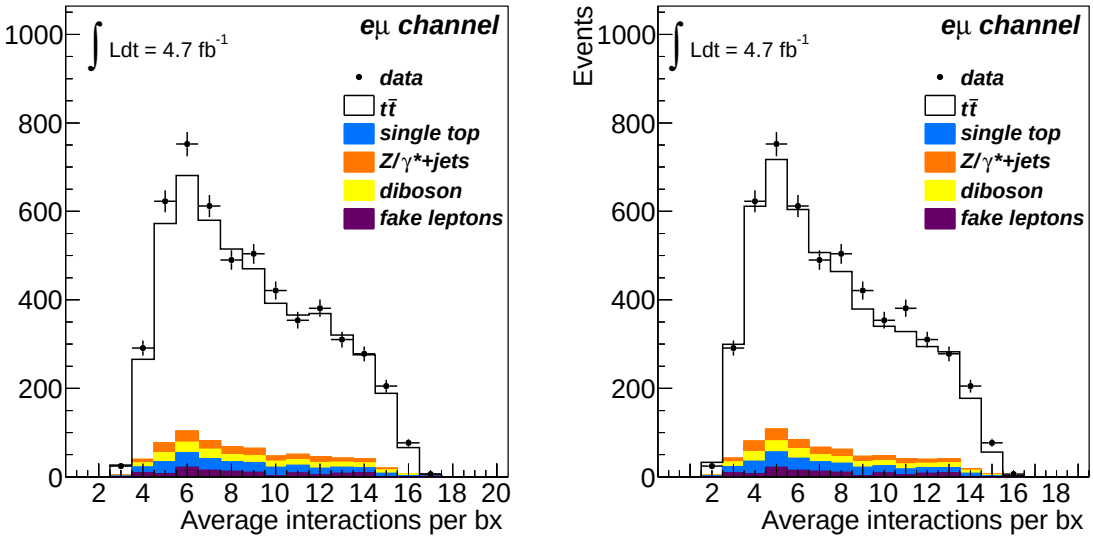

(a) (b)

Figure 6.13: a) Average number of interactions per bunch crossing, a) before, and b) after reweighting, in the $e\mu$ channel.

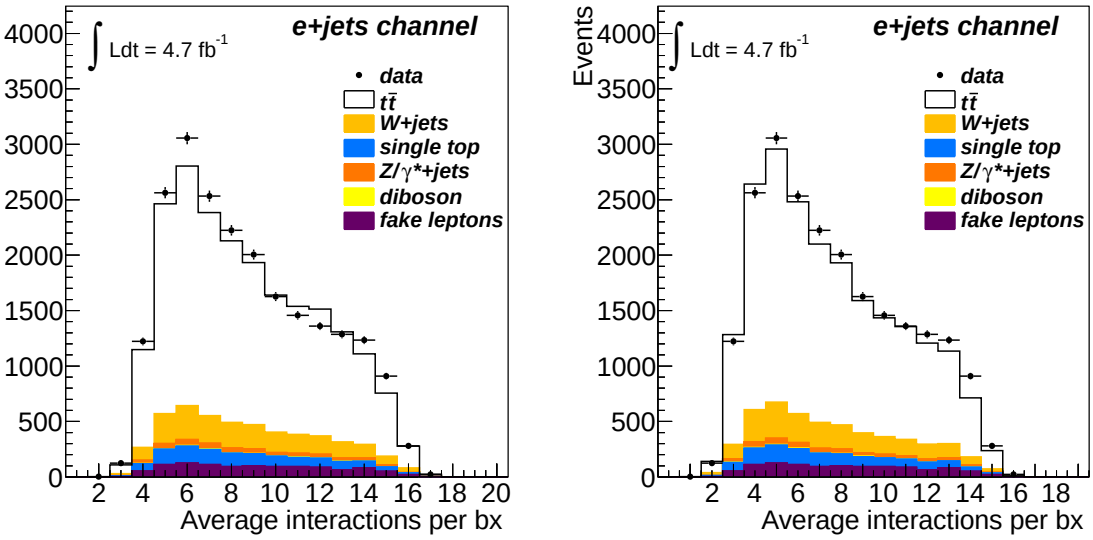

(a) (b)

Figure 6.14: a) Average number of interactions per bunch crossing, a) before, and b) after reweighting, in the e+jets channel.

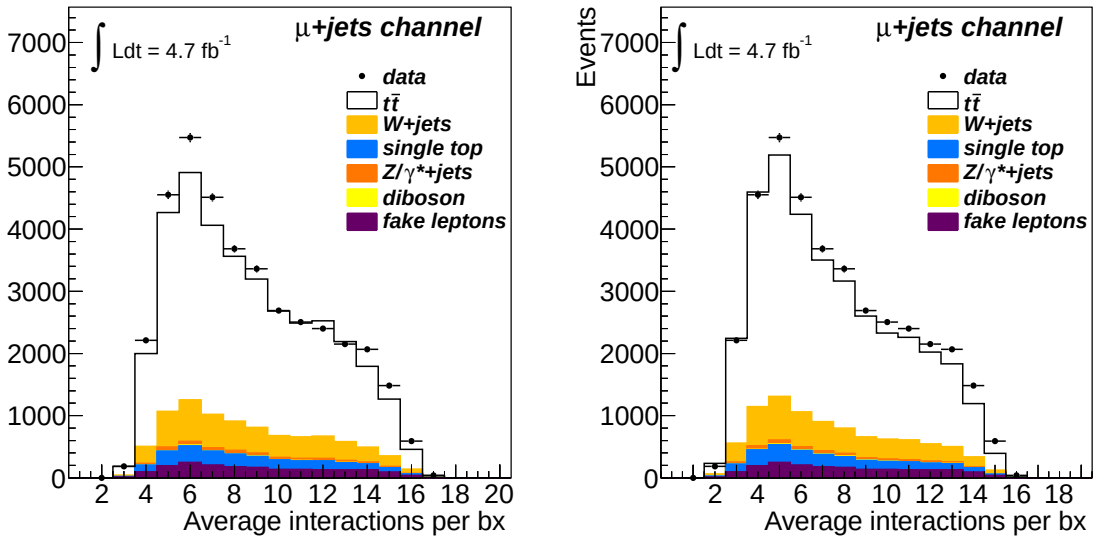

(a) (b)

Figure 6.15: a) Average number of interactions per bunch crossing, a) before, and b) after reweighting, in the μ+jets channel.

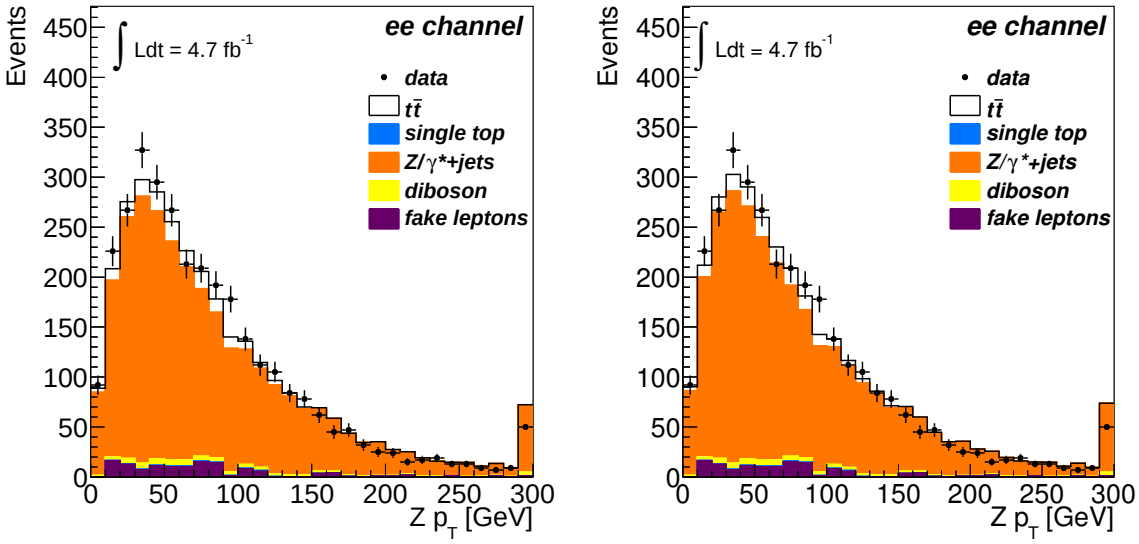

(a) (b)

Figure 6.16: Z-boson p_{T} distribution inside the Z mass window for the ee channel. The $E_{\mathrm{T}}^{\mathrm{miss}}$ cut has also been reduced to 30 GeV in these plots. a) shows the distribution obtained with the nominal MC simulation, b) shows the same distribution after applying a data driven scale factor.

6.5 Data-Monte Carlo Comparison

The agreement between data and Monte Carlo simulation is checked for a range of observable quantities before looking at the $\Delta\phi$ distribution in the signal region, to ensure that the simulation describes the data. Since the event selection is designed to enhance the presence of the signal over background, control regions must be defined in order to check the background description of data. Generally this involves reversing one or more cuts in order to enhance the background contribution. First, the dilepton channel is considered, followed by the semilepton channel in the later chapters.

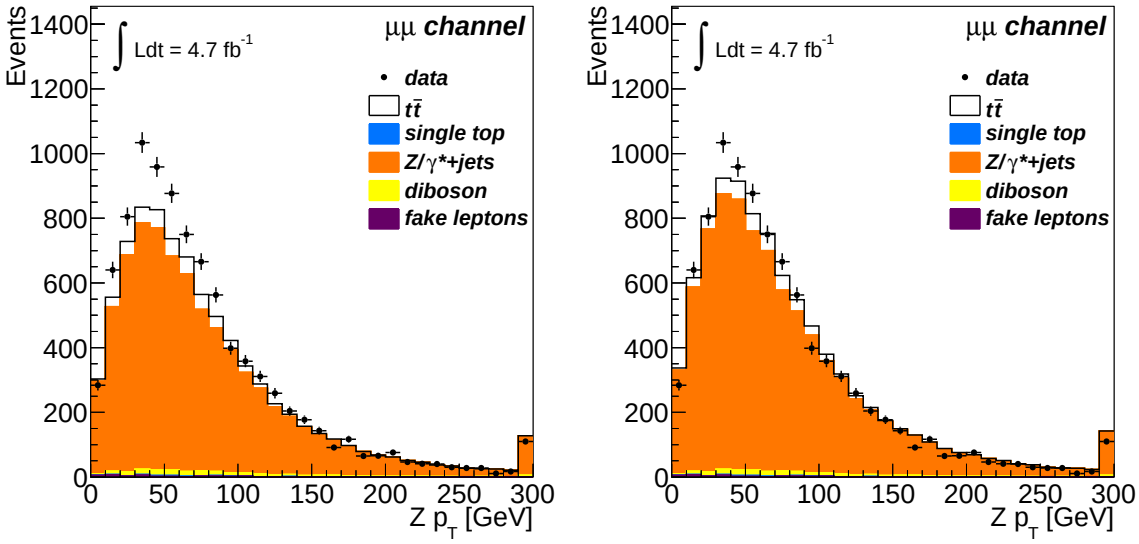

(a) (b)

Figure 6.17: Z-boson p_{T} distribution inside the Z mass window for the $\mu\mu$ channel. The $E_{\mathrm{T}}^{\mathrm{miss}}$ cut has also been reduced to 30 GeV in these plots. a) shows the distribution obtained with the nominal MC simulation, b) shows the same distribution after applying a data driven scale factor.

6.5.1 Dilepton Control and Signal Regions

For dilepton events with both leptons of the same flavour, events with a dilepton mass within the Z boson mass window are dominated by the Z/γ^* process. Figures 6.16 and 6.17 show the Z-boson p_{T} for events with dilepton mass inside the Z mass window. The expected distribution is in reasonable agreement with the ee channel, though falls far below the observed distribution in the $\mu\mu$ channel. This is considered to be due to a mismodelling and is fixed by applying a data driven scale factor to the Z/γ^*+jets MC simulation. Events within the Z boson mass window originating from Z/γ^* are counted, and compared to the number of events in data. The number of events from other sources, including the $t\bar{t}$ signal, are subtracted from the data. The scale factor (SF) is then derived in this control region (CR) as the number of data events after subtraction, divided by the number of Z/γ^* events. This scale factor is then used to normalise the Z/γ^* contribution in the signal region (SR).

The scale factors for the ee and $\mu\mu$ channels are derived using table 6.2. The final scale factors used are shown in table 6.3, where

$$SF(SR) = \frac{N_{data}(CR) - N_{bkg}(CR)}{N_{Z\to l^+l^-}(CR)}. \tag{6.6}$$

	ee	$\mu\mu$
$t\bar{t}$ (CR)	173.0	460.5
$Z \to \tau\tau$ (CR)	0.7	2.2
W+jets (CR)	0.5	0.0
Diboson (CR)	78.1	200.5
Single Top (CR)	8.4	20.0
Fake Leptons (CR)	114.3	29.9
Total Background (CR)	374.9	713.1
$Z \to l^+l^-$ (CR)	2741.6	7586.0
Data (CR)	3170	9194
$Z \to l^+l^-$ (SR)	20.5	74.7

Table 6.2: Number of events in the Z/γ^* control region for each signal and background source. CR denotes events inside the control region, where the control region is defined with $|m_{ll} - m_Z| < 10$ GeV, $E_{\mathrm{T}}^{\mathrm{miss}} > 30$ GeV and requiring at least two jets. SR denotes the signal region.

channel	Scale Factor
ee	1.020
$\mu\mu$	1.118

Table 6.3: Scale factor used to normalise the Z/γ^* background contribution for the dilepton channels.

In the ee and $\mu\mu$ channels, distributions of events with m_{ll} inside the Z mass window ($m_Z \pm 10$ GeV) are dominated by Z/γ^* production. Figures 6.18 and 6.19 show that the data are well described by the background simulation in this control region. To check the background modelling outside of the Z mass window, the $E_{\mathrm{T}}^{\mathrm{miss}}$ cut is reversed to ensure that background processes dominate, such that events are required to have $E_{\mathrm{T}}^{\mathrm{miss}} < 60$ GeV. Figure 6.20 shows that the data are described well by the simulation in this region.

Figures 6.21 and 6.22 show the $\Delta\phi$ distribution inside the Z mass window, before and after applying the data driven scale factor. For the $\mu\mu$ channel, the agreement between the data and MC simulation is much improved after applying a data driven scale factor. The scale factor in the ee channel is of the order 2%, so has only a small effect.

After deriving the scale factors in the control region, they can be applied to the signal region. The scale factor affects only the normalisation of the distribution and not the shape. Table 6.4 shows the number of expected events from the different signal and background sources as well as the number of observed events. The overall yield shows a good agreement with the prediction.

Figures 6.23, 6.24 and 6.25 show the p_{T} distributions for the leading and subleading leptons in the same flavour lepton channels, and for electrons and muons in the opposite flavour channel. The agreement between data and the MC simulation is good.

Channel	ee	$\mu\mu$	$e\mu$
$t\bar{t}$	583.85	1673.42	4413.64
$Z \to l^+l^-$	20.54	83.51	0.00
$Z \to \tau\tau$	18.48	68.43	175.34
Diboson	22.93	61.38	177.60
Single Top (Wt-channel)	31.20	84.00	228.48
Fake Leptons	16.41	28.97	99.21
Expected	693.41	1999.70	5094.28
Observed	740	2058	5328

Table 6.4: Event yields after all event selection criteria for the dilepton channel.

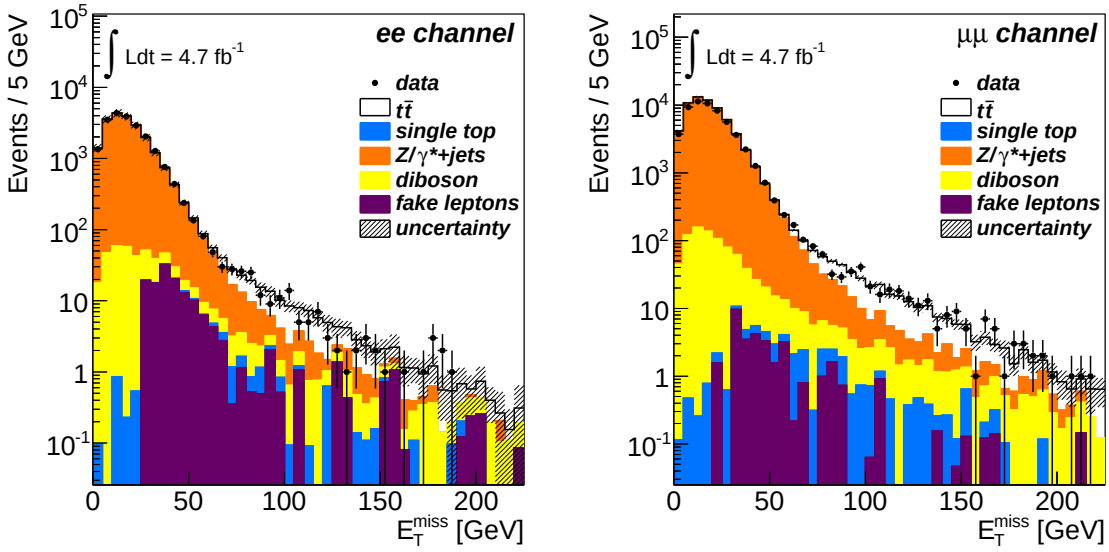

(a) (b)

Figure 6.18: a) $E_{\mathrm{T}}^{\mathrm{miss}}$ for events in the ee channel, b) for events in the $\mu\mu$ channel, with opposite sign leptons and at least two jets. The dilepton invariant mass is required to fall within the Z boson mass window.

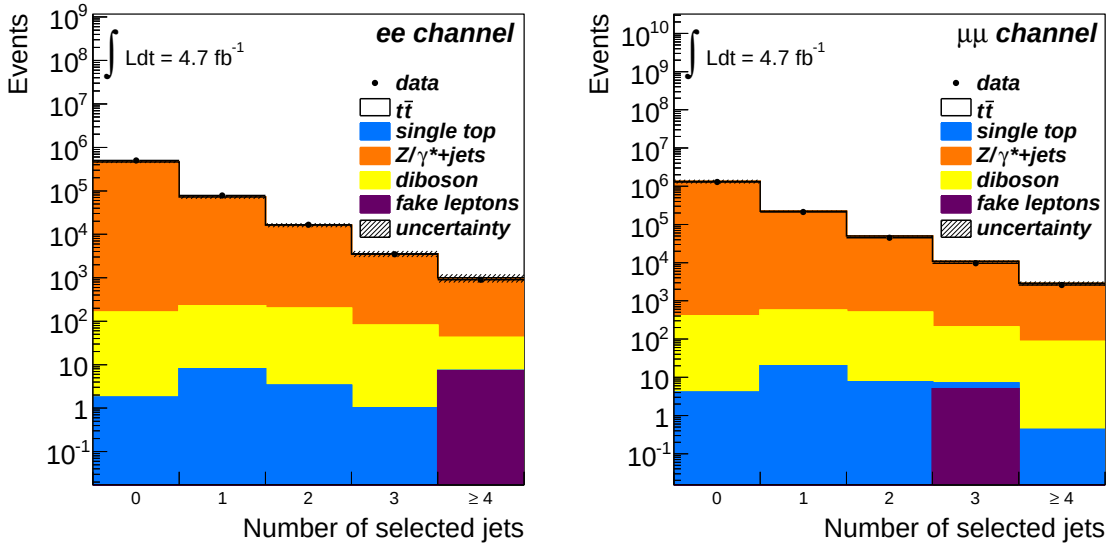

(a) (b)

Figure 6.19: a) Number of selected jets in the ee channel, b) in the $\mu\mu$ channel, for events with opposite sign leptons and at $E_{\mathrm{T}}^{\mathrm{miss}} < 60$ GeV. The dilepton invariant mass is required to fall within the Z boson mass window.

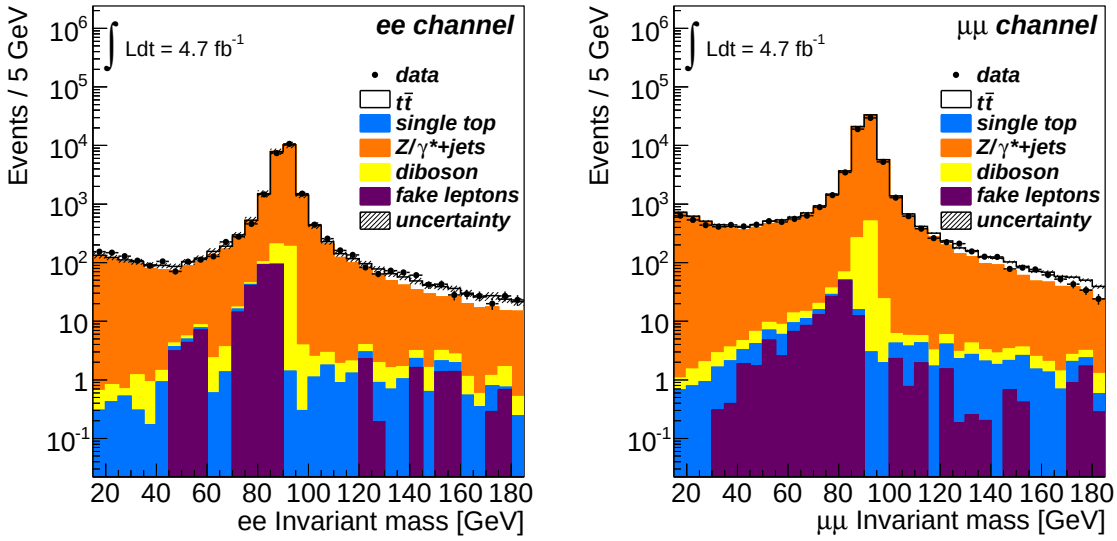

(a) (b)

Figure 6.20: a) Invariant mass of the two electrons, where $E_{\mathrm{T}}^{\mathrm{miss}}$ is required to be less than 60 GeV, in the *ee* channel. b) Invariant mass of the two muons, where $E_{\mathrm{T}}^{\mathrm{miss}}$ is required to be less than 60 GeV, in the $\mu\mu$ channel. Events are required to have at least two jets.

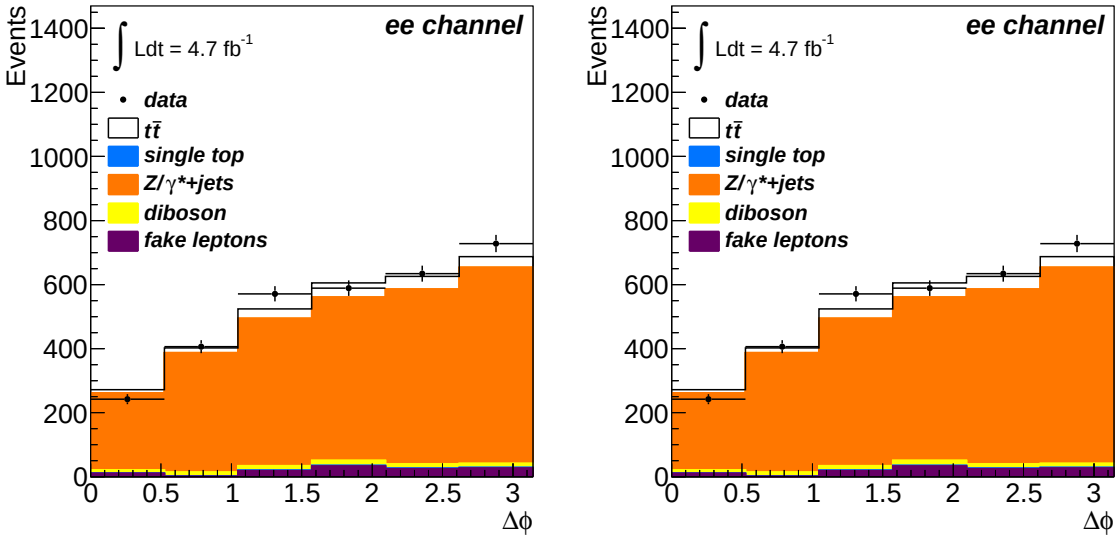

(a) (b)

Figure 6.21: $\Delta\phi$ distribution inside the Z mass window for the *ee* channel. a) shows the distribution obtained with the nominal MC simulation, b) shows the same distribution after applying a data driven scale factor. Events are required to have $E_{\mathrm{T}}^{\mathrm{miss}} > 30$ GeV and at least two jets.

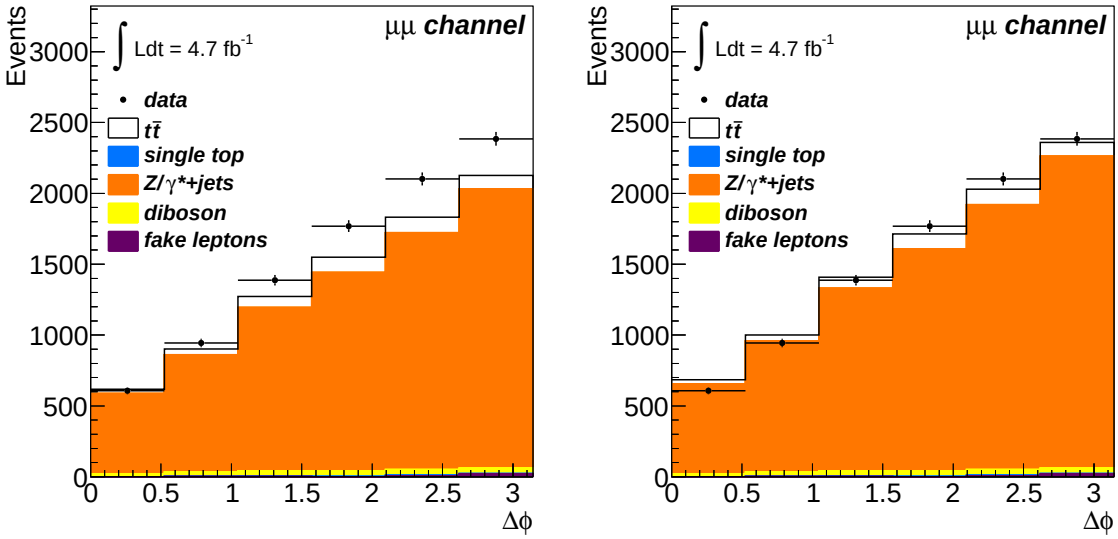

(a) (b)

Figure 6.22: $\Delta\phi$ distribution inside the Z mass window for the $\mu\mu$ channel. a) shows the distribution obtained with the nominal MC simulation, b) shows the same distribution after applying a data driven scale factor. Events are required to have $E_{\mathrm{T}}^{\mathrm{miss}} > 30$ GeV and at least two jets.

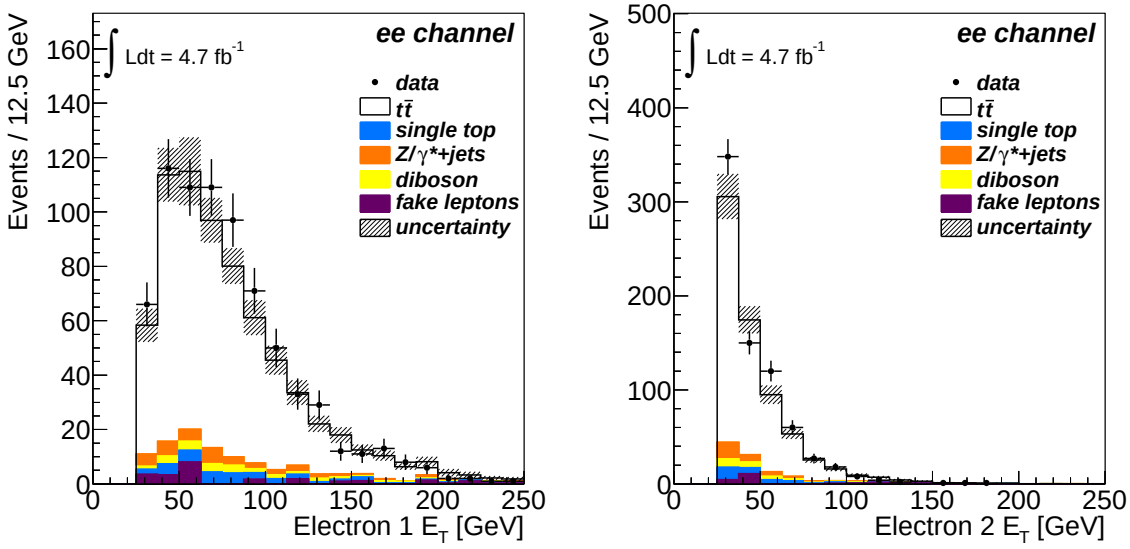

(a) (b)

Figure 6.23: E_{T} of the a) leading, and b) subleading electron for events passing the *ee* channel event selection.

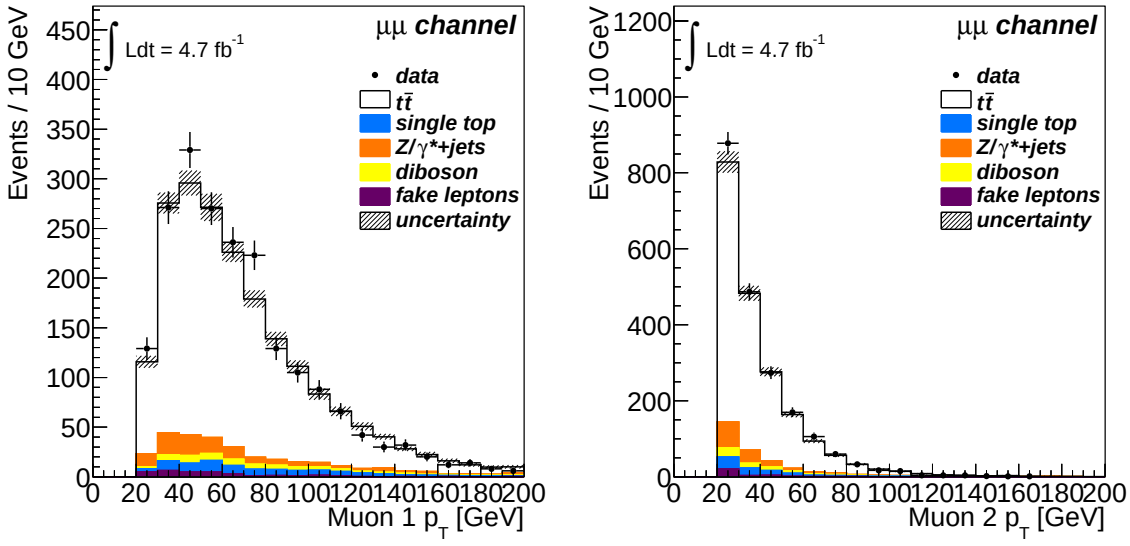

(a) (b)

Figure 6.24: p_{T} of the a) leading, and b) subleading muon for events passing the $\mu\mu$ channel event selection.

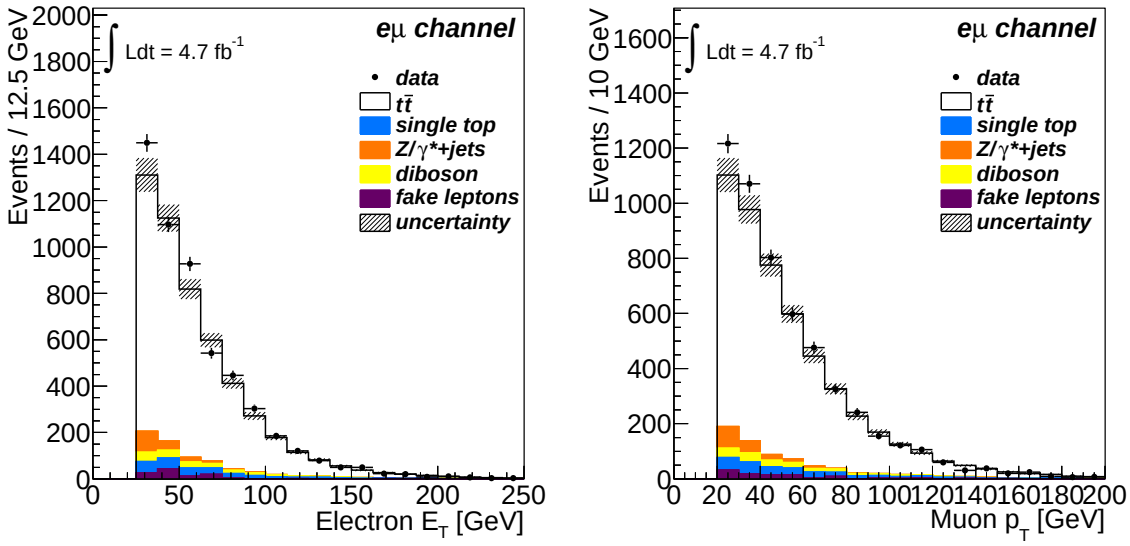

(a) (b)

Figure 6.25: a)E_{T} of the electron, and b) p_{T} of the muon for events passing the $e\mu$ channel event selection.

6.5.2 Lepton+Jet Control and Signal Regions

In the single lepton decay mode, the b–tag requirement is one of the strongest cuts to suppress background contributions. Reversing this cut, requiring exactly zero b–tags, gives a background dominated selection, allowing for a control region to check the background modelling. In this region, the dominant background contributions are from W+jets production and fake leptons. Figures 6.26 and 6.27 show the data are described well by the simulation in this region.

Applying a b–tag in the selection allows a strong suppression of background events; events originating from a $t\bar{t}$ decay will contain two real b-quarks, while the majority of the background sources do not produce hard b-quarks. Before a b–tag requirement is applied, the dominant background sources are from W+jets events, and fake leptons. The MC simulation description of data is shown, for the electron and muon channels respectively, for events with no b–tagging requirement, in figures 6.28 and 6.29. Table 6.5 shows the number of expected events from the different signal and background sources as well as the number of observed events, for events with no b–tag requirement.

After applying a b–tag requirement, the W+jets and fake lepton contributions are significantly reduced, though still remain a dominant background. Notably, the single top background is largely unaffected, due to the presence of a prompt b-quark in the t and s channel production diagrams. The MC simulation description of data is shown for events containing at least one b–tag in figures 6.30 and 6.31.

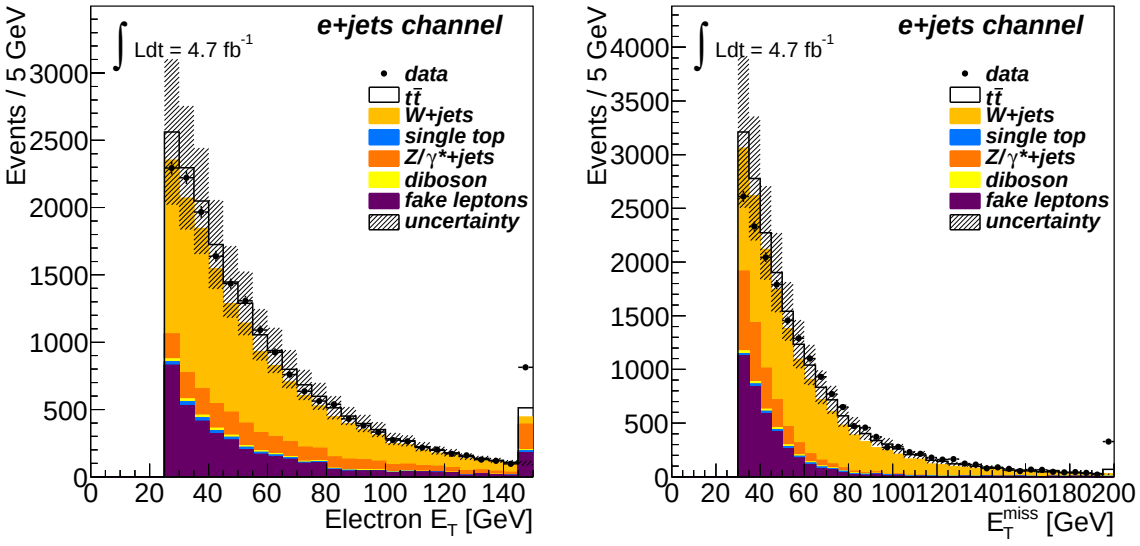

(a) (b)

Figure 6.26: a) E_{T} of the selected electron, requiring exactly zero b-tags. b) $E_{\mathrm{T}}^{\mathrm{miss}}$ distribution of selected events in the e+jet channel, requiring exactly zero b-tags.

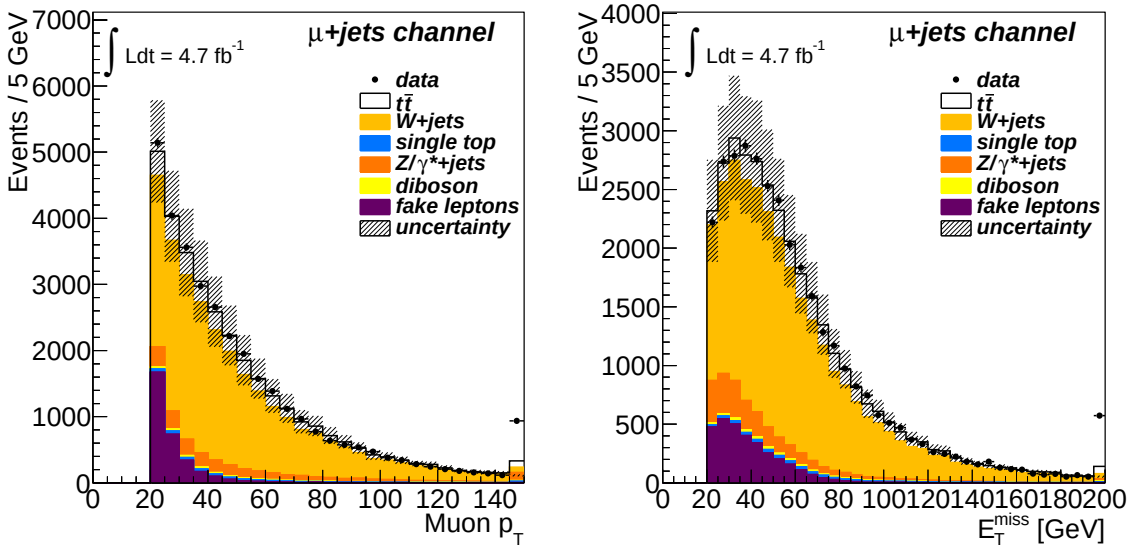

(a) (b)

Figure 6.27: a) p_{T} of the selected muon, requiring exactly zero b-tags. b) $E_{\mathrm{T}}^{\mathrm{miss}}$ distribution of selected events in the μ+jet channel, requiring exactly zero b-tags.

Table 6.6 shows the number of expected events from the different signal and background sources as well as the number of observed events. Worth noting is that the signal to background ratio after applying a b-tag requirement increases almost fourfold.

Channel	e+jets	μ+jets
$t\bar{t}$	18694	30816
W+jets	13225	28316
Z+jets	2894	2929
Diboson	231	377
Single Top	1471	2461
Fake Leptons	5043	5030
Expected	41558	69929
Observed	40875	71521

Table 6.5: Event yields after all event selection criteria, with no b-tag requirement, for the single lepton channel.

Channel	e+jets	μ+jets
$t\bar{t}$	16122	26559
W+jets	2346	4875
Z+jets	447	482
Diboson	47	74
Single Top	1177	1970
Fake Leptons	1071	1846
Expected	21211	35807
Observed	21910	37919

Table 6.6: Event yields after all event selection criteria, including at least one b-tag, for the single lepton channel.

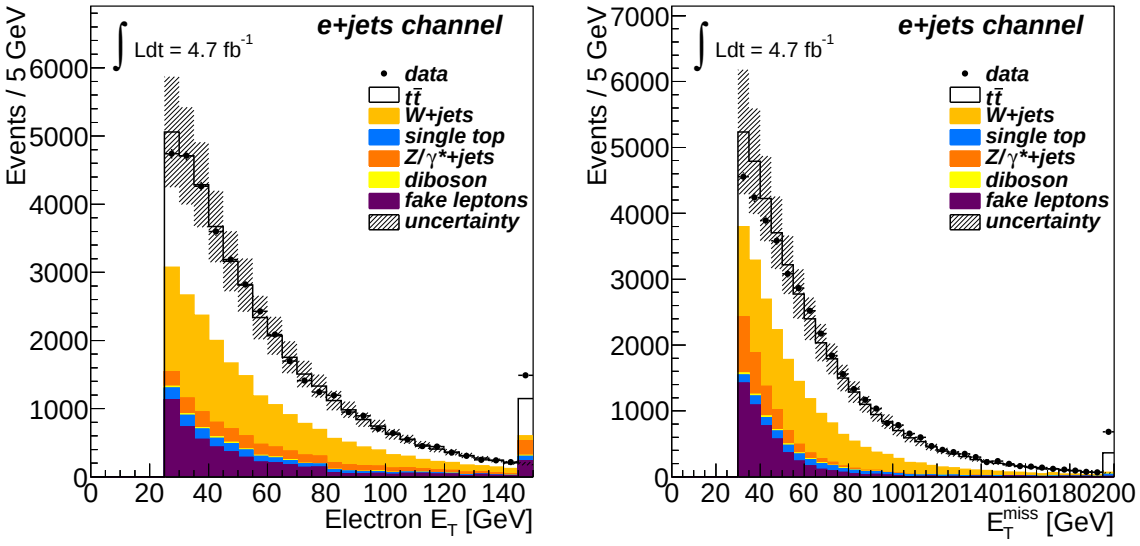

(a) (b)

Figure 6.28: a) E_{T} of the selected electron before b-tagging. b) $E_{\mathrm{T}}^{\mathrm{miss}}$ distribution of selected events before b-tagging.

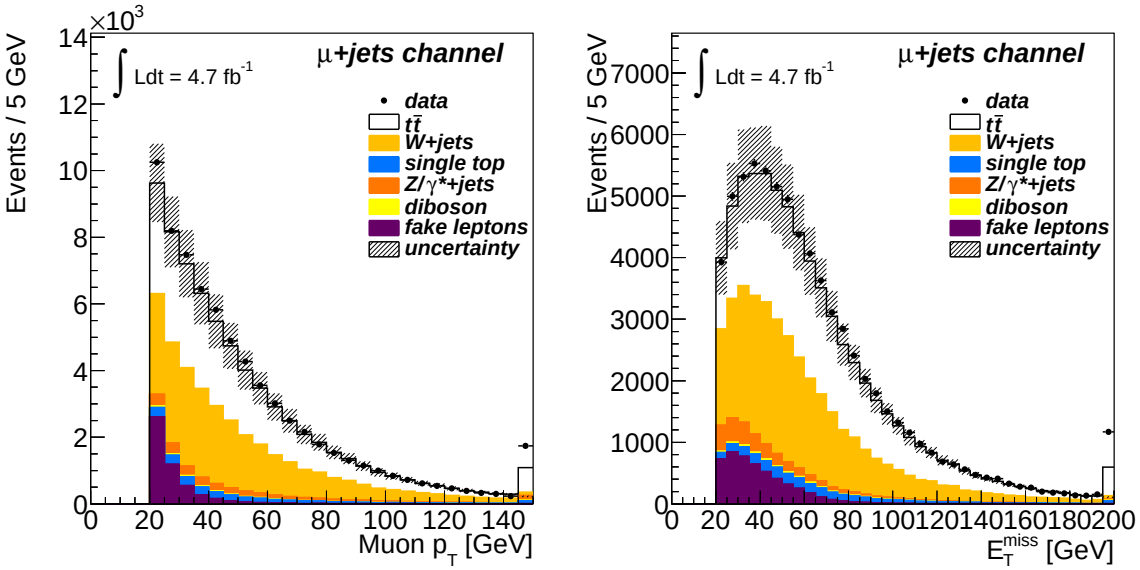

(a) (b)

Figure 6.29: a) p_{T} of the selected muon before b-tagging. b) $E_{\mathrm{T}}^{\mathrm{miss}}$ distribution of selected events before b-tagging.

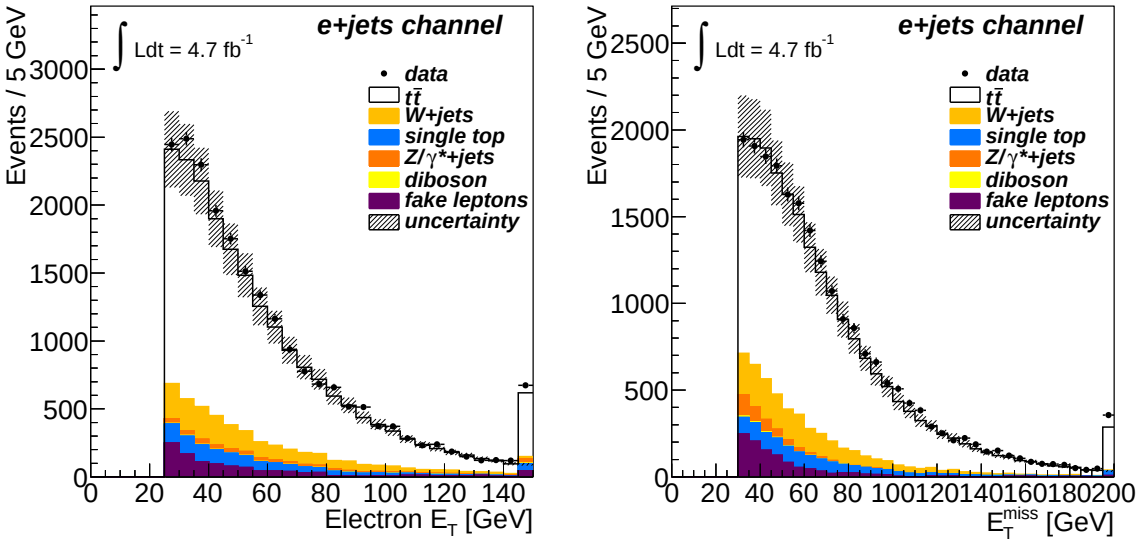

(a) (b)

Figure 6.30: a) E_{T} of the selected electron after b-tagging. b) $E_{\mathrm{T}}^{\mathrm{miss}}$ distribution of selected events after b-tagging.

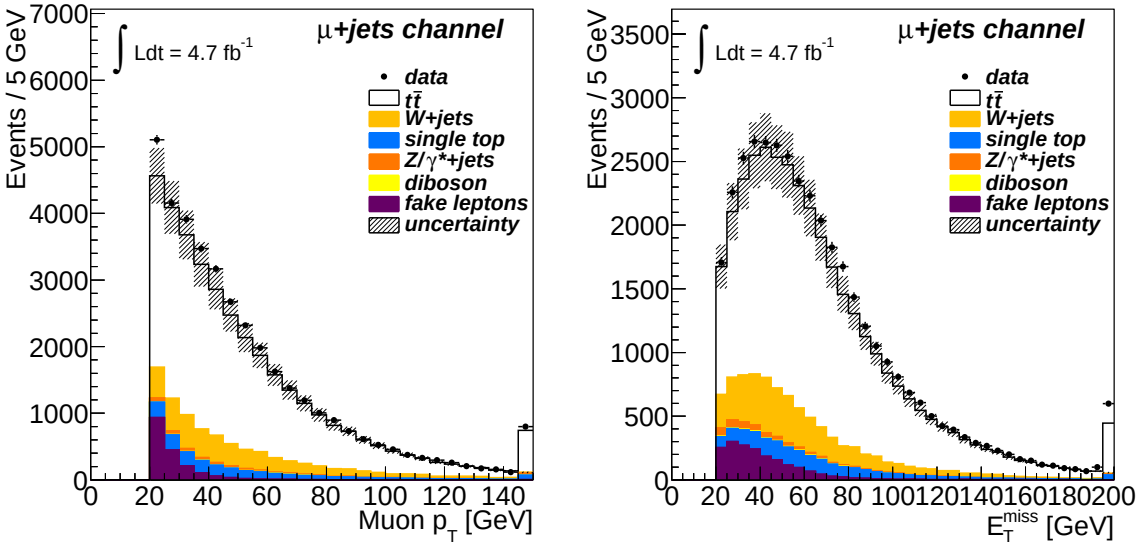

(a) (b)

Figure 6.31: a) p_{T} of the selected muon after b-tagging. b) $E_{\mathrm{T}}^{\mathrm{miss}}$ distribution of selected events after b-tagging.

6.6 Reconstructing the $t\bar{t}$ system in the single lepton channel

In order to construct $\Delta\phi$ in the single lepton channel, the lepton is chosen as the strongest analysing particle, with the second strongest analyser being the down-type quark. Experimentally it is impossible to distinguish a jet produced by a down-type quark or an up-type quark, though it is possible to enhance the selection of the jet originating from the down-type quark through simple kinematic requirements. To do this, reconstruction of at least the hadronic top quark is required.

6.6.1 The $p_{\mathrm{T}}^{\mathrm{max}}$ Method

The hadronic top quark is reconstructed with a simple cut based method. Each combination of three jets in the event is grouped to make a top quark *candidate* and the p_{T} of this candidate is calculated. The candidate with the highest p_{T} is taken as the reconstructed hadronic top quark. Within the reconstructed top quark, the three possible pairings of jets are reconstructed as W boson candidates. If a jet within the W boson candidate is tagged as a b-jet, then the candidate is discarded. If no more candidates remain after the b-jet veto, the event is considered misreconstructed and discarded. If multiple candidates remain after the b-jet veto, the candidate with invariant mass closest to the true W boson mass ($m_W = 80.4$ GeV) is taken as the best reconstructed W boson.

Figure 6.32 shows the reconstructed η distribution after constructing the hadronic top with the $p_{\mathrm{T}}^{\mathrm{max}}$ method.

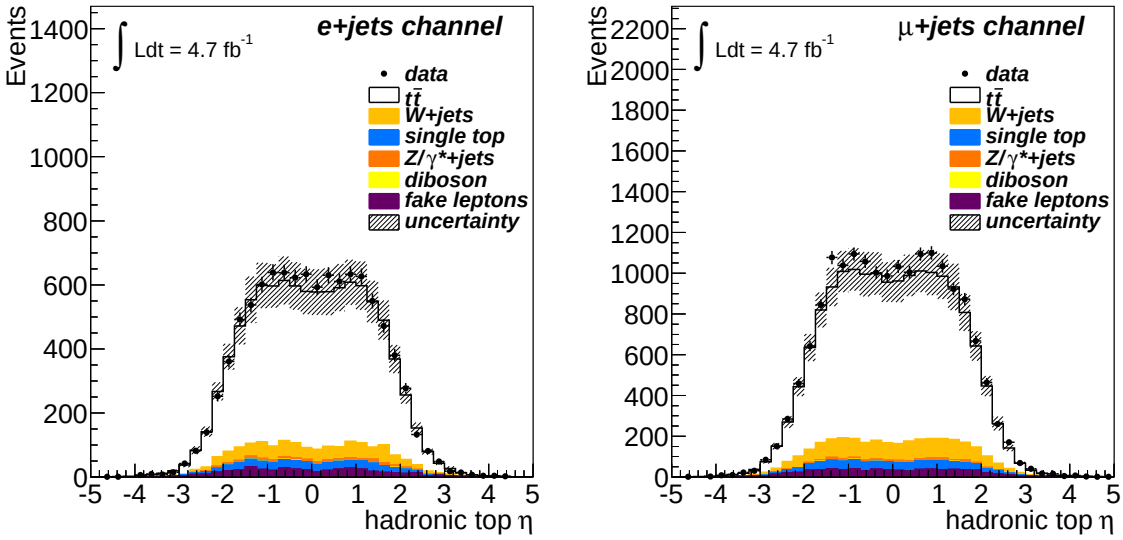

(a) (b)

Figure 6.32: a) Reconstructed η for the hadronically decaying top quark, reconstructed with the $p_{\mathrm{T}}^{\mathrm{max}}$ method in the e+jets channel. b) Reconstructed η for the hadronically decaying top quark, reconstructed with the $p_{\mathrm{T}}^{\mathrm{max}}$ method in the μ+jets channel.

Selecting the down-type quark

For this analysis, it is important to be able to reconstruct the jet from the down-type quark originating from the W boson decay, and distinguish this from the up-type quark from the same decay (and any other jets produced in the event). While up-type quarks and down-type quarks are largely indistinguishable, the fact that the top decays weakly provides a unique opportunity to differentiate between the two. The weak interaction is $V - A$, so only couples to left handed fermions and right handed antifermions. In the top decay, this can be interpreted such that the down-type quark is analogous to the charged lepton, and the up-type quark to the neutrino, and the same spin arguments can be applied. The W decay will tend to emit the down-type quark anti-parallel to its direction of flight in the top rest frame, making it spatially closest to the b-quark from the top decay. This suggests that the down-type quark has, on average, a lower energy than the up-type quark, in the rest frame of the parent top quark.

A study at parton level, in the fiducial range of the single lepton event selection, shows that this difference allows the down-type quark to be selected around 56% of the time over the up-type quark.

Improvements to reconstruction

The $p_{\mathrm{T}}^{\mathrm{max}}$ method can be improved by applying simple invariant mass requirements to the top and W candidates. The reconstructed top quark candidate must satisfy the condition $|m_{\mathrm{top}}^{\mathrm{candidate}} - m_{\mathrm{top}}| <$ XX GeV. If the highest p_{T} candidate does not satisfy this condition, the next highest p_{T} candidate is considered until a successful candidate is chosen. If no successful candidate is found, the event is tagged as *misreconstructed* and discarded.

A similar requirement can be applied to the W-boson candidate, which must satisfy $|m_{\mathrm{W}}^{\mathrm{candidate}} - m_W| <$ YY GeV. If no candidate satisfies this requirement, then the event is tagged as misreconstructed and discarded.

A plot showing reconstruction efficiency as a function of top mass window, XX, and W mass window, YY, is shown in Figure 6.33. In this plot, each bin represents a specific configuration of mass windows. For example, the bin where $XX = 45$ GeV and $YY = 25$ GeV shows the purity of selected down quarks for events where $|m_{\mathrm{top}}^{\mathrm{candidate}} - m_{\mathrm{top}}| < 45$ GeV and $|m_{\mathrm{W}}^{\mathrm{candidate}} - m_W| < 25$ GeV.

A tighter window around both the candidate $W-$boson and top quarks tends to give a higher purity of selected down-type quarks, though this suffers from loss in statistics.

Without these additional constraints, the $p_{\mathrm{T}}^{\mathrm{max}}$ method correctly selects the true down-type quark in simulated $t\bar{t}$ events 32.0% of the time. After requiring, for example, $|m_{\mathrm{top}}^{\mathrm{candidate}} - m_{\mathrm{top}}| < 25$ GeV and $|m_{\mathrm{W}}^{\mathrm{candidate}} - m_W| < 25$ GeV, the down-quark is correctly selected 39.5% of the time, at the sacrifice of statistics, as shown

in figure 6.33.

If a simple selection of one of the four highest p_{T} jets were to be selected as the down-quark candidate, the down-quark purity is 15.8%, 18.0%, 22.7% and 23.5% for the first, second, third and fourth jet respectively, measured in a counting experiment with a NLO simulation. The down quark is observed to appear most frequently in the leading 5 jets, as expected for $t\bar{t}$ pair events simulated with a non multi-leg NLO generator, such as MC@NLO.

The increase of purity at the loss of statistics suggests an optimal window configuration may exist, such that the expected uncertainty of the result is minimised. An optimisation of this reconstruction method is discussed in section 7.3.

6.7 Summary

The event selection for the dilepton and semilepton channels discussed in this chapter provides a strong suppression of background processes, allowing preferentially $t\bar{t}$ events to be selected. This allows a fairly clean sample of events with which to perform the analysis. The dilepton channel benefits from not requiring any reconstruction of the $t\bar{t}$ system, while this is not possible for the semilepton channel due to the ambiguity in finding the jets resulting from the quarks from a hadronic top decay. However, the reconstruction performs well at selecting the down-type quark, over the up-type quark — also from the W boson decay — and the other jets produced in the event.

The next chapter uses the event selection and reconstruction described here in order to perform a measurement of the spin correlation in the $t\bar{t}$ system in events at $\sqrt{s} = 7$ TeV, with 4.7fb^{-1} of 2011 data recorded at ATLAS.

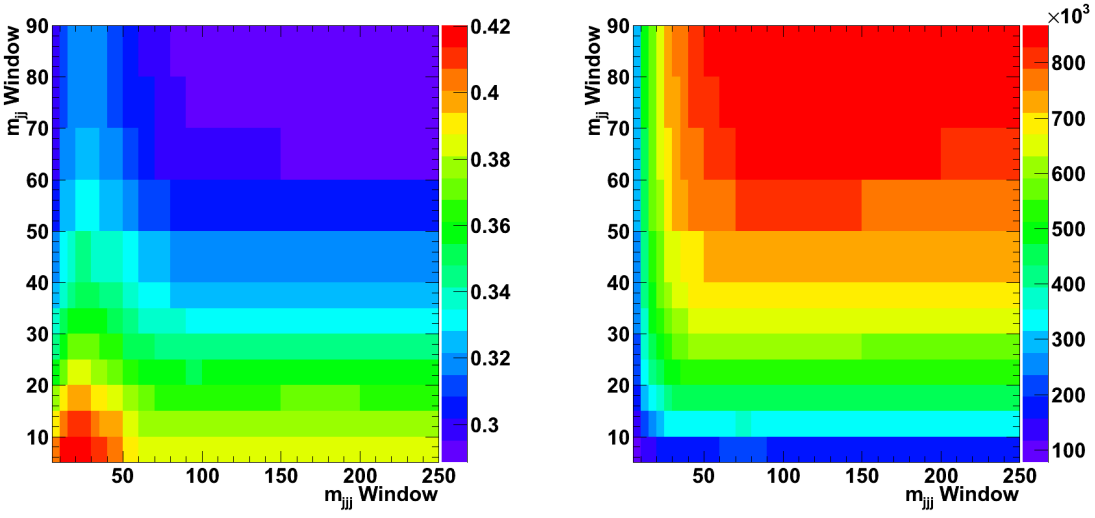

(a) (b)

Figure 6.33: a) Efficiency of correctly selecting a down quark from all reconstructed events. b) Total number of reconstructed events.

Chapter 7

Measuring Spin Correlation in $t\bar{t}$ events

Chapter 6 outlines the MC simulation, event selection and reconstruction used for the purposes of constructing the $\Delta\phi$ distribution, which is sensitive to the presence of spin correlation. This chapter outlines the process used in order the measure the degree of spin correlation using this distribution. The data used for this measurement corresponds to the full 2011 recorded dataset of 4.7 fb^{-1}, at a centre of mass energy of 7 TeV.

7.1 Delta Phi

After event selection the difference in azimuthal angle, $\Delta\phi$, is calculated between the two charged leptons in the dileptonic channel, or the charged lepton and the reconstructed down-type quark candidate in the semileptonic channel. $\Delta\phi$ is defined as the smallest azimuthal angle difference, which implies $0 \leq \Delta\phi \leq \pi$. This quantity is calculated for each source of background and the two signal models (Standard Model, and without spin correlation), as well as for data.

Figure 7.1 shows the reconstructed $\Delta\phi$ for the dileptonic channels, and figure 7.2

for the semileptonic channels.

7.2 Fitting Procedure

In order to extract the spin correlation information from the $\Delta\phi$ distribution, a template fitting method is employed. Two signal MC models are considered: A model with the degree of spin correlation corresponding to the Standard Model prediction, and a model which does not consider spin correlation. These two models are described in the previous chapter.

Templates are constructed from both signal models, as well as the background expectation. A fit with two free parameters is then performed. The first parameter is the 'fraction of Standard Model', or f_{SM}*. In the case of the Standard Model template, this has a value of $f_{\mathrm{SM}} = 1$. For the model without spin correlation, $f_{\mathrm{SM}} = 0$. In the helicity basis, $f_{\mathrm{SM}} = 1$ corresponds to the Standard Model expectation of $A = 0.31$. The spin correlation parameter is assumed to be a linear mix of the two models. The value of f_{SM} is allowed to float above 1 and below 0, but care must be taken when measuring close to the boundary of $A = \pm 1$ (in the helicity basis, this corresponds to a measured value of $f_{\mathrm{SM}} \sim 3.2$. Section 7.5 discusses how to treat cases where the measurement is close to the boundary. The second parameter is the $t\bar{t}$ cross section, introduced as a normalisation parameter on the MC simulation.

In the case where a measurement would observe $f_{\mathrm{SM}} > 1$, the physical meaning is simply that there are more like spin top quark pairs produced than expected in the Standard Model.

* f_{SM} is used in place of A due to the $\Delta\phi$ distribution not being associated with any given basis

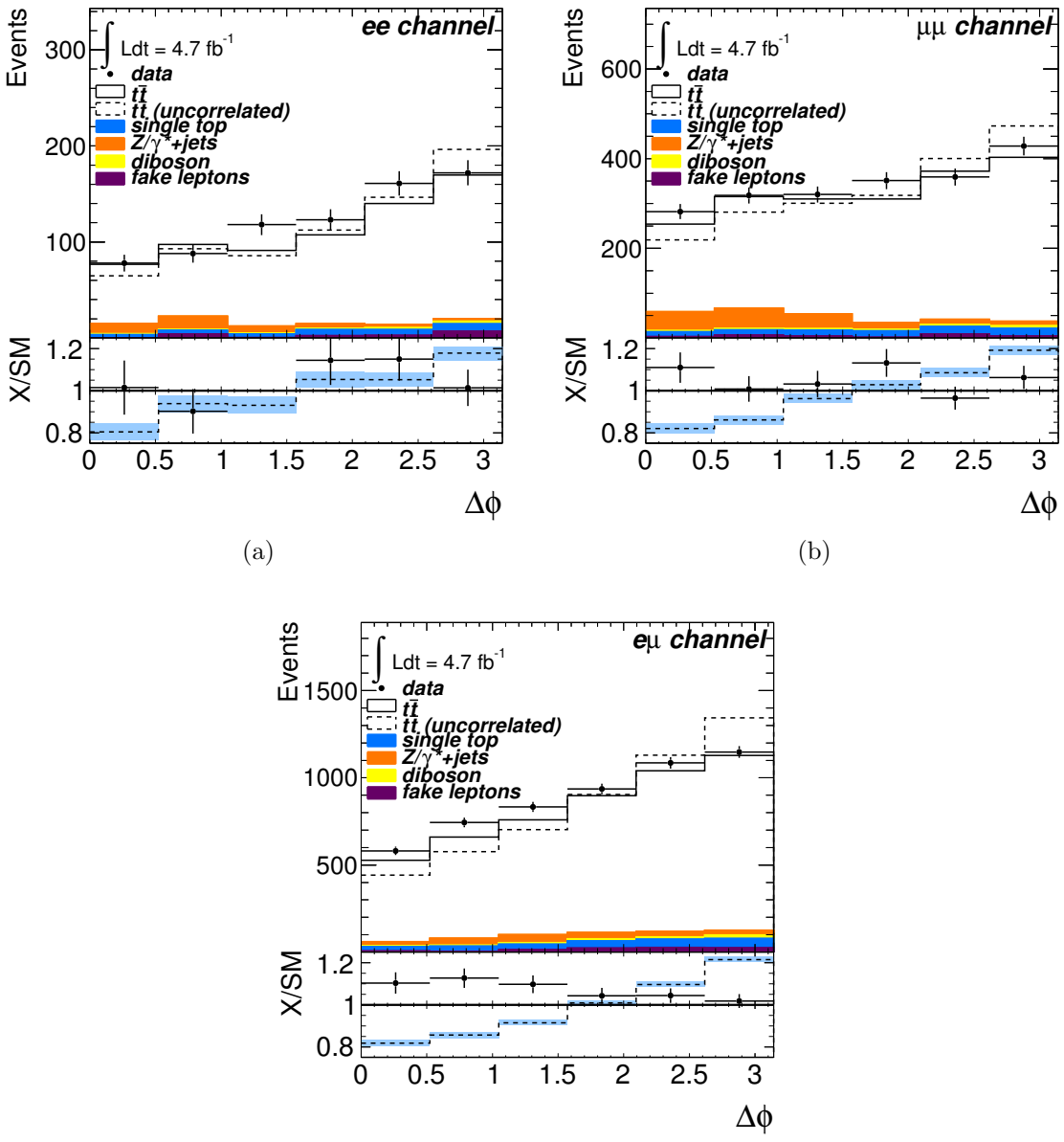

(a)

(b)

(c)

Figure 7.1: Distribution of $\Delta\phi$ for events in the a) ee, b) $\mu\mu$ and c) $e\mu$ channel. The solid line represents Standard Model spin correlation and the dashed line represents a model with no spin correlation. The ratio of the two samples is shown as the dashed line in the lower portion of the plot, with the uncertainty on the simulation shown as the blue band.

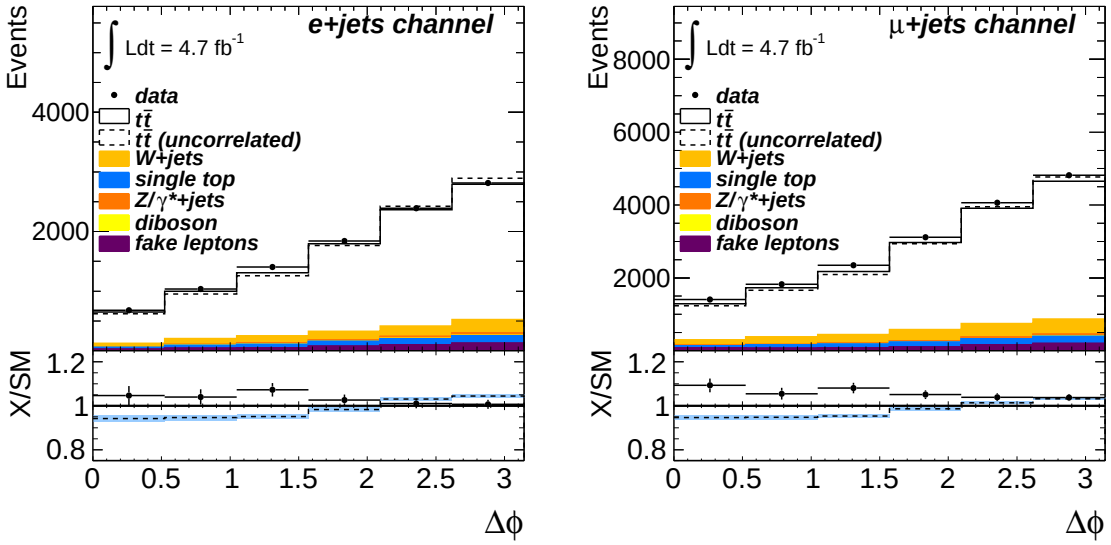

(a) (b)

Figure 7.2: Distribution of $\Delta\phi$ for events in the a) e+jets and b) μ+jets channel. The solid line represents Standard Model spin correlation and the dashed line represents a model with no spin correlation. The ratio of the two samples is shown as the dashed line in the lower portion of the plot, with the uncertainty on the simulation shown as the blue band. Note: these plots are produced using the optimised reconstruction described in section 7.3.

The fit uses a binned maximum likelihood function, which is defined as

$$\mathcal{L} = \prod_{i=1}^{B} \mathbf{P}(n_i; x_i), \tag{7.1}$$

where $\mathbf{P}(n_i; \alpha)$ is the Poisson probability of observing n events in bin i, given a model α — which generates x_i events in bin i — and B is the number of bins.

The Poisson distribution is defined as

$$\mathbf{P}(n_i; x_i) = \frac{e^{-x_i} x_i^{n_i}}{n_i!}, \tag{7.2}$$

with

$$x_i = \frac{\sigma_{fit}}{\sigma_{t\bar{t}}}(N_i^{\mathrm{SM}} f_{\mathrm{SM}} + N_i^{\mathrm{UC}}(1 - f_{\mathrm{SM}})) + N^{\mathrm{BG}}, \tag{7.3}$$

where σ_{fit} is the fitted $t\bar{t}$ cross section, N_i^{SM} is the number of expected events from the Standard Model template in bin i, N_i^{UC} is the number of expected events from the 'uncorrelated' template in bin i, N_i^{BG} is the number of expected background events in bin i, and f_{SM} is the 'fraction of Standard Model', as explained earlier.

Figures 7.3 and 7.4 shows example log likelihood distributions obtained from the fit for each channel, performed on pseudo-data. The likelihood value for each point is transformed as $-2\ln(\mathcal{L}) + C$, where C is a constant used to shift the minimum of the distribution to 1. The maximum likelihood (or the minimum in the plot) corresponds to the best fit value for f_{SM} and $\sigma_{t\bar{t}}$, with an uncertainty given by the ellipse where $-2\ln(\mathcal{L}) + C = 2$. It is clearly evident that the $e\mu$ channel performs best, due to the large separation between the two signal models, and high statistics, in comparison to the small separation in both semilepton channels, or the low statistics in the ee and $\mu\mu$ channels.

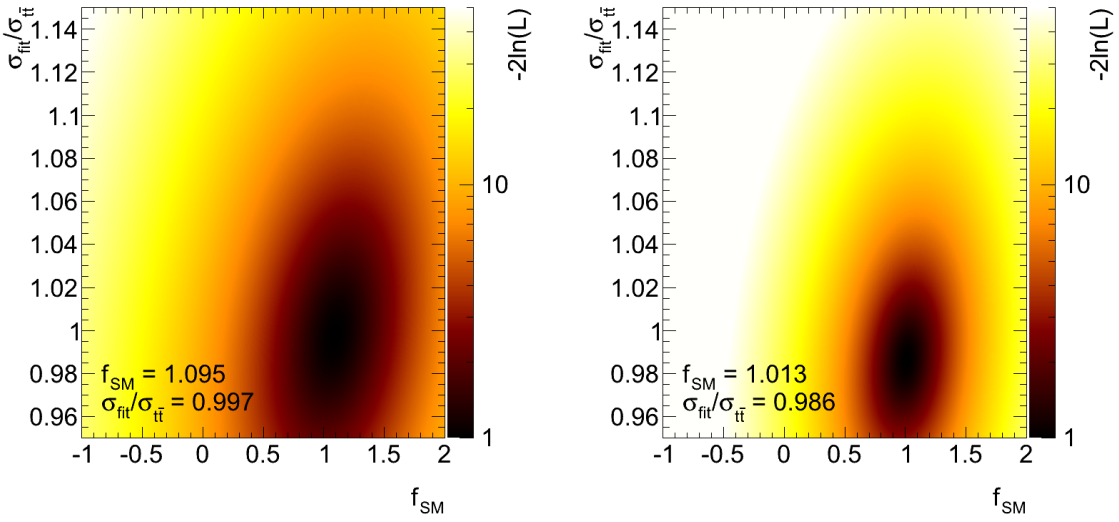

(a)

(b)

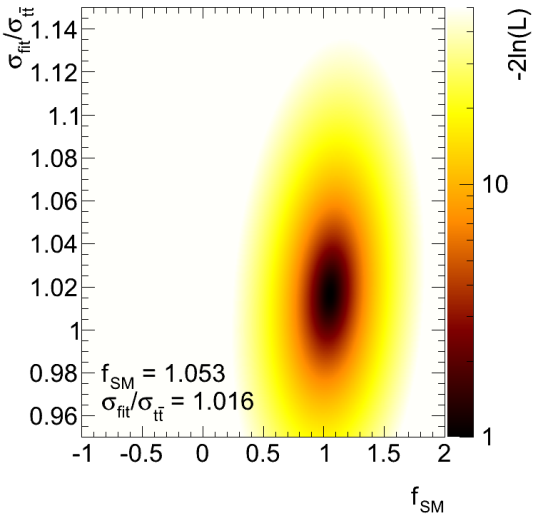

(c)

Figure 7.3: Log Likelihood distribution for a pseudo-experiment in a) the *ee* channel, b) the $\mu\mu$ channel, and c) the $e\mu$ channel. The minimum point of the distribution is shifted to unity.

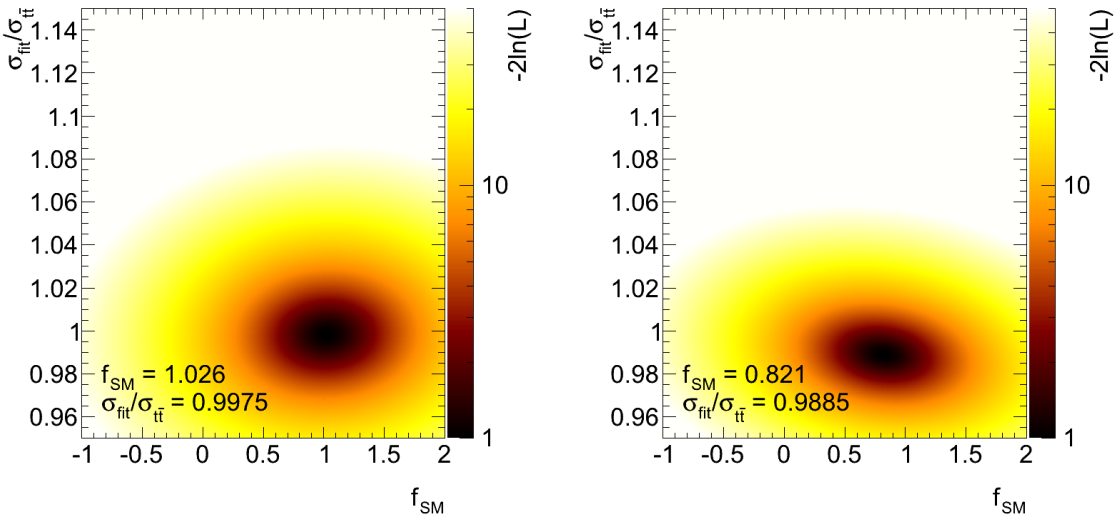

(a) (b)

Figure 7.4: Log Likelihood distribution for a pseudo-experiment in a) the e+jet channel and b) the μ+jet channel. The minimum point of the distribution is shifted to unity.

7.2.1 Pseudo-experiments

In order to deterimine expected statistical and systematic uncertainties, pseudo-experiments are used. For each bin in the $\Delta\phi$ distribution, pseudo-data are generated by selecting a random number in the Poisson distribution for expected number of signal events, plus another random number from the Poisson distribution for the expected number of background events.

Each bin then contains

$$N_{pseudo-data} = N_{sig}^{rand} + N_{bkg}^{rand}. \tag{7.4}$$

The generated pseudo-data are then fitted using the likelihood function defined in equations 7.1, 7.2 and 7.3, where $N_{pseudo-data}$ becomes n_i in 7.2.

Figure 7.5 shows an example distribution of f_{SM} obtained from 20,000 pseudo-

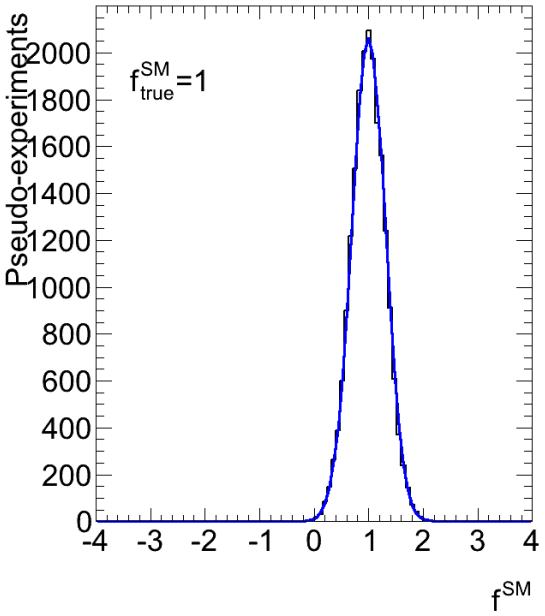

Figure 7.5: Distribution of measured f_{SM} for 20,000 pseudo-experiments. The width of the distribution provides an estimate for the statistical uncertainty obtained from fitting to data.

experiments in the e+jet channel. The Standard Model $t\bar{t}$ template, where $f_{\mathrm{SM}} = 1$ was used to generate the pseudo-data for this distribution. The result of the pseudo-experiments is fitted with a Gaussian, where the width corresponds to the expected statistical uncertainty obtained by fitting the data. The mean is around $f_{\mathrm{SM}} = 1$, which is consistent with the input value.

In order to check the performance and linearity of the fit, several input distributions are created, corresponding to several values of f_{SM}, with 20,000 pseudo-experiments generated for each distribution. To generate the f_{SM} distributions, the two model templates are used. The number of events in each bin is defined as

$$N_{mix} = f_{\mathrm{SM}} N_{\mathrm{SM}} + (1 - f_{\mathrm{SM}}) N_{\mathrm{UC}}, \tag{7.5}$$

where N_{SM} and N_{UC} are the number of events in the Standard Model and 'uncorrelated' templates. The background is unaffected by the presence of spin correlations in $t\bar{t}$, so the same background template is used for each input distribution.

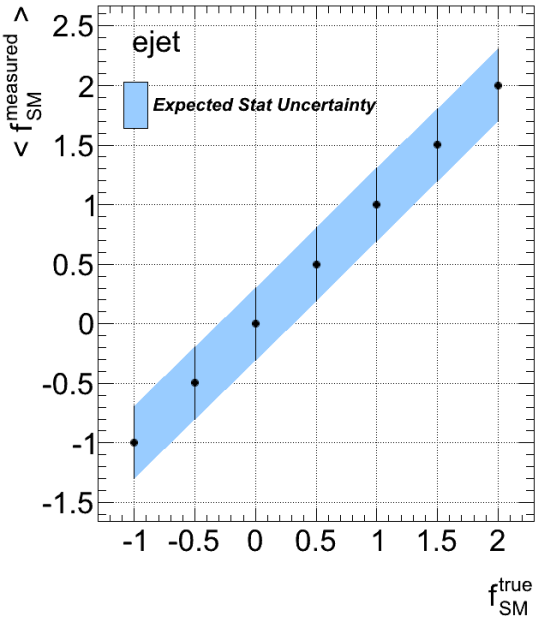

Figure 7.6: Distribution of measured f_{SM} for 20,000 pseudo-experiments and seven input values of f_{SM} between -1 and 2.

The generated pseudo-data for each value of f_{SM} are then fitted following equations 7.1, 7.2 and 7.3. Figure 7.6 shows the mean measured value for seven input values of f_{SM}, between -1 and 2, along with the corresponding expected statistical uncertainty, in the e+jet channel. The linearity and consistency in the expected statistical uncertainty is a good indicator that the fit performs well over the tested range.

7.3 Optimising the lepton+jets reconstruction

In order to determine the optimal size of the mass windows for each reconstructed object, the width of the gaussian generated by fitting several pseudo-experiments is used to estimate the statistical uncertainty on the measurement. This estimated uncertainty is then minimised to find the optimal reconstruction configuration. For each combination of mass windows (as seen in figure 6.33), 20,000 pseudo-experiments are performed, and the width of the gaussian distribution of measured

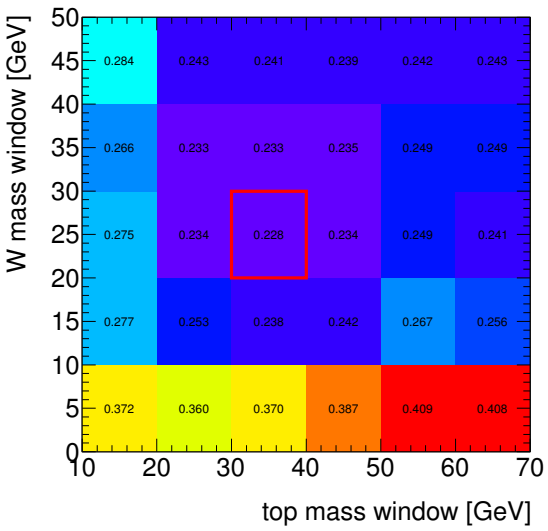

Figure 7.7: Expected statistical uncertainty when fitting pseudo-data to Monte Carlo templates of the distribution of $\Delta\phi$ for Standard Model and Uncorrelated scenarios. The sensitivity was estimated for various permutations of the reconstructed object mass window requirements. The optimal set of mass windows are 35 GeV around the reconstructed top and 25 GeV around the reconstructed W.

f_{SM} for each set of pseudo-data is recorded.

After performing this optimisation, it is determined that having a window around the top mass of 35 GeV and a window around the W boson mass of 25 GeV results in the smallest expected statistical uncertainty (± 0.228), based on only signal events. This corresponds to a down-quark purity of 39.0%. This is illustrated in Figure 7.7.

The number of events passing the optimised reconstruction is shown in table 7.1. While around half of the data is removed after performing the reconstruction, the down quark purity is increased, allowing for a more sensitive measurement to be made.

channel	e+jets	μ+jets
$t\bar{t}$	8063	13386
W+jets	823	1708
Z+jets	151	172
diboson	17	28
single top	431	735
fake leptons	422	689
exp	9908	16718
data	10162	17579

Table 7.1: Event yields after reconstruction with p_{T}-max, implementing the optimised mass windows.

7.3.1 Reconstructed Delta Phi versus Truth

As it is not expected that the down-type quark is reconstructed correctly for every semileptonic event, the true $\Delta\phi$ distribution in the lepton + jets channel will be diluted somewhat, resulting in a reduced separation between the two spin correlation models, or a change in the shape of the distribution with respect to the expectation. To check if this has a significant effect on the reconstruction of the $\Delta\phi$ variable, the reconstructed $\Delta\phi$ for each event is plotted against the true $\Delta\phi$. Figure 7.8 shows this distribution for both Standard Model and Uncorrelated MC simulation samples. There is a strong correlation between truth and reconstructed $\Delta\phi$, suggesting that the loss of down-quarks does not have a strong shape changing impact on the variable, though only around $35 - 45\%$ of the reconstructed events give the $\Delta\phi$ value measured at parton level, suggesting the separation between the two models will be reduced somewhat.

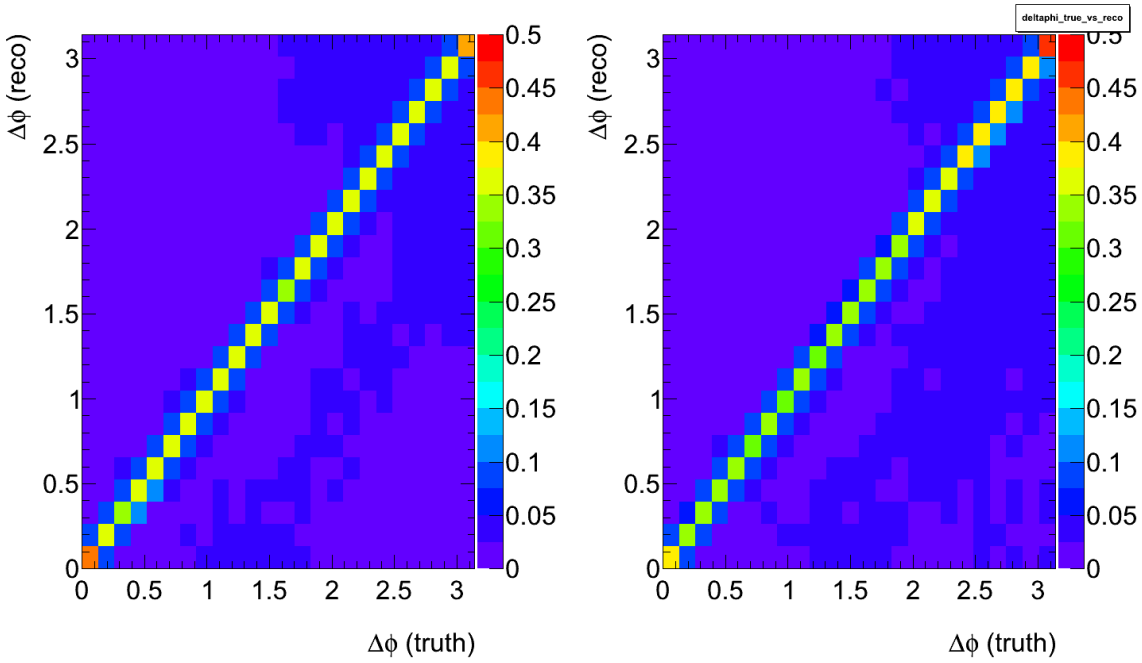

Figure 7.8: Distribution of $\Delta\phi$ at parton level, for semileptonic events, against the fully reconstructed value of $\Delta\phi$ for a) Standard Model Monte Carlo, b) Uncorrelated Monte Carlo.

7.4 Systematic Uncertainties, Corrections and Calibrations

A major source of uncertainty in the measurement comes from systematic effects, such as jet energy calibration and MC generator tuning. Each calibration or simulation model has an associated uncertainty, the effect of which is estimated for each source of uncertainty. This section describes the sources of the systematic uncertainties considered in this analysis.

In order to estimate the size of a systematic uncertainty, the parameter under consideration (for example the parton shower model) is varied in the analysis, and the full analysis chain repeated. The two signal templates and the background template used to perform the fitting procedure are left unchanged. The systematically shifted $\Delta\phi$ distribution is then fitted to the unchanged templates for 20,000 pseudo-experiments, and the mean result noted. Subtracting the mean result from the systematically shifted analysis from the unchanged analysis provides an estimate of the systematic effect. Some estimations of systematic uncertainty differ from this and are described in the text where necessary.

Figure 7.9 shows an illustrative example of evaluating a systematic uncertainty, in this case for evaluating the uncertainty due to parton shower modelling. The black line shows the $\Delta\phi$ distribution using the PYTHIA parton shower model, while the red line shows the same using HERWIG. Each model is then used to generate pseudo-data, which is fitted to the spin correlation templates. The resulting gaussian distributions are shifted relative to each other and the difference in mean is taken as the systematic uncertainty.

Table A.1 shows a complete summary of the systematic uncertainties considered in this analysis. Each uncertainty considered is described in the following sections.

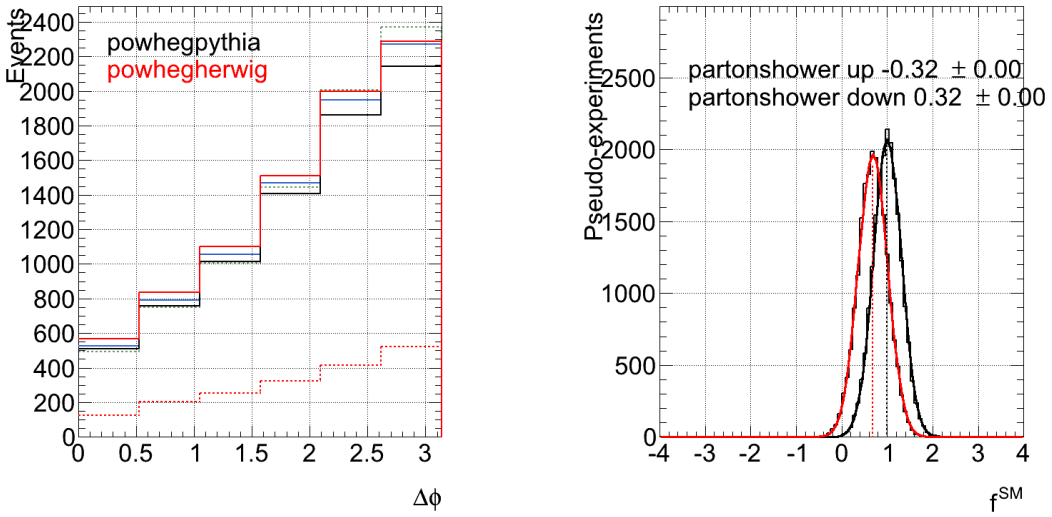

(a) (b)

Figure 7.9: An example illustrating how a systematic uncertainty is evaluated. a) shows the $\Delta\phi$ distribution for the two systematic samples in red and black, with the templates shown in blue (Standard Model) and dashed green (zero spin correlation). The background is shown as the dashed red histogram. b) shows the results for fitting each systematic difference for 20,000 pseudo-experiments. The difference between the two means is taken as the systematic uncertainty.

Generator	A_{helicity}
NLO calculation	0.309 [17]
MC@NLO (Standard Model)	0.301 ± 0.003
POWHEG+Herwig (Standard Model)	0.243 ± 0.003
POWHEG-BOX (Standard Model)	0.282 ± 0.003
MC@NLO+Herwig (Uncorrelated)	-0.003 ± 0.004
POWHEG-BOX+Herwig (Uncorrelated)	0.001 ± 0.003

Table 7.2: Directly observed values for the spin correlation parameter, A, for both Standard Model and 'uncorrelated' MC simulation, comparing MC@NLO to POWHEG. POWHEG+Herwig (Standard Model) is the version generated for ATLAS.

7.4.1 Monte Carlo Generator Uncertainty

The uncertainty due to modelling of the MC simulation is generally considered as a difference between two MC generators. The most common way to evaluate this uncertainty within ATLAS is as the difference observed when switching from MC@NLO to POWHEG. However, a bug present in POWHEG affecting only the spin correlation was found, which makes this comparison an unreliable method of estimating the systematic uncertainty.

Figure 7.10 shows a comparison of $\cos\theta_1 \cos\theta_2$ in the helicity basis, at parton level, between MC@NLO and POWHEG, for both Standard Model and 'uncorrelated' cases. The version of POWHEG used for the ATLAS MC simulation production is known to have a bug affecting some NLO diagrams with relation to spin correlation; the qg and $g\bar{q}$ production diagrams did not include the $t\bar{t}$ spin correlation. A later version with a fix addressing this bug (denoted POWHEG-BOX) was also investigated, with a simulation of only the hard scatter. The measured value of A_{helicity} is improved but still shows a significant departure from the MC@NLO simulation. The value of A_{helicity} measured in MC@NLO is consistent with the NLO prediction. The directly observed values of the spin correlation parameter, A, in the helicity basis for all five samples are shown in table 7.2.

The POWHEG generated sample shows large a deviation from the Standard Model

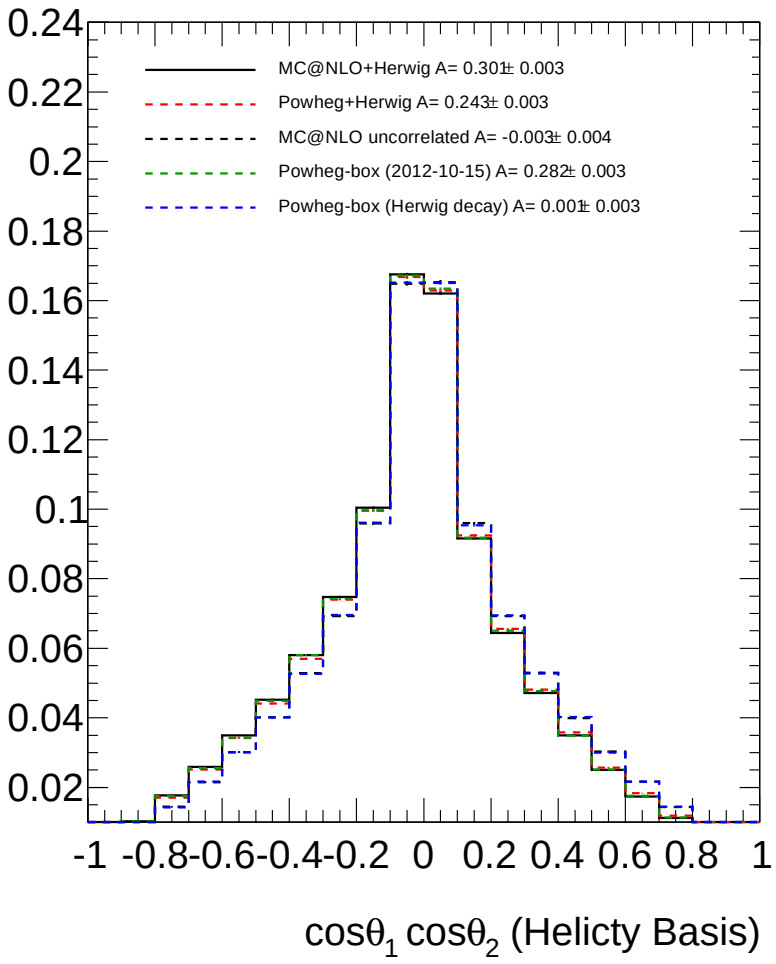

Figure 7.10: Parton level distribution of $\cos\theta_1 \cos\theta_2$ for the dilepton channel, comparing MC@NLO and POWHEG for both Standard Model spin correlation and zero spin correlation models. Two versions of POWHEG are considered, where POWHEG-BOX includes a bug fix addressing the spin correlation. Both versions differ significantly from the MC@NLO version.

value, where the MC@NLO sample shows consistency with the Standard Model prediction of $A = 0.309$. This difference at parton level suggests that evaluating the difference between MC@NLO and POWHEG in order to estimate the uncertainty introduced by the MC simulation will lead to an overestimation.

Instead, to estimate the uncertainty on the MC generator, the factorisation and renormalisation scales in MC@NLO are varied. Renormalisation is a procedure used to ensure processes are calculable at a given order. For example, at NLO, a process may include several loops, some of which diverge in the calculation. Renormalisation absorbs these divergences in order to produce finite results. The factorisation scale separates processes calculable with perturbation theory from those calculated in the PDF. The choice of scales directly affects the matrix element calculation for NLO generators [93].

In order to estimate the uncertainty on the hard scatter calculation, these scales are varied by a factor of two up and down, and the difference between the two evaluated as an envelope. The observed full difference between the mean value of the fit parameter f_{SM}, as measured from both samples is halved and used as an up/down uncertainty. This uncertainty only affects the $t\bar{t}$ signal MC simulation.

7.4.2 Parton Shower Model

To evaluate the uncertainty due to the parton shower generator, two samples with identical Matrix Element generation but with different parton shower models (using HERWIG and PYTHIA) are considered. Both samples are generated with POWHEG calculating the hard scatter. Since both samples use POWHEG, the incorrect modelling of the spin correlation is present in both systematic samples and should have a small effect; the only difference between the two samples is the parton shower model used. Both samples are used in place of the $t\bar{t}$ signal in the analysis and the fit performed on 20,000 pseudo-experiments. The measured full

Parameter	MorePS	LessPS
PARP(67)	1.75	0.70
PARP(71)	0.6450	0.2150
PARP(64)	0.6	3.60
PARJ(82)	0.5	1.66

Table 7.3: Variation of the PYTHIA parameters used for the estimation of ISR/FSR uncertainties.

difference of f_{SM} between these two samples is taken as the systematic uncertainty. This uncertainty only affects the $t\bar{t}$ signal MC simulation.

7.4.3 ISR/FSR Model

In order to estimate the uncertainty due to modelling of the ISR/FSR, samples are generated (with nomenclature 'MorePS' and 'LessPS') identical but for the ISR/FSR parameters in the parton shower. The PYTHIA parameters controlling ISR and FSR in the generator, PARP(67), PARP(71), PARP(64) and PARJ(82), are varied as shown in table 7.3. PARP(67) and PARP(71) are multiplicative factors to the Q^2 hard scattering scale in initial and final state radition, affecting space-like and time-like showers respectively. PARP(64) is a multiplicative scale factor for the squared transverse momentum evolution scale, $K_{\perp}^2$, used as a scale in α_s. PARJ(82) is the invariant mass cut off for parton showers, below which partons are not assumed to radiate [94].

This uncertainty only affects the $t\bar{t}$ signal MC simulation. The two models are used to replace the $t\bar{t}$ MC simulation in the analysis, with the average result for each model evaluated using pseudo-experiments. The two models are considered as an envelope and as such half of the full difference is taken as a systematic uncertainty.

7.4.4 Parton Distribution Function

The uncertainty due to the choice of PDF is evaluated by reweighting the templates used in the analysis, with different PDF sets. The analysis is then performed once for each PDF set, and the value of f_{SM} observed is recorded.

Three PDFs are considered for this uncertainty:

- CTEQ66 - central value + 44 error sets [95]
- MSTW2008NLO68CL - central value + 40 error sets [96]
- NNPDF20 - 100 error sets (mean taken as central value) [97]

It is not feasible for each of the individual PDFs along with their errors to be simulated fully in MC in order to evaluate the uncertainty, due to the vast amount of computing time required. Instead, the full PDF information from the simulation of the nominal MC samples is stored, and used to reweight the events for a chosen PDF, using LHAPDF [98] and following the PDF4LHC [99] recommendations.

The results for the CTEQ66 PDF sets are combined using a symmetric Hessian method [95],

$$\Delta x = \frac{1}{2}\sqrt{\sum_i (x_i^+ - x_i^-)^2}, \tag{7.6}$$

where $x_i^{\pm}$ are the up and down variations for a given error set, and the sum runs over all error sets.

MSTW2008NLO68CL PDF sets are combined with an asymmetric Hessian method [96],

$$\Delta x^{+} = \sqrt{\sum_{i} (x_i - x_0)^2}, \qquad x_i - x_0 > 0 \tag{7.7}$$

$$\Delta x^{-} = \sqrt{\sum_{i} (x_i - x_0)^2}, \qquad x_i - x_0 < 0, \tag{7.8}$$

where x_0 is the measured value of f_{SM} from the central PDF set and x_i are the f_{SM} results from the variations.

NNPDF20 PDFs are not provided as up/down shifts in sets, but instead are produced by varying parameters within the PDF. As such, the results for NNPDF20 are combined with a simple RMS method. The total PDF uncertainty is then evaluated as the envelope containing the largest error band up shift and the largest error band down shift.

Figures 7.11 and 7.12 show the results of the PDF uncertainty evaluation for all five analysis channels. The red band represents the combined variation due to the CTEQ66 PDF set, the blue band the variation due to the NNPDF20 PDF set, and the green band the variation due to the MSTW2008NLO68CL PDF set. In figure 7.11 a), the largest value covered by any given band is around 1.16, with the smallest value covered by any given band around 0.88. The size of the systematic uncertainty on f_{SM} is then $(1.16-0.88)/2 = 0.14$. In the *ee* channel, each of the PDF sets presents a fairly distinct mean value. This may be due to statistical fluctuations, as each PDF set is in effect a statistically separate sample, while the variations within the PDF sets are based on the same mean result.

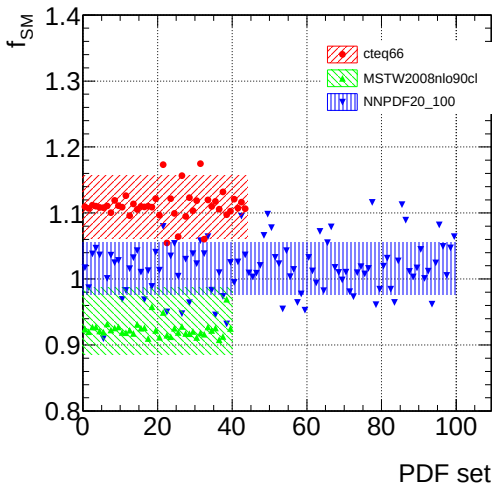

(a)

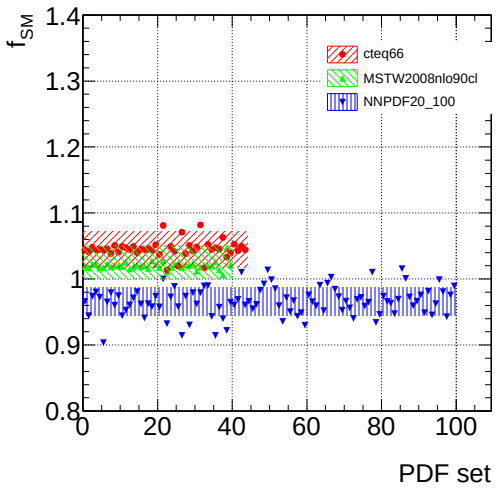

(b)

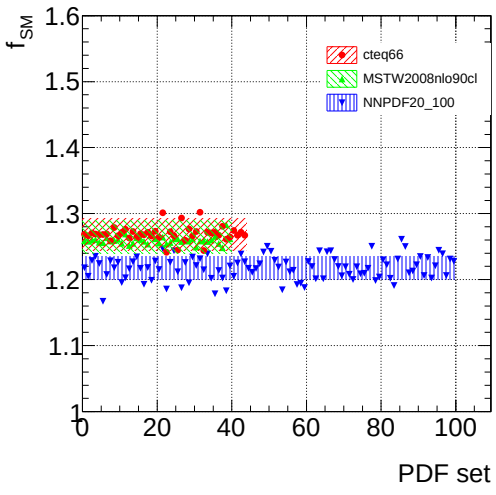

(c)

Figure 7.11: Measured values of f_{SM} for each PDF set variation for a) the ee channel, b) the $\mu\mu$ channel, and c) the $e\mu$ channel. The coloured bands show the combined uncertainty for each PDF set. The total uncertainty is the overall spread of all three of these bands.

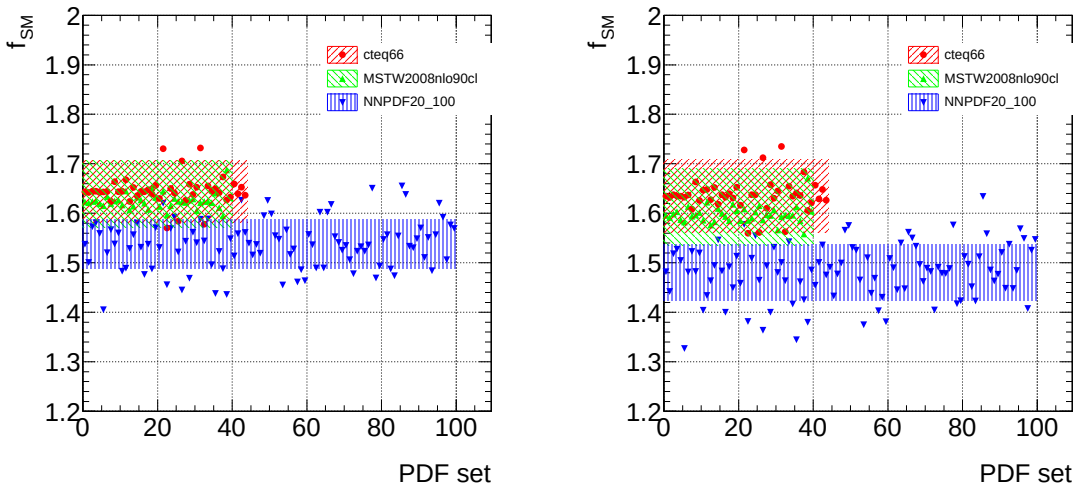

(a) (b)

Figure 7.12: Measured values of f_{SM} for each PDF set variation for a) the e+jets channel, and b) the μ+jets channel. The coloured bands show the combined uncertainty for each PDF set. The total uncertainty is the overall spread of all three of these bands.

7.4.5 Template Statistics

The MC simulation used to construct the templates for the analysis are limited in size due to the large amounts of processing time required in production. This has the effect that the statistical uncertainty on the templates is non-negligible and must be taken into account.

To do this, the templates for the two signal models and the background are varied within their statistical uncertainties. For each bin in each template, the number of events is smeared within the uncertainty. This then generates a set of 'variation' templates which are used in place of the 'nominal' templates in the analysis. The effect of varying the templates alters the result of a fit to data, and the results are recorded for 20,000 different variations. The width of the resulting distribution of measured f_{SM} is taken as the systematic uncertainty.

7.4.6 Luminosity Uncertainty

The integrated luminosity of the 2011 dataset recorded in ATLAS was measured to be 4.7 fb^{-1}, for the GRL used in this analysis, with a $\pm 1.8\%$ uncertainty [100]. The luminosity is used in the analysis to normalise the templates before performing the fitting procedure. As the $t\bar{t}$ cross section is a free parameter in the fit, but the background contribution normalisation is fixed, a change in luminosity will affect the background contamination which may alter the fitted result.

The MC simulation is scaled up/down corresponding to the luminosity uncertainty and pseudo-data are picked from the resulting distributions. These pseudo-data are then fitted to the unchanged templates. The fitting procedure is performed on the pseudo-data for 20,000 pseudo-experiments, and the systematic uncertainty is obtained by taking the difference between the nominal sample and the luminosity scaled up/down samples.

7.4.7 Jet Energy Scale

While the dilepton channel does not rely on jets to produce the $\Delta\phi$ distribution, the event selection does impose jet requirements. This can indirectly affect the measurement by adding or removing events based on the jet cuts. The semileptonic channel is more directly affected by jet uncertainties due to the jet used in calculating $\Delta\phi$.

The Jet Energy Scale (JES) applies calibrations to jets in the analysis, based on calorimeter response and noise studies [101]. This is required due to differences between the ATLAS detector response and the detector simulation. These calibrations introduce uncertainties to the jet energy determination, which are estimated within the scope of the JES uncertainty. In total, the energy scale uncertainty on a central, high p_{T} jet is generally between 2.5% and 5% [101].

There are 16 nuisance parameters as part of the JES systematic, addressing factors included in the calibration, as well as treating the flavour response of the detector, its performance with pileup, and the effect of nearby jets on the calibration. Each of these components is evaluated separately — varying the parameter within its uncertainty, performing pseudo-experiments and recording the average value of f_{SM} — and the resulting uncertainties added in quadrature to give an estimate of the total JES uncertainty. The largest contribution to the JES uncertainty comes from the flavour composition and response and b–jet calibrations.

7.4.8 Jet Energy Resolution

After calibration, jets still have an uncertainty on their energy measurment. The effect of this measurment resolution can alter the number of jets passing the event selection cuts, or change the reconstruction in the semileptonic channel, thus affecting the spin correlation measurement, if the energy is varied within its uncer-

tainty. To estimate the uncertainty due to the jet resolution, the energies of the jets are smeared within their resolutions and the analysis repeated for 20,000 pseudo-experiments [101].

7.4.9 Jet Reconstruction Efficiency

The efficiency with which a jet is reconstructed was measured in data and is used to remove randomly jets from an event, simulating cases where a jet may be present but unreconstructed, with respect to the nominal analysis [101]. The jet reconstruction efficiency plateaus close to 100% for jets with p_{T} larger than around 25 GeV. Pseudo-data are generated from the changed MC simulation for 20,000 pseudo-experiments. Each set of pseudo-data is fitted to the nominal templates and the average result over all pseudo-experiments is recorded. The difference between the result with randomly removed jets is subtracted from the nominal result and taken as a systematic uncertainty.

7.4.10 Lepton Momentum Scale and Resolution

The primary reconstructed objects used for this analysis are leptons. Calibration of the measured lepton momentum is performed in order to ensure the MC simulation best describes the data. This calibration comes with associated uncertainties, which must be evaluated by propagating them through the analysis and estimating the effect. The muon momentum is calculated in the reconstruction by combining measurements from the muon spectrometer and the inner detector. The momentum resolution for each of the subdetectors is varied within the associated uncertainty [102] and the momentum recalibrated again. This produces four results, two shifts up and two down, of which the largest up and largest down uncertainty is taken as the systematic. The uncertainty on the electron momentum is estimated by investigating differences between simulation and data in resonances [103]. The electron

momentum is then varied within the measured uncertainty in order to estimate the effect on the value of f_{SM}.

In both cases, pseudo-data are generated from the $\Delta\phi$ distribution reconstructed from each of the momentum scale/resolution variations. The pseudo-data are fitted to the nominal templates and the process repeated for several pseudo-experiments. The average measurement of f_{SM} for each of the varied samples is compared to the central measurement and the uncertainty is taken as the difference.

7.4.11 Lepton Scale Factors

As the reconstruction and trigger efficiencies are different between data and the MC simulation, the total number of events after event selection can be over or under-estimated. To address this, scale factors are calculated on a tag and probe sample and applied to each individual lepton. These scale factors also carry an uncertainty, the effect of which is estimated on the measured value of f_{SM} by varying the scale factors within the uncertainty. Again, pseudo-data are generated from the MC simulation, but with the lepton scale factors shifted up or down. The pseudo-data are then fitted to the nominal templates and the results averaged and compared to the central value of f_{SM}. The difference between up (down) and nominal is taken as the up (down) systematic shift.

7.4.12 Missing Transverse Energy

After each reconstructed object is corrected for resolution, energy scale, etc, the change must be propagated into the $E_{\mathrm{T}}^{\mathrm{miss}}$. For example, if a jet is removed by the jet reconstruction efficiency procedure, the $E_{\mathrm{T}}^{\mathrm{miss}}$ would be calculated differently and must be reevaluated. For each systematic procedure, the $E_{\mathrm{T}}^{\mathrm{miss}}$ is recalcualted.

In addition to this, an uncertainty on the $E_{\mathrm{T}}^{\mathrm{miss}}$ calculation for parameters outside the scope of reconstructed objects, such as energy deposits not associated with a selected jet or electron, is estimated. These contributions to $E_{\mathrm{T}}^{\mathrm{miss}}$ are modelled in the MC simulation and calibrated against data. The calibration is then varied within its uncertainty to provide an estimate for the systematic uncertainty. The effect of pileup on the $E_{\mathrm{T}}^{\mathrm{miss}}$ calculation is also estimated and included in the systematic evaluation.

7.4.13 Pileup dependence

In order to check the affect of pileup on the $\Delta\phi$ observable, events are categorised as 'low' or 'high' pileup events. A good approximation of the pileup content of an event is the number of vertices. The $\Delta\phi$ distribution is constructed for events with less than four vertices, and for events with at least four vertices. The splitting at four is chosen to ensure roughly equal statistics in each distribution, as well as providing a distinction between very low, and high pileup events. The ratio of these two regions is taken, and any shape difference between the two would constitute a dependence on the pileup content.

Figures 7.13 and 7.14 show these ratios for all five analysis channels. No significant shape difference is observed in both $t\bar{t}$ models, nor data, suggesting that there is no spin correlation dependence on pileup.

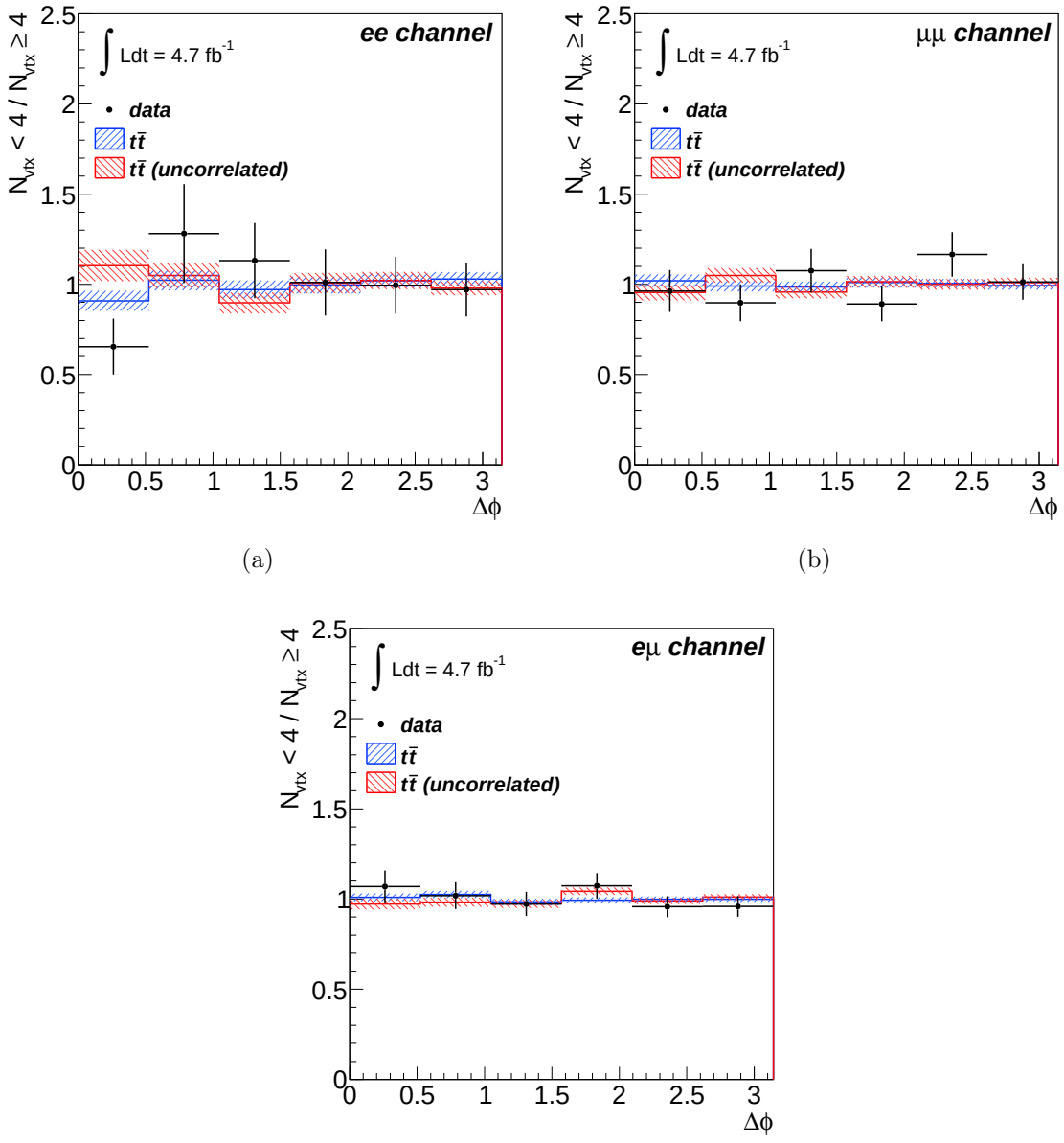

(a) (b)

(c)

Figure 7.13: Ratio of $N_{vtx} < 4/N_{vtx} \geq 4$ for the $\Delta\phi$ distribution, in the a) ee, b) $\mu\mu$ and c) $e\mu$ channels.

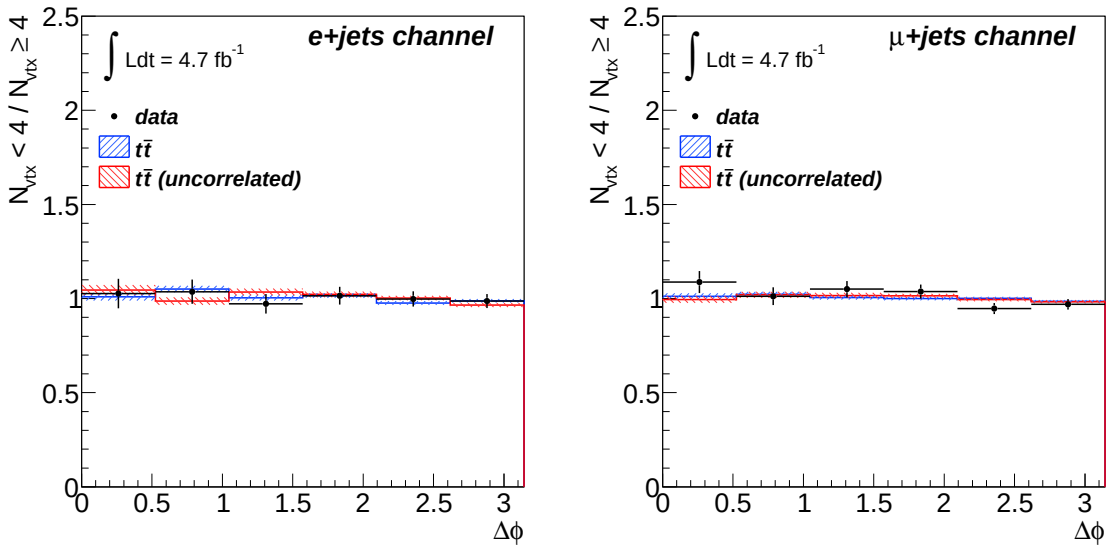

(a) (b)

Figure 7.14: Ratio of $N_{vtx} < 4/N_{vtx} \geq 4$ for the $\Delta\phi$ distribution, in the a) e+jet and b) μ+jet channels.

7.4.14 Background Model Uncertainties

A good model for the various sources of background is crucial for a template based analysis, as any small change in the shape of the distribution can affect the measurement. In order to ensure the background model uncertainties are properly treated, each background source is considered individually. In the case of the semileptonic channel, the dominant sources of background events are from W+jets production and fake leptons. For the dilepton channel, the Z/γ^* process produces the dominant background.

Z/γ^*+Jets

The uncertainty on the scale factor (calculated in section 6.5.1) is estimated by varying the $E_{\mathrm{T}}^{\mathrm{miss}}$ cut used to define the control region by 5 GeV up and down. This then affects the number of events used to derive the normalisation. The difference relative to the nominal analysis is evaluated using pseudo-experiments for both up and down shifts.

Diboson

A theory uncertainty on the diboson cross section of 5% is evaluated, as well as an extra uncertainty originating from the number of extra jets in the simulation. The diboson MC simulation is generated with ALPGEN, a multi-leg generator. This allows additional hard jets in the matrix element calculation without performing the full NLO calculation. These additional jets carry an associated uncertainty on the cross section of 24% per jet, which is added in quadrature. The background sample is scaled up and down within the uncertainty and the fit is repeated for each new sample. The difference between the up and down scaled samples with respect to the nominal analysis is taken as a systematic uncertainty.

Single Top

The single top cross section is normalised to the approximate NNLO cross sections for the t-channel [104], s-channel [105], and Wt-channel [106]. The normalisations of the MC samples are varied up and down within the calculated uncertainties to estimate the systematic effect. The difference between up and down shifts with respect to nominal is taken as a systematic uncertainty.

W+Jets

The W+jets cross section is derived from a data driven method, due to the large uncertainty on the MC based prediction. The normalisation is calculated using the charge asymmetry of W boson production.

In a proton-proton collider, there is an expected asymmetry between the number of W^+ and W^- bosons produced, due to the larger positive charge content of the incoming protons. The ratio of cross sections for these bosons can be predicted with high precision [107]. The number of events containing a single charged lepton are then counted in data and MC and categorised.

The equation

$$N_{W^+} + N_{W^-} = \frac{(N_{W^+} + N_{W^-})}{(N_{W^+} - N_{W^-})}(D^+ - D^-) = (\frac{r_{MC} + 1}{r_{MC} - 1})(D^+ - D^-) \qquad (7.9)$$

is used, where the contributions from $t\bar{t}$, fake leptons and Z+jets are charge symmetric, relates $N_{W^\pm}$, the number of simulated $W^\pm$ events, to $D^\pm$ the number of $W^\pm$ events observed in data. The single top background contribution is not charge symmetric and is subtracted from the data. r_{MC} is the predicted ratio of W^+ to W^- production, measured in MC. The scale factor is applied to the left hand side in order to match the observation in data.

In addition, scale factors due to the different b-tag rates from W+heavy flavour (bb, cc, c) are calculated. The total uncertainty for the W+jets normalisation is split into the flavour fractions and then combined in quadrature.

To estimate the shape uncertainty on the W+jets prediction, parameters in ALPGEN, corresponding to theoretical scales, are changed and the analysis is performed again, using pseudo-data to estimate the effect of changing the W+jets shape parameters.

Fake Leptons

The fake lepton contribution to the analysis is entirely data driven, as described in section 6.4.2. The uncertainty is evaluated by varying the measured efficiencies used in the matrix method. The real and fake efficiencies have associated uncertainties derived from the methods used in measuring the efficiencies. In analysis channels involving electrons, the real and fake contributions are varied independently and the largest deviation from the central measurement is taken as the systematic uncertainty for both upwards and downwards deviations. For the muon contribution, the difference between two paramaterisations of the estimate is taken as the uncertainty, with the central value being the average of these two methods.

7.4.15 Top Mass dependence

The default MC simulation used for both the Standard Model template and the $A = 0$ template model a top quark with $m_t = 172.5$ GeV. The current best measurement for the top quark mass is $m_t = 173.5 \pm 0.6 \pm 0.8$ GeV [4], differing slightly from the MC simulation used. Changing the top quark mass affects the production cross section, which could feasibly alter the spin correlation, if the ratio of production mechanisms changes.

channel	Δf_{SM}
ee	± 0.01
$\mu\mu$	± 0.03
$e\mu$	$\pm < 0.01$
e+jets	± 0.05
μ+jets	± 0.07

Table 7.4: Variation in f_{SM} with top mass for each analysis channel. The variation is computed using a ± 2.5 GeV range around the central top mass ($m_t = 172.5$ GeV).

In order to estimate the effect of a top mass variation on the spin correlation, simulated samples with a different input top mass are used. Seven different mass points, with 2.5 GeV spacing are used to generate pseudo-data, in order to estimate the expected mean of the spin correlation parameter. All of the points are then fitted with a straight line, and the variation between 172.5 ± 2.5 GeV is taken as an estimate of the systematic effect due to varying top mass.

Figures 7.15 and 7.16 show the results of 20,000 pseudo-experiments for each mass point. The uncertainty on each point represents the width of the f_{SM} distribution obtained through pseudo-experiments. The parameters of the fitted line are then used to estimate the variation in f_{SM} over a 5 GeV range. Table 7.4 shows the effect of varying the top mass numerically.

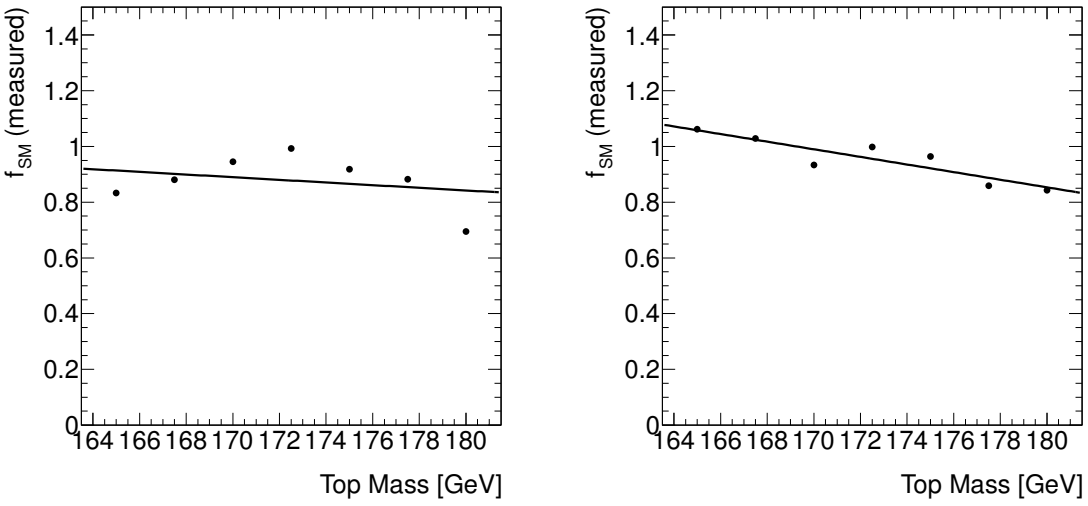

(a)

(b)

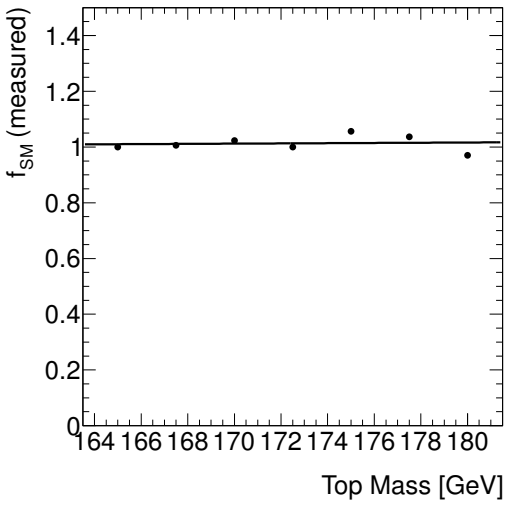

(c)

Figure 7.15: Average fitted value of f_{SM} for seven different mass points between 165 GeV and 180 GeV, for the a) ee, b) $\mu\mu$, and c) $e\mu$ channels.

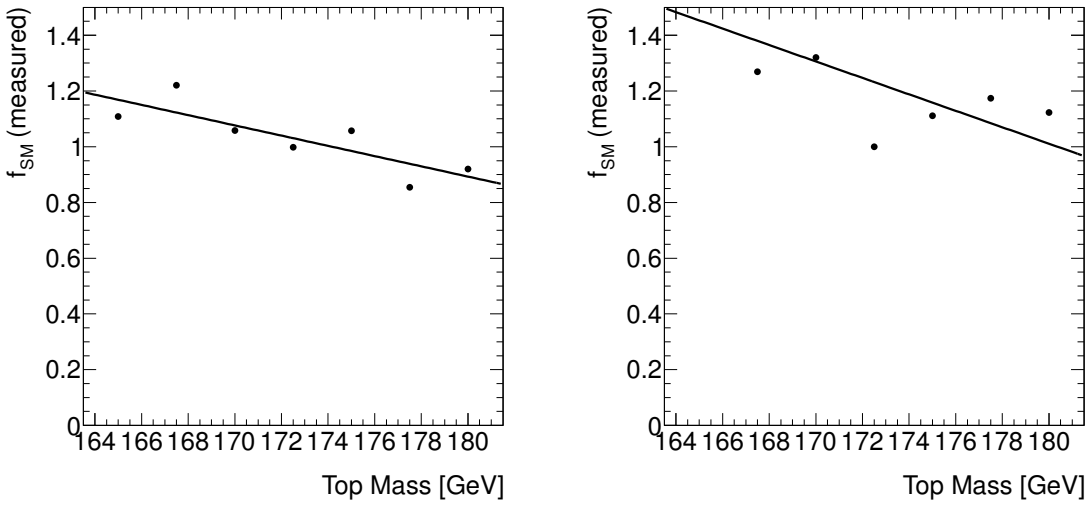

(a) (b)

Figure 7.16: Average fitted value of f_{SM} for seven different mass points between 165 GeV and 180 GeV, for the a) e+jets and b) μ+jets channels.

7.4.16 Total Systematic Uncertainty

Table 7.5 shows a summary of the systematic uncertainties evaluated for all five analysis channels. The final rows of the table show the total systematic uncertainty, statistical uncertainty and combined statistical plus systematic uncertainty.

The largest contributions to the systematic uncertainty arise from the MC generator uncertainties and the jet energy scale. Much of the uncertainties in the $e\mu$ channel are much smaller than for other channels. Within the dilepton channels, the $e\mu$ channel has a much larger number of events, leading to a more well defined separation between the two templates. This makes it more robust to small changes due to systematic shifts. Similarly, the lepton+jet channels have a much smaller separation, making them extremely sensitive to subtle variations in the distribution.

channel	ee	$\mu\mu$	$e\mu$	$e + jets$	$\mu + jets$
Luminosity	$+0.06/-0.10$	$+0.08/-0.12$	$\pm < 0.01$	$\pm < 0.01$	± 0.01
Jet Energy Scale	$+0.22/-0.38$	$+0.25/-0.26$	$+0.02/-0.02$	$+0.11/-0.09$	$+0.11/-0.22$
Jet Energy Resolution	± 0.08	± 0.11	$\pm < 0.01$	± 0.02	± 0.11
Jet Reconstruction Efficiency	± 0.15	± 0.14	$\pm < 0.01$	± 0.03	± 0.12
Lepton Momentum Scale and Resolution	$+0.11/-0.24$	$+0.17/-0.22$	$\pm < 0.01$	± 0.02	± 0.02
Lepton Scale Factor	$+0.09/-0.18$	$+0.10/-0.16$	$\pm < 0.01$	± 0.01	± 0.01
Background Estimation	$+0.10/-0.16$	$+0.16/-0.20$	$\pm < 0.01$	$+0.10/-0.09$	$+0.07/-0.08$
Missing Energy Uncertainty	$+0.13/-0.21$	$+0.13/-0.17$	$\pm < 0.01$	$+0.05/-0.03$	± 0.03
MC Generator	± 0.37	± 0.18	± 0.10	± 0.42	± 0.29
PDF	± 0.14	± 0.06	± 0.05	± 0.11	± 0.14
Top Mass	± 0.10	± 0.10	$\pm < 0.01$	± 0.05	± 0.07
MC Template Statistics	± 0.20	± 0.07	± 0.05	± 0.14	± 0.13
Total Systematic Uncertainty	$+0.57/-0.74$	$+0.47/-0.54$	± 0.12	± 0.49	$+0.41/-0.45$
Data Statistics	± 0.38	± 0.21	± 0.11	± 0.30	± 0.29
Total Uncertainty	$+0.68/-0.83$	$+0.52/-0.58$	± 0.17	± 0.57	$+0.50/-0.54$

Table 7.5: Systematic uncertainties on the measurement of f_{SM} for all five analysis channels. The total systematic uncertainty is obtained by adding each systematic in quadrature.

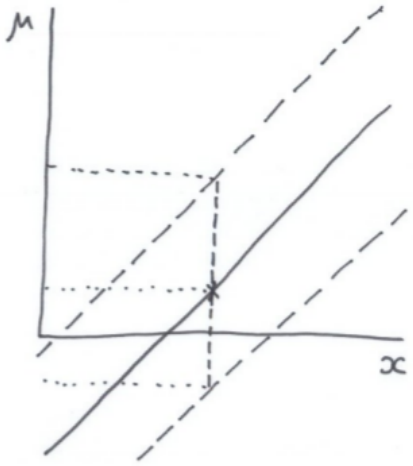

Figure 7.17: Simple confidence band construction, ignoring the physical boundary. The measured value, x maps onto μ by the solid line. The uncertainty is given by the diagonal dashed line.

7.5 Feldman Cousins confidence interval

When measuring a parameter with strict physical boundaries and a large uncertainty, it is possible to measure a value outside of the physical region. This is an expected occurence given the size of the uncertainty. When using the naïve Frequentist approach, measuring a value close to or outside of the physical region may give confidence intervals which extend outside of the physical region.

In figure 7.17 suppose the physical boundary on the parameter μ is at 0. The measurement of x, which maps to μ results in a value of μ such that the uncertainty overshoots the physical boundary. This leads to a confidence interval which partially covers a non physical region. If the measured value of x were to map to a value of μ below the physical boundary, the confidence interval tends to give undercoverage of the result in the upper bound, with an unphysical central value and lower bound.

In figure 7.18 the diagram has been modified. If x generates a value of μ outside the physical boundary, μ is fixed at the boundary, with the lower bound on the confidence interval being fixed at the boundary. For values of x which generate

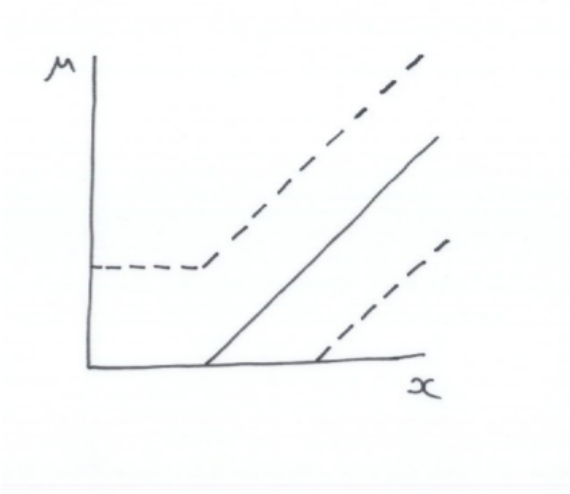

Figure 7.18: Confidence band construction where μ is limited to a physical boundary, and the uncertainty on μ follows a similar treatment.

$\mu < 0$, the confidence interval is fixed at 1σ from 0. For example, if the physical boundary were at $\mu = 0$ and x generated a value of $\mu = -0.1$, then μ is replaced with the value of the boundary. The confidence interval is also modified for such values, giving the 1σ uncertainty for all measurements below $\mu = 0$. This is clearly a conservative estimate.

Feldman and Cousins proposed an approach using a likelihood ratio ordering principle in order to provide full coverage when measuring values close to the physical boundary [108].

To illustrate the Feldman-Cousins confidence interval, consider this example of a gaussian with standard deviation 1, where,

$$P(x|\mu) = \frac{1}{\sqrt{2\pi}} e^{\frac{-(x-\mu)^2}{2}} \tag{7.10}$$

with x being a measurement, and μ the corresponding true value. A second gaussian probability can be constructed, which constrains μ to be within the physical boundary. $P(x|\mu_{best})$ is defined as in equation 7.10 with a simple added constraint.

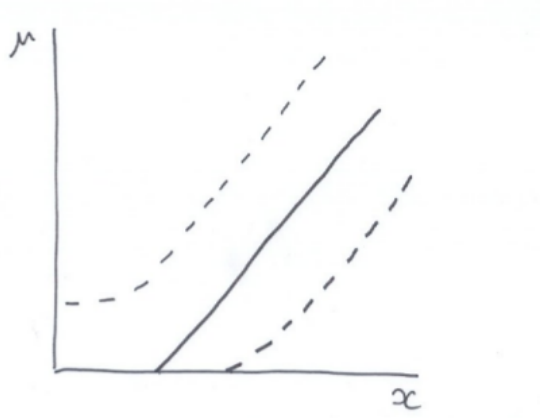

Figure 7.19: Feldman-Cousins construction of the confidence band. This construction allows a smooth transition near the physical boundary, transitioning from a two sided boundary to an upper limit automatically.

When x is in the physical region, let $\mu_{best} = x$ and when x is outside the boundary, let μ_{best} be equal to the value at the boundary. Following this, all values of x map to a physical value of μ. A likelihood ratio can then be constructed where,

$$R(x) = \frac{P(x|\mu)}{P(x|\mu_{best})}. \tag{7.11}$$

For any given value of μ, values of x_1 and x_2 are chosen such that the integral,

$$\int_{x_1}^{x_2} P(x|\mu) = 0.68 \tag{7.12}$$

for a 68% confidence level, and that $R(x_1) = R(x_2)$.

Figure 7.19 shows the confidence interval for the Feldman-Cousins construction. Interesting to note is that, far away from the physical boundary, the interval given in figure 7.19 becomes that given in figure 7.17 (as well as in figure 7.18).

The next section discusses the results of the fit to data, with the corresponding Feldman-Cousins confidence intervals constructed for each channel.

7.6 Fit to Data

Figure 7.20 shows all five results, including the statistical and systematic uncertainties. The dashed line represents the Standard Model prediction. All five results are consistent with the Standard Model. Figures 7.21 and 7.22 show the Feldman-Cousins confidence intervals for each channel. The blue band represents the statistical uncertainty only, while the red and green bands represent the 68% and 95% confidence intervals for the statistical and systematic uncertainties combined. The results are sufficiently far from the boundary that no special treatment of the confidence interval is required for any of the channels. The $e\mu$ channel alone can exclude the alternate model with $A = 0$ at a significance of 7.8σ.

This may be improved with a combination of all five results, though care must be taken to address correlations in some systematic uncertainties between channels. Given the large uncertainty of the four remaining channels, a combination may not yield a significant improvement.

The result presented here is consistent with the previous result [70], which was performed in the dilepton channel only, with a subset of the data used here. The previous result for a combination of all three dilepton channels was $f_{\mathrm{SM}} = 1.30 \pm 0.14(\mathrm{stat})^{+0.27}_{-0.22}(\mathrm{syst})$. This thesis more than doubles the dataset in the dilepton channel, as well as presenting the first measurement in ATLAS of the spin correlation in the lepton+jets channel.

Interesting to note is that all of the central fitted values lie above $f_{\mathrm{SM}} = 1$. If a charged Higgs were introduced into the top decay, as discussed in section 5.3.2, the spin correlation may be expected to fall below $f_{\mathrm{SM}} = 1$.

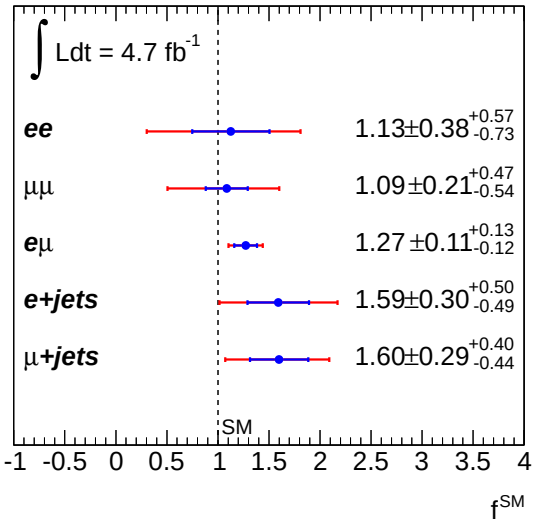

Figure 7.20: Summary of the results obtained for all five analysis channels.

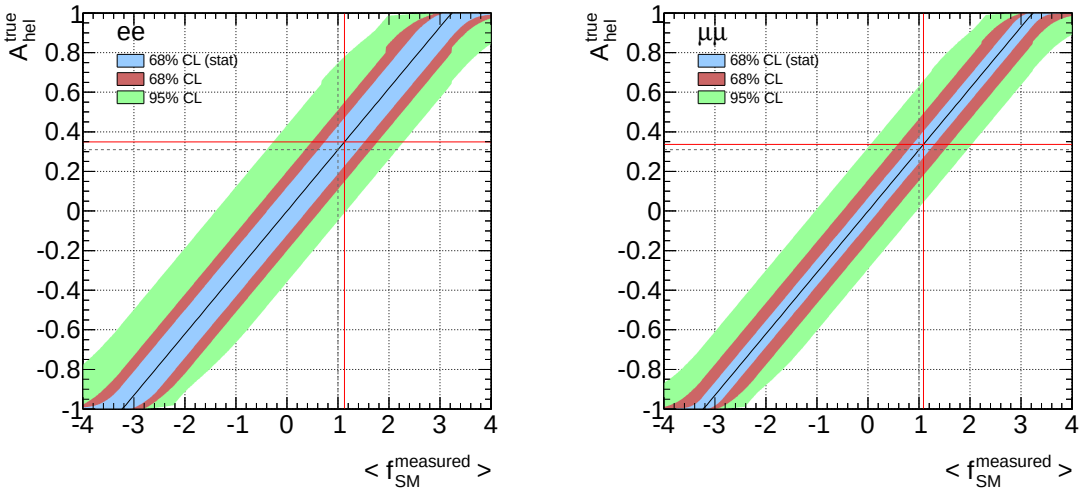

(a)

(b)

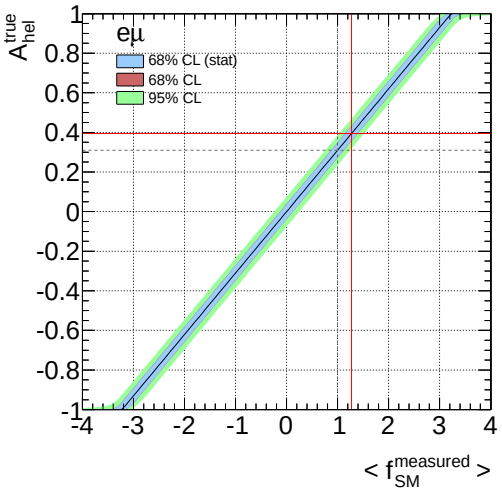

(c)

Figure 7.21: Feldman-Cousins confidence interval for the a) ee, b) $\mu\mu$, and c) $e\mu$ channels. The result of the fit to data is shown as the red line. The Standard Model expectation is shown as the dashed line.

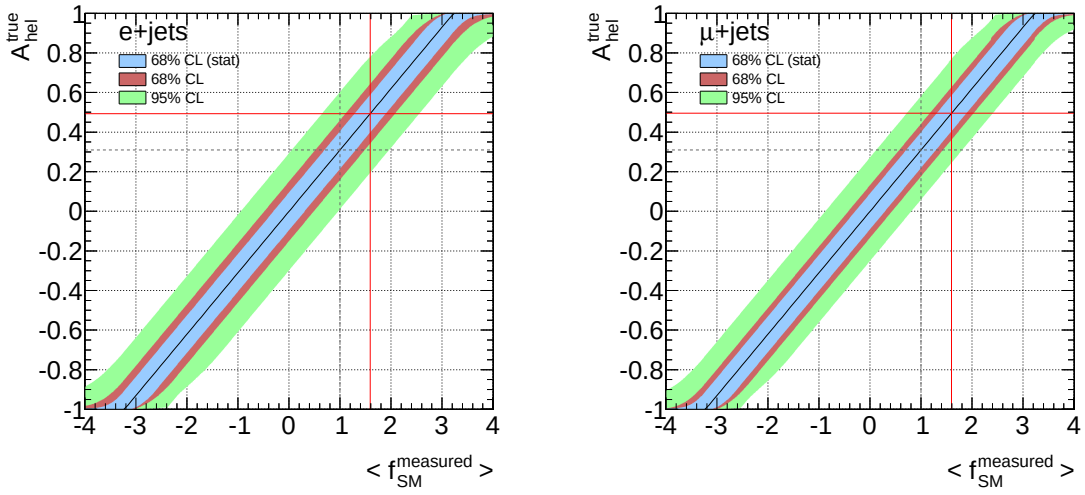

(a) (b)

Figure 7.22: Feldman-Cousins confidence interval for the a) e+jets, and b) μ+jets channels. The result of the fit to data is shown as the red line. The Standard Model expectation is shown as the dashed line.

Chapter 8

Concluding Remarks

The top quark is the most massive elementary particle in the Standard Model. This large mass leads to an interesting property of the top quark, in that it decays weakly before forming a bound state. This means the top quark is unaffected by strong interactions before it decays, leaving properties such as its spin intact and propagated to the decay products. This in turn implies that properties such as the spin correlation in $t\bar{t}$ pair production can be studied.

Several studies of the $t\bar{t}$ spin correlation have been performed since the discovery of the top quark in 1995. The CDF and DØ experiments have both published studies of spin correlation at 1.96 TeV centre of mass energy [68, 69], with DØ claiming the first 3σ evidence for non zero spin correlation. The amount of spin correlation is dependent on the centre of mass energy of the system, as well as the production mechanisms*, meaning the measurements performed at the Tevatron and at the LHC are complementary. At the LHC, ATLAS and CMS have both presented studies of spin correlation [70, 71], finding results consistent with the Standard Model prediction, with the ATLAS result [70] being the first observation of non zero spin correlation at a confidence level of five standard deviations.

*At the Tevatron, $q\bar{q}$ production dominates, while gg fusion is the dominant production method at the LHC

This thesis presented a further study, building on the previous publication from ATLAS, using more than double the dataset. Several updates to systematic procedures were included, after much work performed by the ATLAS collaboration. These procedures are circulated through internal working groups, going through several stages of approvals before becoming the standard systematic procedure to use for any given analysis. One particular change to the systematic uncertainty is that of the MC generator procedure. Previously, a comparison of MC@NLO and POWHEG was performed, but recently a bug was found, affecting mainly the spin correlation, in POWHEG, suggesting that this would provide an overestimation of the uncertainty. An alternative procedure was adopted to estimate the MC generator uncertainty, varying theory parameters in the generator. This approach is strongly dependent on MC@NLO however, so further work may be needed in order to generate valid samples with POWHEG for comparisons.

Ongoing work within the spin correlation working group in ATLAS suggests the use of more sophisticated reconstruction techniques, based on a kinematic fitter, which may yield a more sensitive analysis in the single lepton channel.

As well as for the 2011 dataset, a much larger dataset has been collected in 2012, with a higher centre of mass energy at 8 TeV. This presents another exciting opportunity to investigate the spin correlation, where the larger dataset may help to constrain some uncertainties further, with the potential to improve on the low statistics dilepton channels. In addition, the lepton+jets channel may be improved with stricter cuts in the reconstruction. Following the LHC long shutdown, the collider may restart with almost double the centre of mass energy as was used in the 2011 run, with $\sqrt{s} = 13 - 14$ TeV. The cross section for $t\bar{t}$ production at $\sqrt{s} = 14$ TeV increases more than five fold relative to the cross section at $\sqrt{s} = 7$ TeV [109]. This will provide yet more statistics, potentially allowing all five analysis channels presented in this thesis to provide sensitive measurements of the spin correlation.

Appendix A

Appendix A

A.1 Complete Table of Systematic Uncertainties

An expanded table of systematic uncertainties, as detailed in section 7.4, is presented in table A.1. Instances of an uncertainty where no prescription exists for a given channel are left blank. The total uncertainty is evaluated by summing the individual uncertainties in quadrature, assuming all of the systematics are uncorrelated.

Uncertainty	ee	$\mu\mu$	$e\mu$	$e+jets$	$\mu+jets$
Top Mass	± 0.01	± 0.03	± 0.00	± 0.05	± 0.07
MC Statistics	± 0.20	± 0.07	± 0.05	± 0.14	± 0.13
MC Scale Variation	+ 0.10/ - 0.10	+ 0.10/ - 0.10	+ 0.05/ - 0.05	+ 0.16/ - 0.16	+ 0.04/ - 0.04
Parton Shower	+ 0.21/ - 0.21	+ 0.11/ - 0.11	+ 0.04/ - 0.04	+ 0.30/ - 0.30	+ 0.23/ - 0.23
ISR/FSR	+ 0.26/ - 0.26	+ 0.10/ - 0.10	+ 0.08/ - 0.08	+ 0.22/ - 0.22	+ 0.16/ - 0.16
Underlying Event	+ 0.13/ - 0.13	± 0.01	± 0.00	+ 0.12/ - 0.12	+ 0.05/ - 0.05
Luminosity	+ 0.06/ - 0.10	+ 0.08/ - 0.12	± 0.00	± 0.00	± 0.01
(JES) EffectiveNP_1	± 0.03	± 0.04	± 0.01	± 0.03	+ 0.00/ - 0.02
(JES) EffectiveNP_2	+ 0.05/ - 0.07	+ 0.05/ - 0.03	± 0.01	+ 0.04/ - 0.06	+ 0.04/ - 0.09
(JES) EffectiveNP_3	+ 0.04/ - 0.06	± 0.05	± 0.00	+ 0.01/ - 0.02	± 0.03
(JES) EffectiveNP_4	± 0.04	+ 0.05/ - 0.03	± 0.00	± 0.00	± 0.02
(JES) EffectiveNP_5	± 0.04	+ 0.05/ - 0.03	± 0.00	± 0.00	± 0.02
(JES) EffectiveNP_6restTerm	± 0.05	± 0.05	± 0.00	± 0.01	± 0.01
(JES) EtaIntercalibration_TotalStat	+ 0.04/ - 0.07	± 0.05	± 0.00	+ 0.03/ - 0.01	+ 0.00/ - 0.03
(JES) EtaIntercalibration_Modelling	+ 0.05/ - 0.08	± 0.06	± 0.00	+ 0.07/ - 0.02	+ 0.02/ - 0.05
(JES) SingleParticle_HighPt	+ 0.05/ - 0.06	± 0.05	± 0.00	± 0.00	± 0.00
(JES) RelativeNonClosure_FrozenShowers	+ 0.04/ - 0.06	± 0.05	± 0.00	± 0.00	± 0.00
(JES) NPVOffsetTerm	+ 0.04/ - 0.07	± 0.05	± 0.00	± 0.02	± 0.03
(JES) MuOffsetTerm	+ 0.05/ - 0.10	± 0.07	± 0.01	+ 0.04/ - 0.02	+ 0.03/ - 0.10
(JES) Closeby	+ 0.07/ - 0.12	± 0.07	± 0.00	± 0.03	+ 0.01/ - 0.07
(JES) FlavorComp	+ 0.08/ - 0.13	± 0.09	± 0.01	± 0.02	+ 0.06/ - 0.12
(JES) FlavorResponse	+ 0.07/ - 0.17	+ 0.09/ - 0.12	± 0.00	± 0.01	+ 0.01/ - 0.06
(JES) BJES	+ 0.09/ - 0.17	+ 0.10/ - 0.13	± 0.01	+ 0.02/ - 0.00	+ 0.01/ - 0.02
Jet Energy Scale	+ 0.22/ - 0.38	+ 0.25/ - 0.26	+ 0.02/ - 0.02	+ 0.11/ - 0.09	+ 0.10/ - 0.22
Jet Energy Resolution	+ 0.08/ - 0.08	+ 0.11/ - 0.11	± 0.00	+ 0.02/ - 0.02	+ 0.11/ - 0.11
Jet Reconstruction Efficiency	+ 0.15/ - 0.15	+ 0.14/ - 0.14	± 0.00	+ 0.03/ - 0.03	+ 0.12/ - 0.12
Muon Momentum Scale	+ 0.07/ - 0.07	+ 0.09/ - 0.09	± 0.00	± 0.00	+ 0.02/ - 0.02
Electron Momentum Scale	+ 0.04/ - 0.16	+ 0.10/ - 0.15	± 0.00	± 0.02	± 0.00
ee SF	+ 0.09/ - 0.18	-	-	-	-
DY Normalisation	+ 0.06/ - 0.09	± 0.07	-	-	-
MET Pileup Component	+ 0.09/ - 0.15	+ 0.10/ - 0.12	± 0.00	± 0.02	± 0.01
MET Soft Jet Component	+ 0.09/ - 0.14	+ 0.09/ - 0.12	± 0.00	+ 0.05/ - 0.02	± 0.03
Fake Lepton Normalisation	+ 0.02/ - 0.05	+ 0.09/ - 0.11	± 0.02	± 0.02	± 0.01
Diboson	+ 0.06/ - 0.10	± 0.07	± 0.00	± 0.00	± 0.00
Single Top	+ 0.06/ - 0.08	± 0.07	± 0.00	± 0.00	± 0.00
PDF	± 0.14	± 0.06	± 0.05	± 0.11	± 0.14
Muon Momentum Resolution	+ 0.08/ - 0.17	+ 0.10/ - 0.14	± 0.00	± 0.00	± 0.00
ee Fake Lepton Shape	± 0.01	± 0.00	± 0.00	± 0.00	± 0.00
$e\mu$ Fake Lepton Shape	± 0.00	± 0.00	± 0.00	± 0.00	± 0.00
$\mu\mu$ SF	-	+ 0.10/ - 0.16	-	-	-
$\mu\mu$ Fake Lepton Shape	-	+ 0.02/ - 0.00	-	-	-
$e\mu$ SF	-	-	± 0.00	-	-
e+jets SF	-	-	-	± 0.01	-
l+jets Fake Lepton Shape	-	-	-	+ 0.06/ - 0.03	± 0.00
(W+jet) ptjmin10	-	-	-	± 0.00	± 0.00
(W+jet) iqopt3	-	-	-	± 0.00	+ 0.02/ - 0.02
(W+jet) WJet2000	-	-	-	± 0.03	± 0.04
(W+jet) WJet2001	-	-	-	± 0.06	± 0.01
(W+jet) WJet2005	-	-	-	+ 0.03/ - 0.04	+ 0.04/ - 0.06
(W+jet) WJet2003_4	-	-	-	± 0.01	± 0.02
(W+jet) WJet2004_4	-	-	-	± 0.01	± 0.02
(W+jet) WJet2003_5	-	-	-	± 0.01	± 0.00
(W+jet) WJet2004_5	-	-	-	± 0.02	± 0.00
znorm	-	-	-	± 0.01	± 0.00
μ+jets SF	-	-	-	-	± 0.01
Total Systematic	+ 0.57/ - 0.74	+ 0.47/ - 0.54	± 0.12	± 0.49	+ 0.41/ - 0.45
Data Statistics	± 0.38	± 0.21	± 0.11	± 0.30	± 0.29
Total Uncertainty	+ 0.68/ - 0.83	+ 0.52/ - 0.58	± 0.17	± 0.57	+ 0.50/ - 0.54

Table A.1: Systematic uncertainties for all five analysis channels. The total systematic uncertainty is obtained by adding each systematic in quadrature.

Bibliography

[1] E. O. Lawrence and M. S. Livingston, *The Production of High Speed Light Ions Without the Use of High Voltages*, Phys. Rev. **40** (Apr, 1932) 19–35. http://link.aps.org/doi/10.1103/PhysRev.40.19.

[2] J. Thomson, *Cathode Rays*, Phil. Mag. **44** (1897) .

[3] M. Gell-Mann, *A Schematic Model of Baryons and Mesons*, Phys.Lett. **8** (1964) 214–215.

[4] Particle Data Group Collaboration, J. Beringer et al., *Review of Particle Physics*, Phys. Rev. D **86** (Jul, 2012) 010001. http://link.aps.org/doi/10.1103/PhysRevD.86.010001.

[5] S. Weinberg, *A Model of Leptons*, Phys.Rev.Lett. **19** (1967) 1264–1266.

[6] H. Georgi and S. L. Glashow, *Unity of All Elementary-Particle Forces*, Phys. Rev. Lett. **32** (Feb, 1974) 438–441. http://link.aps.org/doi/10.1103/PhysRevLett.32.438.

[7] G. M. Harry and the LIGO Scientific Collaboration, *Advanced LIGO: the next generation of gravitational wave detectors*, Classical and Quantum Gravity **27** (2010) no. 8, 084006. http://stacks.iop.org/0264-9381/27/i=8/a=084006.

[8] K. A. Strain et al., *The status of GEO 600*, 2004. Proc. SPIE **5500** (2004) 25–36, http://dx.doi.org/10.1117/12.551127.

[9] F. Englert and R. Brout, *Broken Symmetry and the Mass of Gauge Vector Mesons*, Phys. Rev. Lett. **13** (Aug, 1964) 321–323. http://link.aps.org/doi/10.1103/PhysRevLett.13.321.

[10] G. S. Guralnik, C. R. Hagen, and T. W. B. Kibble, *Global Conservation Laws and Massless Particles*, Phys. Rev. Lett. **13** (Nov, 1964) 585–587. http://link.aps.org/doi/10.1103/PhysRevLett.13.585.

[11] P. W. Higgs, *Broken Symmetries and the Masses of Gauge Bosons*, Phys. Rev. Lett. **13** (Oct, 1964) 508–509. http://link.aps.org/doi/10.1103/PhysRevLett.13.508.

[12] ATLAS Collaboration, G. Aad et al., *Observation of a new particle in the search for the Standard Model Higgs boson with the ATLAS detector at the LHC*, Phys.Lett. **B716** (2012) 1–29, arXiv:1207.7214 [hep-ex].

[13] CMS Collaboration, S. Chatrchyan et al., *Observation of a new boson at a mass of 125 GeV with the CMS experiment at the LHC*, Phys.Lett. **B716** (2012) 30–61, arXiv:1207.7235 [hep-ex].

[14] *Study of the spin of the Higgs-like boson in the two photon decay channel using 20.7 fb-1 of pp collisions collected at $\sqrt{s}$ = 8 TeV with the ATLAS detector*, Tech. Rep. ATLAS-CONF-2013-029, CERN, Geneva, Mar, 2013.

[15] *Study of the spin properties of the Higgs-like particle in the $H \to WW^{(*)} \to e\nu\mu\nu$ channel with 21 fb^{-1} of $\sqrt{s} = 8$ TeV data collected with the ATLAS detector.*, Tech. Rep. ATLAS-CONF-2013-031, CERN, Geneva, Mar, 2013.

[16] *Measurements of the properties of the Higgs-like boson in the four lepton decay channel with the ATLAS detector using 25 fb1 of proton-proton collision data*, Tech. Rep. ATLAS-CONF-2013-013, CERN, Geneva, Mar, 2013.

[17] W. Bernreuther and Z. G. Si Nucl. Phys. B **837** (2010) 90. and private communication.

[18] A. Team, *The scale of the LHC. Vue arienne du CERN avec le trac du tunnel LHC*, Jan, 2001.

[19] Gargamelle Neutrino Collaboration, F. Hasert et al., *Observation of Neutrino Like Interactions Without Muon Or Electron in the Gargamelle Neutrino Experiment*, Phys.Lett. **B46** (1973) 138–140.

[20] UA1 Collaboration, G. Arnison et al., *Experimental Observation of Isolated Large Transverse Energy Electrons with Associated Missing Energy at s**(1/2) = 540-GeV*, Phys.Lett. **B122** (1983) 103–116.

[21] ATLAS Collaboration, G. Aad et al., *Measurement of the cross section for top-quark pair production in pp collisions at $\sqrt{s} = 7$ TeV with the ATLAS detector using final states with two high-pt leptons*, JHEP **1205** (2012) 059, arXiv:1202.4892 [hep-ex].

[22] UA2 Collaboration, M. Banner et al., *Observation of Single Isolated Electrons of High Transverse Momentum in Events with Missing Transverse Energy at the CERN anti-p p Collider*, Phys.Lett. **B122** (1983) 476–485.

[23] A. Team, *Diagram of an LHC dipole magnet. Schma d'un aimant diple du LHC*, Jun, 1999.

[24] O. S. Brning, P. Collier, P. Lebrun, S. Myers, R. Ostojic, J. Poole, and P. Proudlock, *LHC Design Report*. CERN, Geneva, 2004.

[25] `http://lhc-machine-outreach.web.cern.ch/lhc-machine-outreach/components/cable.htm`.

[26] S. Baird, *Accelerators for pedestrians; rev. version*, Tech. Rep. AB-Note-2007-014. CERN-AB-Note-2007-014. PS-OP-Note-95-17-Rev-2. CERN-PS-OP-Note-95-17-Rev-2, CERN, Geneva, Feb, 2007.

[27] `http://lhc-machine-outreach.web.cern.ch/lhc-machine-outreach/collisions.htm`.

[28] on behalf of the ATLAS Collaboration Collaboration, K. Sliwa, *"ATLAS Overview and Main Results"*, `arXiv:1305.4551 [hep-ex]`.

[29] *ATLAS Luminosity Public Results*, July, 2013. `https://twiki.cern.ch/twiki/bin/view/AtlasPublic/LuminosityPublicResults`.

[30] LHCb Collaboration, R. Aaij et al., *First evidence for the decay $B_s \to \mu^+\mu^-$*, `arXiv:1211.2674 [Unknown]`.

[31] LHCb Collaboration, R. Aaij et al., *Evidence for CP violation in $B^\pm \to \pi^\pm\pi^+\pi^-$ and $B^\pm \to K^+K^-\pi^\pm$ decays*, . Link to LHCb-ANA-2012-077.

[32] ALICE Collaboration, K. Aamodt et al., *Elliptic Flow of Charged Particles in Pb-Pb Collisions at $\sqrt{s_{NN}} = 2.76$ TeV*, Phys. Rev. Lett. **105** (Dec, 2010) 252302. `http://link.aps.org/doi/10.1103/PhysRevLett.105.252302`.

[33] ATLAS Collaboration, G. Aad et al., *Observation of a new χ_b state in radiative transitions to $\Upsilon(1S)$ and $\Upsilon(2S)$ at ATLAS*, Phys.Rev.Lett. **108** (2012) 152001, `arXiv:1112.5154 [hep-ex]`.

[34] ATLAS Collaboration, G. Aad et al., *Measurement of the $W \to \ell\nu$ and $Z/\gamma^* \to \ell\ell$ production cross sections in proton-proton collisions at $\sqrt{s} = 7$ TeV with the ATLAS detector*, JHEP **1012** (2010) 060, `arXiv:1010.2130 [hep-ex]`.

[35] ATLAS Collaboration, G. Aad et al., *Measurement of the top quark-pair production cross section with ATLAS in pp collisions at $\sqrt{s} = 7$ TeV*, Eur.Phys.J. **C71** (2011) 1577, `arXiv:1012.1792 [hep-ex]`.

[36] ATLAS Collaboration, G. Aad et al., *The ATLAS Experiment at the CERN Large Hadron Collider*, JINST **3** (2008) S08003.

[37] ATLAS Collaboration, G. Aad et al., *The ATLAS Experiment at the CERN Large Hadron Collider*, Journal of Instrumentation **3** (2008) no. 08, S08003. http://stacks.iop.org/1748-0221/3/i=08/a=S08003.

[38] ATLAS Collaboration Collaboration, *Estimating Track Momentum Resolution in Minimum Bias Events using Simulation and K_s in $\sqrt(s) = 900$ GeV collision data*, Tech. Rep. ATLAS-CONF-2010-009, CERN, Geneva, Jun, 2010.

[39] *The Expected Performance of the ATLAS Inner Detector*, Tech. Rep. ATL-PHYS-PUB-2009-002. ATL-COM-PHYS-2008-105, CERN, Geneva, Aug, 2008.

[40] A. Andronic and J. P. Wessels, *Transition radiation detectors*, Nuclear Instruments and Methods in Physics Research A **666** (Feb., 2012) 130–147, arXiv:1111.4188 [physics.ins-det].

[41] *ATLAS liquid-argon calorimeter: Technical Design Report*. Technical Design Report ATLAS. CERN, Geneva, 1996.

[42] *ATLAS tile calorimeter: Technical Design Report*. Technical Design Report ATLAS. CERN, Geneva, 1996.

[43] ATLAS Collaboration, M. Bosman, *Effect of the Tile Calorimeter thickness in the ATLAS Barrel Calorimeter Performance*, .

[44] A. Rimoldi, *The {ATLAS} muon trigger chamber system*, Nuclear Instruments and Methods in Physics Research Section A: Accelerators, Spectrometers, Detectors and Associated Equipment **409** (1998) no. 13, 669 – 674. http://www.sciencedirect.com/science/article/pii/S016890029701348X.

[45] *ATLAS Magnetic Field*, July, 2013. http://atlas.web.cern.ch/Atlas/GROUPS/MUON/magfield/mag_page1.html.

[46] ATLAS Collaboration, G. Aad et al., *Measurement of the Inelastic Proton-Proton Cross-Section at $\sqrt{s}$=7 TeV with the ATLAS Detector.*, Nature Commun. **2** (2011) no. arXiv:1104.0326. CERN-PH-EP-2011-047, 463. 19 p.

[47] P. Jenni, M. Nessi, M. Nordberg, and K. Smith, *ATLAS high-level trigger, data-acquisition and controls: Technical Design Report*. Technical Design Report ATLAS. CERN, Geneva, 2003.

[48] C. Eck, J. Knobloch, L. Robertson, I. Bird, K. Bos, N. Brook, D. Dllmann, I. Fisk, D. Foster, B. Gibbard, C. Grandi, F. Grey, J. Harvey, A. Heiss, F. Hemmer, S. Jarp, R. Jones, D. Kelsey, M. Lamanna, H. Marten, P. Mato-Vila, F. Ould-Saada, B. Panzer-Steindel, L. Perini, Y. Schutz,

U. Schwickerath, J. Shiers, and T. Wenaus, *LHC computing Grid: Technical Design Report. Version 1.06 (20 Jun 2005)*. Technical Design Report LCG. CERN, Geneva, 2005.

[49] J. H. Christenson, J. W. Cronin, V. L. Fitch, and R. Turlay, *Evidence for the 2π Decay of the K_2^0 Meson*, Phys. Rev. Lett. **13** (Jul, 1964) 138–140. http://link.aps.org/doi/10.1103/PhysRevLett.13.138.

[50] J. E. Augustin, A. M. Boyarski, M. Breidenbach, F. Bulos, J. T. Dakin, G. J. Feldman, G. E. Fischer, D. Fryberger, G. Hanson, B. Jean-Marie, R. R. Larsen, V. Lüth, H. L. Lynch, D. Lyon, C. C. Morehouse, J. M. Paterson, M. L. Perl, B. Richter, P. Rapidis, R. F. Schwitters, W. M. Tanenbaum, F. Vannucci, G. S. Abrams, D. Briggs, W. Chinowsky, C. E. Friedberg, G. Goldhaber, R. J. Hollebeek, J. A. Kadyk, B. Lulu, F. Pierre, G. H. Trilling, J. S. Whitaker, J. Wiss, and J. E. Zipse, *Discovery of a Narrow Resonance in e^+e^- Annihilation*, Phys. Rev. Lett. **33** (Dec, 1974) 1406–1408. http://link.aps.org/doi/10.1103/PhysRevLett.33.1406.

[51] J. J. Aubert, U. Becker, P. J. Biggs, J. Burger, M. Chen, G. Everhart, P. Goldhagen, J. Leong, T. McCorriston, T. G. Rhoades, M. Rohde, S. C. C. Ting, S. L. Wu, and Y. Y. Lee, *Experimental Observation of a Heavy Particle J*, Phys. Rev. Lett. **33** (Dec, 1974) 1404–1406. http://link.aps.org/doi/10.1103/PhysRevLett.33.1404.

[52] M. Kobayashi and T. Maskawa, *CP-Violation in the Renormalizable Theory of Weak Interaction*, Progress of Theoretical Physics **49** (1973) no. 2, 652–657. http://ptp.ipap.jp/link?PTP/49/652/.

[53] G. Sterman, *An Introduction to Quantum Field Theory*. Cambridge University Press, Cambridge, 1993.

[54] M. L. Perl et al., *Evidence for Anomalous Lepton Production in $e^+ - e^-$ Annihilation*, Phys. Rev. Lett. **35** (Dec, 1975) 1489–1492. http://link.aps.org/doi/10.1103/PhysRevLett.35.1489.

[55] S. W. Herb, D. C. Hom, L. M. Lederman, J. C. Sens, H. D. Snyder, J. K. Yoh, J. A. Appel, B. C. Brown, C. N. Brown, W. R. Innes, K. Ueno, T. Yamanouchi, A. S. Ito, H. Jöstlein, D. M. Kaplan, and R. D. Kephart, *Observation of a Dimuon Resonance at 9.5 GeV in 400-GeV Proton-Nucleus Collisions*, Phys. Rev. Lett. **39** (Aug, 1977) 252–255. http://link.aps.org/doi/10.1103/PhysRevLett.39.252.

[56] D0 Collaboration, S. Abachi et al., *Search for High Mass Top Quark Production in $p\overline{p}$ Collisions at $\sqrt{s} = 1.8$ TeV*, Phys. Rev. Lett. **74** (Mar, 1995) 2422–2426. http://link.aps.org/doi/10.1103/PhysRevLett.74.2422.

[57] CDF Collaboration, F. Abe et al., *Observation of Top Quark Production in $\overline{p}p$ Collisions with the Collider Detector at Fermilab*, Phys. Rev. Lett. **74** (Apr, 1995) 2626–2631. http://link.aps.org/doi/10.1103/PhysRevLett.74.2626.

[58] K. Nakamura and P. D. Group, *Review of Particle Physics*, Journal of Physics G: Nuclear and Particle Physics **37** (2010) no. 7A, 075021. http://stacks.iop.org/0954-3899/37/i=7A/a=075021.

[59] U. Langenfeld, S. Moch, and P. Uwer, *New results for t anti-t production at hadron colliders*, arXiv:0907.2527 [hep-ph].

[60] H. Baer, S. Dawson, and L. Reina, *Measuring the top quark Yukawa coupling at a linear e+ e- collider*, Phys.Rev. **D61** (2000) 013002, arXiv:hep-ph/9906419 [hep-ph].

[61] CDF, D0 Collaboration, R. C. Lopes de Sa, *Precise measurements of the W mass at the Tevatron and indirect constraints on the Higgs mass*, arXiv:1204.3260 [hep-ex].

[62] I. I. Bigi, Y. L. Dokshitzer, V. Khoze, J. Khn, and P. M. Zerwas, *Production and decay properties of ultra-heavy quarks*, Phys. Lett. B **181** (Jul, 1986) 157–163. 20 p.

[63] G. Mahlon and S. J. Parke, *Spin Correlation Effects in Top Quark Pair Production at the LHC*, Phys.Rev. **D81** (2010) 074024, arXiv:1001.3422 [hep-ph].

[64] S. J. Parke and Y. Shadmi, *Spin correlations in top quark pair production at e^+e^- colliders*, Phys.Lett. **B387** (1996) 199–206, arXiv:hep-ph/9606419 [hep-ph].

[65] C. Kao, G. Ladinsky, and C. Yuan, *Leading electroweak corrections to the production of heavy top quarks at hadron colliders*, arXiv:hep-ph/9305270 [hep-ph].

[66] G. Mahlon and S. J. Parke, *Maximizing spin correlations in top quark pair production at the Tevatron*, Phys.Lett. **B411** (1997) 173–179, arXiv:hep-ph/9706304 [hep-ph].

[67] G. Mahlon, *Spin issues in t anti-t production and decay*, arXiv:hep-ph/9811281 [hep-ph].

[68] CDF Collaboration, CDF, *Measurement of $t\bar{t}$ Helicity Fractions and Spin Correlation Using Reconstructed Lepton+Jets Events*, .

[69] D0 Collaboration, K. Bloom, *Measurements of Spin Correlation in $t\bar{t}$ Events at D0*, arXiv:1109.3691 [hep-ex].

[70] ATLAS Collaboration, G. Aad et al., *Observation of spin correlation in $t\bar{t}$ events from pp collisions at sqrt(s) = 7 TeV using the ATLAS detector*, Phys.Rev.Lett. **108** (2012) 212001, arXiv:1203.4081 [hep-ex].

[71] *Measurement of Spin Correlations in ttbar production*, Tech. Rep. CMS-PAS-TOP-12-004, CERN, Geneva, 2012.

[72] K. Smolek, *Measurement of spin correlations of top-antitop pairs in the ATLAS experiment and influence of heavy Higgs boson*, Czechoslov. J. Phys. **54 suppl .** (2004) A451–4.

[73] M. Cacciari, G. P. Salam, and G. Soyez, *The anti- k t jet clustering algorithm*, Journal of High Energy Physics **2008** (2008) no. 04, 063. http://stacks.iop.org/1126-6708/2008/i=04/a=063.

[74] D. W. Miller, A. Schwartzman, and D. Su, *Jet-Vertex Association Algorithm*, Tech. Rep. ATL-COM-PHYS-2008-008, CERN, Geneva, Jan, 2008.

[75] *Commissioning of the ATLAS high-performance b-tagging algorithms in the 7 TeV collision data*, Tech. Rep. ATLAS-CONF-2011-102, CERN, Geneva, Jul, 2011.

[76] ATLAS Collaboration, G. Aad et al., *Expected Performance of the ATLAS Experiment - Detector, Trigger and Physics*, arXiv:0901.0512 [hep-ex].

[77] S. Frixione and B. R. Webber, *Matching NLO QCD computations and parton shower simulations*, JHEP **0206** (2002) 029, arXiv:hep-ph/0204244 [hep-ph].

[78] S. Frixione, P. Nason, and G. Ridolfi, *A Positive-weight next-to-leading-order Monte Carlo for heavy flavour hadroproduction*, JHEP **0709** (2007) 126, arXiv:0707.3088 [hep-ph].

[79] M. L. Mangano, M. Moretti, F. Piccinini, R. Pittau, and A. D. Polosa, *ALPGEN, a generator for hard multiparton processes in hadronic collisions*, JHEP **0307** (2003) 001, arXiv:hep-ph/0206293 [hep-ph].

[80] M. L. Mangano, M. Moretti, and R. Pittau, *Multijet matrix elements and shower evolution in hadronic collisions: $Wb\bar{b}$ + n jets as a case study*, Nucl.Phys. **B632** (2002) 343–362, arXiv:hep-ph/0108069 [hep-ph].

[81] J. Butterworth, J. R. Forshaw, and M. Seymour, *Multiparton interactions in photoproduction at HERA*, Z.Phys. **C72** (1996) 637–646, arXiv:hep-ph/9601371 [hep-ph].

[82] T. Sjostrand, S. Mrenna, and P. Z. Skands, *A Brief Introduction to PYTHIA 8.1*, Comput.Phys.Commun. **178** (2008) 852–867, arXiv:0710.3820 [hep-ph].

[83] A. Kupco, *Cluster hadronization in HERWIG 5.9*, arXiv:hep-ph/9906412 [hep-ph].

[84] GEANT4 Collaboration, S. Agostinelli et al., *GEANT4: A Simulation toolkit*, Nucl.Instrum.Meth. **A506** (2003) 250–303.

[85] E. Richter-Was, D. Froidevaux, and L. Poggioli, *ATLFAST 2.0 a fast simulation package for ATLAS*, Tech. Rep. ATL-PHYS-98-131, CERN, Geneva, Nov, 1998.

[86] M. Bahr, S. Gieseke, M. Gigg, D. Grellscheid, K. Hamilton, et al., *Herwig++ Physics and Manual*, Eur.Phys.J. **C58** (2008) 639–707, arXiv:0803.0883 [hep-ph].

[87] ATLAS Collaboration, G. Aad et al., *Measurement of the top quark-pair production cross section with ATLAS in pp collisions at* $\sqrt{s} = 7$ *TeV*, Eur.Phys.J. **C71** (2011) 1577, arXiv:1012.1792 [hep-ex].

[88] M. Aliev, H. Lacker, U. Langenfeld, S. Moch, P. Uwer, et al., *HATHOR: HAdronic Top and Heavy quarks crOss section calculatoR*, Comput.Phys.Commun. **182** (2011) 1034–1046, arXiv:1007.1327 [hep-ph].

[89] A. Martin, W. Stirling, R. Thorne, and G. Watt, *Parton distributions for the LHC*, Eur.Phys.J. **C63** (2009) 189–285, arXiv:0901.0002 [hep-ph].

[90] A. Martin, W. Stirling, R. Thorne, and G. Watt, *Uncertainties on alpha(S) in global PDF analyses and implications for predicted hadronic cross sections*, Eur.Phys.J. **C64** (2009) 653–680, arXiv:0905.3531 [hep-ph].

[91] M. Cacciari, M. Czakon, M. Mangano, A. Mitov, and P. Nason, *Top-pair production at hadron colliders with next-to-next-to-leading logarithmic soft-gluon resummation*, Phys.Lett. **B710** (2012) 612–622, arXiv:1111.5869 [hep-ph].

[92] M. Czakon and A. Mitov, *Top++: A Program for the Calculation of the Top-Pair Cross-Section at Hadron Colliders*, arXiv:1112.5675 [hep-ph].

[93] G. Ridolfi and S. Forte, *Renormalization and factorization scale dependence of observables in QCD*, Journal of Physics G: Nuclear and Particle Physics **25** (1999) no. 7, 1555. http://stacks.iop.org/0954-3899/25/i=7/a=351.

[94] T. Sjostrand, S. Mrenna, and P. Z. Skands, *PYTHIA 6.4 Physics and Manual*, JHEP **0605** (2006) 026, arXiv:hep-ph/0603175 [hep-ph].

[95] P. M. Nadolsky, H.-L. Lai, Q.-H. Cao, J. Huston, J. Pumplin, et al., *Implications of CTEQ global analysis for collider observables*, Phys.Rev. **D78** (2008) 013004, arXiv:0802.0007 [hep-ph].

[96] A. Martin, W. Stirling, R. Thorne, and G. Watt, *Parton distributions for the LHC*, Eur.Phys.J. **C63** (2009) 189–285, arXiv:0901.0002 [hep-ph].

[97] S. Forte, L. Garrido, J. I. Latorre, and A. Piccione, *Neural network parametrization of deep inelastic structure functions*, JHEP **0205** (2002) 062, arXiv:hep-ph/0204232 [hep-ph].

[98] M. Whalley, D. Bourilkov, and R. Group, *The Les Houches accord PDFs (LHAPDF) and LHAGLUE*, arXiv:hep-ph/0508110 [hep-ph].

[99] M. Botje, J. Butterworth, A. Cooper-Sarkar, A. de Roeck, J. Feltesse, et al., *The PDF4LHC Working Group Interim Recommendations*, arXiv:1101.0538 [hep-ph].

[100] ATLAS Collaboration, G. Aad et al., *Improved luminosity determination in pp collisions at sqrt(s) = 7 TeV using the ATLAS detector at the LHC*, arXiv:1302.4393 [hep-ex].

[101] ATLAS Collaboration, G. Aad et al., *Jet energy measurement with the ATLAS detector in proton-proton collisions at* $\sqrt{s} = 7$ *TeV*, Eur.Phys.J. **C73** (2013) 2304, arXiv:1112.6426 [hep-ex].

[102] *Muon Momentum Resolution in First Pass Reconstruction of pp Collision Data Recorded by ATLAS in 2010*, Tech. Rep. ATLAS-CONF-2011-046, CERN, Geneva, Mar, 2011.

[103] *Electron performance measurements with the ATLAS detector using the 2010 LHC proton-proton collision data*, The European Physical Journal C **72** (2012) no. 3, 1–46. http://dx.doi.org/10.1140/epjc/s10052-012-1909-1.

[104] N. Kidonakis, *Next-to-next-to-leading-order collinear and soft gluon corrections for t-channel single top quark production*, Phys.Rev. **D83** (2011) 091503, arXiv:1103.2792 [hep-ph].

[105] N. Kidonakis, *NNLL resummation for s-channel single top quark production*, Phys.Rev. **D81** (2010) 054028, arXiv:1001.5034 [hep-ph].

[106] N. Kidonakis, *Two-loop soft anomalous dimensions for single top quark associated production with a W- or H-*, Phys.Rev. **D82** (2010) 054018, arXiv:1005.4451 [hep-ph].

[107] A. Martin, W. Stirling, R. Thorne, and G. Watt, *Parton distributions for the LHC*, Eur.Phys.J. **C63** (2009) 189–285, arXiv:0901.0002 [hep-ph].

[108] G. J. Feldman and R. D. Cousins, *A Unified approach to the classical statistical analysis of small signals*, Phys.Rev. **D57** (1998) 3873–3889, arXiv:physics/9711021 [physics.data-an].

[109] M. Cacciari, S. Frixione, M. L. Mangano, P. Nason, and G. Ridolfi, *Updated predictions for the total production cross sections of top and of heavier quark pairs at the Tevatron and at the LHC*, JHEP **0809** (2008) 127, arXiv:0804.2800 [hep-ph].